2010

ASSESSMENT OF WIND-INDUCED RESPONSE AND DRIVABILITY OF THE CONFEDERATION BRIDGE

Bilal Bakht

ASSESSMENT OF WIND-INDUCED RESPONSE AND DRIVABILITY OF THE CONFEDERATION BRIDGE

(Spine Title: Wind-Induced Response & Drivability of Confederation Bridge)

Thesis Format: Integrated Article

by

Bilal Bakht

Graduate Program

in

Civil and Environmental Engineering

Submitted in partial fulfillment

of the requirements for the degree of

Doctor of Philosophy

School of Graduate and Postdoctoral Studies

The University of Western Ontario

London, Ontario

Canada

THE UNIVERSITY OF WESTERN ONTARIO

SCHOOL OF GRADUATE AND POSTDOCTORAL STUDIES

CERTIFICATE OF EXAMINATION

NSERC-IPS Industrial Supervisor

_____

J. P. C. King

Supervisor

_____

F. M. Bartlett

_____

H. P. Hong

Supervisory Committee

Examiners

_____

J. P. Newhook

_____

E. Savory

_____

J. Galsworthy

_____

W. Zhou

The thesis by

Bilal Bakht

entitled:

Assessment of Wind-Induced Response and Drivability of the Confederation Bridge

is accepted in partial fulfillment of the

requirements for the degree of

Doctor of Philosophy

Date: _____

_____

Chair of the Thesis Examination Board

ABSTRACT

The Confederation Bridge is a 13 km long precast concrete structure, constructed between 1993 and 1997, comprised of 43 – 250 m spans in an alternating rigid frame/cantilevered drop-in span arrangement. Wind studies were conducted in the early '90s at the Boundary Layer Wind Tunnel Laboratory to predict the design wind speed and associated design wind loads for the bridge. The dynamic wind loads were developed using full-aeroelastic model test data for the first time. The bridge owners implemented a comprehensive bridge monitoring programme to document the interaction of the bridge with its environment by installing a complex instrumentation system along a one kilometre section of the bridge in 1998. The research reported in this thesis analyses this dataset, augmenting it as necessary with data from other instrumentation on the bridge, to determine the accuracy of the original design wind speeds and wind loads predicted in 1994. Based on ten years of wind records it is shown that the design ten-minute mean wind speed with a 100-year return period is within 1.5% of the 1994 design value, and that the bridge has been subjected to this design event once during the November 7, 2001 storm. The dynamic load effects predicted using the 1994 loads adjusted for the actual damping of the prototype are 6% and 28-58% greater than those determined from the on-site monitoring data for the transverse and vertical effects, respectively. The research therefore validates the aerodynamic model-based methodology developed in 1994 which can be used to derive wind loads using on-site monitoring or full-aeroelastic model test data. A second research topic is the challenge of driving high lightly loaded vehicles across the bridge during wind storms. Data are presented from an instrumented bus and truck-trailer that were driven repeatedly across the bridge during a severe windstorm. The drivers' perceptions of the severity of the wind effect on the control of the vehicle are strongly correlated to the transverse accelerations that they are subjected to, which increase with increasing vehicle speed. Current operating procedures that restrict high-sided vehicles from crossing the bridge when the wind speed exceeds 70 km/h in any direction were not perceived to be unsafe by either participating driver. The response of a bus and a truck-trailer crossing the bridge under wind conditions are different: the truck-trailer seems to be much more susceptible to roll-over than the bus.

Keywords: Aerodynamic damping, dynamic wind loads, equivalent static loads, full-aeroelastic model, on-site monitoring, wind-induced vehicle roll-over.

CO-AUTHORSHIP

All of the work presented in this thesis was performed by Bilal Bakht. Chapters 2 to 6 of the thesis will be submitted to scholarly journals as manuscripts co-authored by Bilal Bakht, J. Peter C. King and F. M. Bartlett.

ACKNOWLEDGEMENTS

I feel privileged to have worked with two charismatic mentors, Dr. Peter King and Prof. Michael Bartlett, who possess uncanny advisory skills. Their enthusiasm kept my spirit high and urged me to do more. They provided me the room to grow as a researcher and taught me a great deal about research methodology and its application to solve real world problems. In four years, I met Dr. King almost every day and occasionally several times a day to discuss my research. Knowing that wind engineering was new to me he always welcomed me and taught complex ideas using simple approach. I can't thank him enough for his unrelenting guidance and support. Prof. Bartlett is a true researcher and a dedicated advisor. He not only focused on research but how it is presented. He read my thesis several times with diligence and gave constructive feedback. His favourite question "so what" made me ponder over every line I wrote. He believes a good researcher must acquire good technical writing skills and so encouraged me to master both traits. His pearls of wisdom are an asset for me.

There are several other people who made possible the work described in this thesis. Mike Mikitiuk and Gary Lythe explained the underlying theory to characterize wind climate and return period using field data. Dave Morrish and Adrian Costache helped with MATLAB programming and provided useful tips to handle gigabytes of on-site monitoring data. Dr. Eric Ho offered valuable suggestions to present wind tunnel data. Dr. Lingzhe Kong helped with the wind-tunnel proximity model. Gerry Dafoe and Chris Gauvin helped in instrumenting and testing the model. Anthony Burggraaf provided the technical support required to keep my computer running and Karen Norman helped with administrative work. I am grateful to all for their guidance and support.

I acknowledge the support of the staff at the bridge site during several visits to the on-site monitoring programme. The professional drivers, bridge staff and RCMP personnel who participated in the drivability study are also acknowledged. I am also thankful to John Egan, technical specialist at the Public Works and Government Services Canada

(PWGSC), for reconfiguring the monitoring programme during the passage of Hurricane Noel which provided valuable data for analysis.

I would like to thank my industrial partner Strait Crossing Bridge Limited (SCBL), who provided on-site monitoring data and sponsored several visits to the bridge site. In particular I would like to thank Mr. Donald McGinn, Director of Engineering and Maintenance for SCBL for his encouragement and continued support of my research. The sponsoring of two scholarship applications to Natural Sciences and Research Council (NSERC) of Canada, and Mathematics of Information Technology and Complex Systems (MITACS) is greatly acknowledged. The generous funding through various sources including NSERC, MITACS, Western Engineering Scholarship (WES), Western Graduate Research Scholarship (WGRS), Alan G. Davenport Award, Graduate Thesis Research Awards Fund and supervisors, made this possible and is greatly acknowledged.

Finally, I would like to thank my wife, Rabia, and kids, Hooria and Abdul Hadi, for their patience and sacrifice. Without their support this couldn't have been accomplished.

TABLE OF CONTENTS

LIST OF TABLES

LIST OF FIGURES

NOMENCLATURE

A	cross-sectional area
A_v	projected area of vehicle exposed to wind
a, b, c	regression parameters estimated by regression analysis
$a_j(x)$	modal load distribution function for the j^{th} mode
a_m	transverse acceleration of Gross Vehicle Mass (GVM)
$a_{r_{jmax}}$	maximum RMS acceleration for the j^{th} mode
a_v	transverse vehicle acceleration
B	width of the bridge
b_v	out-to-out distance between wheels on an axle
C	regression constant
C_d	static drag coefficient
C_d'	normalized static drag coefficient
C_{dyn_j}	dynamic load coefficient for the j^{th} mode
C_e	exposure coefficient
$\overline{C}_m$	mean overturning moment coefficient
C_{xy}	magnitude squared coherence
D	concrete box girder depth
E	modulus of elasticity
E_c	concrete modulus of elasticity
$E_c(t)$	concrete modulus of elasticity at age t
$E_c(28)$	28-day elastic modulus of concrete
F_d'	normalized static force
F_r	Froude Number
FS	factor of safety
Fs	sampling frequency
f	frequency
f_j	natural frequency of vibration for j^{th} mode
g	peak factor, also acceleration due to gravity
h	height above Mean Sea Level (MSL)
h_m	distance from the road surface to the centre of Gross Vehicle Mass (GVM)
h_v	overall height of the vehicle
I, J	node numbers
$I_{j_{max}}$	maximum modal displacement coefficient for j^{th} mode of vibration
$I_j(x)$	modal displacement coefficient function for j^{th} mode of vibration
$\overline{I}_u$	mean longitudinal turbulence intensity
I_u, I_v	longitudinal and vertical turbulence intensities
I_2, I_3	flexural inertias

J	torsional inertia
j	mode number
k	calibration factor
k_x, k_y, k_z	longitudinal, vertical and transverse stiffnesses, respectively
k_{xx}, k_{zz}	torsional stiffnesses about x and z axes, respectively
L	span length, also characteristic length
L_{c_j}	maximum modal load for j^{th} mode corrected for prototype damping
L_j	maximum modal load for j^{th} mode
M_{dy}	dynamic overturning moment
M_o	overturning moment
M_s	stabilising moment
M_{st}	static overturning moment
nfft	number of Fast Fourier Transform
q	mean wind velocity pressure
q'	unit wind pressure
q_{ref}	reference wind velocity pressure at 10 m above Mean Sea Level (MSL)
R^2	coefficient of determination
$\overline{R}$	mean response
$\hat{R}$	peak response
R_b	background response
R_{max}	maximum response
R_{r_j}	resonant response for mode j
R_{RMS}	RMS response
R_{t_d}	total dynamic response
R_x, R_y, R_z	rotational boundary condition codes for the x, y and z axes, respectively
$S(f)$, S_{xx}, S_{yy}	power spectral density
$\overline{T}$	mean pier tilt
$\overline{T}'$	normalized mean pier tilt
T_N	normalized time
T_x, T_y, T_z	translation boundary condition codes in the x, y and z directions, respectively
t	age of concrete in days
$V, \overline{V}, V_{mean}$	mean wind speed
V^*	reduced velocity
$V(h)$	mean wind speed at elevation h above Mean Sea Level (MSL)
V_{max}	maximum wind speed
$\overline{V}_{P31}$	mean wind speed at the Pier 31-32 anemometer
$\overline{V}_{P20}$	mean wind speed at the Pier 20 anemometer
V_{ref}	reference mean wind speed
V_{rms}	RMS wind speed

$W_{dyn\,j(x)}$	dynamic wind load for j^{th} mode at location x along the span
w	load per unit length
x	length coordinate along bridge axis
z_o	roughness length
z_{ref}	reference height above Mean Sea Level (MSL)
α	exponent parameter determined by regression
β	constant parameter determined by regression
Δ	beam deflection
$\Delta_{j_{max}}$	maximum modal displacement for j^{th} mode
Δ_{n_j}	normalized modal response for j^{th} mode
$\Delta_x, \Delta_y, \Delta_z$	displacements in the x, y and z directions, respectively
ζ_{a_j}	aerodynamic damping for j^{th} mode
ζ_{am_j}	model aerodynamic damping for j^{th} mode
ζ_{ap_j}	prototype aerodynamic damping for j^{th} mode
ζ_j	structural damping for j^{th} mode
ζ_{m_j}	model structural damping for j^{th} mode
ζ_{p_j}	prototype structural damping for j^{th} mode
ζ_{tm_j}	total model damping for j^{th} mode
θ	wind azimuth
$\theta_x, \theta_y, \theta_z$	rotation about the x, y and z axes, respectively
λ_a	acceleration scaling factor
λ_{BM}	bending moment scaling factor
λ_{CwE}	warping stiffness scaling factor
λ_{EA}	axial stiffness scaling factor
λ_{EI}	flexural stiffness scaling factor
λ_F	force scaling factor
$\lambda_{F/L}$	force per unit length scaling factor
λ_{GC}	torsional stiffness scaling factor
λ_I	mass moment of inertia scaling factor
$\lambda_{I/L}$	mass moment of inertia per unit length scaling factor
λ_L	length scaling factor
λ_m	mass scaling factor
$\lambda_{m/L}$	mass per unit length scaling factor
λ_T	time scaling factor
λ_V	wind speed scaling factor
λ_ζ	damping scaling factor

λ_ρ	density scaling factor
ν	Poisson's ratio
ρ	air density at sea level (1.25 kg/m^3)
σ^2	variance
$\sigma(h)$	RMS wind speed at height h above Mean Sea Level (MSL)
σ_V	RMS wind speed
ω_j	circular frequency for j^{th} mode of vibration

1. INTRODUCTION

1.1 On-Site Monitoring of Long-Span Bridges

The on-site monitoring of long-span bridges is a relatively new area of bridge engineering. With increasing spans and innovative designs that have surpassed the limits set by bridge design codes, it is imperative to protect the considerable investment in these bridges and to ensure safe and secure transportation links for the users. On-site monitoring is required to answer questions regarding: as-constructed structural properties, response to traffic, creep, shrinkage, thermal effects, wind conditions and response, earthquake response, fatigue, etc. The scope of an on-site monitoring programme depends on topography, traffic loading, bridge type and geographical location; however, almost all long-span bridges are wind sensitive and so require a wind monitoring component as part of the monitoring programme.

The important questions regarding the safety of a long span bridge with regard to wind excitation are related to serviceability, strength and aerodynamic stability. Wind tunnel testing of dynamically scaled models can assist the designer by providing estimates of the behaviour under a variety of wind conditions. The opportunity to observe full-scale behaviour under wind conditions approaching the stability limits of the structure, however, rarely occurs in practice. Only a handful of long-span bridges are monitored for extended durations of 10 to 15 years even though the critical wind speeds associated with these structures involve return periods of several hundred years. This makes the likelihood of capturing significant responses rather remote [King et al. 2000a].

The most notable bridges currently being monitored are the Tsing Ma, Ting Kau and Kap Shui Mun Bridges in Hong Kong, which have a combined Wind and Structural Health Monitoring System [Yeung et al. 1995] that archives data from more than 900 sensors attached to critical bridge locations. These bridges are wind-sensitive structures located in a typhoon region, therefore, wind monitoring is considered to be an important component in their maintenance and evaluation. The accelerometer data quantify the dynamic

response for a range of wind speeds and are compared to the wind tunnel responses to detect any incipient strong motion. The accelerometer data are also used to determine mode shapes and natural frequencies which are compared to the values assumed at the design stage. Any changes in the dynamic properties could be indicative of changes in condition of the structures, such as fatigue cracking or overstress conditions leading to failure of critical components [Flint et al. 1995]. The monitoring system has been in service for over 10 years. The system is well-maintained and is one of the most comprehensive systems in the world. No reported work, however, computes wind loads from the on-site monitoring data for comparison with the loads assumed for the bridge design.

The Bronx-Whitestone Bridge in New York was constructed in the late '30s, an era when wind tunnel testing of bridges was not performed, and consequently has had a history of minor oscillations in wind. A number of structural modifications have been conducted to reduce the amplitudes of these motions. The dead load of these retrofits increased cable stresses to levels that were compromising the desired useful life of the structure. Thus the bridge superstructure underwent a complete retrofit in 2000 based on wind studies carried out at the Boundary Layer Wind Tunnel Laboratory (BLWTL) [King et al. 2000b]. The BLWTL also installed a comprehensive, full-scale monitoring system, which included three accelerometers, six strain gauges and a wind anemometer to monitor the bridge response through out the rehabilitation period to verify the changes in aerodynamic and structural behaviour of the reconstructed bridge. After completion of the bridge rehabilitation, the monitoring programme entered a second phase to monitor long-term dynamic properties and the response to wind action [King et al. 2000a]. The monitoring programme was expanded to include four additional accelerometers and a second anemometer and is still operational. The monitoring has confirmed the predicted bridge behaviour during several wind storms of exceptional severity, however, the data have not been used to verify the wind loads assumed for the bridge design derived at the BLWTL in 2000 [King et al. 2000b].

The Millau Viaduct in France is a long-span bridge that holds several world records. It has the highest bridge piers, towers and road deck in the world [Buonomo et al. 2004]. The viaduct is exposed to severe winds, strong gusts and adverse funneling effects from the valley; therefore, wind loading was a critical factor in the design of the bridge [Ben Fredj et al. 2004]. Comprehensive wind tunnel studies were carried out to find the stresses and deflections of the structure under wind loading. To monitor the wind-induced response of viaduct during construction and during its service life a network of accelerometers, anemometers, inclinometers, and temperature sensors were fixed to the piers, deck, pylons, stay-cables, foundation shafts and foundation slabs [Buonomo et al. 2004]. The observed wind-induced bridge response has validated the design assumptions [Scott 2010]; however, the data have not been used to derive the actual wind loads for comparison with the bridge design loads.

Other notable bridges that are monitored include the Donghai Bridges [Sun et al. 2005] and the Binzhou Yellow River Highway Bridge [Li et al. 2006] in China, the Akashi Kaikyo Bridge [Kashima et al. 2001] in Japan, the Rio-Antirion Bridge [Stathopoulos-Vlamis 2008] in Greece, the Humber Bridge [Ashkenazi and Roberts 1997] in UK, and the Golden Gate [Kim et al. 2007] and Sunshine Skyway [Shahawy and Arockiasamy 1996] bridges in USA. The wind excitation data from the monitoring systems for these bridges are used to monitor wind speeds, measure dynamic properties and wind-induced bridge responses. However, no reported efforts have been made to use these data to corroborate wind loads acting on the bridge with those assumed at the design stage. The present research intends to address this knowledge gap using on-site monitoring data from the Confederation Bridge.

1.2 On-Site Monitoring of the Confederation Bridge

The Confederation Bridge connecting Prince Edward Island and New Brunswick across Northumberland Strait, shown in Figure 1.1, is a 13 km long precast concrete structure constructed between 1993 and 1997. The main superstructure is comprised of 43 – 250 m spans in an alternating rigid frame/cantilevered drop-in span arrangement. A detailed

description of the bridge, including its design and construction, has been presented by Tadros [1997]. Wind studies were conducted in the early '90s at the Boundary Layer Wind Tunnel Laboratory (BLWTL) to predict the 100-year wind speed and associated wind loads for the design of the bridge. Traditionally, section models are used to obtain wind loading information; however, since the Confederation Bridge has a varying deck cross-section the section model approach could not be used. Therefore, a new methodology was developed for the derivation of dynamic wind loads using the full-aeroelastic model of the Confederation Bridge [King et al. 1994, King and Davenport 1994a, King et al. 1995]. Project-specific load factors, load combinations and resistance factors were derived concurrently [MacGregor et al. 1997].

Recognising the scale and novelty of the structure, the owners of the bridge, Strait Crossing Development Inc. (SCDI) and Public Works and Government Services Canada (PWGSC), jointly implemented a comprehensive bridge monitoring programme to capture and archive the interaction of the bridge with its environment. The complex instrumentation system shown in Figure 1.2, including accelerometers, tiltmeters, force and displacement transducers, anemometers, strain gauges and thermocouples, was installed along a one-kilometre section of the bridge between Piers 30 and 33, on the western approach to the central "navigation" spans. The dynamic motions of the bridge are captured by 76 accelerometers located along the continuous span between Piers 31 and 32, the three cantilevers beside Piers 30, 31 and 32, the drop-in span between Piers 30 and 31, and at Piers 30, 31, 32 and 33. Tiltmeters at Piers 31 and 32 measure pier rotations in the transverse and longitudinal directions. Anemometers mounted atop the lamp standards located at five different locations along the bridge, including two along the span between Piers 31 and 32, record wind speed and direction data that are archived as statistical summaries and time histories. Six High Speed Data Loggers (HSDLs) [Montreuil 1999b] and nine Slow Speed Data Loggers (SSDLs) [Montreuil 1999a] are connected by a fibre-optic network to a central computer system that transmits the data through the internet to various research institutions for archiving and analysis [Cheung et al. 1997]. The bridge monitoring system has been operational since 1998, providing statistical and time history data for different wind, ice and traffic conditions.

The initial aims of the monitoring programme were focused on the ice and traffic loads and the post-construction structural properties. An opportunity to assess the performance of the bridge under extreme winds and hence investigate the accuracy of the original design loads was presented due to the occurrence of several winter storms of exceptional severity [King et al. 2007]. Strait Crossing Bridge Limited (SCBL) provided the BLWTL with on-site monitoring data obtained from 1998 to 2007 to compare the actual bridge response with that assumed at the design stage. The present study will take a new approach and use on-site monitoring data from the Confederation Bridge to derive wind loads, for the first time, that will be compared to loads assumed for the design of the bridge in the early 90's based on wind studies carried out at the BLWTL [King et al. 1994, King and Davenport 1994a, King et al. 1995]. This will be the first time that wind loads will have been derived from the observed response of the full-scale structure, and the first time that the accuracy of wind loadings determined from aeroelastic model studies will be investigated.

1.3 Drivability

It has long been recognized that it can be unsafe to drive lightly loaded high-sided vehicles, including buses, across high-level bridges during strong wind conditions [Baker 1986, 1987a & b, and 1998, Coleman and Baker 1990, and 1992, Huang et al. 1998, King et al. 1994, Pritchard 1985, and PWC 1988]. The procedures used around the world to regulate traffic on exposed bridges under high wind conditions vary significantly and have evolved over many years to suit conditions prevailing at existing bridge sites. This knowledge of practical experience is generally adapted for future bridges [MBA 1999, Pritchard 1985, and PWC 1988]. Knowing the complexity of problem, extensive research has been carried out by researchers [Baker 1986, 1987a & b, 1991a, b, & c, and 1998, Bearman and Mullarkey 1994, Coleman and Baker 1990, and 1992, Emmelmann 1986, Ryan and Dominy 1998 and Stewart 1977] to study wind effects on high-sided vehicles. These studies are mainly based on theoretical models and wind tunnel test data. For example, Baker [1986] has proposed an analytical model to predict accident wind speeds for different accident types over a wide range of yaw angles, provided vehicle

aerodynamic coefficients are known in detail from wind tunnel tests. The different accident types include overturning, sideslip and rotation. Based on the analysis results, Baker [1987a] proposed a "two level" system of control with high sided vehicle speed restricted to 10 m/s at a wind gust speed of 17.5 m/s and vehicle movement stopped completely at a wind gust speed of 22.5 m/s. The proposed limits do not account for wind azimuth.

Generalizing the closure limits for all bridge types without considering their topography and traffic loading seems unrealistic. Further, the first level of control (vehicle speed restricted to 10 m/s at a wind gust speed of 17.5 m/s) should essentially be related to driver's perception of the wind effect and degree of control of the vehicle. Also, experience shows for most bridges winds blowing along the bridge axis do not require speed restriction or bridge closure to high-sided vehicles and it's only the yaw or cross winds that are critical to vehicle roll-over [Pritchard 1985].

Extensive research has been conducted to quantify acceleration limits associated with motion perceived by pedestrians on pedestrian bridges [CSA 2006, Kasperski 2006, Pimental et al. 2001] and drivers on highway bridges [Oehler 1957, Wright and Green 1964, Shahanadi 1977]. Wind-tunnel studies have been conducted to determine average wind speeds that could roll-over stationary high-sided vehicles for the Bronx-Whitestone Bridge [King and Kong 2001]. There are no studies, however, that address the driver's perceptions of motion and degree of control of high-sided transport vehicles under strong wind conditions. Despite the high cost involved, SCBL decided to conduct a preliminary study to investigate how the wind direction and speed, vehicle speed, and travelled lane or vehicle travelling along the bridge centreline may influence the driver's perception of motion and degree of control.

SCBL currently closes the bridge to all traffic when the mean wind speed from any direction exceeds 70 km/h, which occurred on average 42.6 hours per year between 2002 and 2006. Cheung and Chan [2010] recently proposed that the limiting wind speed to trigger bridge closure could be increased to 90 km/h, based on vehicle responses

predicted using a complex theoretical model. Cheung and Chan [2010] do not seem to differentiate between the stability and operational limits for the high-sided vehicles travelling across the Confederation Bridge. The authors have implicitly used a bus model for the vehicle instability analysis and the factors of safety against roll-over are considered representative of all high-sided vehicles. These claims are based on computer simulations and are yet to be verified through field experiments.

1.4 Research Objectives

The primary objectives of the present study are threefold, namely

i) To investigate the accuracy of the wind loads originally specified for the design of the Confederation Bridge [King et al. 1994, King and Davenport 1994a, King et al. 1995], using on-site monitoring data and new wind tunnel test data, to validate the state-of-the-art algorithms and procedures developed for deriving wind loads from bridge test data obtained from aerodynamic model testing.

ii) To validate the 100-year wind speed specified for the design of the Confederation Bridge [King et al. 1994], using wind data from the on-site monitoring programme which is imperative for the derivation of wind loads.

iii) To investigate the challenge of driving large light vehicles across the Confederation Bridge during wind storms and to study the effect of extreme winds on the drivers' control of light high-sided vehicles, including buses, crossing the bridge, as a basis for a rational refinement of current bridge closure policies.

1.5 Description of this Study

The organization of the material presented in this thesis is outlined in Figure 1.3. Although this is an Integrated-Article Thesis, as detailed below, several of the chapters

are linked. Specifically, Chapter 2 is a necessary basis for Chapter 3 which, with Chapter 4, provides the foundation for Chapter 5.

Chapter 2 describes the analysis of the 1998-2007 wind data from the anemometers located on the bridge deck atop lamp standards [Montreuil 1999a]. The data are used to characterize the wind climate for the Northumberland Strait and investigate the accuracy of the 100-year wind speed and turbulence conditions originally specified for the design of the Confederation Bridge by King et al. [1994].

Chapter 3 describes the analysis of the accelerometer data obtained from the on-site monitoring programme. The wind data from Chapter 2 are correlated with the accelerometer data to determine the total and modal dynamic responses of the bridge. The accelerometer data are also used to estimate dynamic characteristics of the bridge including frequencies, mode shapes and damping, which are compared to values reported by other researchers [Londoño 2006, Brown and Bruce 1997].

Chapter 4 describes new wind tunnel testing and data analysis for the full-aeroelastic model of the Confederation Bridge carried out in 2009 as part of the current research programme. The data are used to derive the equivalent full-scale total and modal dynamic responses of the bridge. The dynamic characteristics of the wind tunnel model are estimated to establish scaling parameters, which are necessary to translate model-scale results to the full-scale prototype.

The modal responses derived in Chapters 3 and 4 are used to compute the dynamic wind loads for the Confederation Bridge in Chapter 5. The total dynamic responses predicted using loads derived from the on-site monitoring data and the wind tunnel test data are compared to the 1994 wind tunnel predictions [King et al. 1994, King and Davenport 1994a, King et al. 1995]. In addition, the results of the tiltmeter data analysed by Bruce and Croasdale [2001] are used to determine the static force coefficients and are compared to the values used for the bridge design [JMI-Stanley 1995].

Finally, Chapter 6 presents an empirical study of the drivers' perception of the difficulty to control light high-sided vehicles on the Confederation Bridge during severe crosswinds. The driver's perception of the vehicle control difficulty under different vehicle and wind conditions are quantified in terms of the vehicle accelerations observed in the region of the driver's head. A crude estimate of the factor of safety for a bus or truck-trailer overturning due to dynamic wind loads is also derived from the accelerometer data.

1.6 Thesis Format

This thesis is prepared in accordance with the regulations for an Integrated-Article Thesis as set out in the "Thesis Regulation Guide" by the School of Graduate and Postdoctoral Studies at the University of Western Ontario [SGPS 2010]. Each chapter, except for the first and last chapters, is presented in a paper format without an abstract but with its own bibliography. Table and figures for each chapter are grouped at the end of each chapter after the bibliography. The nomenclature is consistent throughout the thesis, and is listed in the prefatory pages.

A considerable quantity of material, typically details of calculation methods, explanatory figures and Ethics Approval for the drivability study, is presented in appendices which follow the last chapter. Each appendix is identified by a number, which indicates which chapter it pertains to, and a letter. For example, Appendix 6A is the first of the four appendices containing material that relates to Chapter 6. References cited in an appendix are included in the list at the end of the associated chapter.

The System International (SI) system of units is used through out the thesis.

1.7 References

Ashkenazi, V., Roberts, G. W. 1997. Experimental Monitoring of the Humber Bridge Using GPS. *Proceedings of the Institution of Civil Engineers*, 120:4, 177-182.

Baker, C. J. 1986. A Simplified Analysis of Various Types of Wind-Induced Road Vehicle Accidents. *Journal of Wind Engineering and Industrial Aerodynamics*, 22: 69-85.

Baker, C. J. 1987a. Measures to Control Vehicle Movement at Exposed Sites during Windy Periods. *Journal of Wind Engineering and Industrial Aerodynamics*, 25: 151-161.

Baker, C. J. 1987b. High Sided Articulated Road Vehicles in Strong Cross Winds. *Journal of Wind Engineering and Industrial Aerodynamics*, 31: 67-85.

Baker, C. J. 1991a. Ground Vehicles in High Cross Winds Part I: Steady Aerodynamic Forces. *Journal of Fluids and Structures,* 5: 69-90.

Baker, C. J. 1991b. Ground Vehicles in High Cross Winds Part II: Unsteady Aerodynamic Forces. *Journal of Fluids and Structures,* 5: 91-111.

Baker, C. J. 1991c. Ground Vehicles in High Cross Winds Part III: The Interaction of Aerodynamic Forces and the Vehicle System. *Journal of Fluids and Structures,* 5: 221-241.

Baker, C. J. 1998. The Effects of High Winds on Vehicle Behaviour. *Proceedings of the International Symposium on Advances in Bridge Aerodynamics,* Copenhagen, Denmark, pp. 267-282.

Bearman, P. W., and Mullarkey, S. P. 1994. Aerodynamic Forces on Road Vehicles due to Steady Side Winds and Gusts, *Road Vehicle Aerodynamics, Royal Aeronautical Society Conference,* pp. 4.1-4.12.

Ben Fredj, I., Pincent, B., Servant, C., and Virlogeux, M. 2004. Millau Viaduct (France) – Monitoring Design and Implementation, *fib Symposium: Concrete Structures: the Challenge of Creativity,* Avignon, France, pp. 290-291.

Brown, T. G., and Bruce, J. R. 1997. *Confederation Bridge Ice Force Monitoring Joint Industry Project Annual Report – 1997*, IFN Engineering Ltd.

Bruce, J. R., and Croasdale K. R. 2001. *Confederation Bridge Ice Force Monitoring Joint Industry Project Annual Report,* Report Number 00-1-001, IFN Engineering Ltd.

Buonomo, M., Servant, C., Virlogeux, M., Cremer, J.-M., de Ville de Goyet, V., and Del Forno, J.-Y. 2004. The Design and Construction of the Millau Viaduct. *International Symposium on Steel Bridges, Steelbridge,* Millau, France, pp 1-18.

Canadian Standards Association (CSA) 2006. *Canadian Highway Bridge Design Code (CAN/CSA S6-06) and Commentary (CAN/CSA S6.1-06)*, Canadian Standards Association, Mississauga Ontario.

Cheung, M. M. S., Tadros, G. S., Brown, T., Dilger, W. H., Ghali, A., and Lau, D. T. 1997. Field Monitoring and Research on Performance of the Confederation Bridge. *Canadian Journal of Civil Engineering,* 24: 951-962.

Cheung, M. M. S., and Chan, B. Y. B., 2010. Operational Requirements for Long-Span Bridges under Strong Wind Events. *Journal of Bridge Engineering,* ASCE, 15:2, 131-144 pp.

Coleman, S. A. and Baker, C. J. 1990. High Sided Road Vehicles in Cross Winds. *Journal of Fluids and Structures,* 36: 1383-1392.

Coleman, S. A. and Baker, C. J. 1992. The Reduction of Accident Risk for High Sided Road Vehicles in Cross-Winds. *Journal of Fluids and Structures,* 44: 2685-2695.

Emmelmann, H. 1986. Driving Stability in Side Winds. *Aerodynamics of Road Vehicles,* London, Butterworths, pp 214-235.

Flint, A. R., McFadyen, A. N., Lau, C. K., and Wong, K. Y. 1995. Wind and Structural Health Monitoring System (WASHMS) for Lantau Fixed Crossing – Part 2: Performance Requirements for the Bridge Instrumentation System. *Bridges into the 21st Century, Hong Kong Institution of Engineers,* Hong Kong, pp 661-668.

Huang, C. J., Kilpatrick, J., and Irwin, P. A. 1998. *Review of Wind Criteria for Traffic Management on the Confederation Bridge,* Project Report 98-231, Rowan Williams Davies and Irwin Inc. (RWDI), Guelph, Ontario, Canada.

JMI-Stanley. 1995. *Design Criteria Northumberland Strait Crossing Project*, Jean Muller International, Stanley Joint Venture Inc., California, USA.

Kashima, S., Yanaka, Y., Suzuki, S. and Mori, K. 2001. Monitoring the Akashi Kaikyo Bridge: First Experiences. *Structural Engineering International, SPIE,* 11:2, 120-123.

Kasperski, M. 2006. Vibration Serviceability for Pedestrian Bridges, *Proceedings of the Institution of Civil Engineers,* Structures and Buildings 159, Issue SB5, pp. 273-282.

Kim, S., Pakzad, S., Culler, D., Demmel, J., Fenves, G., Glaser, S., and Turon, M. 2007. Health Monitoring of Civil Infrastructures Using Wireless Sensor Networks. *Proceedings of the 6th international conference on Information processing in sensor networks*, Cambridge, Massachusetts, USA, pp 254-263.

King, J. P. C., Mikitiuk, M. J., Davenport, A. G., and Isyumov, N. 1994. *A Study of Wind Effects for the Northumberland Straits Crossing,* BLWT-SS8-1994, Boundary Layer Wind Tunnel Laboratory, University of Western Ontario (Parts of this report have been published in King and Davenport 1994b and King 1999).

King, J. P. C., and Davenport, A. G. 1994a. *The Estimation of Dynamic Wind Load Coefficients for the Northumberland Straits Crossing, PEI,* BLWT-IR-N62-16-1994, Boundary Layer Wind Tunnel Laboratory, University of Western Ontario (parts of this report have been published in King and Davenport 1994b and King 1999).

King, J. P. C., and Davenport, A. G. 1994b. P.E.I. Fixed Link – The Treatment of Wind Effects for the Northumberland Strait Crossing. *Fourth International Conference on Short and Medium Span Bridges,* Halifax, Nova Scotia, Canada, pp 1377-1388.

King, J. P. C., Crooks, G. J., and Davenport, A. G. 1995. *The Northumberland Straits Crossing, Prince Edward Island, Testing of Marine Span Aeroelastic Model and Analysis of Dynamic Wind Loads,* BLWT-SS24-1995, Boundary Layer Wind Tunnel Laboratory, University of Western Ontario (parts of this report have been published in King and Davenport 1994b and King 1999).

King, J. P. C. 1999. Integrating Wind Tunnel Tests of Full-Aeroelastic Models into the Design of Long Span Bridges. *Proceedings of the Tenth International Conference on Wind Engineering (ICWE),* Copenhagen, Denmark, pp 927-934.

King, J. P. C., Morrish, D. P., Isyumov, N., and Fanjiang, G-N. 2000a. Full Scale Monitoring of the Bronx-Whitestone Bridge. *3rd Structural Specialty Conference of the Canadian Society for Civil Engineering (CSCE),* London, Ontario, Canada, pp 328-335.

King, J. P. C., Kopp, G. A., Kong, L. Z., Hirai, S., and Isyumov, N. 2000b. *A Study of Wind Effects for the Bronx-Whitestone Bridge,* BLWT-SS4-2000, Boundary Layer Wind Tunnel Laboratory, University of Western Ontario

King, J. P. C., and Kong, L. Z. 2001. *A study of Wind Effects for Bronx-Whitestone Bridge,* BLWT-SS25-2001, Boundary Layer Wind Tunnel Laboratory, University of Western Ontario, London, Ontario, Canada.

King, J. P. C., Bakht, B., and Bartlett, F. M. 2007. The Validation of Wind Tunnel Model Tests of Long Span Bridges through Long Term Full Scale Monitoring. *12th International Conference on Wind Engineering (ICWE),* Cairns, Australia, (8 page paper in CD-ROM Proceedings).

Li, H., Ou, J., Zhao, X., Zhou, W., Li, H., and Zhou, Z. 2006. Structural Health Monitoring System for the Shandong Binzhou Yellow River Highway Bridge. *Computer Aided Civil and Infrastructure Engineering,* 21, 306-317.

Londoño, N. A. 2006. *Use of Vibration Data for Structural Health Monitoring of Bridges,* Department of Civil and Environmental Engineering, Carleton University, Ottawa, Canada.

MacGregor, J. G., Kennedy, D. J. L., Bartlett, F. M., Chernenko, D., Maes, M. A., and Dunaszegi, L. 1997. Design Criteria and Load and Resistance Factors for the Confederation Bridge. *Canadian Journal of Civil Engineering,* 24: 882-897.

MBA.1999, *Wind Warning, Escort, and Closure Procedures,* Mackinac Bridge Authority.

Montreuil, M. A. 1999a. *Confederation Bridge Monitoring Project Slow-Speed Data Logger System,* Technical Manual, Preliminary Version, Thermal Technology Centre, National Research Council Canada.

Montreuil, M. A. 1999b. *Confederation Bridge Monitoring Project High-Speed Data Logger System,* Technical Manual, Preliminary Version, Thermal Technology Centre, National Research Council Canada.

Oehler, L. T. 1957. *Vibration Susceptibilities of Various Highway Bridge Types,* Report No.272, Project 55 F-40, Michigan State Highway Department.

Pimentel, R. L., Paric, A., and Waldron, P. 2001. Evaluation of Design Requirements for Footbridges Excited by Vertical Forces from Walking, *Canadian Journal of Civil Engineering,* 28:769-777.

Pritchard, R. J. 1985. Wind Effects on High Sided Vehicles. *Journal of the Institution of Highways and Transportation,* 32/4: 22-25.

PWC. 1988. *Investigations into the Effect of High Winds on Vehicular Traffic,* Northumberland Strait Crossing Project, Public Works Canada.

Ryan, A., and Dominy, R. G. 1998. *Aerodynamic Forces Induced on a Passenger Vehicle in Response to a Transient Cross-Wind Gust at a Relative Incidence of 30 Degrees,* Developments in Vehicle Aerodynamics, SAE Special Publication 1318, 181-189.

School of Graduate and Postdoctoral Studies, 2010. *Thesis Regulation Guide,* School of Graduate and Post Doctoral Studies, University of Western Ontario, pp. 1-24.

Scott, G. R. 2010. A Critical Overview of the Millau Viaduct. *Second Bridge Engineering Conference, University of Bath,* Bath, UK. pp 294-303.

Shahanadi, A. 1977. *Bridge Vibration Studies. Joint Highway Research Project,* Report No. JHRP – 77 – 17, Purdue University and Indiana State Highway Commission, September 1977.

Shahawy, M., Arockiasamy, M. 1996. Field Instrumentation to Study Time-Dependent Behaviour in Sunshine Skyway Bridge, Part I. *ASCE Journal of Bridge Engineering,* 1:2, 76-86.

Stathopoulos-Vlamis, A. 2008. Structural Health Monitoring of Rion-Antirion Bridge and Management In Case of Special Events. *36th Study and Information Days of ASECAP,* Marrakech, Morocco, pp 235-245.

Stewart, M. 1977. *Transient Aerodynamic Forces on Simple Road Vehicle Shapes in Simulated Cross Wind Gusts,* Motor Industries Research Association (MIRA) Report 77/5, Nuneaton, U.K.

Sun, L. M., Dan, D. H., Zhang, Q. W., and Yue, Q. 2005. Conceptual Design and Key Issues of Structural Health Monitoring System for Donghai Bridges. *Structural Health Monitoring and Intelligent Infrastructure: Proceedings of the 2nd International Conference on Structural Health Monitoring of Intelligent Infrastructure,* Shenzhen, China, pp 255-264.

Tadros, G. 1997. The Confederation Bridge: An Overview. *Canadian Journal of Civil Engineering,* 24: 850-866.

Wright, D. T. and Green, R. 1964. *Highway Bridge Vibrations,* Part II: Report No. 5. Ontario Test Programme. Ontario Department of Highways and Queen's University. Kingston, Ontario, May 1964.

Yeung, K. C., Lau, C. K., Wong, K. Y., Flint, A. R., and McFadyen, A. N. 1995. Wind and Structural Health Monitoring System (WASHMS) for Lantau Fixed Crossing – Part 1: System Planning and Design. *Bridges into the 21st Century, Hong Kong Institution of Engineers,* Hong Kong, pp 539-545.

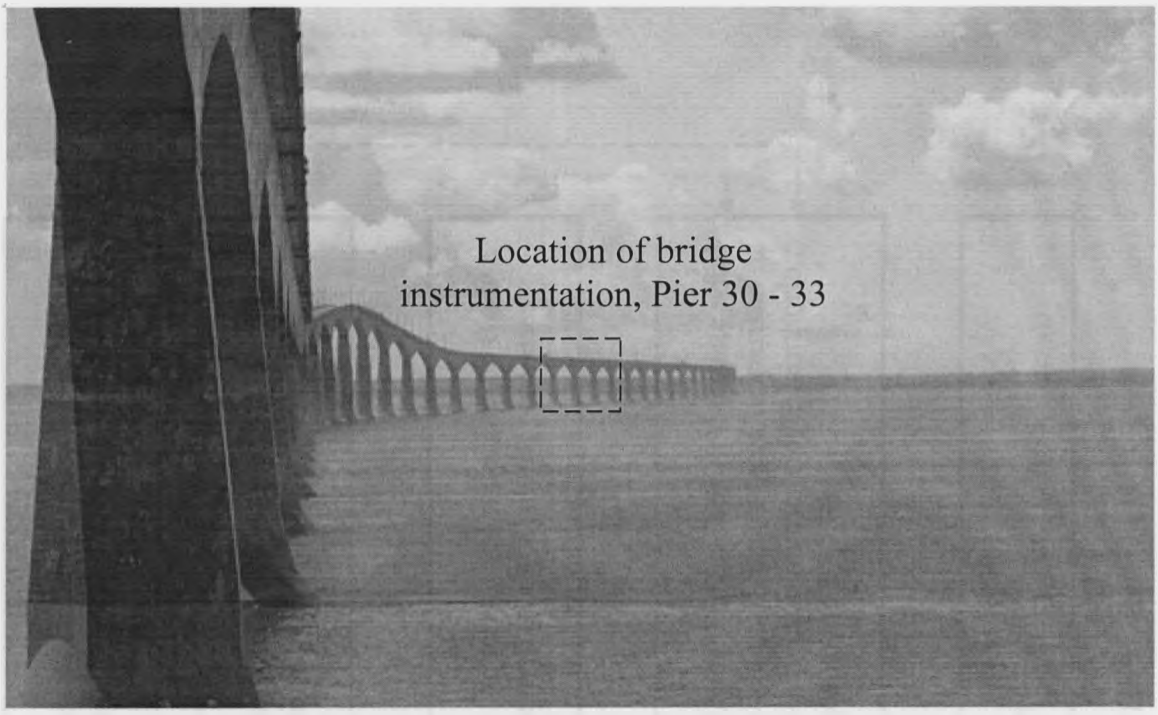

Figure 1.1 – Confederation Bridge Looking towards New Brunswick [courtesy Strait Crossing Bridge Limited]

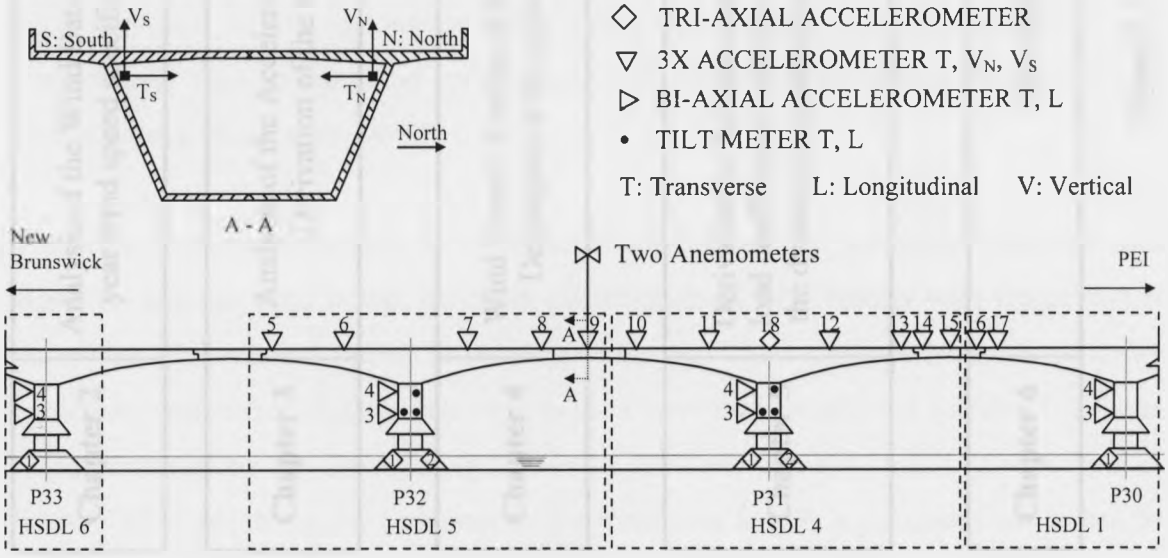

Figure 1.2 – Instrumentation Layout for the On-Site Monitoring Programme [adapted from Montreuil 1999b]

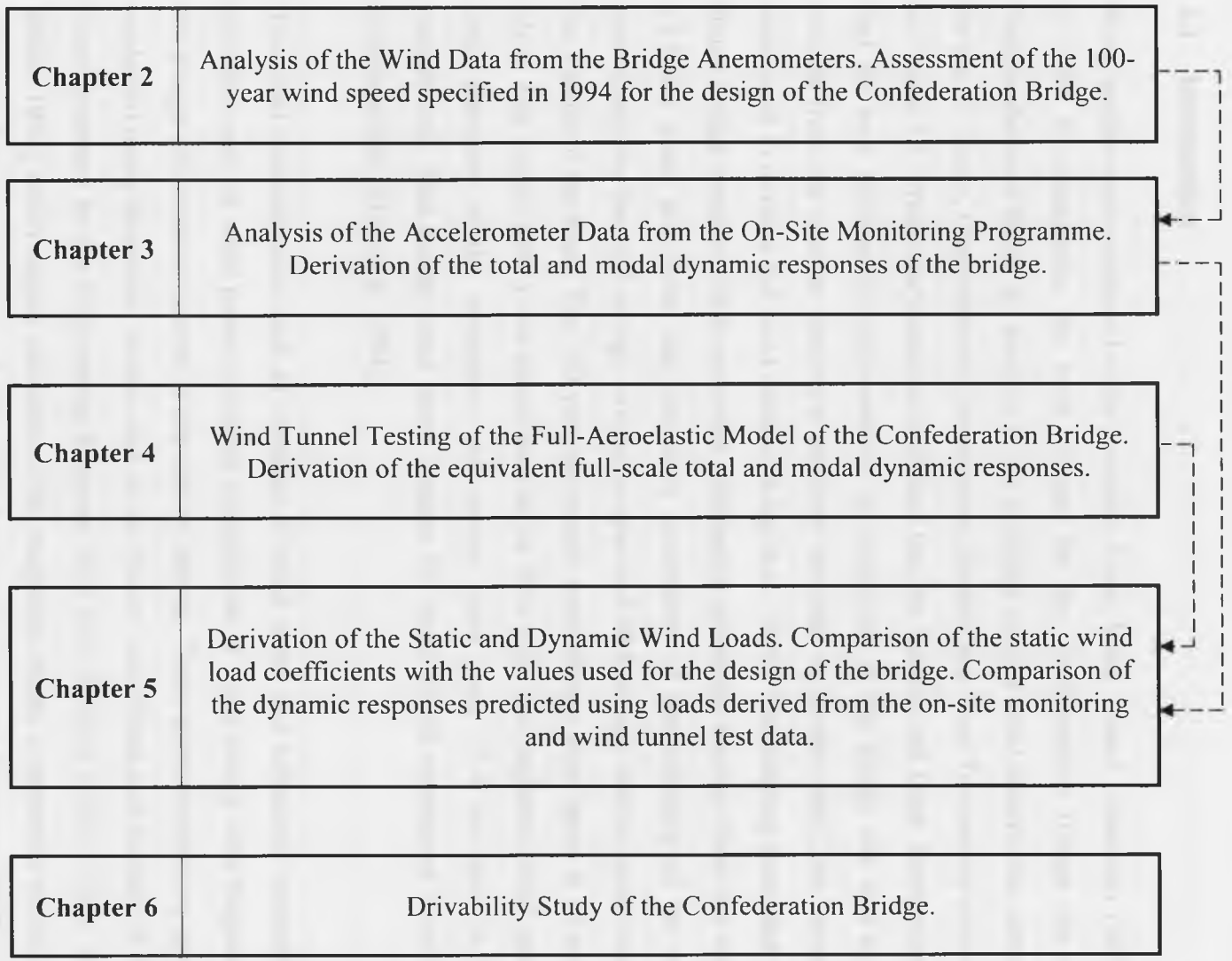

Figure 1.3 – Organization of Thesis Material

2. ANALYSIS OF ON-SITE MONITORING WIND DATA

2.1 Introduction

Wind studies were conducted at the Boundary Layer Wind Tunnel Laboratory (BLWTL) in 1994 to characterize the wind climate for the Confederation Bridge site at the Northumberland Strait. An analysis of the available surface wind records was carried out for the O' Leary, Charlottetown, Summerside, Borden and Cape Tormentine sites shown in Figure 2.1. Preliminary analysis indicated that the Borden and Cape Tormentine sites had the best information representative of conditions at the bridge site and so wind records from the weather stations at the ferry terminals in Borden and Cape Tormentine were used to develop the wind climate [King et al. 1994]. Transferring these data to the future bridge location was a somewhat challenging procedure because these two sites are 14.5 km apart and there was inevitable uncertainty of the accuracy of the results, particularly for the 60.3 m high navigation span and 40.8 m high marine spans located in the middle of the strait. The 100-year ten-minute mean design wind speed at 10 m above Mean Sea Level (MSL) was determined to be 29.6 m/s. The projected wind speeds at deck elevation of the navigation and marine spans were 35.4 m/s and 34.1 m/s, respectively. This design wind speed became the basis for all subsequent wind tunnel investigations [King et al. 1994].

The wind characteristics such as variation of wind speed and turbulence intensity with elevation and the wind power spectrum (distribution of wind energy with frequency) at the bridge site were not known at the time of testing. These characteristics are generally explained using theoretical models such as the Power Law [Simiu and Scanlan 1978] and those presented by the Engineering Sciences Data Unit (ESDU) [ESDU 1993a, b, & c, ESDU 1974] which require estimates of the roughness length, a parameter which can be established from estimates of full-scale turbulence intensity [Holmes 2007]. In the absence of actual on-site turbulence intensity values, two exposures with 6% and 11% turbulence intensities, respectively, at the deck elevation were selected to bracket the

expected full-scale conditions and used to model the flow regime at the bridge site in the wind tunnel [King et al. 1994].

To verify the design wind characteristics and to control the operation of the bridge during extreme wind events, the wind speed and direction at different locations along the Confederation Bridge are continuously monitored. Six anemometers were installed along the length of the bridge on light standards, shown in Figure 2.2b, and some have been collecting data since 1998. As shown in the table in Figure 2.2b, three are used for bridge operations, one for Environment Canada and two are part of the on-site monitoring system in the instrumented span region. As will be described in detail later, these instruments are mounted at different elevations on both sides of the bridge at different points along the span and so do not typically give identical readings.

To date, the data collected by these anemometers have not been organized systematically to build a complete wind database for bridge during this period. There are questions about whether the bridge has already been exposed to its 100-year return period wind speed during its first ten years of operation. Analysis of wind data by Naumoski et al. [2004] suggests that the specified design wind speed was exceeded once in November 2001. However, the values reported by Naumoski et al. [2004] exceed the reported 1000-year return period of 43 m/s and so seem excessively high. The bridge owner Strait Crossing Bridge Limited (SCBL) has also questioned whether the passage of Hurricane Noel in November 2007 caused the design wind speed to be exceeded [SCBL 2008].

The data acquisition system was reconfigured, temporarily, to collect useful data for a strong wind event during the passage of Hurricane Noel on November 4, 2007. The initiative was taken after serious anomalies were encountered in the data available for the previous years. The present study will address these issues with the aim of creating a data base of wind records for the bridge site that will be used in Chapter 3 to determine the full-scale bridge response and subsequently the wind loads in Chapter 5.

2.1.1 Research Objectives

The aim of the present study is to carry out a comprehensive analysis of the available wind data from the on-site monitoring programme to form a complete database of wind statistics that will be used:

i) To characterise wind climate for the Northumberland Strait to investigate the frequency of prevailing winds and the probability of strong wind events for the 16-point compass azimuths at the bridge site.

ii) To estimate the 100-year wind speed at the marine span deck elevation of 40.8 m and compare it to the originally specified design wind speed of 34.1 m/s [King et al. 1994].

iii) To investigate the accuracy of the claim by Naumoski [2004] that the bridge experienced wind speeds significantly greater than the specified design speed during the November 2001 storm.

iv) To investigate if the 100-year specified design wind speed was exceeded during the passage of Hurricane Noel.

v) To establish the roughness length based on the measured full-scale turbulence intensity and used to model the flow regime in the wind tunnel in Chapter 4.

vi) To investigate a possible reconfiguration of the current data acquisition system to gather information more useful for wind engineering purposes.

2.1.2 Chapter Organization

This chapter will describe the various anemometers used to gather wind data from different sections of the Confederation Bridge and the methodology for processing these

data. The processed data are used to determine the longitudinal turbulence intensity for different wind speeds and probability contours for the longitudinal turbulence intensity with wind azimuth, for wind speeds greater than 10 m/s. As the anemometers located at midspan between Piers 31 and 32 have not functioned continuously between 1998 and 2007 due to complications resulting from the harsh marine environment, a procedure for correcting data obtained by the reliable Pier 20 anemometer to fill the gaps in the Pier 31-32 anemometer record is derived and implemented. The complete dataset is then used to characterize the wind climate at the bridge site, including the maximum ten-minute mean wind speed in the dataset and the forecast 100-year wind speed for comparison with the original design values [King et al. 1994]. The time histories collected by the Pier 31-32 anemometers during Hurricane Noel are also used to calculate ten-minute statistical summaries, to see if the 100-year design wind speed was exceeded during the event, and turbulence intensities to establish the roughness length. The anemometer time histories from Hurricane Noel are also used to derive wind spectra for comparison to a theoretical spectrum to evaluate the assumption of an open sea exposure.

2.2 Analysis of the 1998-2007 Wind Data

2.2.1 Available Anemometers

The harsh marine environment of the Northumberland Strait has caused anemometers to fail intermittently, which has affected the overall continuity and availability of the wind speed and direction data. The two primary anemometers, one Handar (ultrasonic) and the other Gill (propeller type) [Montreuil 1999], were initially installed at 12.85 m above the bridge deck atop a light standard midway between Pier 31 and Pier 32, as shown in Figure 2.2b, to monitor wind speeds and directions. The Gill instrument became damaged during a February 1997 storm and was replaced by a second Handar anemometer that caused electrical interference with the original Handar unit and so was removed. In 2007 an R. M. Young anemometer (propeller type) was installed beside the functioning Handar anemometer as a backup to the Handar unit but has only provided data for Hurricane Noel. Both anemometers are scanned at 1 Hz sampling frequency by the Slow Speed

Data Logger (SSDL) 8 located at Pier 31 (Figure 2.2b) which archives maximum, average, minimum and RMS statistics for wind speed and azimuth every ten minutes. When the wind speed exceeds 15 m/s the wind speed and azimuth are also recorded at one-second intervals [Montreuil 1999]. The accuracy of the measured wind speed and direction by the Handar anemometer is within ± 0.135 m/s and ± 2°, respectively, [Montreuil 1999a] and that for the R. M. Young anemometer is within ± 0.3 m/s and ± 3°, respectively [Campbell Scientific 2010a].

Two other anemometers have been installed 6 m above the bridge deck 42 m west of Pier 20 and 42 m west of Pier 41 that are used for bridge operations. These are cup and vane type anemometers that collect six-minute mean and maximum wind speeds and azimuths using a 16-point compass. Both are located on the north side of the bridge. A third cup and vane type anemometer was installed in 2008 on the south side of the bridge, 82 m west of Pier 20, to provide additional information relevant for winds from the south. These are well-maintained, reliable instruments. The accuracy of the measured wind speed and direction by these anemometers is within ± 0.5 m/s and ± 5°, respectively [Campbell Scientific 2010b].

Environment Canada has installed an R. M. Young anemometer (propeller type) on the navigation span between Pier 21 and Pier 22 which is located 12.85 m above the bridge deck and collects maximum, average, minimum and RMS statistics for wind speed and azimuth every hour. This anemometer is part of the national system of instruments used for weather forecasts.

2.2.2 Data Analysis

Data collected during each calendar year from the SSDL 8 were downloaded and imported into MATLAB [Math Works 1995] files. Plots of mean wind speed, azimuth and turbulence intensity for each year were initially developed to assess the quality of the raw data. The plots indicated various data anomalies. For example, negative mean wind

speed values and mean wind azimuth values outside the range of 0^{o} to 360^{o} were present and, as these values are physically impossible, they were removed from the dataset.

Figure 2.3a shows a typical ten-minute record of speeds measured at one-second intervals by the Handar anemometer at midspan of Piers 31 and 32. The typical wind speed recorded is less than 25 m/s but there are over 50 instances where the Handar anemometer registers a wind speed of 52 m/s, which is considered to be physically impossible for the wind to fluctuate that drastically. Accordingly, all data were filtered to remove instances where a wind speed greater than 50 m/s was recorded in a time history recorded at one-second intervals, and the corresponding ten-minute summary statistics were also rejected as spurious. Figure 2.3b shows a typical ten-minute time history that passed this filter and looks much more realistic than Figure 2.3a.

Turbulence intensities for the remaining data were computed as the RMS wind speed divided by the mean wind speed, i.e., $\sigma_v / \overline{V}$. High turbulence intensities corresponding to very low wind speeds were discarded by setting filters for the minimum acceptable mean wind speed at 0.1 m/s. Figure 2.4a shows the variation of turbulence intensity with wind speed, which generally reduces with an increase in the wind speed and becomes horizontally asymptotic. The figure shows that majority of the data points follow this trend, however, there are some data points that are randomly distributed along the wind speed axis with turbulence intensities as high as 100%, which are unlikely. To identify these spurious data for removal and to keep data acquisition system transparent, peak factors were calculated for each dataset as

$$g = \frac{(V_{max} - V_{mean})}{V_{rms}} \qquad [2\text{-}1]$$

where V_{max}, V_{mean} and V_{rms} are the maximum, minimum and RMS of the wind speeds in each dataset. It has been proven that naturally occurring wind turbulence has a Gaussian distribution of velocity fluctuation [Davenport 1964]. The corresponding peak factors have a mean value of 3.5 and are very unlikely to be less than 2 or greater than 5. The

ten-minute summary statistics were therefore filtered to remove all instances where peak factors outside this range were recorded. A minimum turbulence intensity of 0.01 was also specified to further remove unreasonably high wind speeds recorded perhaps as a result of a power failure or other instrument malfunction. The effect of these filters is indicated by Figure 2.4b, which looks much more realistic [Barthelmie 1999, Charnock 1955, Garratt 1977, Smith 1980, Türk and Emeis 2010, Wu 1980] than Figure 2.4a and will be discussed in detail in Section 2.2.3.

Constant wind azimuths for durations exceeding several days were recorded in the years 2003 and 2004 and, as this again is physically impossible, were deemed to be spurious. To remove these data, the minimum value of standard deviation for wind azimuth was set at 1^{o} for each of ten-minute summary statistics.

It was discovered in October 2004 by a data logger programmer that the mean wind direction statistics were computed from the time histories using an inappropriate algorithm affecting indicated wind azimuths in the vicinity of the $0^{o}/360^{o}$ direction. Two data filtering conditions on wind azimuth values were therefore necessary to identify and remove any data suspected of having this problem. The first condition rejected cases where the mean wind azimuth did not fall between the minimum and maximum values in the set of ten-minute summary statistics. The second condition discarded any data point with a minimum wind azimuth less than 90^{o} and maximum wind azimuth greater than 270^{o}.

The assembly of the Handar anemometer data into a single, coherent and reliable dataset therefore proved to be both difficult and time consuming. Figure 2.5 shows data remaining after spurious values were removed using the criteria defined above as a percentage of the maximum number of datasets possible for each month. The figure shows fairly consistently that the dataset is incomplete because the anemometer or data logger was not functioning properly approximately 40% to 50% of the time.

2.2.3 Turbulence Intensity

The cleansed set of ten-minute summary statistics obtained from the Handar anemometer may be incomplete but, with 184719 records (37% of total possible records) between 1998 and 2007, still represents a very significant dataset. Accordingly, these data were used to determine the variation of the longitudinal turbulence intensity with mean wind speed shown in Figure 2.6. The data shows a rapid decrease in the envelope of turbulence intensity with increase in the mean wind speed. The high turbulence intensity values at low wind speeds are due to thermally induced turbulence during unstable atmospheric conditions where water surface temperatures are significantly above the air temperature [Barthelmie 1999, Türk and Emeis 2010]. At higher wind speeds the turbulence due to mechanical mixing dominates the thermal effects and the variation of the turbulence intensity is proportional to the surface characteristics such as the roughness length, z_o [Charnock 1955, Garratt 1977, Smith 1980, Wu 1980]. The mean fit to the data, shown by the solid line, indicates that the turbulence intensity asymptotically approaches 7.5 % which is consistent with that expected for an open sea condition [ESDU 1993a].

Figure 2.7 shows the annual probability distribution of the longitudinal turbulence intensity with wind azimuth for wind speeds greater than 10 m/s at the Pier 31-32 anemometer elevation of 54 m. A point on the innermost contour represents the turbulence intensity exceeded 1% of the time within the 10^o sector centred in that direction. Other contours represent probability levels of 0.1%, 0.01% and 0.001%. The maximum turbulence intensity for prevailing winds from Bridge West with a 1% probability of exceedance exceeds a value of 0.125 or 12.5%. This is perhaps due to the anemometer being close to the New Brunswick side, as shown in Figure 2.2b, so these prevailing winds approach over land, Figure 2.1, not water and so are more turbulent.

2.2.4 Data Correlation between Anemometers at Midspan between Piers 31 & 32 and near Pier 20

To develop estimates of extreme winds the incomplete dataset from the Handar anemometer shown in Figure 2.5 must be considerably supplemented with data from another source to be made complete. Data from the most reliable anemometer, located 2.83 km east of the Handar anemometer and 41.67 m west of Pier 20 on the north side of the bridge, as shown in Figure 2.2b, were used for this purpose. The Pier 20 anemometer records six-minute mean and maximum wind speeds and wind directions on a 16-point compass, and has a reliability of almost 100%. However the Pier 20 data must be adjusted to be compatible with the Pier 31-32 data: for example, the former report wind azimuth with respect to True North and the latter uses a datum of Bridge North that is 45° west of True North. More subtle factors can cause the readings to be different. These will be discussed in detail subsequently and include the different averaging time, different elevation with respect to the bridge deck at MSL, and different location with respect to midspan.

It is therefore necessary to develop factors to convert the Pier 20 anemometer reading to an equivalent Pier 31-32 anemometer reading that may depend on the wind azimuth. There are 2079 instances between 1999 and 2007 when the window used to determine the ten-minute mean wind speed at Pier 31-32 overlaps the window used to determine the six-minute wind speed at Pier 20. Figure 2.8a shows strong correlation between these values for winds from the Northwest (i.e., Bridge North) direction: the fitted line

$$\overline{V}_{P31} = 0.927\,\overline{V}_{P20} \qquad [2\text{-}2]$$

has a coefficient of determination, R^2, of 0.96 and a standard error of 0.25%. The dashed lines are the upper and lower confidence intervals which are two standard deviations from the mean and include more than 95% of the observed data. Thus, using Equation [2-2], the predicted wind speed of 30.5 m/s could vary within ±6%.

Similar graphs and fitted lines were determined for each of the 16-point compass directions as summarized in Table 2.1. The ratio of the mean velocity at Pier 31-32 to the mean velocity at Pier 20 for the 16-point compass directions ranges from 0.873 to 1.251. The variation of these values can be attributed to the following four factors:

- The ten minute averages from the Pier 31-32 anemometer can be expected to be 2% less than the six-minute averages from the Pier 20 anemometer [ASCE 7 2005], irrespective of wind direction.

- The wind velocity at the Pier 31-32 anemometer, at 54 m above MSL, can be expected to be 2.5% less than the wind velocity at the Pier 20 anemometer, at 61 m above MSL, given the open sea exposure [ESDU 1993a], irrespective of the wind direction.

- The effect of the bridge as a bluff body on wind speeds for two different cross-sections of the bridge deck. The cross-section depth at the Pier 31-32 anemometer including the side barrier is 5.5 m, and is uniform for 30 m on each side of the anemometer. Conversely the Pier 20 anemometer is located where bridge cross-section depth is 10 m and non-uniform, gradually decreasing on one side and increasing on the other. The flow around the shallower bridge deck might be expected to cause a smaller local velocity increase at the Pier 31-32 anemometer as it is mounted 12.85 m above the bridge deck whereas the Pier 20 anemometer is mounted only 6 m above the bridge deck and so is expected to record a larger velocity increase.

- The Pier 20 anemometer is located very close to Pier 20 and so may be shielded for winds from this direction.

The directional dependence of the correction coefficients shown in Table 2.1 and graphed in Figure 2.9 indicate that the proximity of the anemometer to the bridge deck and adjacent pier are the dominant effects in comparison to the first two factors. The effects

of averaging period and elevation indicate that the ratio of $\overline{V}_{P31}/\overline{V}_{P20}$ should average (0.98 x 0.975) = 0.956). For the SE and SSE wind directions, the relatively large correction coefficients suggest that significant shielding is provided by the bridge at Pier 20 anemometer. For the SSW, WNW, NW and NNW wind directions, the deeper bridge cross-section increases the wind speeds recorded by the Pier 20 anemometer as shown in Figure 2.9.

The coefficients of determination, R^2, shown in Table 2.1, have eleven values greater than 0.9 and all values are greater than 0.8. The standard errors for all azimuths are less than 0.5% except for the ESE azimuth which is less than 1%, demonstrating that the correction coefficients applied to the Pier 20 anemometer data to estimate the equivalent Pier 31-32 anemometer readings are reasonable. The ESE sector has the least number of overlapping data points which explains the relatively lower value of the coefficient of determination, 0.8, and higher standard error, 0.69%.

The best fit relationships shown in Table 2.1 were used to estimate the 297591 missing ten-minute mean wind speeds at the Pier 31-32 anemometer from the six-minute mean wind speeds at the Pier 20 anemometer. As a check, predicted wind speeds for the Bridge North azimuth computed using Equation [2-2] were compared to the actual wind speeds recorded when the Pier 31-32 anemometer was functioning properly. Figure 2.8b summarizes the predicted and observed values for a 14-day period starting on 1st November 1999: the correlation between predicted and observed values is excellent.
The improved dataset from January 1998 to June 2007, with all missing points filled in, has 482310 values of ten-minute mean wind speeds and wind azimuth directions for the anemometer between Pier 31-32 at 54 m elevation above the water level.

2.2.5 Maximum Wind Speed Recorded between January 1998 and June 2007

Inspection of the complete dataset (January 1998 – June 2007) indicates that the maximum ten-minute mean wind speed occurred at 21:00 on 7th November 2001. The

maximum ten-minute mean wind speed was 31.3 m/s and the wind direction was normal to the bridge axis within a 22.5°-wide sector. This speed value reflects the wind speed at the 54 m elevation of the anemometer and, assuming open sea exposure, is equivalent to a speed of 30.5 m/s at the deck elevation of 40.8 m, a factor of 1.025 [ESDU 1993a]. The originally specified design wind speed of 34.1 m/s at this elevation is a ten-minute mean wind speed considering winds from all directions [King et al. 1994]. If only winds normal to the bridge axis are considered, a corresponding design wind speed of 30.5 m/s at the deck level was suggested [King et al. 1994]. Thus the November 2001 storm represents the only wind event in ten years, from 1998 to 2007, when the recorded ten-minute mean wind speed approached the specified design wind speed for 20 minutes for the Confederation Bridge. It is important to note that the bridge is actually designed to resist a factored wind load that is 1.9 times the specified wind load and therefore corresponds to a wind speed that is 38% greater than the specified design wind speed of 30.5 (or 34.1) m/s.

Naumoski et al. [2004] report that the Confederation Bridge was subjected to wind speeds that were significantly greater than the design wind speed during the November 2001 storm. The maximum wind speed they report, 43 m/s (155 km/h) at the Pier 20 anemometer, is a three-second gust speed at 61 m above MSL. Naumoski et al. [2004] exaggerate the severity of this reading because they have not accounted for the difference between the three-second gust and ten-minute mean wind speed, which is a factor of 1.44 [ASCE 7 2005]. They have also not corrected the wind speed recorded at 61 m to the bridge deck elevation of 40.8 m, which is an additional factor of 1.025 [ESDU 1993a]. Adjusting the reported value of 43 m/s by these factors results in a corresponding mean wind speed of 29.1 m/s, which is close to the observed value of 30.5 m/s.

2.2.6 Characterization of Wind Climate at the Confederation Bridge

Figure 2.10 is a wind rose showing the wind speed for various wind azimuths defined using a 16-point compass. The figure is derived using all (482310) ten-minute mean values recorded at or estimated using the corrected Pier 20 values for the Pier 31-32

anemometer. The wind speeds are further adjusted to correspond to the deck elevation of 40.8 m. Wind speeds less than 0.5 m/s are considered calm and are shown in the centre circle with no direction. Approximately 12% of all wind occurrences are the prevailing or common winds from Bridge West that are less than 12.5 m/s. The figure shows a marked lack of symmetry about the north/south and east/west axes. Winds from the west and north are more common than those from the east and south. The prevailing winds from Bridge West are not structurally significant to the bridge as they are parallel to the bridge axis. The wind climate characterized by King et al. [1994] also shows prevailing winds from the Bridge West and winds from the north are more common than those from the south.

Figure 2.11 shows the annual probability distribution of the mean wind speed from various wind azimuths at the deck elevation of 40.8 m above MSL. The radial distance to a probability contour for a particular wind direction indicates the wind speed which is exceeded with that probability level for a given wind azimuth within a sector of 22.5°. The innermost contour indicates the wind speed for a given wind azimuth which is exceeded annually 1% of the time. The outermost contours of the plot indicate the wind speeds from a given direction that are exceeded annually 0.001% of the time. The greatest wind speeds that occur in a year come from Bridge North and approximately 160° from Bridge North which are consistent with the directions of the strong wind events that the bridge has experienced to date during its service life.

Figure 2.12 compares the ten-minute mean wind speeds for various return periods computed using the on-site monitoring data recorded between 1998 and 2007, corrected to the 40.8 m deck elevation, with the values predicted at the design stage using data from the weather stations in Borden and Cape Tormentine [King et al. 1994]. The crossing rate for different wind speed intervals integrated over all wind directions was determined from the 1998-2007 data and fitted using bi-modal Weibull Distribution and Rice's Theory extended by Davenport [Davenport 1977, Xu et al. 2008]. The return period is the inverse of the annual probability of exceedance for a given wind speed interval. The figure shows the ten-minute mean wind speed for a 100-year return period based on the

on-site monitoring data is 33.6 m/s at the deck elevation. This value is in remarkably close agreement with the originally specified design wind speed of 34.1 m/s.

2.3 Analysis of the Wind Data Recorded during Hurricane Noel

Hurricane Noel provided an opportunity to collect useful data during a strong wind event and high-lighted problems with the existing configuration and set-up of the data acquisition system. The data also helped illuminate the effect of the bridge deck as a bluff body and so influencing the associated power spectra measured for different wind azimuths, which raised interesting new questions that require further investigation.

The two anemometers at midspan between Pier 31-32 were programmed to capture wind data at 2 Hz and triggered once to capture the entire 18 hours duration of the storm. The wind direction during Hurricane Noel, as obtained from the Handar and R. M. Young anemometers at midspan between Piers 31 and 32 changed continuously from 125° to 320° as shown in Figure 2.13. The maximum half-second gust speed is 44 m/s, from a wind direction of 206° at an elevation of 12.85 m above the bridge deck or 54 m above MSL. Correcting for the elevation and averaging time results in a corresponding ten-minute average wind speed at the deck level of 33.2 m/s.

Figure 2.14 shows time histories of wind speed and wind azimuth recorded by the two anemometers sampling at 2 Hz during the passage of Hurricane Noel. The wind azimuth data and upper range of wind speed data are very consistent. However, the Handar anemometer wind speed record in Figure 2.14a shows numerous "drop-offs", where the wind speed is momentarily reduced to 50%, that are not present in the R. M. Young anemometer wind speed record in Figure 2.14b. These "drop-offs", due to some unknown instrument malfunction, will seriously complicate the estimation of the power spectra. Therefore, it was decided to analyse only the R. M. Young anemometer data. Time histories archived in the slow speed data logger between 1998 and 2007 show similar drop-offs in the Handar wind speed record and so yield power spectra that are suspect [Bakht et al. 2008 – see also Appendix 2A].

The wind data recorded during Hurricane Noel do not comprise a continuous dataset. For example, the first six and a half hours of data (1199 x 40 = 47960 data points) had 39 missing data points, i.e., one point missing after every 1199 data points. The reason for this systematic data loss may be due to the data transmission software. Compared to the total number of data points, the missing points are small in number and have little impact on the wind spectra [Bakht et al. 2008]. During the last four hours of the storm, 42% of the data points are missing and accurate wind spectra could not be derived [Bakht et al. 2008]. Thus, after this detailed examination of all the sub-datasets, the initial 14 hours of data were used to derive wind spectra and the last four hours of data were not analysed further.

The slow speed data logger time histories files also show numerous seemingly random missing data. It is suspected that data were lost because the data acquisition system was automatically turned off when the instantaneous wind speed dropped to below 15 m/s. If this is the cause, the logic regarding the data logger triggering and shutdown clearly needs revision to prevent this loss of valuable data.

2.3.1 Wind Statistics

The time histories recorded by the R. M. Young anemometer during the passage of Hurricane Noel were used to calculate the ten-minute mean wind statistics and turbulence intensities. Figure 2.15a shows the maximum ten-minute mean wind speed at the anemometer elevation of 54 m above MSL to be 34 m/s which corresponds to 33.2 m/s at the deck elevation of 40.8 m. This maximum ten-minute mean wind speed corresponds to a mean wind azimuth of 200° with respect to Bridge North as shown in Figure 2.15b. Figure 2.15c shows a mean turbulence intensity of 8% at the anemometer elevation, which is consistent with an open sea condition [ESDU 1993a].

For the azimuth associated with this maximum mean wind speed, the wind is approaching from the south side of the bridge but measured on the north side in the region of a shear layer. The shear layer region separates the entrained wake region around the deck from

the undisturbed flow region and so causes accelerated wind speeds accompanied by a long series of vortices [Holmes 2007]. This increased wind speed above the downwind side of the deck was also observed during wind tunnel tests of the Confederation Bridge Model in 2009, and quantified as a 10% increase. The influence of the bridge deck on wind speeds recorded by the different anemometers located on the bridge is further discussed in Chapter 4.

The maximum ten-minute mean wind speed of 33.2 m/s at the deck level recorded during Hurricane Noel approaches specified design wind speed of 34 m/s [King et al. 1994]. It will be shown in Chapter 5, however, that Hurricane Noel is much less severe than the design event because the wind azimuth corresponding to the maximum wind speed was not normal to the bridge axis.

2.3.2 Wind Power Spectra

The Hurricane Noel time histories were divided into subsets of 3 to 4 hours duration for derivation of the wind power spectra. The spectra corresponding to two subsets of the Hurricane Noel data for the 5^{th} to 7^{th} and 10^{th} to 14^{th} hours are shown in Figures 2.16 and 2.17, respectively. The mean wind azimuths for the two data subsets are 200^{o} and 300^{o}, respectively. The black smooth lines shown in each figure represent the Engineering Sciences Data Unit (ESDU) 74031 [ESDU 1974] wind spectra that are consistent with the data subsets based on an open-sea roughness length, z_o, of 0.0002 m (consistent with a turbulence intensity of 8%), an anemometer elevation of 54 m and mean wind speeds of 24 m/s and 19 m/s. The gray jagged line is the power spectrum derived from the R. M. Young anemometer data corrected for the instrument distance constant [Davenport 1978]. The agreement between the black smooth and the gray jagged line is excellent, indicating wind characteristics that are consistent with the open sea exposure condition represented by ESDU 74031 [1974].

Figure 2.16 indicates a region where the spectrum derived from the Hurricane Noel data exceeds that predicted by ESDU for frequencies ranging between 0.2 Hz to 0.5 Hz. The

wind data used to derive this spectrum are recorded by an anemometer on the north side of the bridge and so may be influenced by the deck shape because the wind is from the south. Derivation of wind spectra for various subsets of Hurricane Noel data shows the discrepancy with the ESDU spectrum gets more pronounced as the wind becomes normal to the bridge, and reduces as the wind becomes aligned with the bridge axis, and eventually vanishes when wind direction changes to the north side of the bridge as shown in Figure 2.17. This phenomenon requires further investigation.

2.3.3 Reconfiguration of the Monitoring Programme

The results of the analysis of the Hurricane Noel data show that the current data acquisition system could be reconfigured to collect more useful information at least from a wind engineering viewpoint. The data provides a clear picture of the entire storm and the flexibility to work on subsets of data that are relatively stationary. In spite of strenuous efforts, the time histories collected between 1998 and 2007 could not yield a wind power spectrum because they are too short, have missing data points, and are sampled at a very low frequency of 1 Hz. The Hurricane Noel data show that a minimum data time history of two to three hours sampled at 2 Hz is necessary to derive the wind power spectrum. Hurricane Noel also indicated a serious problem with the Handar anemometer that otherwise might not have been highlighted.

2.4 Summary and Conclusions

Analysis of on-site monitoring wind data recorded between 1998 and 2007 by the anemometer located between Piers 31 and 32 indicates that the harsh marine environment has impacted both the quality and quantity of the data collected: only 40% to 50% of the ten years of archived data are useable. The missing data points are regenerated using data from the accurate and reliable anemometer near Pier 20 which is used for bridge operations and is located 2.85 km east of the Pier 31/32 anemometer. Correction factors to modify the Pier 20 anemometer data to make it consistent with the Pier 31-32

anemometer data were derived from cases with overlapping data collection windows for the two instruments. The complete dataset is used to determine ten-minute mean wind speeds for various return periods for comparison with the values recommended by King et al. [1994] as the basis of the original design.

The wind speed and azimuth time histories collected for an 18-hour period during the passage of Hurricane Noel are also investigated. The data from the Handar anemometer located between Piers 31 and 32 were deemed to be unreliable so the time histories from the adjacent R. M. Young anemometer were used to calculate the ten-minute wind statistics, turbulence intensities and wind spectra corresponding to this storm.

The following conclusions are drawn:

1. The ten-minute mean wind speed for a 100-year return period derived from the on-site bridge monitoring data collected between 1998 and 2007 is 33.6 m/s at 40.8 m above MSL. This value is within 1.5% of the corresponding originally specified design wind speed of 34.1 m/s, demonstrating that the design wind speed predicted in 1994 is appropriate.

2. The maximum ten-minute mean wind speed recorded by the on-site monitoring system between January 1998 and June 2007 is equivalent to 30.5 m/s at the deck elevation of 40.8 m and occurred on 7th November 2001. The corresponding wind direction, measured on a 16-point compass was Bridge North, i.e., at right angles to the bridge axis, so this event can be considered to be one occurrence of the originally specified design event. The bridge is actually designed for a factored wind load that corresponds to a wind speed that is 38% greater than this specified value.

3. Naumoski et al. [2004] state that the wind speeds measured during the November 2001 storm greatly exceed the specified wind speeds. This conclusion is erroneous because they have not accounted for the difference between the mean three-second

gust and ten-minute wind speeds, which is a factor of 1.44 [ASCE 7 2005]. They have not corrected the wind speed recorded at the anemometer elevation of 61 m to the bridge deck elevation of 40.8 m, which is an additional factor of 1.025.

4. The maximum ten-minute mean wind speed at the deck elevation during the passage of Hurricane Noel was 33.2 m/s, at mean wind azimuth of 200° with respect to Bridge North. It will be shown in Chapter 5 that the wind loads caused by Hurricane Noel are less than the specified wind loads because the azimuth of the wind was not normal to the bridge axis.

5. Prevailing winds from the west are most common at the bridge site and winds from Bridge North are more common than those from Bridge South. Strong wind events are most likely to come from Bridge North and from 160° with respect to Bridge North.

6. The mean turbulence intensity for the on-site monitoring data between 1998 and 2007 and the Hurricane Noel data is 7.5% and 8%, respectively, at the elevation of 54 m. These turbulence intensities are consistent with open sea conditions.

7. The time histories collected between 1998 and 2007 could not yield a wind power spectrum because the time histories are too short, contain missing data points and are sampled at a very low frequency of 1 Hz. The analysis of Hurricane Noel wind data indicates that a minimum of 2 to 3 hours data with a sampling rate of 2 Hz is necessary to derive a reliable wind power spectrum.

8. The ESDU 74031 wind spectrum is in excellent agreement with the wind spectrum derived using Hurricane Noel data. The ESDU spectrum is based on an open-sea roughness length, z_o, of 0.0002 m, (consistent with a turbulence intensity, I_u, of 8%), an anemometer elevation of 54 m and a mean wind speed consistent with that recorded in the time history of data. This indicates wind characteristics that are consistent with an open sea exposure.

2.5 Recommendations

1. The storage capacity and the sampling frequency for the slow speed data logger must be increased to ensure long time history records with at least 2 Hz sampling rate which are essential to derive reliable wind power spectrum.

2. The Handar anemometer between Piers 30 and 31 often randomly records improbable wind speed drop-offs that make the accurate determination of the associated power spectrum difficult. An explanation of this behaviour should be sought and appropriate maintenance, filtering or other means to correct this should be implemented.

3. The slow speed data logger files show numerous, seemingly random, instances of missing data points. The cause of this apparent malfunction should be further examined and resolved.

4. The spectra derived using data for winds approaching from the south side of the bridge exceed the ESDU spectrum for rough sea conditions for frequencies in the 0.2 Hz to 0.5 Hz range. This phenomenon requires further investigation.

2.6 References

ASCE. 7. 2005. *Minimum Design Loads for Buildings and other Structures*, American Society of Civil Engineers, Reston, Virginia, VA, USA.

Bakht, B., King, J. P. C., and Bartlett, F. M. 2008. *Analysis and Interpretation of Full Scale Monitoring Data for the Confederation Bridge,* 2nd Year Annual Progress Report for Strait Crossing Bridge Limited (SCBL).

Barthelmie, R. J., Monitoring Offshore Wind and Turbulence Characteristics in Denmark, *Proceedings of the BWEA Wind Energy Conference,* pp. 311-321.

Campbell Scientific 2010a. Instruction Manual R. M. Young Anemometers Model No. 05103, 05103-45, 05106, 05305, *Campbell Scientific,* Logan, Utah, USA.

Campbell Scientific 2010b. Instruction Manual R. M. Young Wind Sentry (03002), Wind Sentry Anemometer (03101), and Wind Sentry Vane (03301), *Campbell Scientific,* Logan, Utah, USA.

Charnock, H. 1955. Wind Stress on a Water Surface, Quarterly Journal of the Royal Meteorological Society, 81:639-640.

Davenport, A. G. 1964. Note on the Distribution of the Largest Value of a Random Function with Application to Gust Loading, *Proceedings of the Institution of Civil Engineers. Paper No. 6739, Vol. 28,* pp.187-196.

Davenport, A. G. 1977. The Prediction of Risk under Wind Loading, *2nd International Conference on Structural Safety and Reliability – ICOSSAR,* Munich Germany pp 511-538.

Davenport, A. G. 1978. *Wind Engineering Course Notes,* Department of Civil and Environmental Engineering, University of Western Ontario, Canada.

Engineering Sciences Data Units. 1974. *Characteristics of Atmospheric Turbulence near the Ground, Part II: Single Point Data for Strong Winds (Neutral Atmosphere),* ESDU Report 74031, ESDU International.

Engineering Sciences Data Units. 1993a. *Strong Winds in the Atmospheric Boundary Layer,* Data Items 82026, ESDU International.

Engineering Sciences Data Units. 1993b. *Strong Winds in the Atmospheric Boundary Layer,* Data Items 83045, ESDU International.

Engineering Sciences Data Units. 1993c. *Characteristics of Atmospheric Turbulence near the Ground, Part II: Single Point Data for Strong Winds (Neutral Atmosphere),* ESDU Report 85020, ESDU International.

Garratt, J. R. 1977. Review of Drag Coefficients over Oceans and Continents, *Monthly Weather Review*, 105, pp 915-929.

Holmes, J. D. 2007. *Wind Loading of Structures,* Second Edition, Taylor and Francis, London and New York.

King, J. P. C., Mikitiuk, M. J., Davenport, A. G., and Isyumov, N. 1994. *A Study of Wind Effects for the Northumberland Straits Crossing,* BLWT-SS8-1994. Boundary Layer Wind Tunnel Laboratory, University of Western Ontario (Parts of this report have been published in King and Davenport 1994 and King 1999).

King, J. P. C., and Davenport, A. G. 1994. P.E.I. Fixed Link – The Treatment of Wind Effects for the Northumberland Strait Crossing, *Fourth International Conference on Short and Medium Span Bridges*, Halifax, Nova Scotia, Canada.

King, J. P. C. 1999. Integrating Wind Tunnel Tests of Full-Aeroelastic Models into the Design of Long Span Bridges, *Proceedings of the Tenth International Conference on Wind Engineering (ICWE),* Copenhagen, Denmark.

Math Works. 1995. *The Student Edition of MATLAB – High-Performance Numeric Computation and Visualization Software,* Version 4, User's Guide, The Math Works Inc. Prentice Hall, Englewood Cliffs, New Jersey, USA.

Montreuil, M. A. 1999a. *Confederation Bridge Monitoring Project Slow-Speed Data Logger System,* Technical Manual, Preliminary Version, Thermal Technology Centre, National Research Council Canada.

Naumoski, N., Cheung, M. S., and Foo, S. 2004. Dynamic Performance of the Confederation Bridge due to Traffic and Wind, *Canadian Journal of Civil Engineering,* Volume 31: 487 – 498.

SCBL. 2008. *Personal Correspondence via Email Dated: 28th January 2008,* Strait Crossing Bridge Limited, Prince Edward Island, Canada.

Smith, S. D. 1980. Wind Stress and Heat Flux over the Ocean in Gale Force Winds, *Journal of Physical Oceanography,* 10/5:709-726.

Simiu, E., and Scanlan, R. H. 1996. *Wind Effects on Structures, Fundamentals and Applications to Design,* John Wiley and Sons, In., New York, USA.

Türk, M., and Emeis, S. 2010. The dependence of offshore turbulence intensity on wind speed. *Journal of Wind Engineering and Industrial Aerodynamics,* 98/8-9:466-471.

Wu, J. 1980. Wind-Stress Coefficients over Sea Surface near Neutral Conditions – A Revisit, *Journal of Physical Oceanography,* 10/5:727-740.

Xu, Z., Bekele, S., Mikitiuk, M., Isyumov, N., and Ho, E. 2008. Bi-Modal Weibull Distribution Fit for Climatic Wind Speed Histogram. *13th Australian Wind Engineering Society (AWES) Workshop,* Hobart, Australia.

Table 2.1 – Correction Coefficients for the 16-Point Compass Directions

Wind Azimuth Bridge North	Wind Azimuth True North	Number of Data Points	Correlation Coefficient $\overline{V}_{P31}/\overline{V}_{P20}$	Coefficient. of Determination R^2	Standard Error in %
NE – 45°	0°	3715	1.025	0.88	0.25
ENE – 67.5°	22.5°	1749	0.997	0.93	0.31
E – 90°	45°	1490	1.038	0.92	0.41
ESE – 112.5°	67.5°	956	1.02	0.80	0.69
SE – 135°	90°	2931	1.251	0.88	0.24
SSE – 157.5°	112.5°	3408	1.17	0.92	0.19
S – 180°	135°	2770	0.984	0.88	0.31
SSW – 202.5°	157.5°	1980	0.873	0.91	0.35
SW – 225°	180°	2678	0.911	0.91	0.27
WSW – 247.5°	202.5°	1979	1.049	0.83	0.35
W – 270°	225°	7506	1.032	0.90	0.13
WNW – 292.5°	247.5°	2214	0.905	0.90	0.29
NW – 315°	270°	3954	0.907	0.93	0.19
NNW – 337.5°	292.5°	3556	0.877	0.95	0.18
N – 0°	315°	2079	0.927	0.95	0.20
NNE – 22.5°	337.5°	1979	1.012	0.92	0.27

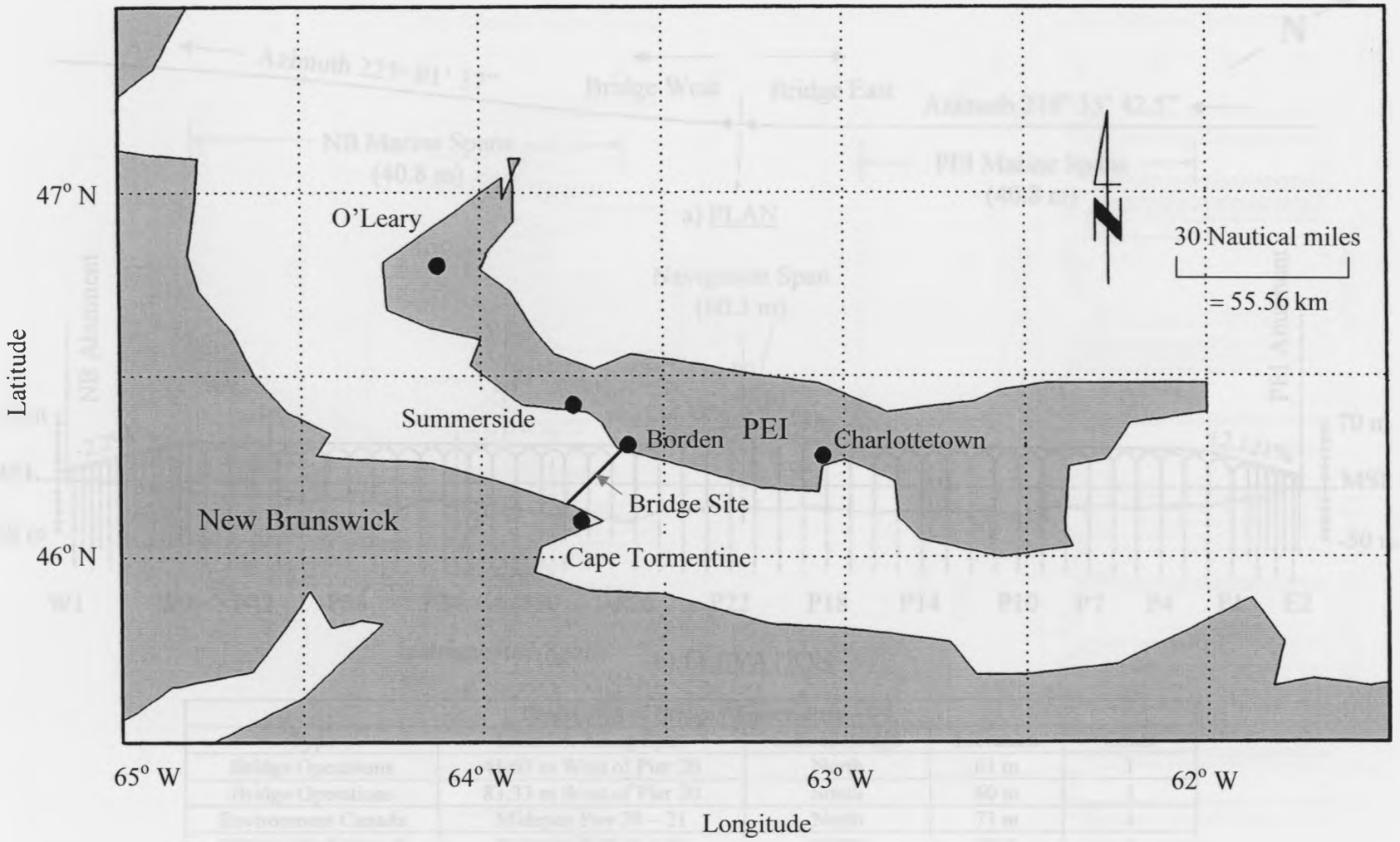

Figure 2.1 – Meteorological Station Locations Used in the 1994 Study [after King et al. 1994]

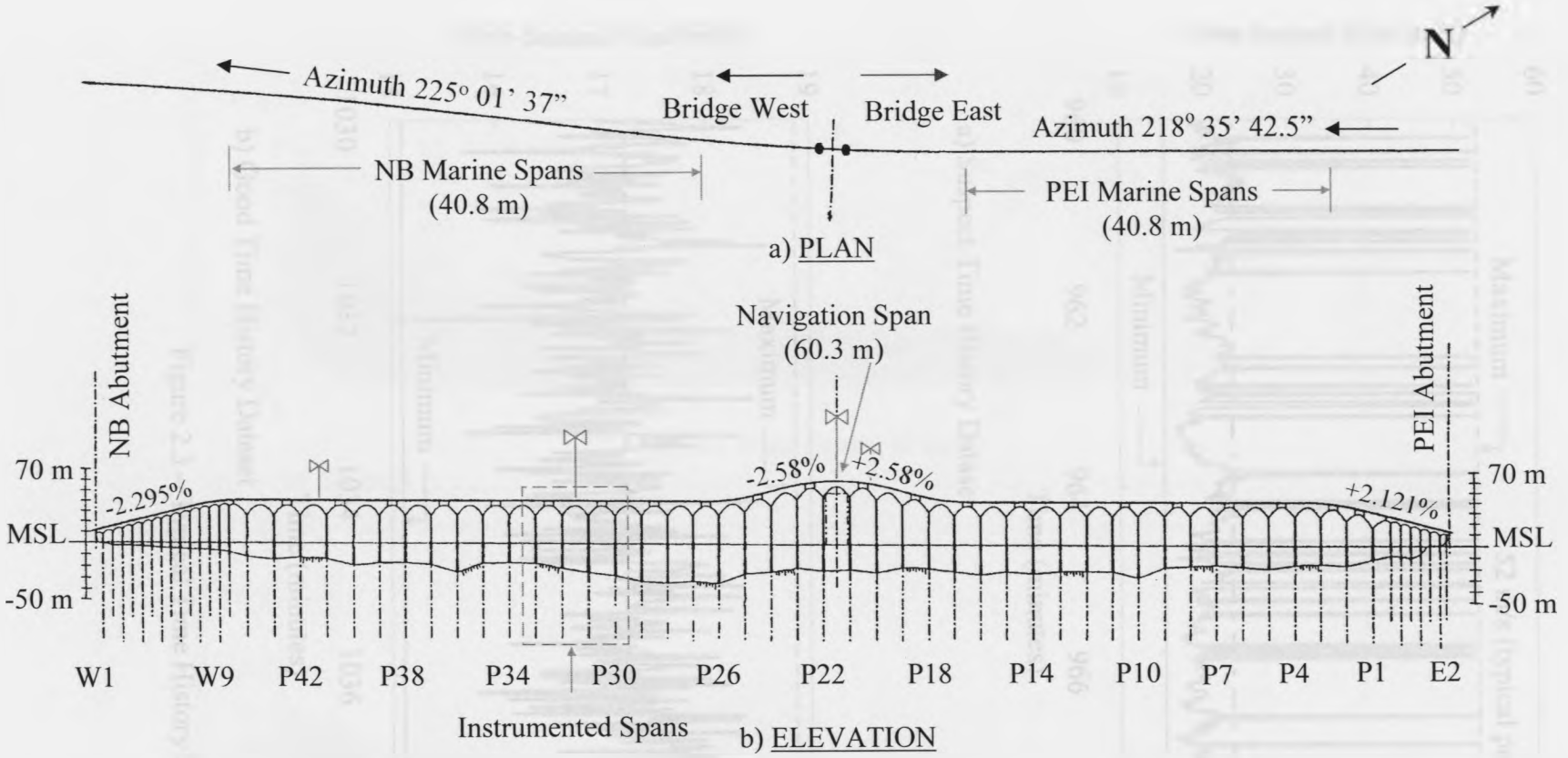

Description of Bridge Anemometers – ⋈				
Type	Location Along Span	Side of Bridge	Elevation	Count
Bridge Operations	41.67 m West of Pier 20	North	61 m	1
Bridge Operations	83.33 m West of Pier 20	South	60 m	1
Environment Canada	Midspan Pier 20 – 21	North	73 m	1
Primary for Research	Midspan Pier 31 – 32	North	54 m	2
Bridge Operations	41.67 m West of Pier 41	North	47 m	1

Figure 2.2 – Bridge Plan and Elevation Showing Anemometer Locations [after King et al. 1994]

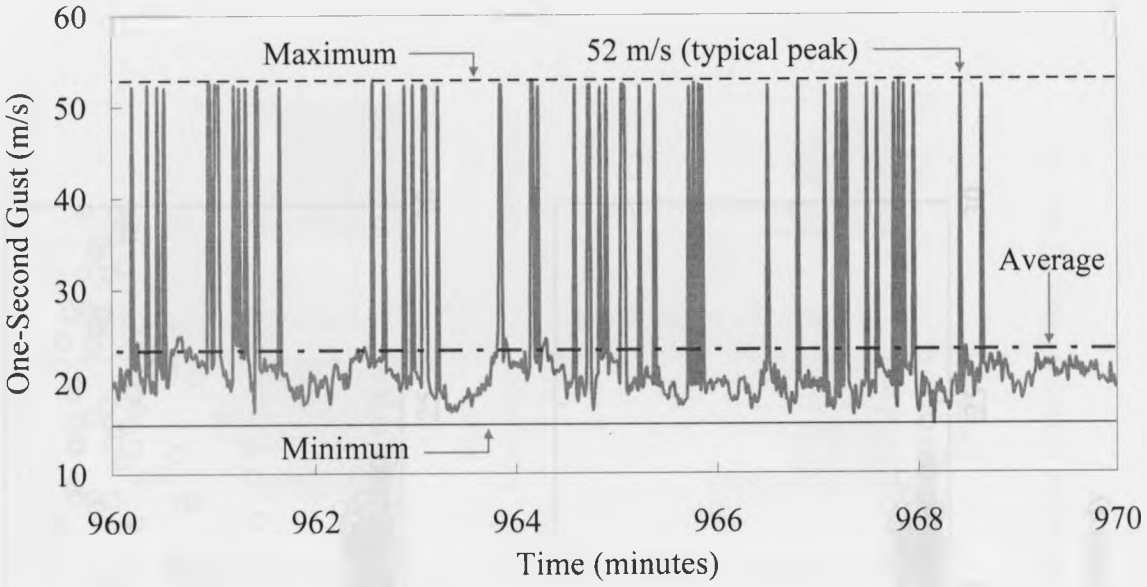

a) Suspect Time History Dataset

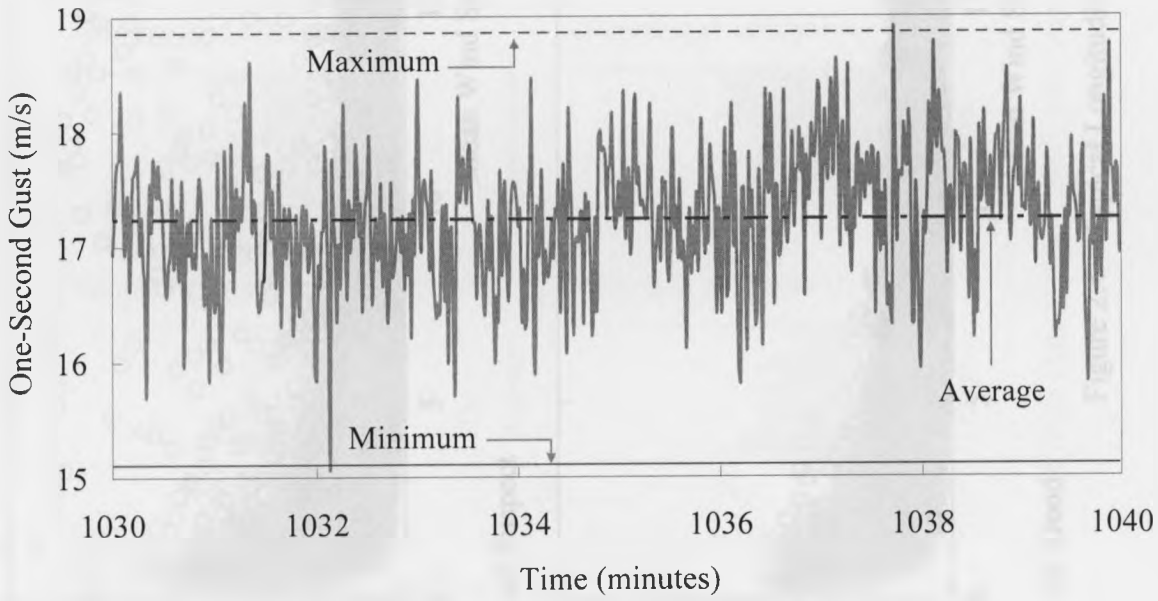

b) Good Time History Dataset

Figure 2.3 – Typical Time History Datasets

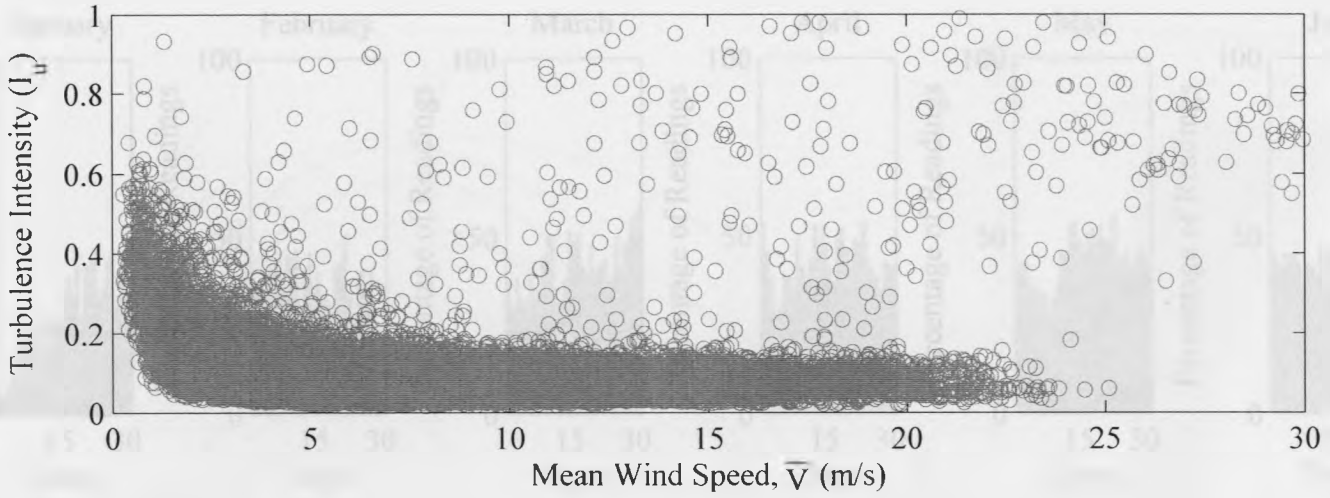

a) Suspect

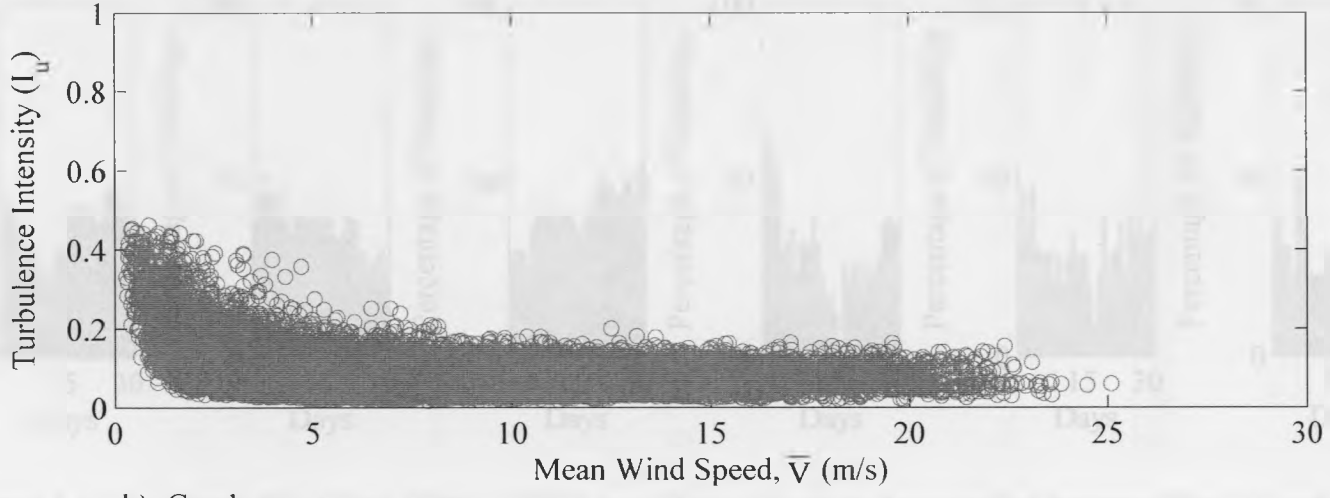

b) Good

Figure 2.4 – Typical Longitudinal Turbulence Intensity

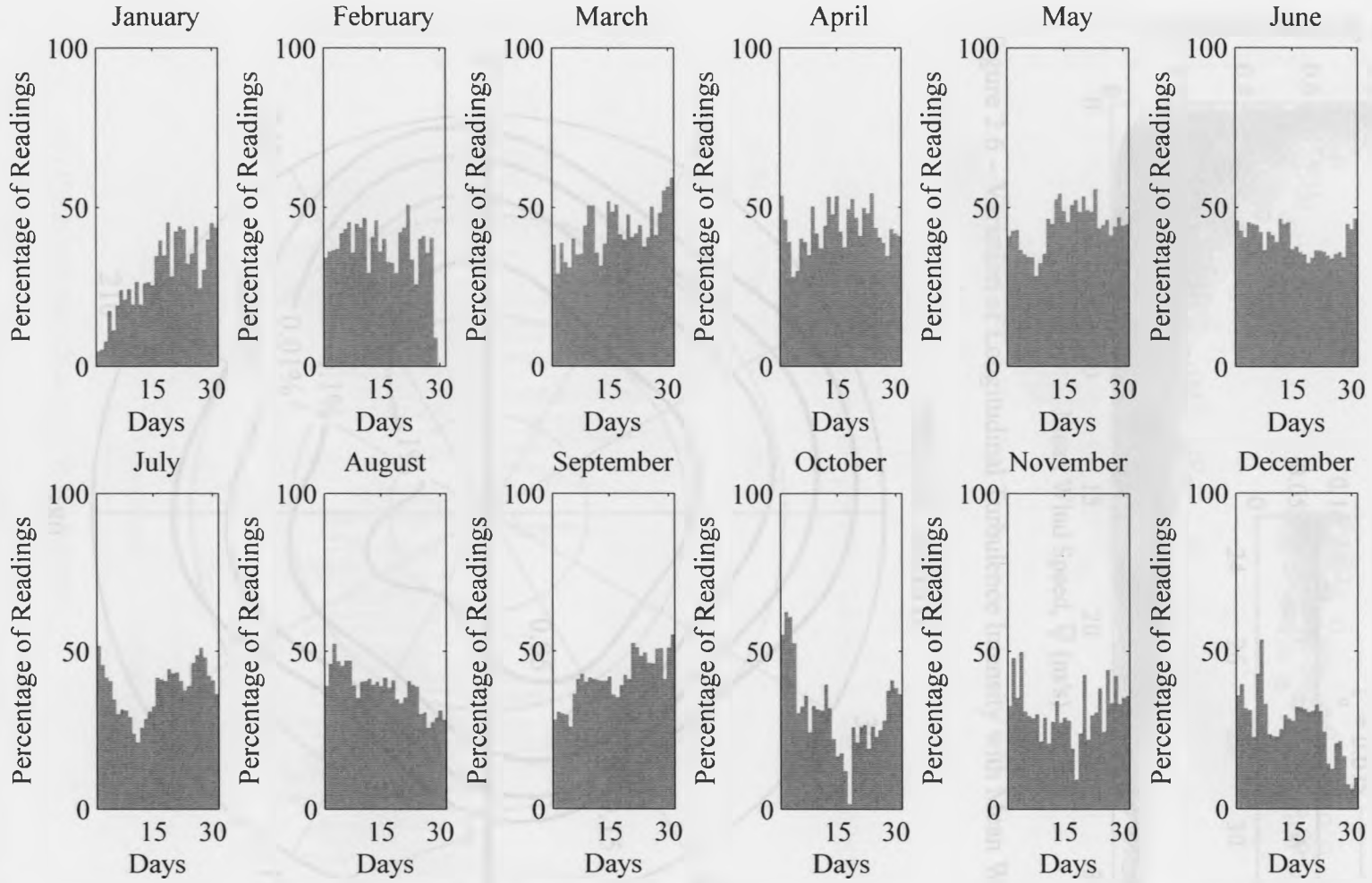

Figure 2.5 – Available Wind Data (1998 – 2007) from Handar Primary Anemometer between Piers 31 and 32

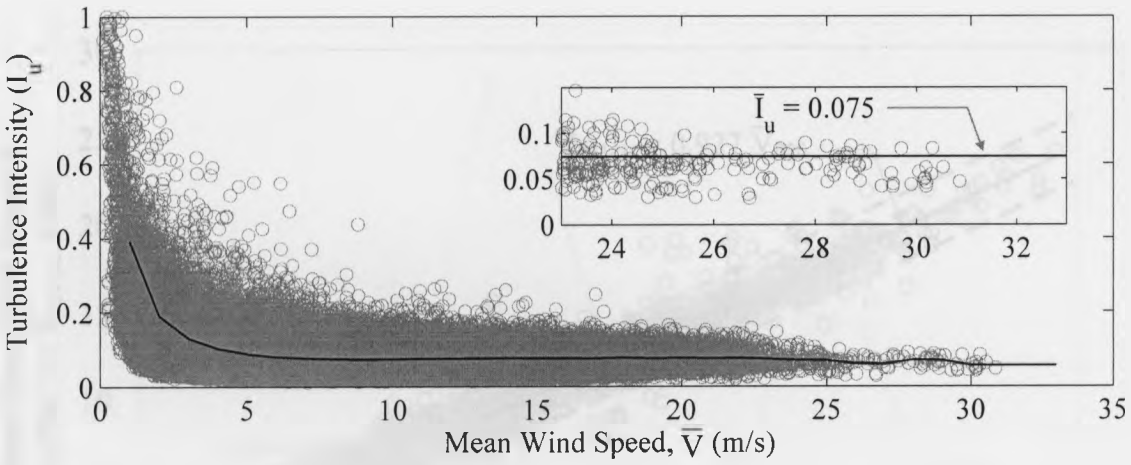

Figure 2.6 – Variation of Longitudinal Turbulence Intensity with Mean Wind Speed

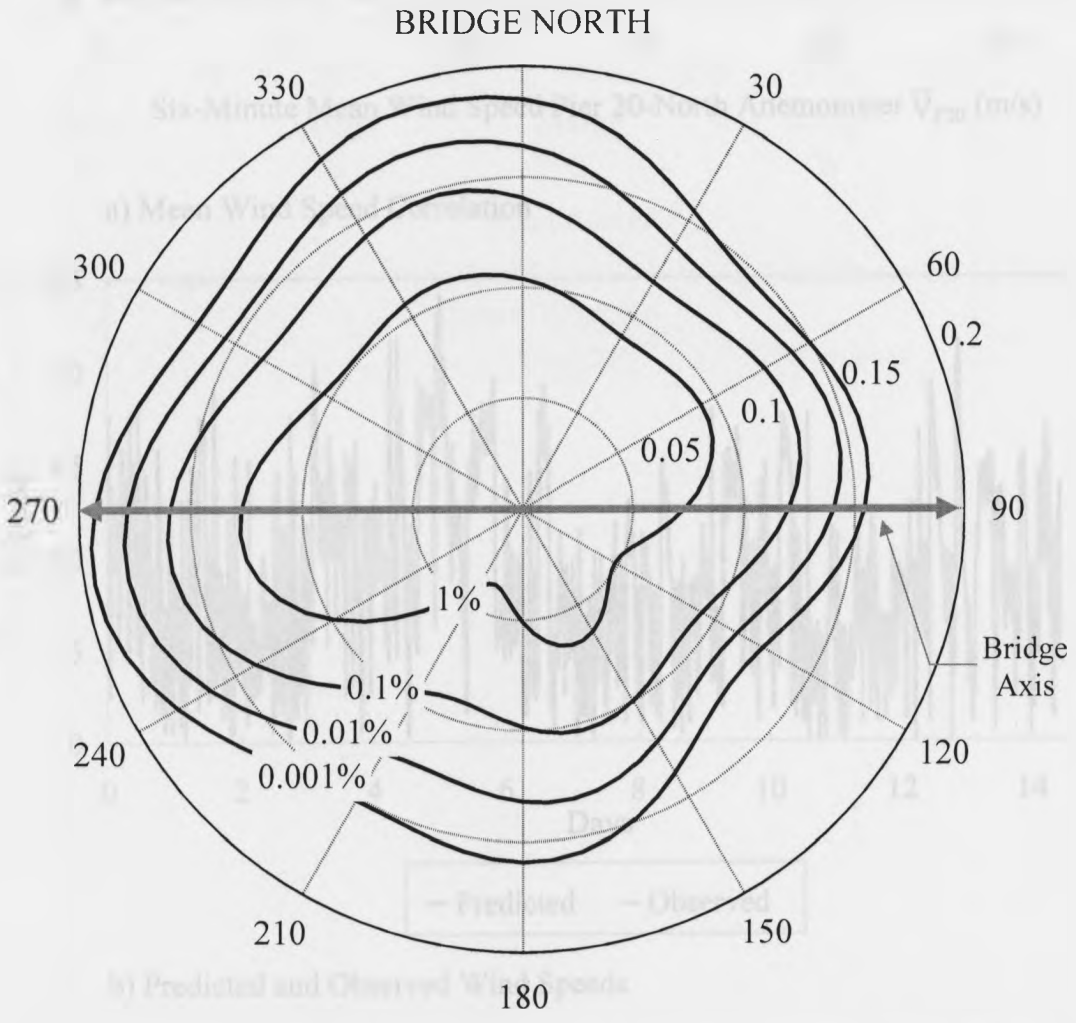

Figure 2.7 – Annual Probability Distribution of Longitudinal Turbulence Intensity with Wind Azimuth for Wind Speeds Greater than 10 m/s.

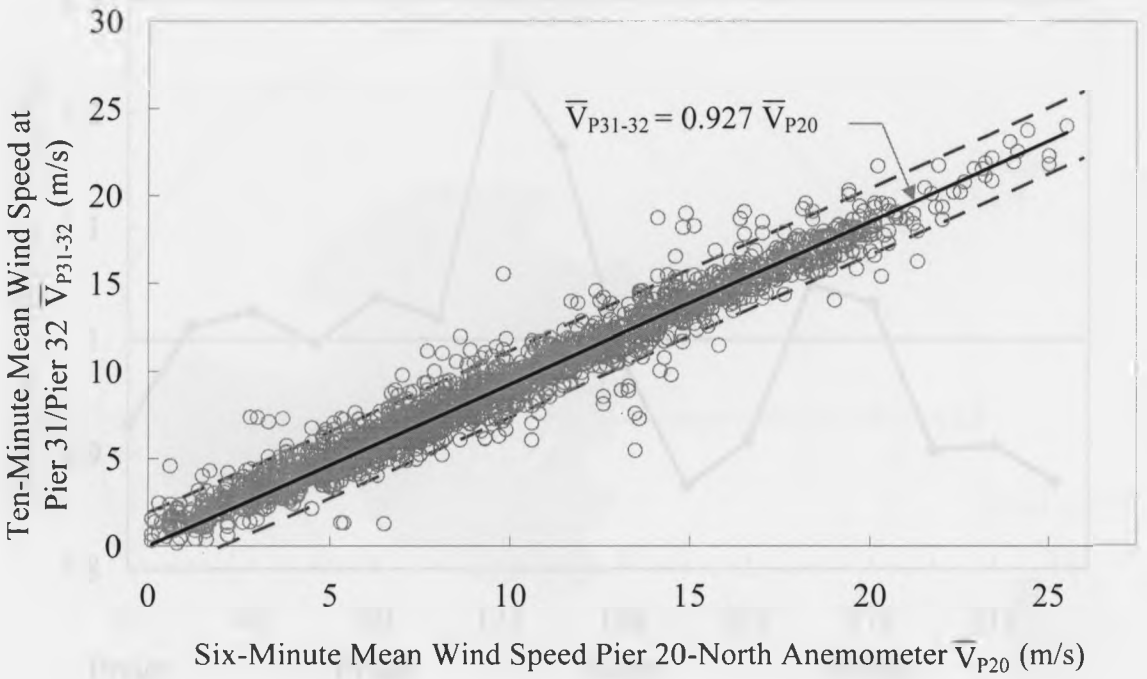

a) Mean Wind Speed Correlation

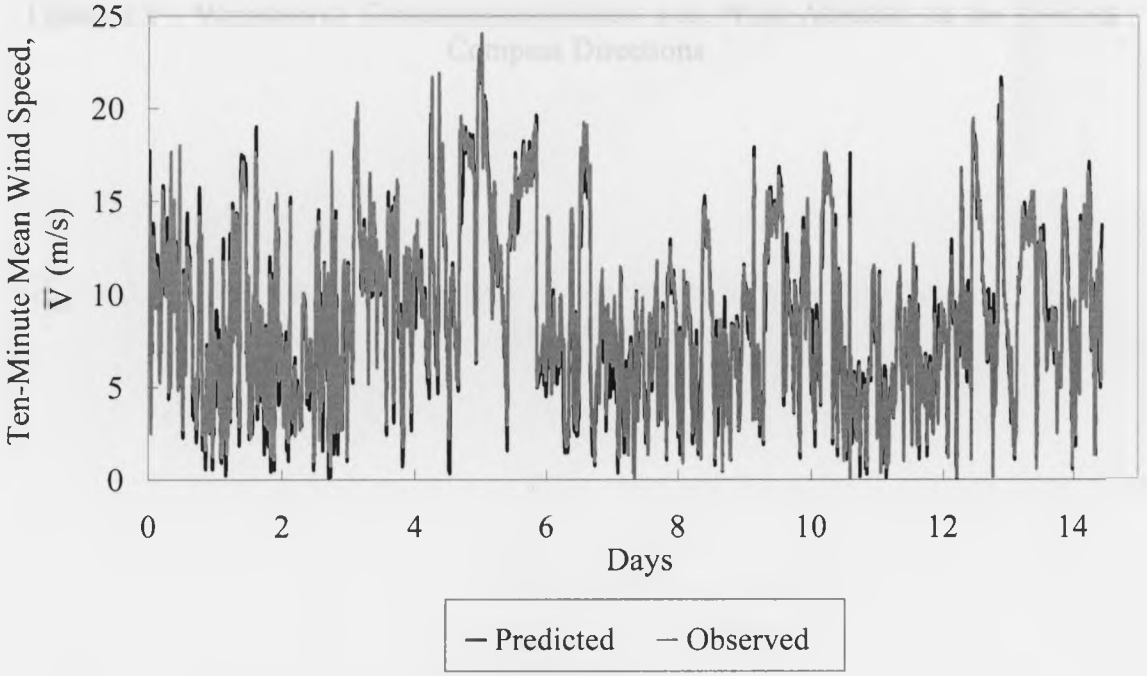

b) Predicted and Observed Wind Speeds

Figure 2.8 – Mean Wind Speed Correlation between Pier 20 and Pier 31-32 Anemometers for the NW Compass Azimuth (i.e., Bridge North)

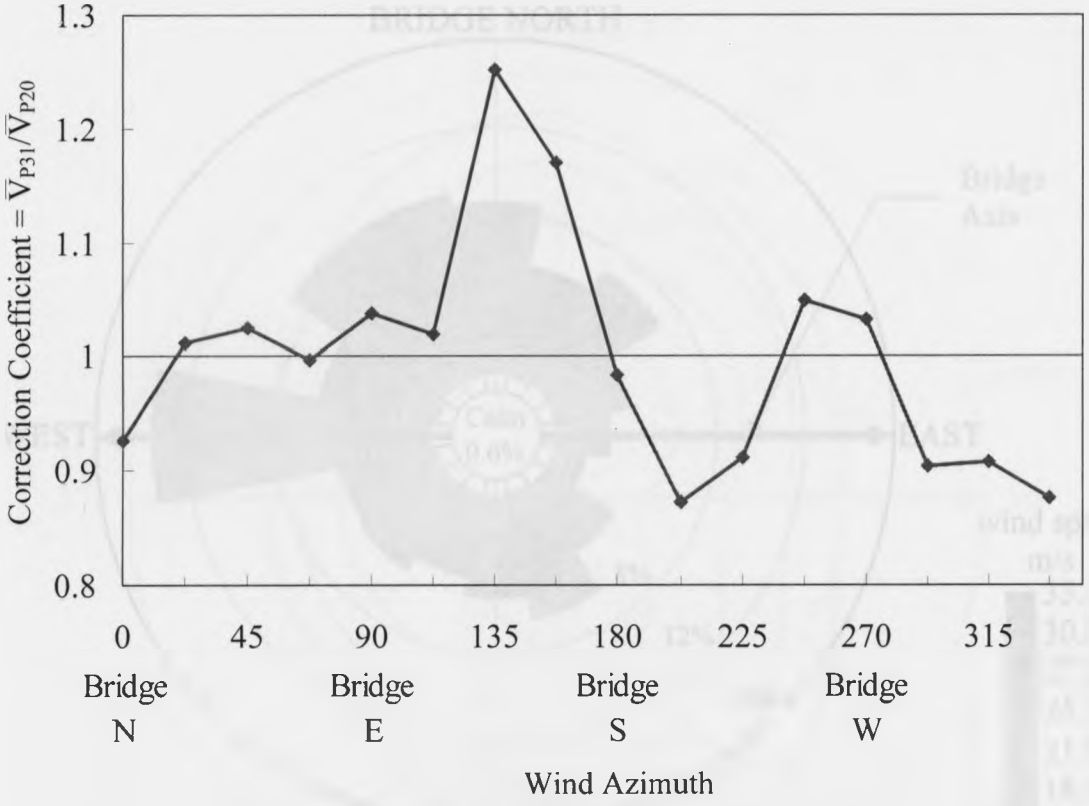

Figure 2.9 – Variation of Correction Coefficient with Wind Azimuth for the 16-Point Compass Directions

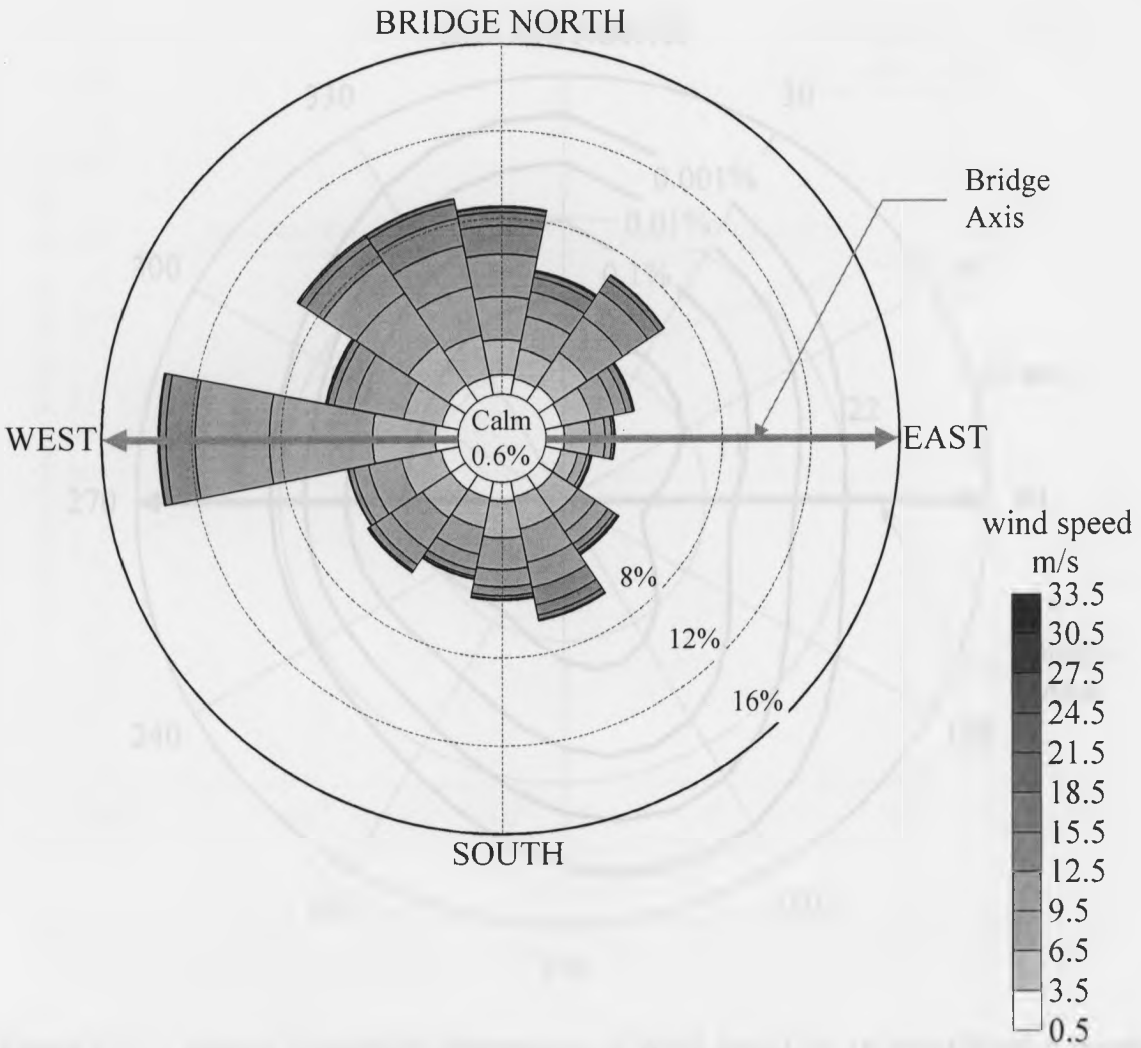

Figure 2.10 – Wind Rose – Frequency of Occurrence of Wind Speeds from Different Directions

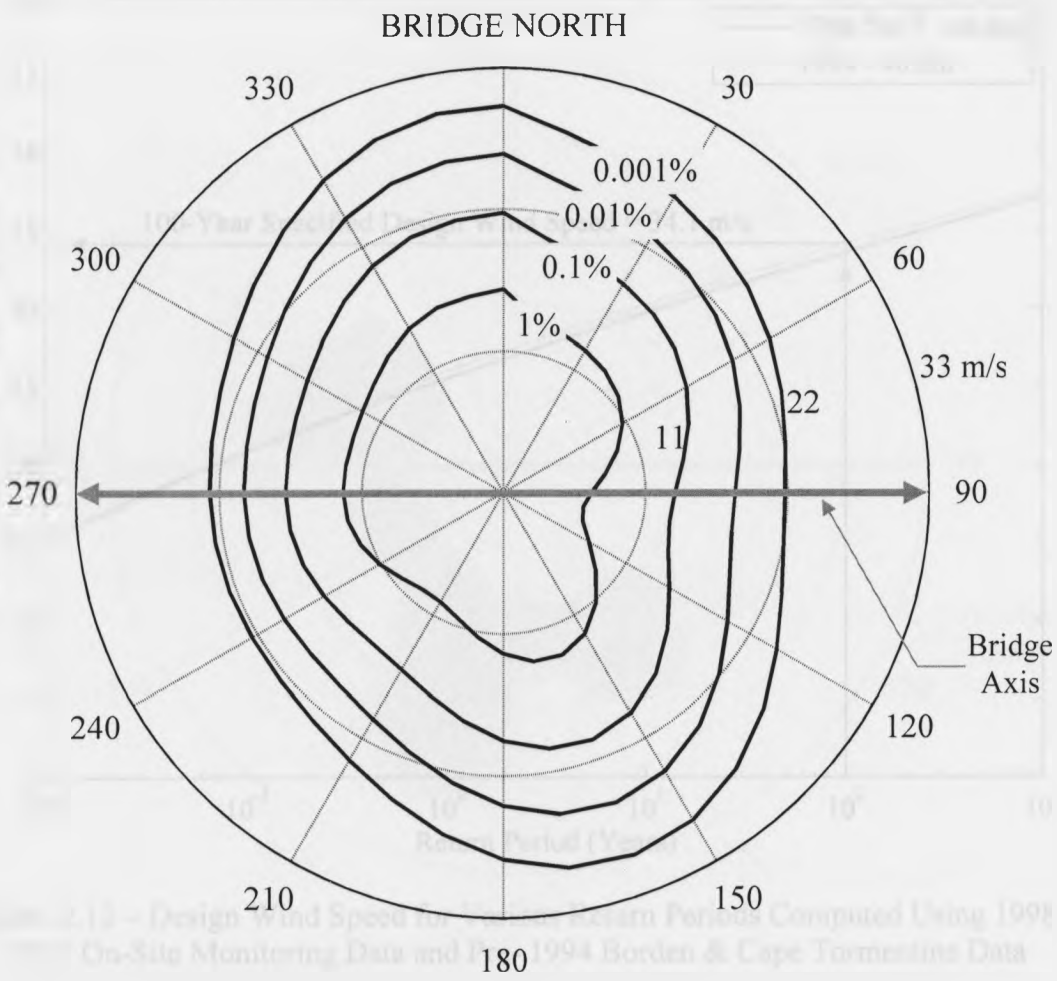

Figure 2.11 – Annual Probability Distribution of Wind Speed for 16-Point Wind Azimuth.

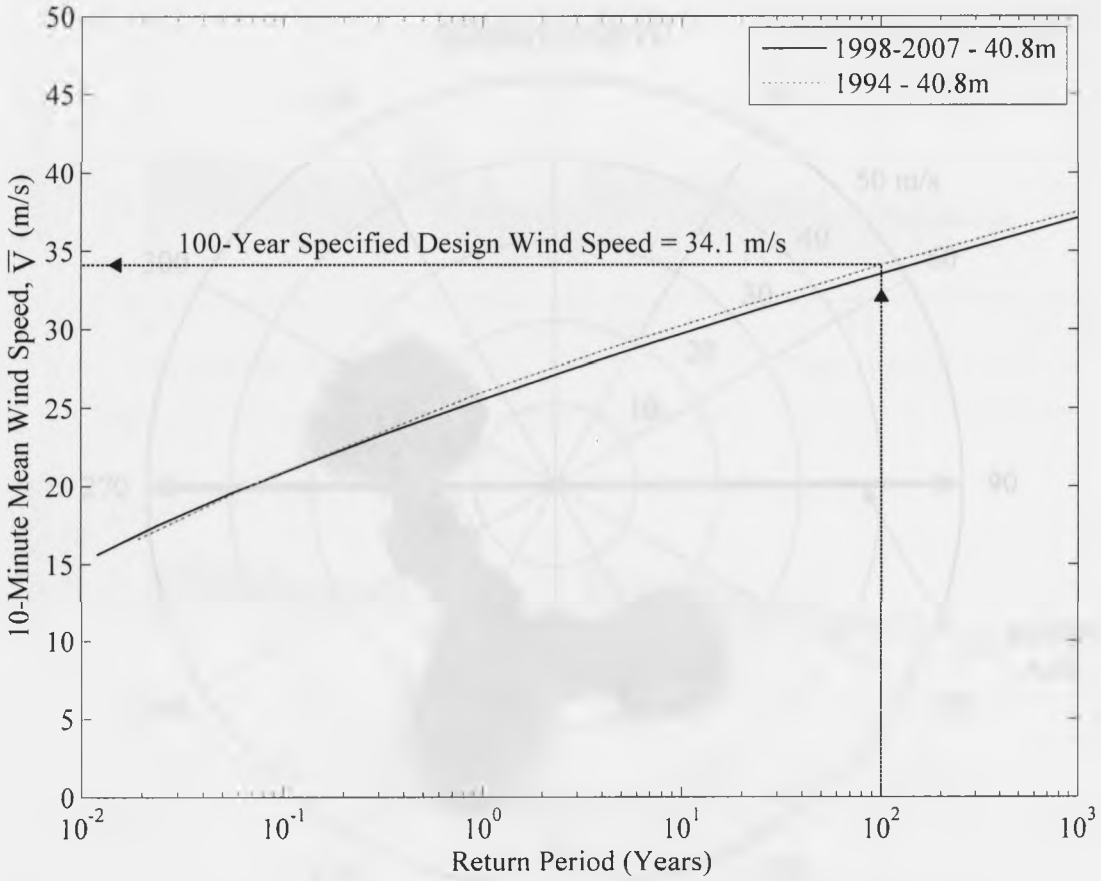

Figure 2.12 – Design Wind Speed for Various Return Periods Computed Using 1998-2007 On-Site Monitoring Data and Pre- 1994 Borden & Cape Tormentine Data

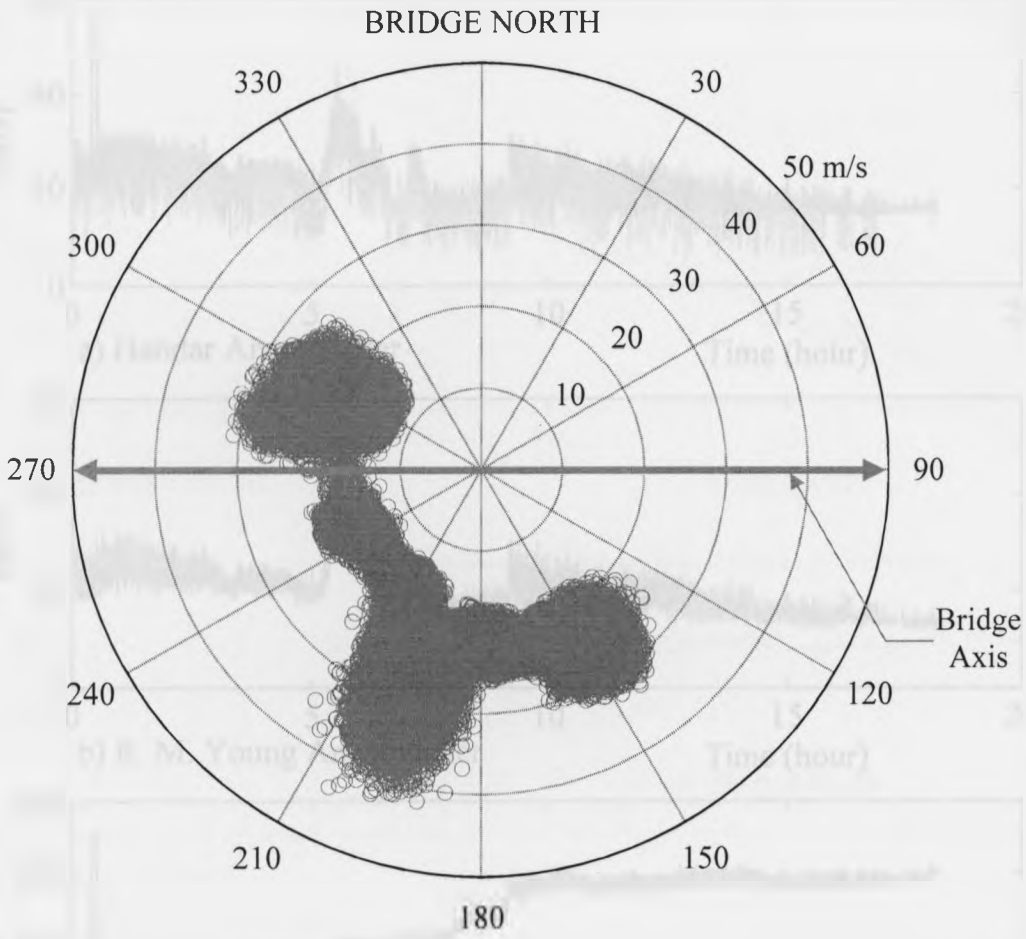

Figure 2.13 – Hurricane Noel Half-Second Wind Data from R. M. Young Anemometer

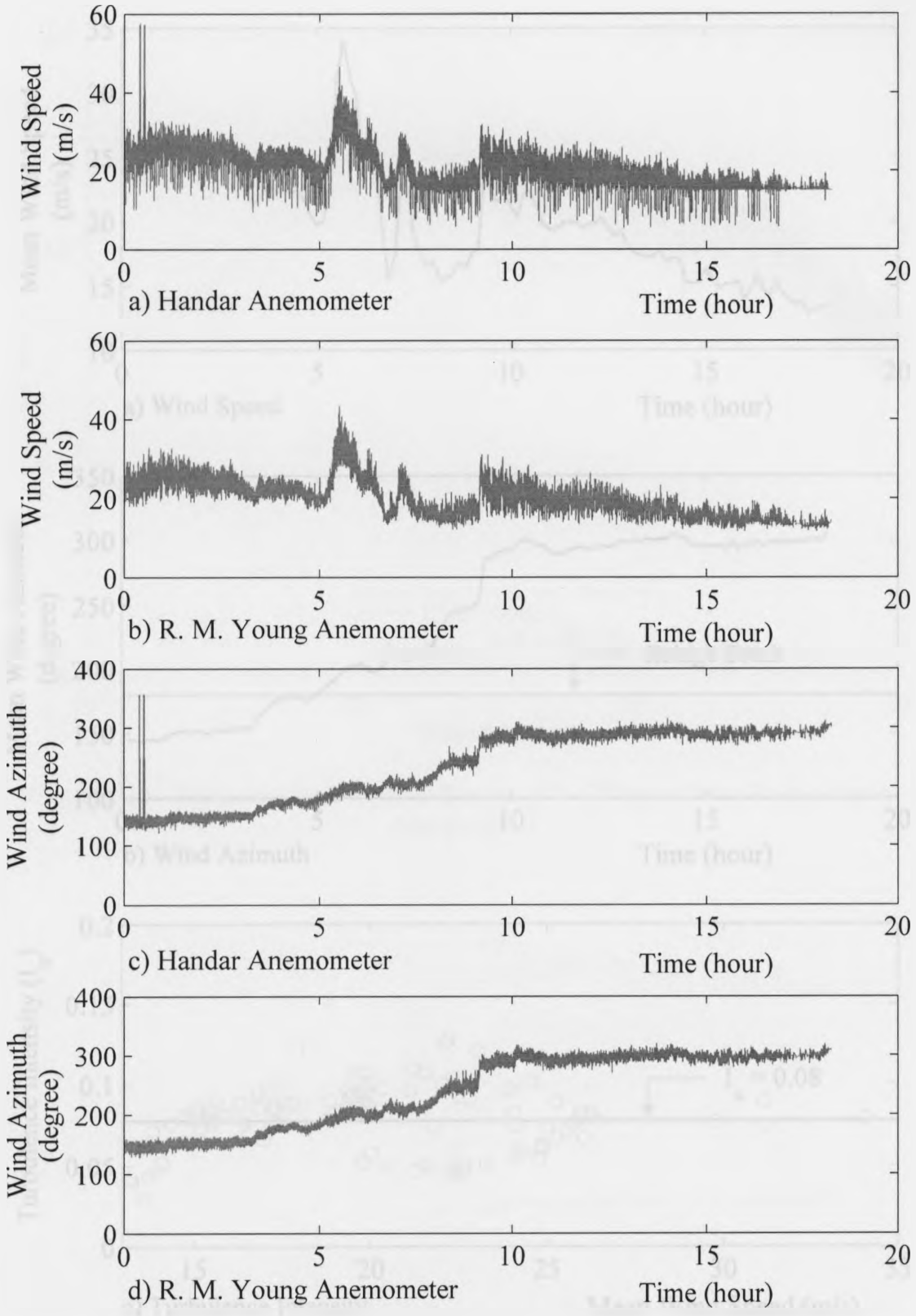

Figure 2.14 – Hurricane Noel – Half-Second Gust Data from Handar and R. M. Young Anemometers

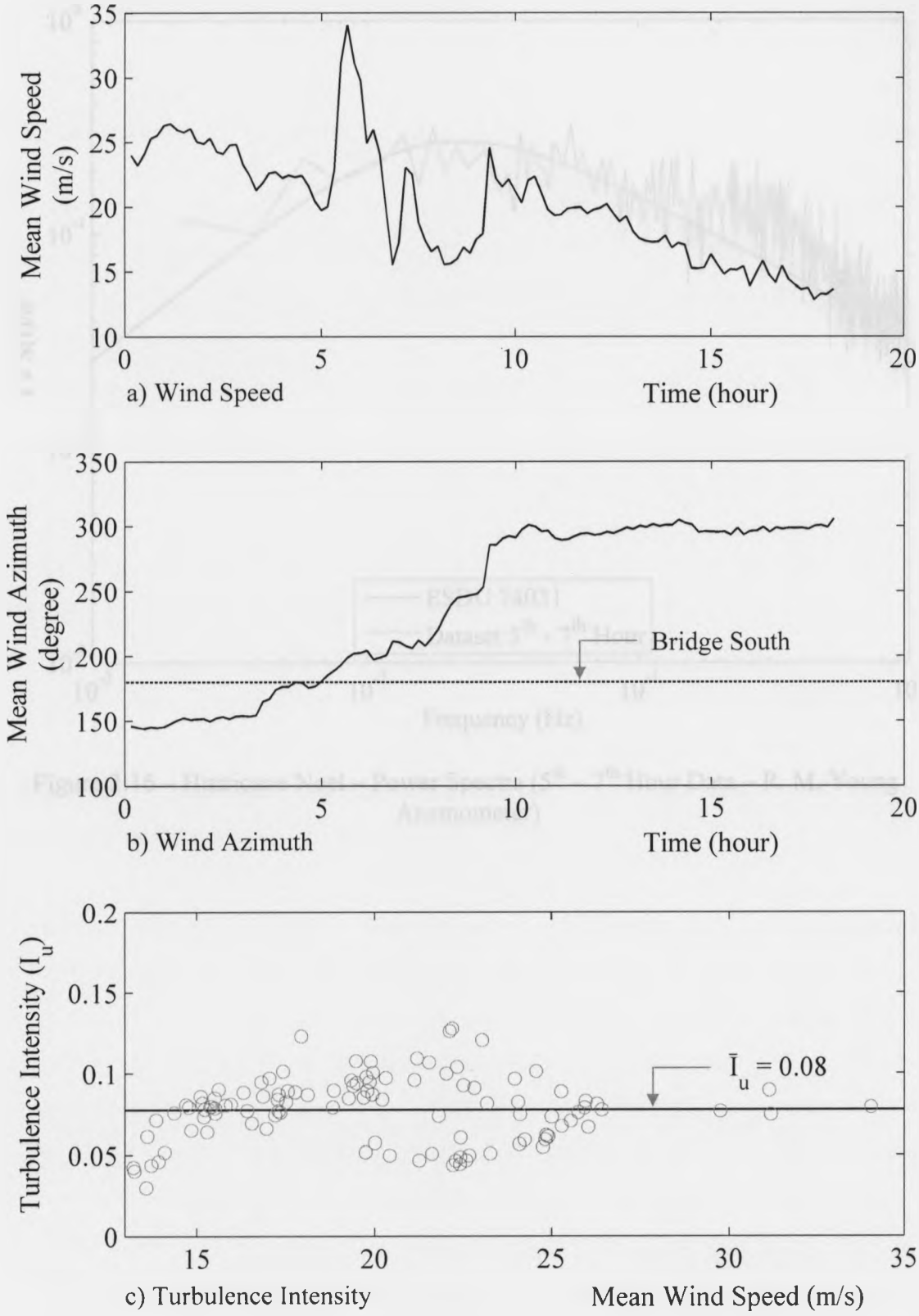

Figure 2.15 – Hurricane Noel – Ten-Minute Mean Wind Statistics

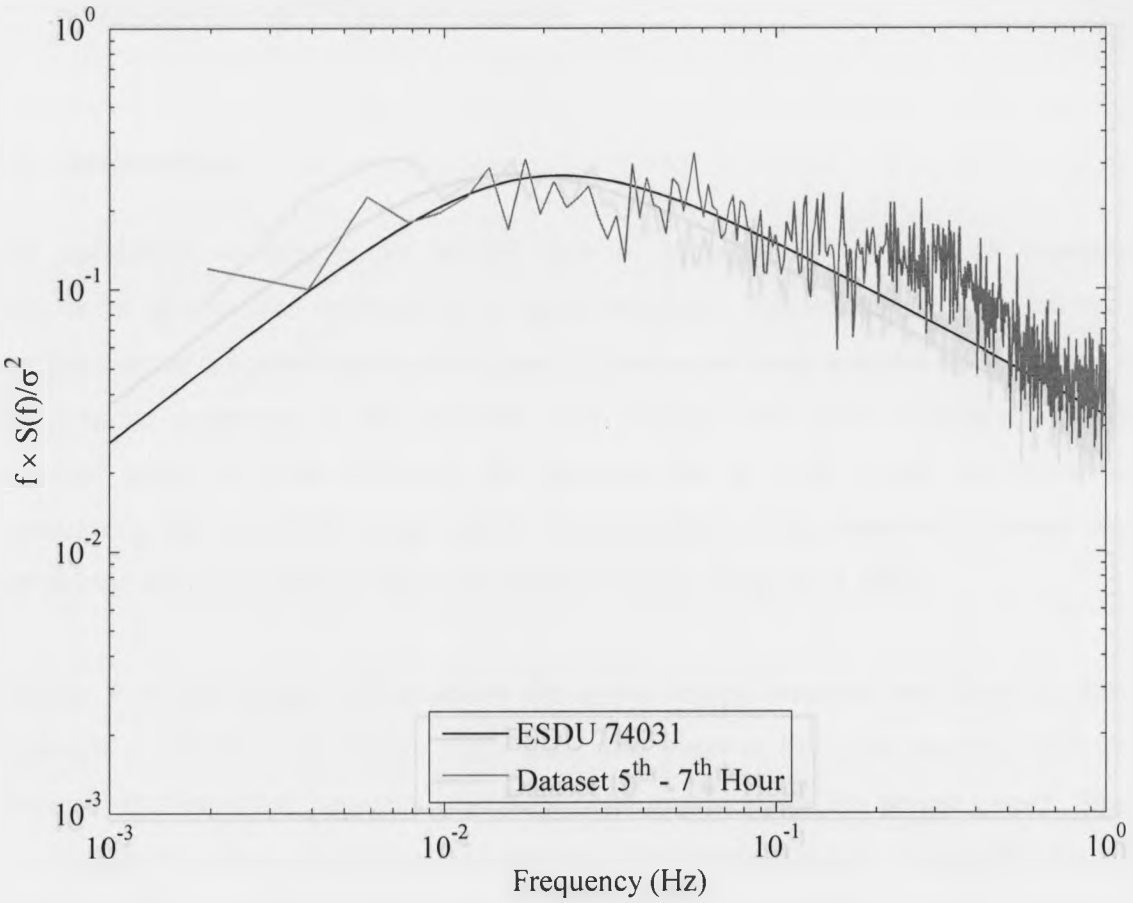

Figure 2.16 – Hurricane Noel – Power Spectra (5^{th} – 7^{th} Hour Data – R. M. Young Anemometer)

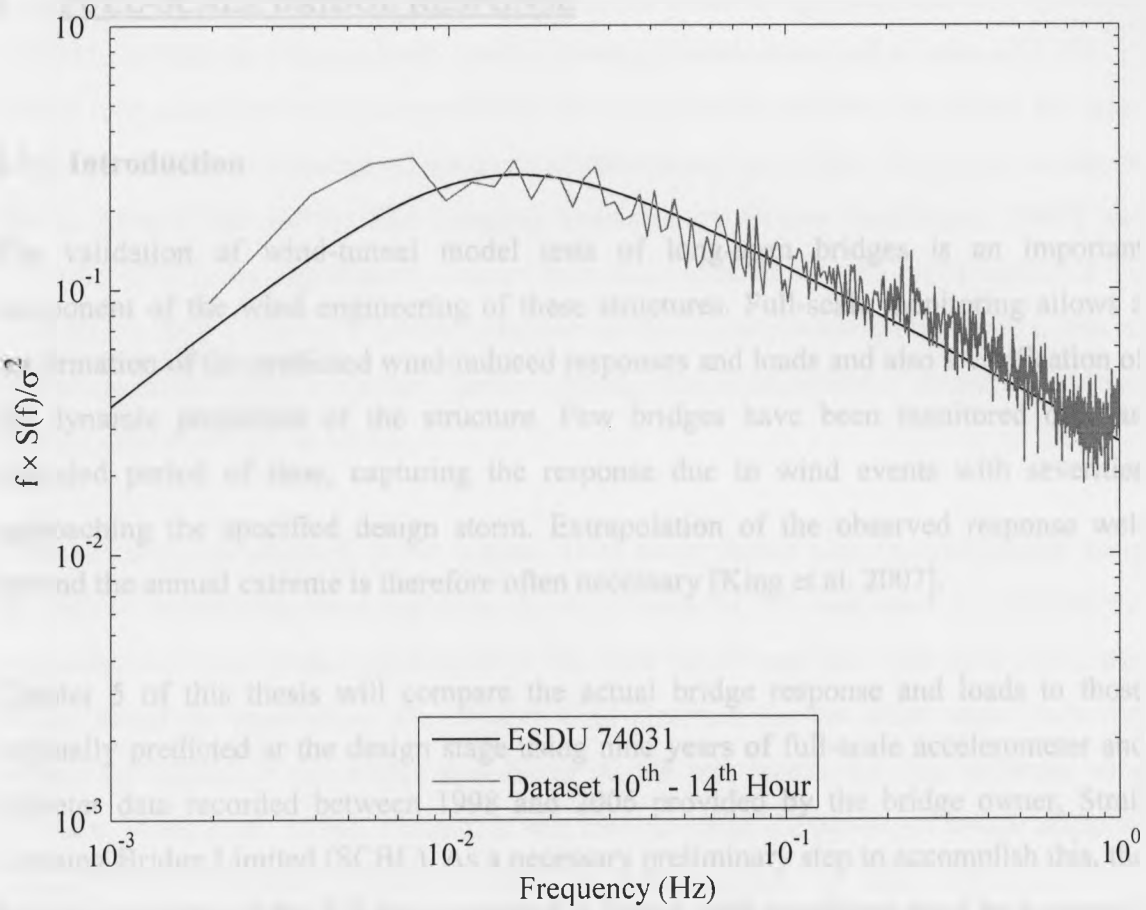

Figure 2.17 – Hurricane Noel – Power Spectra (10^{th} – 14^{th} Hour Data – R. M. Young Anemometer)

3. FULL-SCALE BRIDGE RESPONSE

3.1 Introduction

The validation of wind-tunnel model tests of long-span bridges is an important component of the wind engineering of these structures. Full-scale monitoring allows a confirmation of the predicted wind-induced responses and loads and also a verification of the dynamic properties of the structure. Few bridges have been monitored over an extended period of time, capturing the response due to wind events with severities approaching the specified design storm. Extrapolation of the observed response well beyond the annual extreme is therefore often necessary [King et al. 2007].

Chapter 5 of this thesis will compare the actual bridge response and loads to those originally predicted at the design stage using nine years of full-scale accelerometer and tiltmeter data recorded between 1998 and 2006 provided by the bridge owner, Strait Crossing Bridge Limited (SCBL). As a necessary preliminary step to accomplish this, the dynamic response of the full-scale structure in strong wind conditions must be accurately quantified. In particular the mode shapes, frequencies, damping and other dynamic parameters must be determined.

The natural frequencies and mode shapes assumed at the design stage (needed to perform the wind tunnel tests) were based on the numerical models of the prototype provided by JMI-Stanley [1995]. These models represented three spans of the bridge centred about the navigation span and a typical marine span with typical overall pier heights and assumed material properties. The frequencies reported by Londoño [2006] for the instrumented marine spans (which have different overall pier heights) are different from the values assumed at the design stage. Although the first few frequencies and mode shapes are wind-driven, these values need to be confirmed as they are required to derive wind loads in Chapter 5. Subsequently, the original numerical model of the prototype [JMI-Stanley 1995] needs to be modified accounting for the actual overall pier heights and material properties.

Very little was known about the prototype damping at the design stage and so a low value of 0.13% of critical was originally used to identify instabilities and a value of 0.63% of critical (considered to be more representative of prestressed concrete structures) was used for the remainder of the original wind tunnel tests [King et al. 1994, King and Davenport 1994a, King et al. 1995]. The damping estimates by Brown and Bruce [1997] and Londoño [2006] are significantly higher than this value. Brown's [1997] estimates are even higher than Londoño's [2006] estimates of the prototype damping. Since a lack of consensus exists between the two, further investigation is necessary to determine realistic damping estimates of the bridge.

Other assumptions adopted in the original 1994 study should also be investigated using the on-site monitoring time histories. A peak factor of 3.5 was used to estimate the equivalent full-scale peak responses from the wind tunnel test data. The peak factor was chosen based on experience. The critical wind direction for the wind tunnel tests was considered normal to the bridge axis based on the test results for four different wind azimuths [King et al. 1994]. Further, it was assumed that the prototype bridge response reduces with the square of the cosine of the angle between the wind azimuth and the direction normal to the bridge axis as derived in Appendix 3C. This is generally true for static or mean response provided the wind is stationary; however, the hypothesis has never been verified for the dynamic response of the Confederation Bridge using full-scale data.

Conveniently, the procedures used to analyse wind-tunnel model data in 1994 [King et al. 1994, King and Davenport 1994, King et al. 1995] to predict the dynamic bridge response and loads can be adopted to analyse the on-site monitoring data. Preliminary analysis of the data from the on-site monitoring programme showed serious anomalies in the data acquisition system and so the latter was reconfigured, temporarily, to collect useful data for a strong wind event during the passage of Hurricane Noel on November 4, 2007. Only a portion of the Hurricane Noel data from selected accelerometers was investigated since most of the accelerometers provide redundant information. The extensive arrangement of accelerometers increases maintenance cost and reduces efficiency of the monitoring

programme, which has raised the question whether such extensive instrumentation is essential for monitoring the bridge during extreme wind events.

The present study will address these issues by creating a database of statistics and time histories for all 76 accelerometers, and six tiltmeters attached to the bridge. Much of the tiltmeter data have been analysed by a research group at the University of Calgary, headed by Brown [2007], measuring ice forces on the piers of the instrumented spans. The analysis of these data has been well documented [Bruce and Croasdale 2001], and so need only be briefly reviewed in this chapter for latter use in Chapter 5 to derive the static force coefficients.

In Chapter 5, the frequencies, and mode shapes determined from the on-site monitoring data and the modified numerical model of the Confederation Bridge [JMI-Stanley 1995] will be used to compute wind loads for comparison with those predicted in various wind-tunnel investigations. The damping coefficients presented in this chapter will be used to determine the damping correction required for the analysis of the equivalent full-scale loads.

3.1.1 Research Objectives

The aim of the research presented in this chapter is to carry out a comprehensive analysis of the available accelerometer and tiltmeter data from the Confederation Bridge on-site monitoring programme to form a database of statistics and time histories that will facilitate the load determination in Chapter 5. The specific goals of the study are:

i) To identify dynamic properties of the Confederation Bridge, i.e., natural frequencies, mode shapes and damping for comparison with the values reported by others.

ii) To modify the existing numerical model of the Confederation Bridge and validate it with the full-scale results.

iii) To derive the dynamic bridge response, in the form of RMS accelerations and normalized modal accelerations, that will be used in Chapter 5 to derive the dynamic wind loads.

iv) To estimate peak factors for the fundamental modes for comparison with the value used for the original design in 1994.

v) To determine the variation of the bridge response with wind azimuth that will be compared to the conventional cosine-squared relationship to investigate its accuracy.

vi) To investigate whether the present extensive array of instrumentation to monitor the bridge is necessary for capturing the essential wind responses, and

vii) To determine a relationship between the pier tilt and wind velocity that will be used to derive static force coefficients in Chapter 5.

3.1.2 Chapter Organization

The accelerometer data consist of statistical summaries and time histories, gathered between 1998 and 2006 from the Confederation Bridge, that will be classified based on wind speed and direction. An extended dataset collected during Hurricane Noel will also be analysed. The bridge frequencies identified from power spectra, derived using on-site monitoring data, will be compared to those determined numerically in ALGOR [Logan 2001] and reported by Londoño [2006]. The mode shapes determined using the modified ALGOR model for the Confederation Bridge will be compared to the mode shapes extracted by Londoño [2006]. Both the typical and Hurricane Noel accelerometer datasets will be used to determine the dynamic bridge responses and their results compared. The data from Hurricane Noel will be used to determine peak factors for comparison with those originally assumed for the bridge design. The total bridge damping (the sum of structural and aerodynamic damping) will also be estimated using Hurricane Noel data

and compared to the values reported by Londoño [2006] and Brown and Bruce [1997]. The variation of the bridge displacement with wind azimuth will be compared to the conventional cosine-squared relationship. Finally, the relationship between the pier tilt and wind velocity, proposed by Bruce and Croasdale [2001], will be discussed in light of the onsite monitoring tiltmeter data.

3.2 Available Accelerometer Data

3.2.1 On-Site Instrumentation

Figure 3.1a shows the locations of accelerometers and tiltmeters attached to the bridge between Piers 30 and 33 to facilitate the on-site monitoring programme that was initiated in 1998. The instruments are scanned by High Speed Data Loggers (HSDLs) 1, 4, 5, and 6 represented as dashed rectangles in the figure. The calibration factors for the accelerometers and tiltmeters and the specifications for the data loggers are reported by Montreuil [1999]. Figure 3.1b schematically shows the fundamental modes of vibration developed by Londoño [2006]. The significant transverse modes of vibration are the first and second symmetric and first asymmetric transverse modes, labelled TS1, TS2 and TA1, respectively. The significant vertical modes are the first and second symmetric and first asymmetric modes, labelled VS1, VS2 and VA1, respectively. Accelerometers 5, 7, and 9 scanned by HSDL 5, and Accelerometer 15, scanned by HSDL 4, in each of the transverse and vertical directions, capture data at key locations between the midspans of the drop-in spans, i.e., Pier 30/31 and Pier 32/33, that include the maximum modal displacements and accelerations for these six modes. Therefore data from these accelerometers can be used to determine the corresponding natural frequencies, mode shapes, and damping. Although 76 accelerometers are used to monitor the bridge [Montreuil 1999], it will be demonstrated later that a maximum of four accelerometers at critical bridge locations, as shown, in each of the transverse and vertical directions, are sufficient to fully characterize the dynamic bridge response necessary to quantify the wind loading.

3.2.2 Ten-Minute Accelerometer Data

The accelerometer data scanned by the high speed data loggers are stored as statistical summaries and may also be stored as time histories. The statistical summaries are 15-second mean and Root Mean Square (RMS) records, which are further averaged over ten-minute intervals and so are readily correlated with the ten-minute wind statistical summaries presented in Chapter 2. Figure 3.2 shows the number of available statistical summaries for HSDLs 1, 4, and 5 that were made available for the present study. In years when monitoring system was working well, e.g., 2000 and 2001, HSDLs 1, 4 and 5 collected more than 90% of the 52596 maximum possible ten-minute records available annually. In 2006, HSDLs 4 and 5 collected only 6% of the total records available. No data have been collected on HSDL 1, 4 or 5 since 2006. It is recommended that the data acquisition system be regularly maintained to ensure the uninterrupted collection of the future ten-minute accelerometer statistical summaries.

Figure 3.3 shows the number of ten-minute accelerometer time history records, sampled at a frequency of 125 Hz, available for the HSDLs 1, 4 and 5. Data collection starts when ten-minute mean wind speed exceeds 15 m/s. The datasets obtained from 1998 to 2002 are only 30 or 90 seconds in duration, and so are too short to accurately characterize the acceleration power spectrum: the bridge is designed for a ten-minute mean wind speed as described in Chapter 2 and so a minimum record duration of ten minutes is required for spectral analysis. It will be shown in Section 3.4.2 that continuous data, collected for extended period during a strong wind event, provide more accurate results and offer more flexibility in the analysis. Therefore, it is recommended that, once triggered, time history data should be collected without interruption for the entire wind event. The current programming that stops data collection when the instantaneous wind speed drops below 15 m/s is unsatisfactory because it can create gaps in, and so prevent the analysis of, the time history record. To facilitate the longer time history duration, the data storage capacity can be increased by a factor greater than 6 by simply reducing the sampling frequency from 125 Hz to 20 Hz without affecting the accuracy of the acceleration power spectrum as shown in Appendix 3A. It will be shown in Section 3.4 that the fundamental

modes of vibration in strong wind events have frequencies less than 1 Hz and so the current 125 Hz sampling frequency is excessive to capture wind-related events and severely restricts the maximum possible duration of the time history record.

On-site monitoring accelerometer data, whether in the form of statistical summaries or time histories, were categorized based on wind speeds and azimuths defined using a 16-point compass azimuth. Accelerometer data scanned by HSDLs 4 and 5 cover critical bridge locations for the six modes necessary to characterize the wind response shown in Figure 3.1b and so will be used to determine dynamic bridge response.

3.2.3 Hurricane Noel Data

Hurricane Noel provided an opportunity to collect an 18-hour dataset from a single strong wind event. The analysis of the Hurricane Noel wind data was presented in detail in Chapter 2. To capture the whole wind event, HSDLs 4 and 5 were temporarily programmed to collect only time histories and the associated ten-minute statistical summaries were subsequently computed using MATLAB [Math Works 1995]. The accelerometer time histories were sampled at 29.4 Hz or about 23% of the 125 Hz rate previously used, relieving storage demands and resulting in a time history with an 18-hour duration.

The accelerometer time histories logged by HSDL 5 were therefore divided into ten-minute data records and were used to compute ten-minute statistical summaries of RMS accelerations that are readily correlated with the ten-minute statistical summaries of wind data presented in Chapter 2. The accelerometer data, whether in the form of ten-minute statistical summaries or time history datasets were classified based on wind speed and azimuth, using a 10^{o} azimuth interval. They will be used to determine the dynamic bridge response as described in Section 3.4.

3.3 Frequencies and Mode Shapes

Table 3.1 compares full-scale observed frequencies, derived from power spectra [Davenport and King 1982, 1984, Davenport 1988] in 2009, with the frequencies reported by Londoño [2006]. The ALGOR model developed for a typical marine span by JMI-Stanley [1995] is modified to reflect the properties of the marine span between Piers 31 and 32. The JMI-Stanley model assumed uniform pier depths, whereas the modified model used in the present study accounts for the different pier depths: the base of Pier 31 at 29.3 m below Mean Sea Level (MSL) is 7.6 m deeper than the base of Pier 32 at 21.7 m below MSL [JMI-Stanley 1994]. The modified ALGOR model is described in detail in Appendix 3B. The model frequencies obtained numerically from the modified ALGOR model will also be compared to the frequencies computed from the on-site accelerometer monitoring data in the present study.

As shown in Table 3.1, the frequencies computed from the on-site monitoring data in the present study have a variability of less than 2% of the mean value for Modes 2 through 8 whereas the variability of Mode 1 is roughly 4% of the mean. The frequencies computed from the on-site accelerometer monitoring data by Londoño [2006], have variabilities less than 10% of the mean value for all modes except TS1 and VA1, which have variabilities less than 20% of the mean value. The variabilities in the present study are markedly less than those reported by Londoño because only accelerometer data for wind speeds greater than 15 m/s were used to derive frequencies whereas Londoño used data representing various loading conditions including severe wind events, heavy traffic events and ambient traffic conditions with or without ice loading present [Londoño 2006]. Nevertheless, the mean values of Londoño's observed frequencies are within 3% of the mean values of the observed frequencies derived in the present investigation. The numerical beam-element model frequencies reported by Londoño, are also shown in Table 3.1, and are within 10% of those computed from the full-scale monitoring data in the present investigation. The model frequencies determined using the modified ALGOR model in the present study are generally within 5% of the mean frequencies computed from the full-scale monitoring data. The exception is Mode VA1, where the numerical

model value of 0.5 Hz is 13% less than the full-scale monitoring-based value of 0.57 Hz. At the present time, no explanation has been found for this discrepancy.

The concrete modulus of elasticity, E_c, at an age of 1000 days, 43 GPa, is used in both numerical models to give more accurate frequency estimates. The 1000-day concrete modulus is calculated using the expression proposed by Ghali et al. [2000], based on their assessment of the structural response of the bridge, as:

$$E_c(t) = E_c(28)\sqrt{e^{0.25\left(1-\sqrt{\frac{28}{t}}\right)}} \qquad [3\text{-}1]$$

where $E_c(t)$ is the elastic modulus of concrete at age t, in days, and $E_c(28)$ is the 28-day elastic modulus of concrete, originally specified to be 35 GPa. The constant of 0.25 is for the normal (i.e., A23.1 Type 10) cement.

Figure 3.4 shows a comparison of the mode shapes extracted by Londoño from the accelerometer time histories, shown in open circles, with the mode shapes determined from the modified ALGOR model, shown in solid lines. These mode shapes correspond to the fundamental bridge frequencies having values less than 1 Hz and so are important to characterize the wind-induced response. The horizontal axis in each figure is the horizontal distance from the midspan between Piers 31 and 32, so x = -125 m at Pier 31, x = 125 m at Pier 32 and x = 220 m (or -220 m) at the tips of the cantilevers. The mode shapes from both studies are in good agreement for the seven frequencies of interest. The fit to transverse asymmetric mode TA2 is not ideal at the points where the cantilever tip connects to the drop-in span at x = 220 m (or -220 m) but this is not critical. Thus the mean frequencies and numerical mode shapes computed in the present study will be used to compute dynamic wind loads in Chapter 5.

3.4 Dynamic Bridge Response

The wind-induced bridge dynamic response can be expressed in terms of a wide variety of structural actions including forces, bending moments, stresses, displacements or accelerations. Davenport [1988] has shown that the total dynamic response, R_{t_d}, can be expressed as:

$$R_{t_d} = \sqrt{R_b^2 + \sum_j R_{r_j}^2} \qquad [3\text{-}2]$$

where R_b^2 is the mean square non-resonant background response, R_b, varying slowly and irregularly with time; and $R_{r_j}^2$ are the mean square resonant responses, also called modal dynamic responses, due to oscillations with varying amplitudes in the j^{th} natural vibration mode j = 1, 2, … n.

Figure 3.5 shows the power spectrum, which is the distribution of energy with frequency for a typical response, with the logarithm of frequency on the horizontal axis and the power spectral density on the vertical axis. The relative contributions of the resonant and background responses are dependant on the natural frequencies of the modes of vibration. Resonant behaviour tends to dominate with lower natural frequencies (as with tall buildings or long-span bridges) due to the increased energy in the wind spectrum at these frequencies. Background behaviour can dominate as bridge spans and building heights become shorter (corresponding to higher natural frequencies) and, therefore, coincide with less energy in the wind.

Figure 3.6 shows a typical power spectrum derived from data recorded by an accelerometer at a critical bridge location that captures the dynamic movements of the bridge. The mean square resonant responses of the first and second vertical symmetric modes of vibration (i.e., VS1 and VS2) are shown as R_{r1}^2 and R_{r2}^2 respectively. Together they provide (46.5 + 50.5 =) 97% of the total dynamic response, so the remaining non-

resonant background response is only 3%. Investigation of the acceleration power spectra at different bridge locations has shown that the fundamental modes of vibration contain more than 95% of the energy and the contribution of non-resonant background response is less than 5%. Given this absence of non-resonant background response, i.e., $R_b^2 \cong 0$, Equation [3-2] for the total dynamic response simplifies to

$$R_{t_d} \cong \sqrt{\sum_j R_{r_j}^2} \qquad [3\text{-}3]$$

3.4.1 Ten-Minute Duration Accelerometer Datasets

Figure 3.7 shows ten-minute RMS accelerations in the transverse and vertical directions at the tip of the cantilever, Accelerometer 5 on Figure 3.1a, at quarter-point of the continuous span, Accelerometer 7 on Figure 3.1a, and at midspan of the continuous and drop-in spans, Accelerometers 9 and 15 on Figure 3.1a, respectively. The RMS accelerations shown are the total dynamic responses, expressed by Equation [3-3], caused by winds with azimuths within ± 11.25° of normal to the bridge axis. Large RMS accelerations at low wind speeds, occurring particularly at the two cantilever accelerometers in both transverse and vertical directions, are likely attributable to traffic on the bridge but could be spurious. Since they correspond to low wind speeds, they were not investigated further. As the wind speed exceeds 20 m/s, the wind-induced RMS accelerations become significant. The cantilever tip has the maximum RMS accelerations of approximately 5 and 10 milli-g in the transverse and vertical directions, respectively. The associated wind speed at the deck level (40.8 m) is 30.5 m/s, which also corresponds to the specified design wind speed for the Confederation Bridge [King et al. 1994, JMI-Stanley 1995], and occurred during the November 2001 storm. Although 76 accelerometers are available, data from four transverse and four vertical accelerometers shown in Figure 3.7 are sufficient to fully characterize the bridge response to wind loads. Most of the accelerometers shown in Figure 3.1a provide redundant information or are not located at critical bridge locations. For example, RMS accelerations from

Accelerometers 13 and 17, at the cantilever tip, were similar to the RMS accelerations from Accelerometer 5, again at the cantilever tip, in the transverse and vertical directions. Therefore, only the latter are shown in Figure 3.7. Similarly at a given cross-section of the bridge, two vertical accelerometers, one on each side, are installed to capture torsional modes. Wind studies in 1994 [King et al. 1994] showed that due to high torsional stiffness of the bridge deck, the bridge is not sensitive to torsion and so the additional accelerometer is unnecessary. Thus, monitoring wind-induced response of the Confederation Bridge does not require extensive array of instruments.

The modal dynamic responses can be determined using these acceleration time histories. The steps involved in their derivation are as follows:

i) Power spectra are derived [Davenport and King 1982, 1984, Davenport 1988] to identify spectral peaks for the fundamental modes of vibration. Figures 3.8 shows power spectra derived for a single ten-minute time history from the transverse accelerations at the quarter- and mid-point of the continuous span and at the cantilever tip. Figure 3.9 shows power spectra derived from vertical accelerations at the quarter- and mid-point of the continuous span. The spectral peaks shown in both figures correspond to the fundamental modes of vibration shown in Figure 3.4 and the shaded peaks represent the locations for each mode where the maximum modal displacement occurs. In Figure 3.8a, the first symmetric and asymmetric modes, TS1 and TA1, are very close in frequency and are inseparable. The second asymmetric mode, TA2, is significant only at the quarter point of the continuous span, which is consistent with the large lateral deflection at x = -83.5 m for mode TA2 as shown in Figure 3.4.

ii) The spectral peaks at the locations of the maximum modal displacements are isolated using a band-pass filter and the resulting time histories are used to compute the modal RMS accelerations. Figure 3.4 shows that the maximum modal displacements for the first transverse symmetric and asymmetric modes of vibration (i.e. TS1 and TA1) occur at the cantilever tip. The maximum modal

displacement for the second transverse symmetric mode, TS2, occurs at the middle of the continuous span and that for the second transverse asymmetric mode, TA2, at the quarter-point of the continuous span.

Figure 3.8 shows that the spectral peaks corresponding to Modes TS1 and TA1 overlap and therefore cannot be easily isolated using a single band-pass filter. Consequently, the modal RMS accelerations for these two transverse modes were not estimated using this approach. This does not impact the analysis as it will be shown later that not all modes of vibration are necessary to characterize the modal response. For the second transverse symmetric and asymmetric modes of vibration, the corresponding spectral peaks are shown shaded between the lower and upper limits of the band pass filters in Figure 3.8a and b. The filtered time histories were used to compute the modal RMS accelerations for these two modes of vibration [Davenport 1988, King 2003].

Figure 3.9a shows the spectral peaks for the first vertical asymmetric and symmetric modes, VA1 and VS1, overlap at the quarter-point of the continuous span. Figure 3.9b shows the contribution of Mode VA1 is negligible at the midpoint of the continuous span. Therefore, the spectral peak for Mode VS1 at the midpoint of the continuous span can be used to determine the RMS acceleration for this mode. Figure 3.4 shows that the maximum modal displacement for Mode VS1 occurs at the cantilever tip. Therefore, the RMS acceleration computed from the spectral peak at the mid-point of the continuous span requires a modal correction to estimate the maximum RMS acceleration for this mode. This correction is determined as the ratio of the maximum modal displacement at the cantilever tip to the modal displacement at the mid-point of the continuous span. The second vertical symmetric mode, VS2, does not require this correction because the maximum modal displacement occurs at the mid-point of the continuous span. Thus the spectral peaks shown shaded in Figure 3.9b were band-pass filtered and the resulting time histories were used to calculate the maximum modal RMS accelerations [Davenport 1988, King 2003].

This step was repeated for the 2076 ten-minute time history datasets available in the database.

iii) The maximum modal RMS accelerations and associated mean wind speeds are normalized with respect to the natural frequency of the mode and the width of the bridge. This makes the normalized acceleration independent of frequency and proportional to the normalized wind velocity on a log scale [Davenport 1988]. The maximum RMS acceleration for the j^{th} mode, $a_{r_{jmax}}$, was normalized with respect to the j^{th} mode circular frequency, $\omega_j (= 2\pi f_j)$, and width of the bridge, B, as:

$$\Delta_{n_j} = \frac{a_{r_{jmax}}}{B\omega_j^2} \qquad [3\text{-}4]$$

The wind speed, V, associated with this maximum RMS acceleration is normalized with respect to the j^{th} mode natural frequency, f_j, and width of the bridge deck, B, as:

$$V^* = \frac{V}{f_j B} \qquad [3\text{-}5]$$

where V^* is the reduced velocity. The relationship between the normalized variables defined in Equations [3-4] and [3-5] can be expressed as:

$$\Delta_{n_j} = \beta (V^*)^{\alpha} \qquad [3\text{-}6]$$

where β and α parameters that can be obtained by regression analysis to characterize the normalized modal response, Δ_{n_j}, as a function of the reduced velocity, V^*. The maximum modal RMS accelerations determined in Step (ii) for

the two transverse modes, TS2 and TA2, and the two vertical modes, VS1 and VS2, were normalized using Equation [3-4] and the corresponding wind velocities were normalized using Equation [3-5]. As shown in Figure 3.8, only three accelerometers, two transverse and one vertical, are necessary to characterize the normalized modal response. This reinforces the point made earlier that characterization of the wind-induced bridge response requires only a small number of strategically located accelerometers.

Figure 3.10a and b show the variation of the normalized modal acceleration, Δ_{n_j}, with the reduced velocity, V^*, for the transverse and vertical mode shapes, respectively. Both the horizontal and vertical axes have logarithmic scales. The solid lines have been fitted to the data for wind speeds greater than 10 m/s only, yielding:

$$\Delta_{n_j} = 1.34 \times 10^{-6} (V^*)^{3.1} \qquad [3\text{-}6a]$$

and

$$\Delta_{n_j} = 6.6 \times 10^{-6} (V^*)^{2.9} \qquad [3\text{-}6b]$$

for the transverse and vertical modal responses, respectively. The standard errors for the exponent, parameter α in Equation [3-6] are 0.053 and 0.051 and for the constant, parameter β in Equation [3-6], are 5.38 x 10^{-8} and 1.45 x 10^{-7} for Equations [3-6a] and [3-6b], respectively. These parameter errors indicate that, in spite of scatter in the data shown in Figure 3.9, the accuracy of the estimated parameters in Equations [3-6a] and [3-6b] is reasonably consistent with the precision of the values shown.

Figure 3.10 shows scatter in the data for wind speeds less than 10 m/s (reduced velocity 0.92 and 1.7 for TA2 and TS2, respectively; and 0.89 and 1.23 for VS2

and VS1, respectively) that was not considered in fitting Equations [3-6a] and [3-6b]. This scatter reduces for wind speeds greater than 10 m/s but does not diminish completely, perhaps due to the presence of traffic on the bridge or the fluctuation in the turbulence intensity due to seasonal variation [King 2003]. The scatter reduces for wind speeds greater than 20 m/s ($V^* = 1.84$ and 3.4 for TA2 and TS2, respectively, and 1.78 and 2.46 for VS2 and VS1, respectively). Although, only three data points lie in this region for each mode and the maximum wind speed observed is approximately 23 m/s ($V^* = 2.12$ and 3.91 for TA2 and TS2, respectively; and 2.05 and 2.83 for VS2 and VS1, respectively). The agreement between the regression fits and the data in the upper region is critical for the modal responses because the fundamental modes of vibration for long span bridges are particularly sensitive to high winds.

For the seven spectral peaks identified in Figures 3.8 and 3.9, only two transverse and two vertical peaks, shown shaded in the figures, have been used to derive Equations [3-6a] and [3-6b]. It is therefore necessary to validate these equations for the unshaded spectral peaks. Table 3.2 compares the modal RMS accelerations computed using the full-scale monitoring data for these modes with the corresponding modal RMS accelerations predicted using Equations [3-6a] and [3-6b]. The modal accelerations for the shaded peaks in Figures 3.8 and 3.9 are used to determine Equations [3-6a & b] and so are not shown in the table. The spectra in Figures 3.8 and 3.9 are derived from Accelerometers 5, 7 and 9 time histories corresponding to a mean wind speed of 23 m/s. The associated RMS accelerations for the spectral peaks are within 4% of the values predicted using Equations [3-6a] and [3-6b]. Thus the characteristic curves given by Equations [3-6a] and [3-6b] are representative of the modal responses identified from the power spectra. These curves will be used to derive the dynamic wind loads for the Confederation Bridge as described in Chapter 5.

3.4.2 Hurricane Noel Data

Figure 3.11 shows ten-minute RMS transverse and vertical accelerations recorded during Hurricane Noel at the tip of the cantilever at Pier 32 and at quarter- and mid-point of the continuous span. The data show very little scatter, likely because the bridge was closed to traffic and the measured turbulence intensity, as discussed in Chapter 2, was fairly constant for the entire event. The cantilever tip exhibited maximum ten-minute RMS accelerations of 3 and 5.5 milli-g in the transverse and vertical directions, respectively. The corresponding ten-minute mean wind speed at deck level (40.8 m) was 33.2 m/s at a mean azimuth of 200° with respect to Bridge North, i.e., 20° from perpendicular to the bridge axis.

Figure 3.12 shows ten-minute statistical summaries computed using Hurricane Noel wind and acceleration time histories. The wind speed reaches a maximum of 33.2 m/s and eventually reduces to just below 15 m/s as shown in Figure 3.12a. The wind azimuths vary between 140° and 310° with respect to Bridge North as shown in Figure 3.12b. Only a portion of the time histories from the Hurricane Noel data, bounded between the vertical lines in Figures 3.12a, b, c and d, was used to derive the modal responses following the procedure described in Section 3.4.1. During this 80 minute interval, the mean wind azimuth of 200° varied within ±5° and so was 20° from the perpendicular to the bridge axis as shown in Figure 3.12b. The bridge experienced maximum RMS accelerations in the transverse and vertical directions as shown in Figures 3.12c and d.

The variation of the normalized modal accelerations with reduced velocity for modes TS2/TA2 and VS1/VS2 are shown in Figures 3.13a and b, respectively. The best fit lines to the data are:

$$\Delta_{n_j} = 1.76 \times 10^{-6} (V^*)^{2.6} \qquad [3\text{-}6c]$$

and

$$\Delta_{n_j} = 4.22 \times 10^{-6} (V^*)^{2.7} \qquad [3\text{-}6d]$$

in the transverse and vertical directions, respectively. The scatter of the data about the fitted lines is markedly less than shown in Figures 3.10a and b, likely because, as noted previously, the bridge was closed to traffic during Hurricane Noel and turbulence intensity was relatively constant. The standard errors for the exponent are 0.08 and 0.116 and for the constant are 1.89 x 10^{-7} and 5.27 x 10^{-7} for the fits in Equations [3-6c] and [3-6d], respectively. Although the Hurricane Noel data show less scatter, the error of the parameter estimate for the exponent in Equations [3-6c] and [3-6d] is twice as large as that for Equations [3-6a] and [3-6b], and the error of the parameter estimate for the constant is three times greater. This difference is due to the number of data points used for each regression analyses: 486 for the 1998-2006 dataset and only 14 for the Hurricane Noel dataset. Thus the bigger sample size gives more accurate parameter estimates even though there is more visible scatter. The estimated parameters in Equations [3-6a] and [3-6b] are different from the estimated parameters in Equations [3-6c] and [3-6d], respectively, likely because the wind azimuth is different and the wind speed may be influenced by the bridge deck for Hurricane Noel data. Equations [3-6c] and [3-6d] can still be used, however, to derive the dynamic wind loads caused by Hurricane Noel as described in Appendix 5B.

3.4.3 Discussion

The analysis of the Hurricane Noel data is presented in part to investigate the severity of the wind event and its impact on the bridge. The maximum ten-minute mean wind speed is 33.2 m/s at the deck elevation of 40.8 m above MSL, and so exceeds the specified design wind speed of 30.5 m/s [King et al. 1994, JMI-Stanley 1995]. However, comparing Figures 3.7 and 3.11, the RMS accelerations recorded during Hurricane Noel are less than half those observed when the specified design wind acted normal to the bridge axis in the November 2001 storm. Two factors could account for these lesser-than-expected RMS accelerations. Firstly, the maximum wind speed during Hurricane Noel

occurred at a skew wind angle of 20° from the perpendicular to the bridge axis. It will be shown in Chapter 5 that the bridge accelerations reduce as the mean wind azimuth moves away from normal, and the influence of the changing wind azimuth on the bridge response will also be discussed in Section 3.6. Secondly, the mean wind speeds recorded by the anemometer were somewhat inflated by the presence of bridge deck. The winds approaching from the bridge south during the passage of Hurricane Noel were recorded by the anemometer at 54 m above MSL on a light standard on the north side of the bridge in the region of the shear layer formed by wind separating from the barrier wall. The shear layer region separates the entrained wake around the deck from the undisturbed flow region. In this region wind speeds are accelerated and accompanied by a long series of vortices due to the flow separation [Holmes 2007]. This phenomenon was also confirmed in wind tunnel tests carried out on the Confederation Bridge Model in October 2007 that will be described in Chapter 4 where a 10% increase in the downstream wind speed was observed with respect to that recorded on the upstream side. Thus it is concluded that although the recorded wind speed exceeded the specified design wind speed during the passage of Hurricane Noel, the recorded accelerations are only half of those recorded during the passage of the November 2001 storm. This conclusion is supported by detailed analysis of the loads caused by Hurricane Noel in Appendix 5B.

3.5 Peak Factor

The along-wind response of structures to wind has a Gaussian probability distribution [Holmes 2007]. Davenport [1962] has shown that the peak response of most structures during gusts lies 3.5 to 4.5 standard deviations above the mean response. The statistical peak factor, g, can therefore be defined as:

$$g = \frac{R_{max} - \overline{R}}{R_{RMS}} \qquad [3\text{-}7]$$

where, R_{max}, $\overline{R}$, and R_{RMS} are the maximum, mean and RMS responses, respectively. A peak factor of 3.5, proposed by the Boundary Layer Wind Tunnel Laboratory [King et al.

1994], was used for the design of the Confederation Bridge [JMI-Stanley 1995]. In the present study, the accuracy of this proposed factor was investigated using the ten-minute accelerometer time history records from Hurricane Noel to compute peak factors for the Confederation Bridge. Figure 3.14 shows the distribution of the computed peak factors for the two transverse and vertical modes of vibration. The spectral peaks at the locations of the maximum modal displacements, similar to those shown in Figures 3.8 and 3.9, were used to derive the peak factors. The computed values are therefore representative of the entire structure. The overlapping spectral peaks were not used to compute peak factors for the reasons described earlier in Section 3.4.1. Figure 3.14 shows the range of the observed peak factors is generally between 2.5 and 5, with the exception of one instance greater than 5 for Mode TA2 in Figures 3.14b. The mean peak factor for the four modes shown is 3.47, which is within 1% of the value used for the original bridge design. This empirically determined value of the peak factor will be used to compute peak bending moments for comparison with the moments due to the original design wind loading in Chapter 5.

3.6 Damping Estimates

The Hurricane Noel data were used to estimate bridge damping using the Autocorrelation [Ochi 1990] and Random Decrement Methods (RDM) [Cole 1973] for each mode of vibration. Table 3.3 summarizes the resulting damping values as percentage of critical with those reported by Londoño [2006] and Brown and Bruce [1997]. The Hurricane Noel accelerometer datasets used to compute damping in the present study had an hourly mean wind speed at deck level (40.8 m) between 25 and 29 m/s, which corresponds to a ten-minute mean wind speed between 26.6 and 30.9 m/s, respectively. The bridge is designed for a ten-minute mean wind speed of 30.5 m/s normal to the bridge axis at the deck elevation; therefore, it is assumed that the computed damping estimates are valid when the design wind speed is acting. These tabulated damping values represent the total bridge damping, i.e., the sum of structural and aerodynamic damping components.

Londoño [2006] used datasets with different loading conditions, including high wind events, heavy traffic conditions and ambient traffic conditions with or without ice, to estimate damping for 25 mode shapes of the Confederation Bridge. His damping estimates are not classified based on the type of loading. Since the fundamental modes of vibration with frequencies less than 1 Hz are particularly sensitive to high winds for long span bridges, the tabulated damping estimates after Londoño, shown in Table 3.3, are also considered to be total bridge damping values. The values computed using the Random Decrement Method in the present study are very close to those reported by Londoño. The third transverse symmetric mode (TS3) is an exception as the value computed in the present study is 2.36% whereas Londoño predicts 0.6%. Londoño's reported value does not seem to possess both the structural and aerodynamic damping components, possibly because a traffic event caused the response used to estimate damping for this mode. Furthermore, Londoño does not report the method used to compute damping using on-site monitoring data – but he did not have access to the Hurricane Noel data, so even if his estimates are derived using the Random Decrement Method, they are based on different time histories than those used in the present study.

Table 3.3 shows that the Autocorrelation Method in the present study yields damping estimates that are almost twice as large as those obtained using the RDM. Several factors could account for this discrepancy. Firstly, the closely spaced spectral peaks require tighter filters which artificially introduce energy in the spectrum. Secondly, the full-scale data is weakly stationary whereas the Autocorrelation technique assumes the data to be absolutely stationary. Thirdly, it could also be as a result of spectral leakage; a phenomenon that occurs if a truncated time history has an incomplete last cycle [Brigham 1974]. The spectral leakage artificially introduces secondary frequency effects also called side-lobes, which affects the spectral energy. This phenomenon can be minimized using a window weighting function [Harris 1978] but cannot be avoided completely.

Brown and Bruce [1997] carried out full-scale pull tests at Pier 31 to estimate the pier stiffness using a vessel tethered by a cable to the pier. An unexpected failure of the cable provided an opportunity to collect useful data from the accelerometers and tiltmeters

attached to the pier which were subsequently used to estimate structural damping for the three transverse modes of vibration. The damping estimates by Brown and Bruce [1997], shown in Table 3.3, are higher than those reported by Londoño and higher than those determined in the present study. Brown and Bruce [1997] do not provide details of their damping calculations and so no explanation has been found to explain this difference.

3.7 Effect of Wind Azimuth on Normalized Displacement

The lines fitted to the normalized modal responses shown in Figure 3.10 have two regression parameters as shown in Equation [3-6] – α (exponent) and β (constant). The exponent is fairly constant for the 16-point compass directions except 90^{o} and 270^{o}, which are parallel to the bridge axis. The constant is a measure of the bridge dynamic displacement for a given wind azimuth. Variation of the normalized bridge displacement with wind azimuth for the transverse and vertical directions is shown in Figure 3.15. The open triangle markers are the estimates of the parameter β, normalized with respect to zero wind azimuth value for the transverse and vertical directions. Thus for a given wind azimuth the parameter β is the product of the normalized displacement and the parameter β_o for the zero wind azimuth given in Equations [3-6a] and [3-6b] for the transverse and vertical directions, respectively. The solid line is the variation of the normalized bridge displacement assuming a cosine-squared relationship. It is an accepted assumption that the bridge deflection reduces with the square of the cosine of the angle between the wind azimuth and the direction normal to the bridge axis. The derivation of this relationship is presented in Appendix 3C.

Figure 3.15 shows that this is not necessarily the case for the Confederation Bridge. For winds blowing along the bridge axis, the normalized bridge response is observed to be 55% to 65% when the cosine-squared relationship implies that it should be zero. Several factors could account for this unexpected result. The wave action and/or ice in the strait can excite the bridge under high winds irrespective of the wind azimuth. The bridge alignment is not a straight line and so winds along the bridge axis for the New Brunswick Marine Spans will be 7^{o} normal to the PEI Marine Spans and therefore the combined

effect of the 65 spans of the bridge will always have residual response. Finally, the indicated wind azimuths in Figure 3.15 vary within 22.5° and so it is very unlikely that the wind azimuth on-site be perfectly stationary. Thus the cosine-squared relationship is not necessarily a conservative approach to estimate the bridge response for non-normal wind azimuths.

3.8 Bridge Static Response Determined from Tiltmeter Data

Tiltmeters are used to measure pier tilts (μRad) at water level and the tops of Piers 31 and 32 as shown in Figure 3.1a. Bruce and Croasdale [2001], in their analysis of the ice loads on the bridge, developed a relationship using data from the tiltmeters attached to the Pier 31, to remove the wind load effect from cases where both ice and wind loads acted simultaneously on the bridge piers. They proposed that the mean pier tilt (μRad) at the water level, $\overline{T}$, can be expressed as:

$$\overline{T} = k\overline{V}^2 \qquad [3\text{-}8]$$

where k is an empirically derived calibration factor that represents the drag coefficients, geometric properties and stiffnesses of the bridge superstructure, and $\overline{V}$ is the ten-minute mean wind velocity component which is normal to the bridge in m/s at the anemometer height.

Figure 3.16 shows the variation of the observed tiltmeter data with the ten-minute mean velocity and three fits proposed by Bruce and Croasdale [2001]. The calibration factor, k, for the three fits is 0.19, 0.25 and 0.30 and has been computed using cosine relationship to account for the component of the wind normal to the bridge axis. This relationship is valid for the static bridge response provided the variation of drag coefficient of the bridge piers with wind azimuth does not change. Since the piers of the Confederation Bridge do not have a circular cross-section, the cosine relationship could underestimate wind speeds for certain skew wind azimuths. Nevertheless, the relationship has very little effect on

wind speeds (less than 8%) provided the wind azimuth varies within 22.5°. Since the observed data in Figure 3.16 presumably include data for winds normal to the bridge axis and also for skew wind azimuths, the portion of the data fitted using the calibration factor of 0.25 seems appropriate to represent the pier tilt. Thus, this calibration factor and Equation [3-8] will be used to compute static drag coefficients for the Confederation Bridge in Chapter 5.

3.9 Summary and Conclusions

The on-site monitoring data gathered from 1998 to 2006 at the Confederation Bridge have been analysed to determine the total and modal dynamic responses of the structure during strong wind events. These are compared to the responses predicted using data obtained when Hurricane Noel passed the bridge on 4th November 2007. The time histories for both the nine years of monitoring data and Hurricane Noel datasets are used to determine bridge natural frequencies for comparison to those computed analytically using ALGOR and reported by Londoño [2006]. The fundamental mode shapes, derived using the modified beam element model in ALGOR [King et al. 1994], are also compared to the mode shapes extracted by Londoño [2006].

The total bridge damping for each mode, estimated using the Hurricane Noel time histories, are compared to the damping estimates reported by Londoño [2006] and Brown and Bruce [1997]. Peak factors are also computed using the Hurricane Noel data for comparison with the peak factor used for the original bridge design. The variation of the bridge displacement with wind azimuth is determined using the dynamic modal responses for comparison to the conventional cosine-squared relationship. Finally, the relationship between the pier tilt and wind velocity proposed by Bruce and Croasdale [2001] is discussed and inferences are drawn.

The following conclusions are drawn:

1. The dynamic properties of the instrumented spans of the Confederation Bridge, i.e., natural frequencies, modes shapes and damping, required for the derivation of wind loads in Chapter 5 have been determined and compared to the values reported by others. Good agreement has been found between the properties determined in the present study and reported by others. The specific findings are as follows:

   i) The bridge frequencies reported by Londoño from his analysis of the on-site monitoring data are within 3% of those determined in the present study. The numerical model frequencies from the modified beam element model in ALGOR are within 5% of the observed frequencies except for mode VA1, which differs from the observed value by 13%. The numerical model frequencies by Londoño are within 10% of the observed frequencies in the present study. A concrete modulus of 45 GPa is used for both the numerical models which gives more accurate frequency estimates, as described, compared to the modulus of 35 GPa originally used for the bridge design.

   ii) The mode shapes extracted by Londoño from the accelerometer time histories are in good agreement with the mode shapes determined numerically using the modified ALGOR model for the marine span between Piers 31 and 32.

   iii) The damping values determined using the Hurricane Noel data represent the total bridge damping, i.e., the sum of structural and aerodynamic damping components. The Autocorrelation method [Ochi 1990] gives damping estimates that are almost twice as large as those obtained using the Random Decrement Method (RDM) [Cole 1973]. Londoño does not describe the loading present for the time histories he uses to determine damping values; however, his values are in close agreement with those determined in the present study using RDM except for mode TS3 which is four times smaller. For this mode it is believed that data from a traffic event may have been used

to estimate damping and therefore does not contain any aerodynamic component. Brown's structural damping values for the three transverse modes of vibration are the largest of all the reported values. He does not provide details of his calculations and so no explanation has been found for this difference.

2. The dynamic bridge response, in the form of RMS accelerations and normalized modal accelerations, that are essential for the derivation of wind loads for the bridge, have been derived using the typical ten-minute accelerometer datasets and Hurricane Noel data. The main features of the responses are as follows:

   i) For the typical ten-minute accelerometer datasets, maximum RMS accelerations of 5 and 10 milli-g at the cantilever tip in the transverse and vertical directions, respectively, are observed for a mean wind speed of 30.5 m/s normal to the bridge axis. During the passage of Hurricane Noel the maximum RMS accelerations of 3 and 5.5 milli-g at the same bridge location in the transverse and vertical directions are observed, respectively, for a mean wind speed of 33.2 m/s and a mean wind azimuth of 200^{o} with respect to the bridge north or 20^{o} from perpendicular to the bridge axis. The reduced accelerations observed during Hurricane Noel are attributed to the non-normal wind azimuth, which reduces the bridge response, and the presence of the recording anemometer in the downstream region of the shear layer, which increases the wind speed by up to 10%.

   ii) The variation of the normalized bridge modal acceleration in the transverse and vertical directions with the reduced wind speed, derived using typical ten-minute time history datasets show scatter which is due to the presence of traffic on the bridge and fluctuation in the turbulence intensity due to seasonal variation. As wind speeds increase, the scatter reduces and the data points fall on the characteristic curves that define the modal responses. The standard errors for the parameters defining the characteristic curves indicate that in spite

of scatter in the data, the variation of the exponent, α, is within 2% and constant, β, is within 4%.

iii) The characteristic curves, representing the normalized bridge modal responses in the transverse and vertical directions, derived using the Hurricane Noel dataset show much less scatter likely because the bridge was closed to the traffic and the turbulence intensity was fairly constant for the entire wind event. The variation of the exponent, α, is within 4% and constant, β, is within 12%. Although Hurricane Noel data show less scatter, the error in these parameter estimates is larger than those derived for the ten-minute datasets. This difference is attributable to the difference in the number of data points used for the regression analyses: 486 for the ten-minute dataset and 14 for the Hurricane Noel dataset. Thus bigger sample size gives stable parameter estimates with less variability.

3. The mean peak factor is 3.47 and so is within 1% of the peak factor of 3.5 used for the original bridge design. The peak factors determined using accelerometer data from Hurricane Noel range between 2.5 to 5 for wind speeds greater than 15 m/s.

4. It is an accepted assumption that the bridge response reduces with the square of the cosine of the angle between the wind azimuth and the direction normal to the bridge axis (see Appendix 3C). The present study shows that this is not the case for the Confederation Bridge as winds blowing along the bridge axis caused bridge responses that are 55% to 65% of those caused by winds blowing normal to the bridge axis. Thus the cosine-squared relationship is not necessarily a conservative approach to estimate the response of the Confederation Bridge for non-normal wind azimuths.

5. The static bridge response, in terms of the mean pier tilt, is necessary to derive static force coefficients for comparison with the values used for the bridge design. Bruce and Croasdale [2001] have proposed a relationship to characterize the static

bridge response using tiltmeter data from the on-site monitoring programme. Thus the proposed relationship with a calibration factor of 0.25 will be used to derive the static force coefficients in Chapter 5.

6. The data from 76 accelerometers attached to the Confederation Bridge were analyzed and most of the accelerometers were found to provide redundant information. It is shown that only eight accelerometers (four transverse and four vertical) at critical bridge locations are sufficient to fully characterize the total and modal dynamic responses of the bridge due to wind. Thus an extensive arrangement of accelerometers is not required to determine the wind-induced response of the Confederation Bridge.

3.10 Recommendations

1. The High Speed Data Loggers, once triggered, should collect accelerometer time history data without interruption for the entire wind event as continuous data collected for extended period provide more accurate results and offer more flexibility in the analysis.

2. The current programming that stops collection of time history data when the instantaneous wind speed drops below 15 m/s is unsatisfactory and should be changed as it can create gaps in, and so ruin, the time history record.

3. The sampling frequency of the HSDLs should be lowered to 20 Hz to enable an increase in the duration of time history records by 4 – 5 times without compromising the accuracy of the acceleration power spectrum as shown in Appendix 3A.

3.11 References

Brigham, E. O. 1974. *The Fast Fourier Transform*, Prentice-Hall, Inc. Englewood Cliffs, New Jersey.

Brown, T. G., and Bruce, J. R. 1997. *Confederation Bridge Ice Force Monitoring Joint Industry Project Annual Report* – 1997, IFN Engineering Ltd.

Brown, T. G. 2007. Ice Force Monitoring, *Confederation Bridge Engineering Summit Proceedings,* Charlottetown, PEI, Canada, pp. 224-254.

Bruce, J. R., and Croasdale, K. R. 2001. *Confederation Bridge Ice Force Monitoring Joint Industry Project Annual Report,* IFN Engineering Ltd. Report Number 00-1-001, 40 p.

Cole, A. H. 1973. *On-line Failure Detection and Damping Measurement of Aerospace Structures by Random Decrement Signatures,* NASA, CR-2205.

Davenport, A. G. 1964. Note on the Distribution of the Largest Value of a Random Function with Application to Gust Loading, *Proceedings of the Institution of Civil Engineers,* Paper No. 6739, Vol. 28, pp. 187-196.

Davenport, A. G., and King, J. P. C. 1982. The Incorporation of Dynamic Wind Loads into the Design Specifications for Long Span Bridges, *ASCE Fall Convention and Structures Congress,* New Orleans, Louisiana, USA, pp. 1-31.

Davenport, A. G., and King, J. P. C. 1984. Dynamic Wind Forces on Long Span Bridges, *12th IABSE Congress,* Vancouver, Canada, pp. 705-712.

Davenport, A. G. 1988. The Response of Tension Structures to Turbulent Wind: The Role of Aerodynamic Damping, *1st International Oleg Kerensky Memorial Conference on Tension Structures,* London, England, Session 4: pp. D1-D7.

Ghali, A., Elbadry, M., and Megally, S. 2000. Two-year Deflections of the Confederation Bridge, *Canadian Journal of Civil Engineering,* 27: pp. 1139-1149.

Harris, F. J. 1978. On the Use of Windows for Harmonic Analysis with the Discrete Fourier Transform, *Proceedings of the IEEE,* Vol. 66, No. 1, pp. 51-83.

Holmes, J. D. 2007. *Wind Loading of Structures,* Second Edition, Taylor and Francis, London and New York.

JMI-Stanley. 1994. *Confederation Bridge Construction Drawings,* Jean Muller International, Stanley Joint Venture Inc.

JMI-Stanley. 1995. *Design Criteria Northumberland Strait Crossing Project,* Jean Muller International, Stanley Joint Venture Inc.

King, J. P. C., and Davenport, A. G. 1993. The Treatment of Wind Effects for the Northumberland Strait Crossing, *Canadian Society for Civil Engineering Annual Conference,* Fredericton, New Brunswick, Canada, pp. 405-414.

King, J. P. C., Mikitiuk, M. J., Davenport, A. G., and Isyumov, N. 1994. *A Study of Wind Effects for the Northumberland Straits Crossing,* BLWT-SS8-1994, Boundary Layer Wind Tunnel Laboratory, University of Western Ontario (Parts of this report have been published in King and Davenport 1993, 1994 and King 1999).

King, J. P. C. and Davenport, A. G. 1994a. *The Estimation of Dynamic Wind Load Coefficients for the Northumberland Straits Crossing, PEI,* BLWT-IR-N62-16-1994, Boundary Layer Wind Tunnel Laboratory, University of Western Ontario (parts of the report have been published in King and Davenport 1994b and King 1999).

King, J. P. C., and Davenport, A. G. 1994b. P.E.I. Fixed Link – The Treatment of Wind Effects for the Northumberland Strait Crossing, *Fourth International Conference on Short and Medium Span Bridges,* Halifax, Nova Scotia, Canada, pp. 1377-1388.

King, J. P. C., Crooks, G. J. and Davenport, A. G. 1995. *The Northumberland Straits Crossing, Prince Edward Island Testing of Marine Span Aeroelastic Model and Analysis of Dynamic Wind Loads,* BLWT-SS24-1995, Boundary Layer Wind Tunnel Laboratory, University of Western Ontario.

King, J. P. C. 1999. Integrating Wind Tunnel Tests of Full-Aeroelastic Models into the Design of Long Span Bridges, *Proceedings of the Tenth International Conference on Wind Engineering (ICWE),* Copenhagen, Denmark, pp. 927-934.

King, J. P. C. 2003. *The Aerodynamics of Long Span Bridges, PhD Thesis,* Department of Civil and Environmental Engineering, University of Western Ontario, London, Ontario, Canada.

King, J. P. C., Bakht, B., and Bartlett, F. M. 2007. The Validation of Wind Tunnel Model Tests of Long Span Bridges Through Long Term Full-Scale Monitoring, *12th International Conference on Wind Engineering (ICWE),* Cairns, Australia, (8 page paper in CD-Rom Proceedings).

Logan, D. L., 2001. *A First Course in the Finite Element Method Using ALGOR,* Second Edition, Brooks/Cole, CA, USA.

Londoño, N. A. 2006. *Use of Vibration Data for Structural Health Monitoring of Bridges,* Department of Civil and Environmental Engineering, Carleton University, Ottawa, Canada.

Math Works. 1995. *The Student Edition of MATLAB – High-Performance Numeric Computation and Visualization Software,* Version 4, User's Guide, The Math Works Inc. Prentice Hall, Englewood Cliffs, New Jersey, USA.

Montreuil, M. A. 1999. *Confederation Bridge Monitoring Project High-Speed Data Logger System,* Technical Manual, Preliminary Version, Thermal Technology Centre, National Research Council Canada.

Ochi, M. K. 1990. *Applied Probability and Stochastic Processes in Engineering and Physical Science,* John Wiley and Sons, New York, USA.

Shannon, C. E., 1998. Communication in the Presence of Noise, *Proceedings of the IEEE,* Vol. 86 No.2, pp. 447-457.

Table 3.1 – Comparison of Frequencies Computed from Full-Scale Monitoring Data and Predicted Using Numerical Model for the Marine Span between Piers 31 and 32

Frequencies Computed from Full-Scale Monitoring Data						Numerical Model Frequencies	
Mode	Type	Mean (2009)	Variability (% of Mean)	Mean (Londoño) (2006)	Variability (% of Mean)	Beam Element Model (Londoño) (2006)	Modified Beam Element Model (ALGOR) (2009)
		(Hz)		(Hz)		E_c = 43 GPa	E_c = 43 GPa
1	TS1	0.34	4	0.34 (-1%)	16	0.31 (-10%)	0.35 (+2%)
2	TS2	0.49	1	0.47 (-3%)	5	0.51 (+5%)	0.50 (+2%)
3	VA1	0.57	1	0.57 (0%)	19	0.52 (-9%)	0.50 (-13%)
4	VS1	0.68	1	0.68 (0%)	9	0.69 (+2%)	0.68 (0%)
5	TA2	0.91	2	0.89 (-3%)	5	0.93 (+2%)	0.88 (-4%)
6	VS2	0.94	1	0.92 (-2%)	7	0.88 (-7%)	0.89 (-5%)
7	TS3	1.33	2	1.31 (-2%)	1	1.33 (0%)	1.31 (-1%)
8	VA2	1.81	1	1.81 (0%)	5	1.78 (-2%)	1.87 (+3%)
9	VS3	2.81	1	2.88 (+3%)	4	-	2.87 (+2%)
10	VA3	-	-	3.79	5	3.42	3.58

Note: values in brackets are percentage difference with respect to 2009 mean frequencies computed from full-scale monitoring data

Table 3.2a – Observed and Predicted Modal Transverse RMS Accelerations for Unshaded Spectral Peaks

Mode	TS1/TA1		% Diff.	TS2		% Diff.
Location	RMS Accelerations (milli-g)			RMS Accelerations (milli-g)		
	Obs.	Pred.		Obs.	Pred.	
Cantilever Tip Drop-in Span	2.03	2.09	+3 %	1.22	1.18	-3 %
Quarter Point Continuous Span	0.47	0.48	+2 %	0.86	0.84	-2 %
Mid Point Continuous Span	0.89	0.85	-4 %	-	-	-

Note: Spectral peaks for TS2 and TA2 at mid- and quarter- points of the continuous span, respectively, used to determine Equation [3-6a]

Table 3.2b – Observed and Predicted Modal Vertical RMS Accelerations for Unshaded Spectral Peaks

Mode	VA1/VS1		% Diff.	VS2		% Diff.
Location	RMS Accelerations (milli-g)			RMS Accelerations (milli-g)		
	Obs.	Pred.		Obs.	Pred.	
Quarter Point Continuous Span	1.20	1.17	-3 %	0.59	0.61	+3 %

Note: Spectral peaks for VS1 and VS2 at mid-point of the continuous span used to determine Equation [3-6b]

Table 3.3 – Damping Estimates as Percentage of Critical for Different Modes of Vibration

Mode	TS1	TS2	VA1	VS1	TA2	VS2	TS3	VA2	VS3
Frequency (HZ)	0.34	0.49	0.57	0.68	0.91	0.94	1.33	1.81	2.81
Autocorrelation	4.3	2.74	7.1	4.1	3.75	1.82	4.67	3.08	2.55
Random Decrement	2.04	1.68	3.91	2.06	1.95	1.51	2.36	1.55	1.34
Londoño (2006)	1.9	1.7	3.8	2.1	2.1	1.5	0.6	1.5	1.3
Brown (1997)	-	5.7	-	-	7.7	-	5.7	-	-

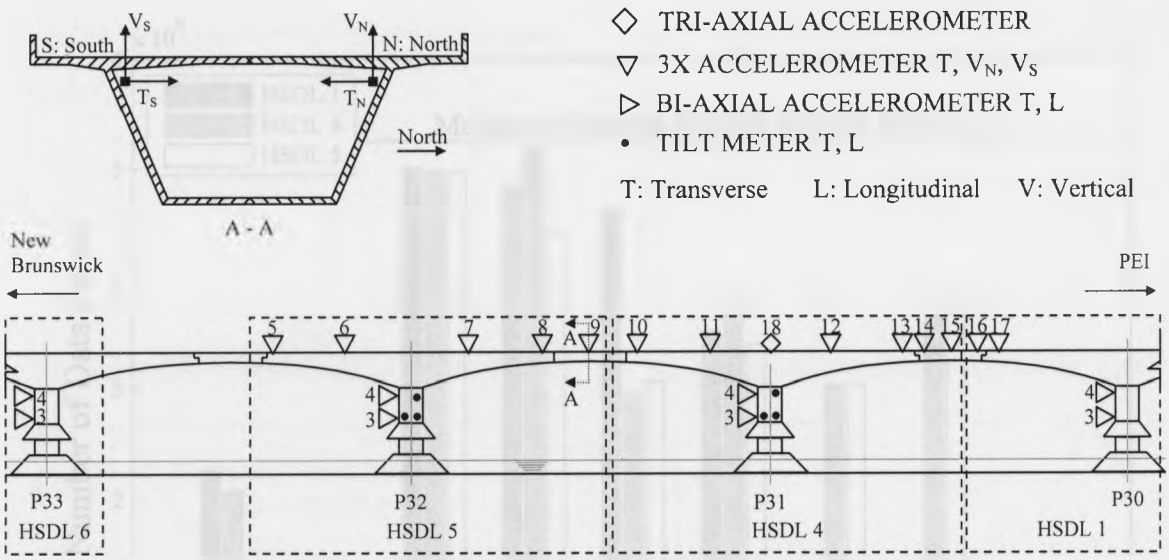

Figure 3.1a – Accelerometer and Tiltmeter Locations for Static and Dynamic Monitoring [adapted from Montreuil 1999]

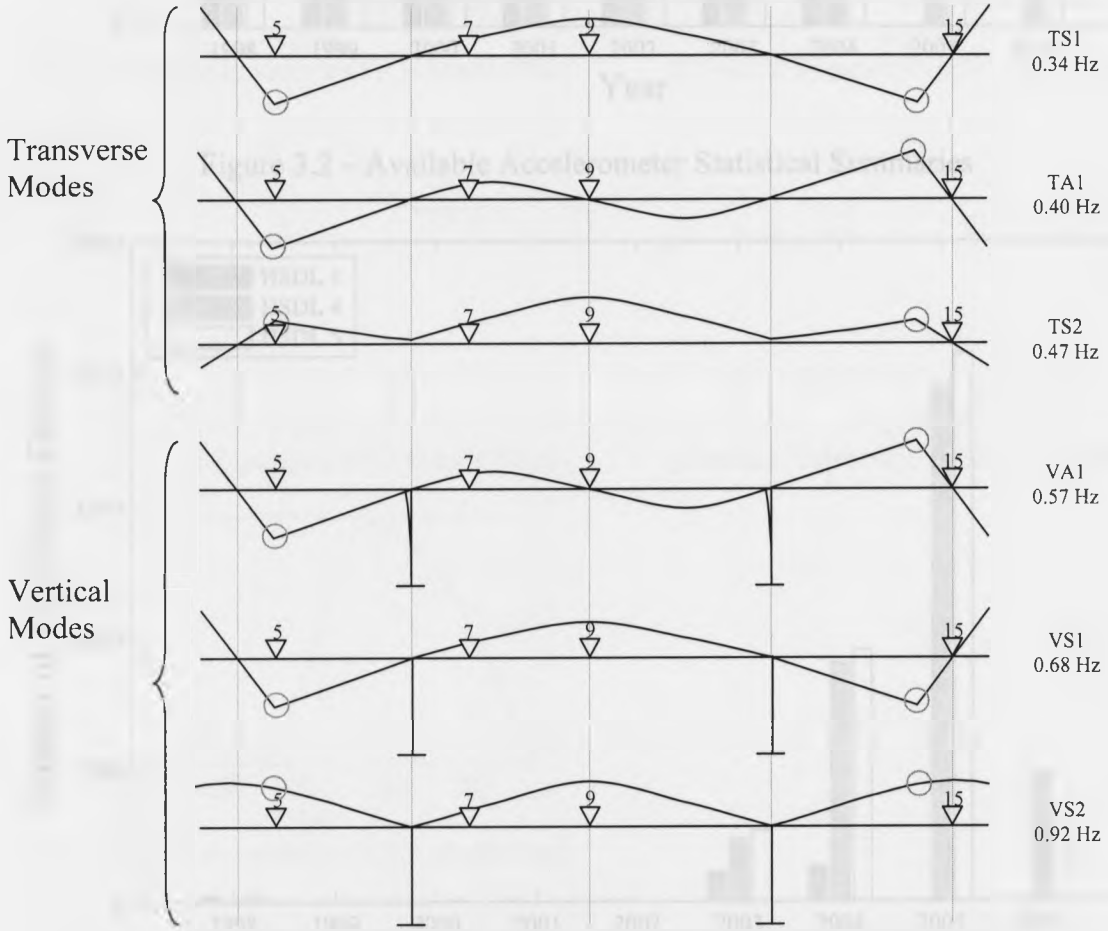

Figure 3.1b – Bridge Vibration Modes Schematic and Location of HSDLs 4 and 5 Accelerometers [adapted from Londoño 2006]

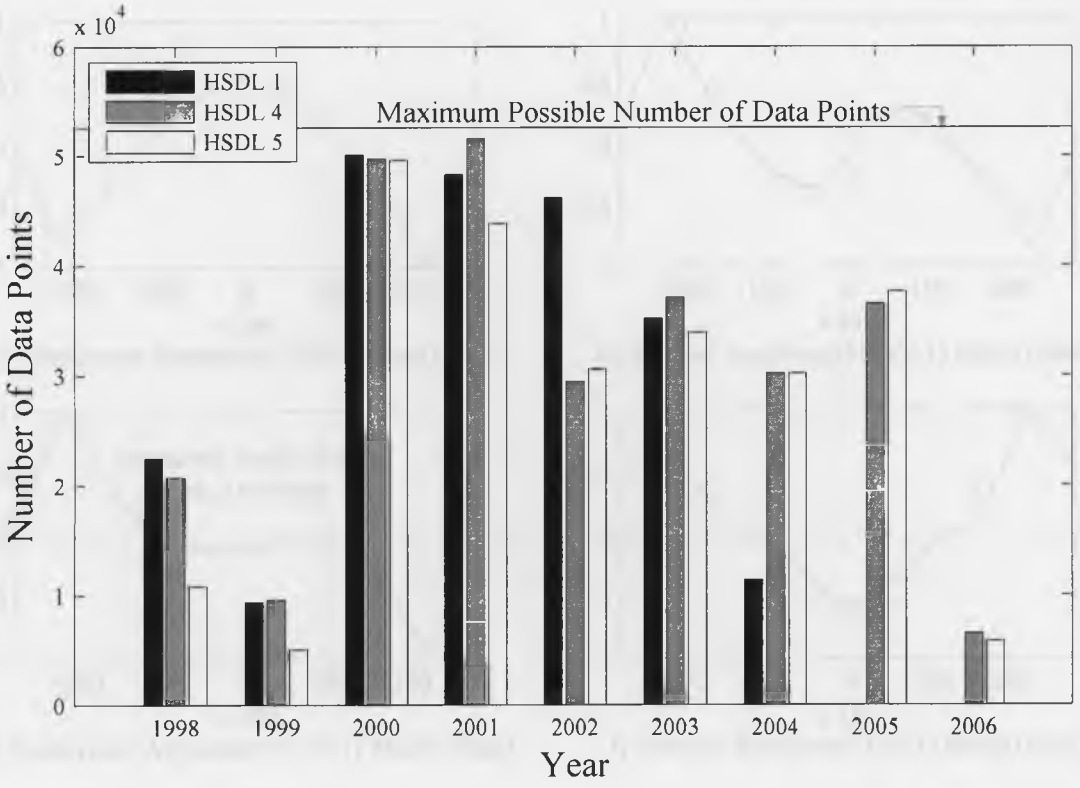

Figure 3.2 – Available Accelerometer Statistical Summaries

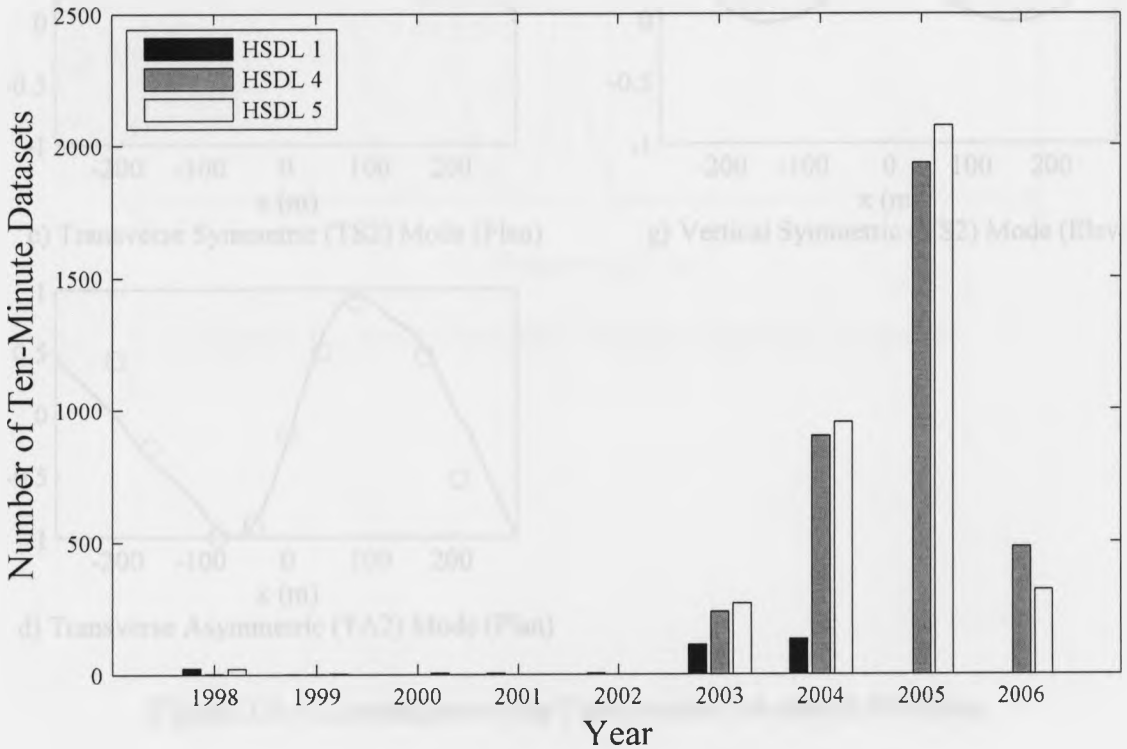

Figure 3.3 – Available Accelerometer Time Histories

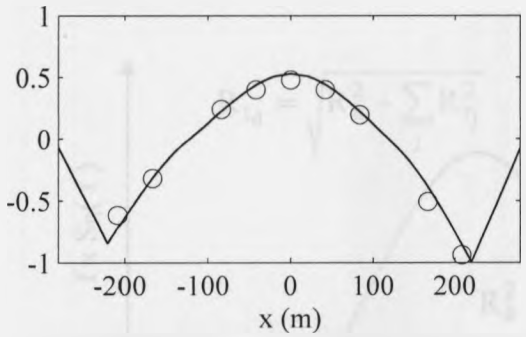

a) Transverse Symmetric (TS1) Mode (Plan)

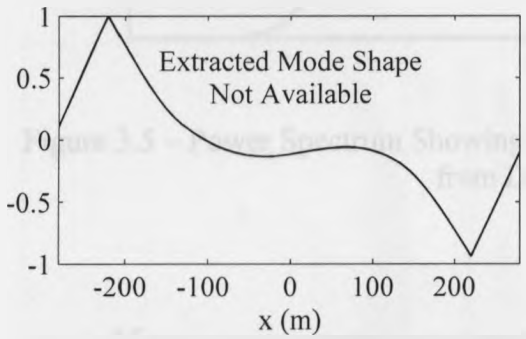

b) Transverse Asymmetric (TA1) Mode (Plan)

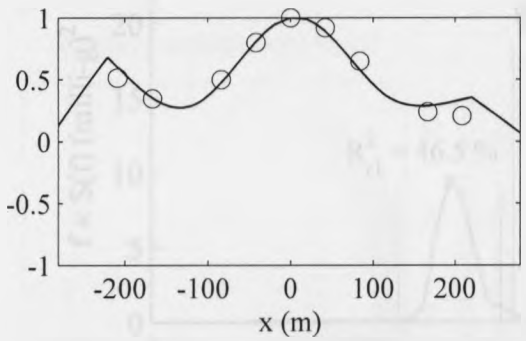

c) Transverse Symmetric (TS2) Mode (Plan)

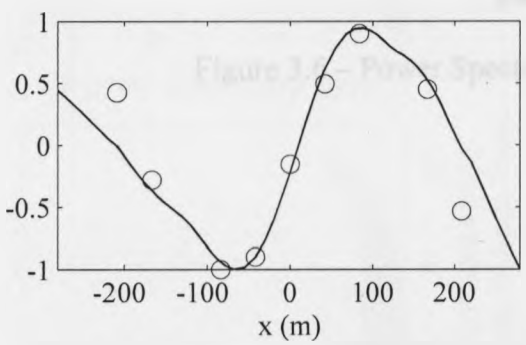

d) Transverse Asymmetric (TA2) Mode (Plan)

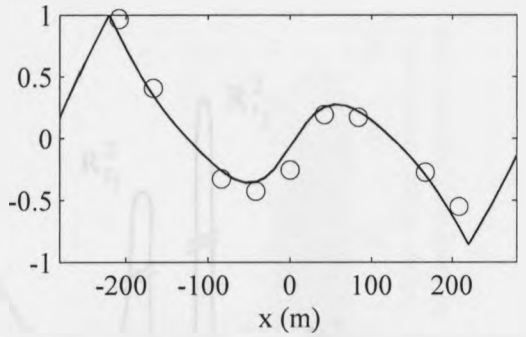

e) Vertical Asymmetric (VA1) Mode (Elev)

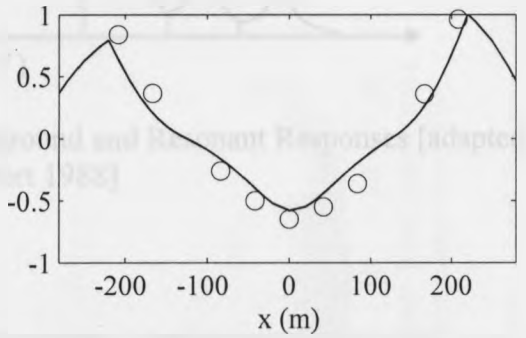

f) Vertical Symmetric (VS1) Mode (Elev)

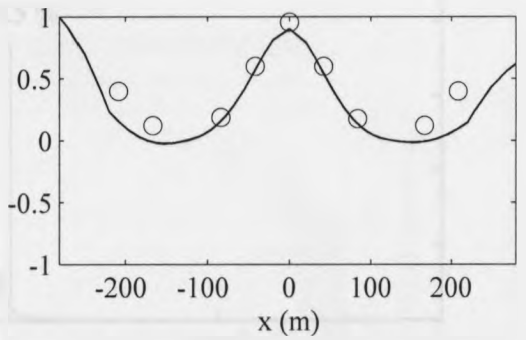

g) Vertical Symmetric (VS2) Mode (Elev)

Figure 3.4 – Comparison of the Fundamental Modes of Vibration

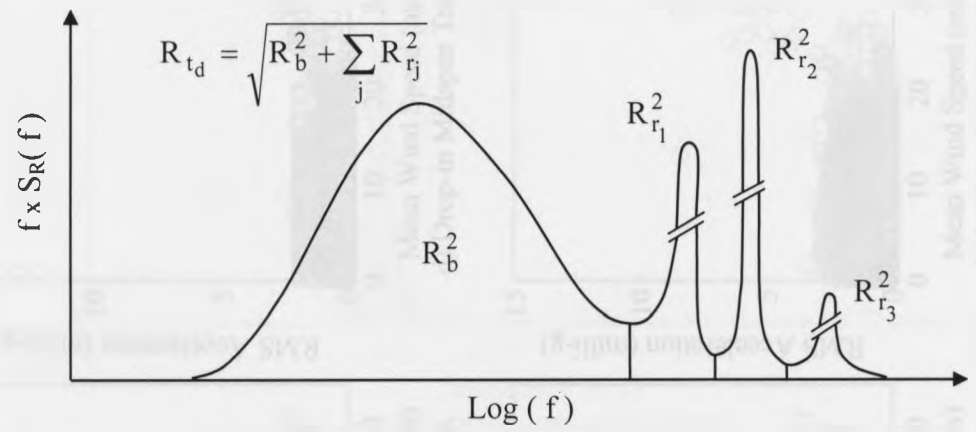

Figure 3.5 – Power Spectrum Showing Background and Resonant Responses [adapted from Davenport 1988]

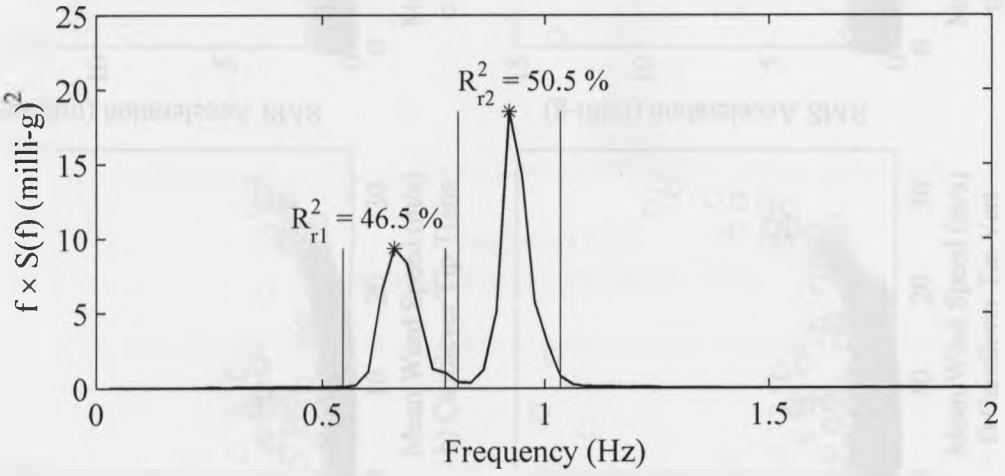

Figure 3.6 – Power Spectrum Showing Resonant Responses

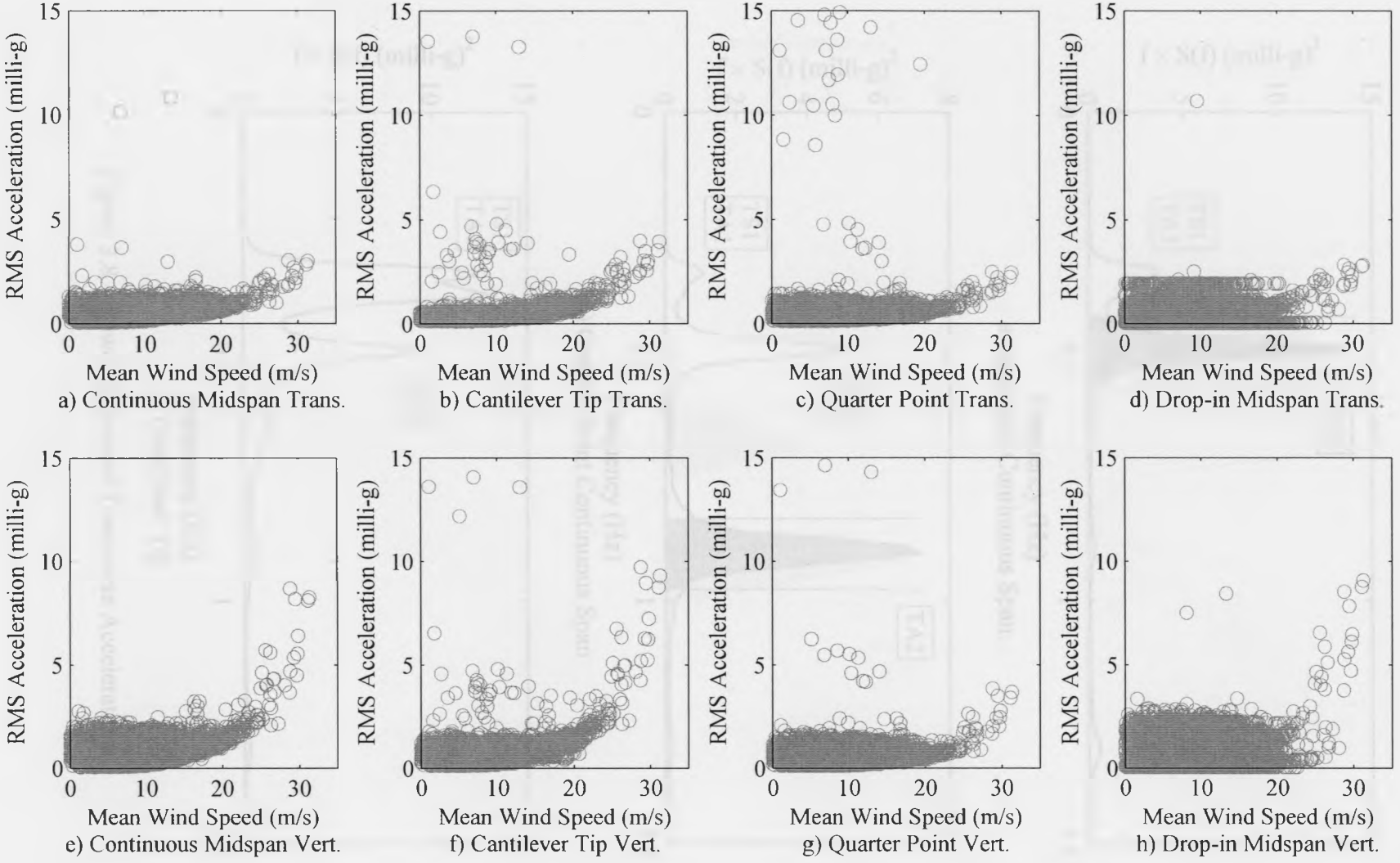

Figure 3.7 – Observed Ten-Minute RMS Accelerations – Total Dynamic Response

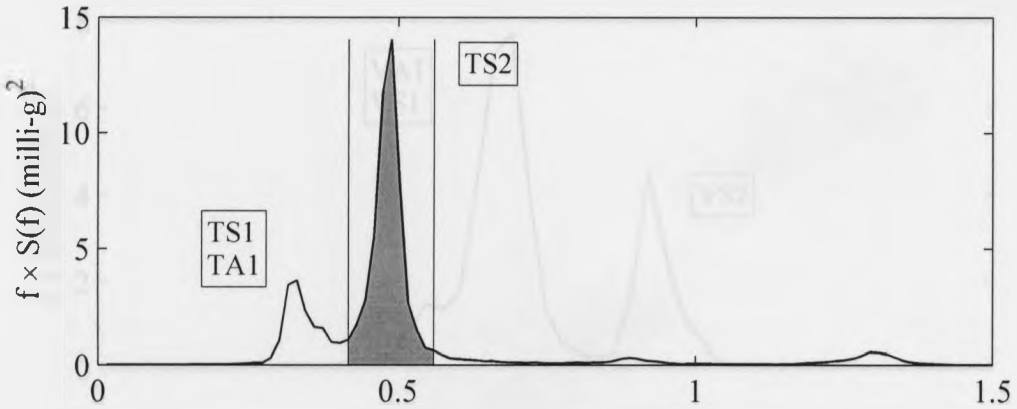

a) Midpoint Continuous Span

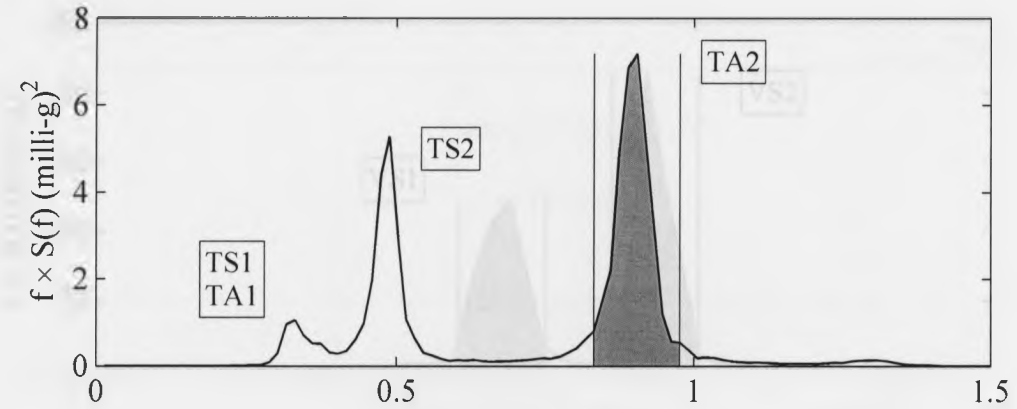

b) Quarter Point Continuous Span

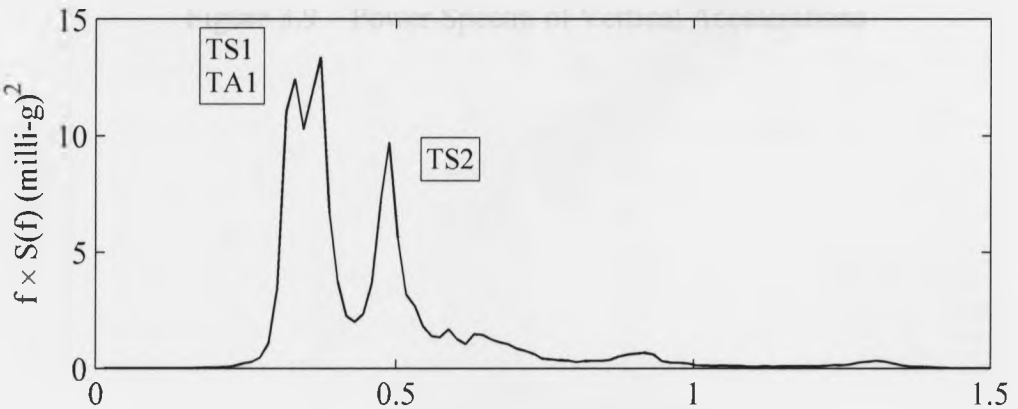

c) Cantilever Tip

Figure 3.8 – Power Spectra of Transverse Accelerations

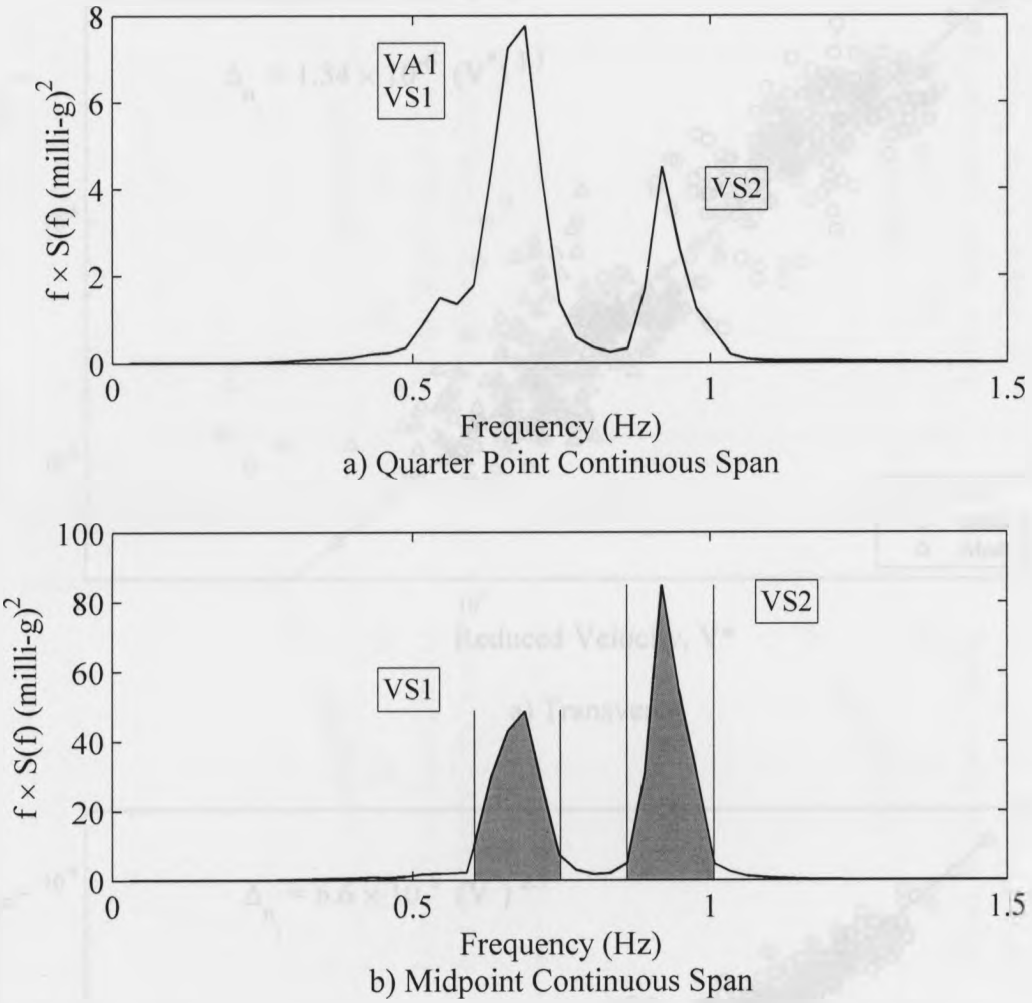

Figure 3.9 – Power Spectra of Vertical Accelerations

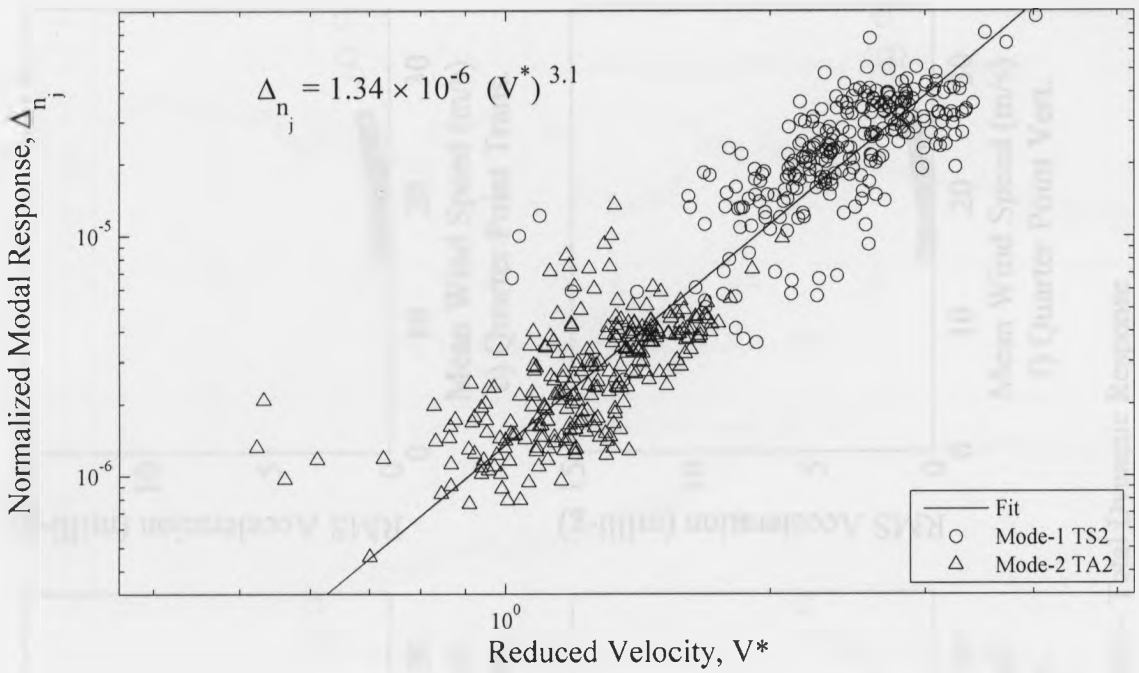

a) Transverse

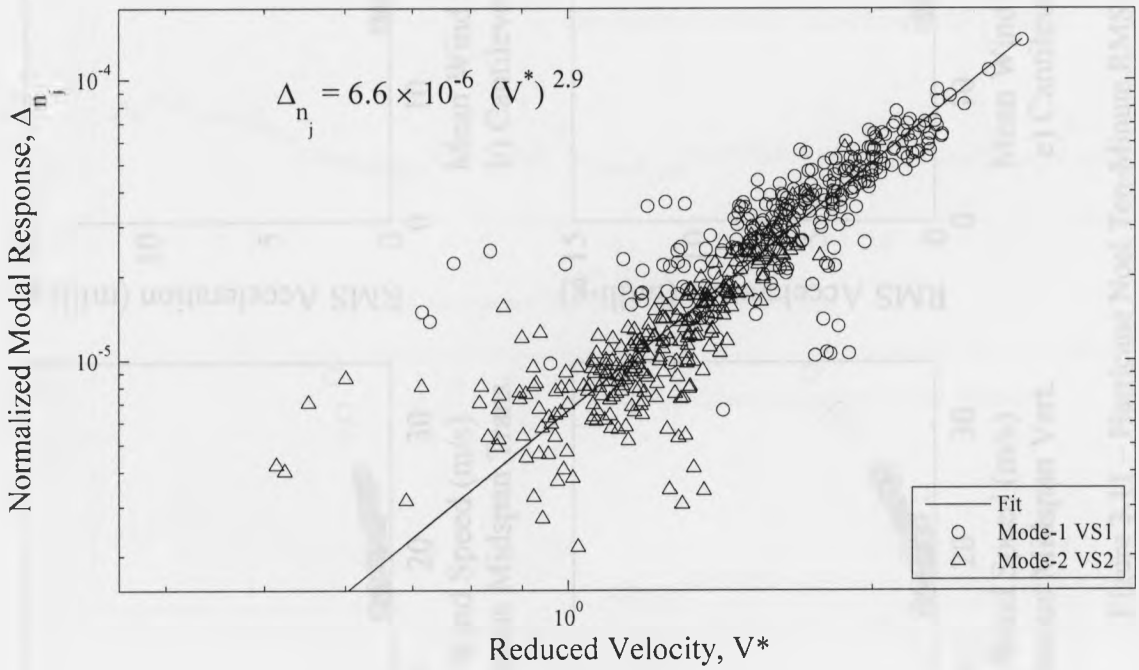

b) Vertical

Figure 3.10 – Variation of Normalized Modal Accelerations Ten-Minute Time History Datasets

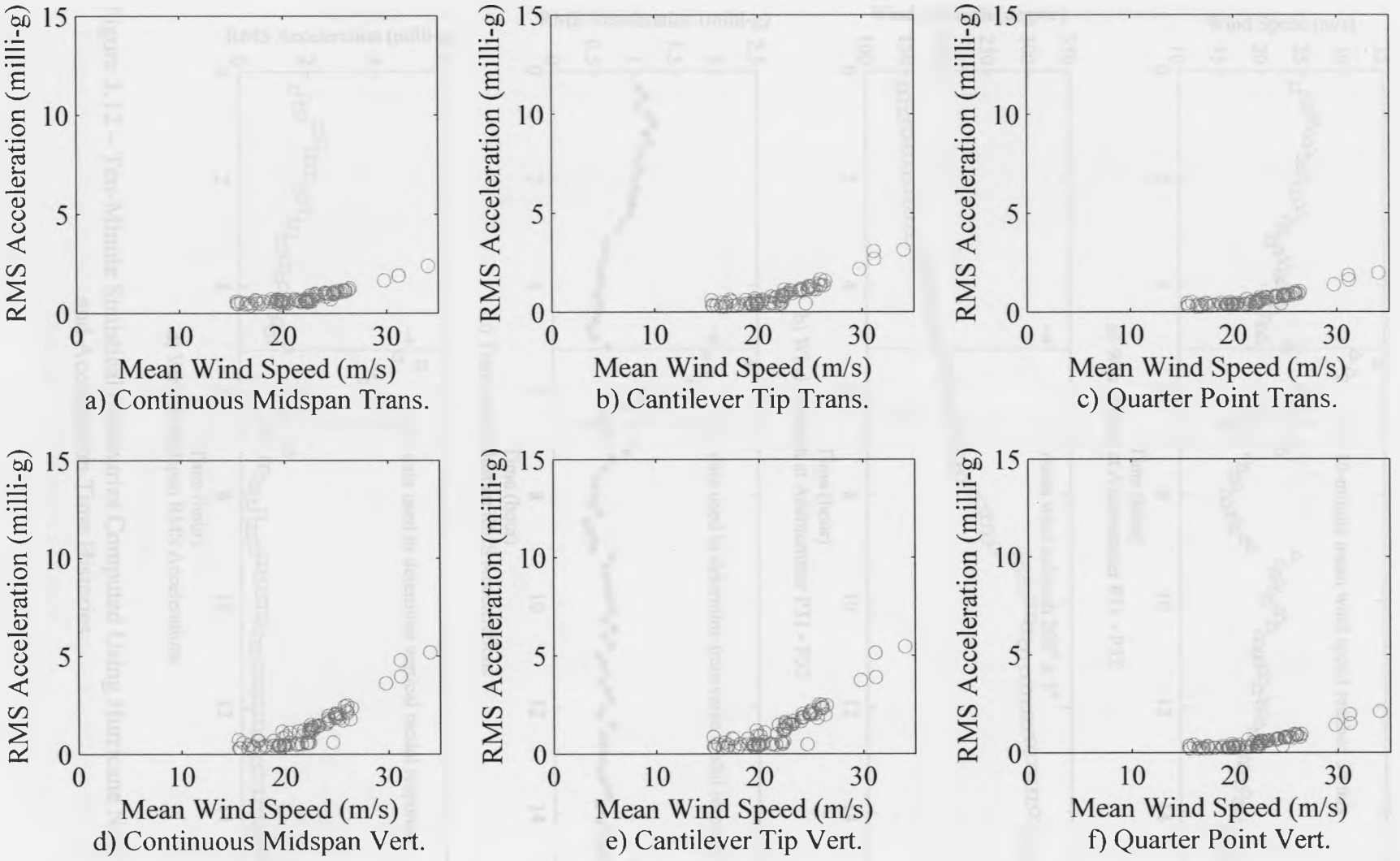

Figure 3.11 – Hurricane Noel Ten-Minute RMS Accelerations – Total Dynamic Response

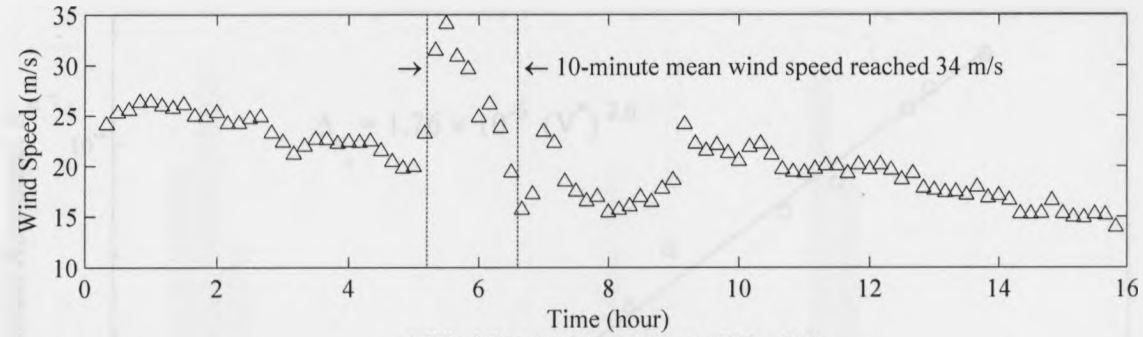

a) Wind Speed at Anemometer P31 - P32

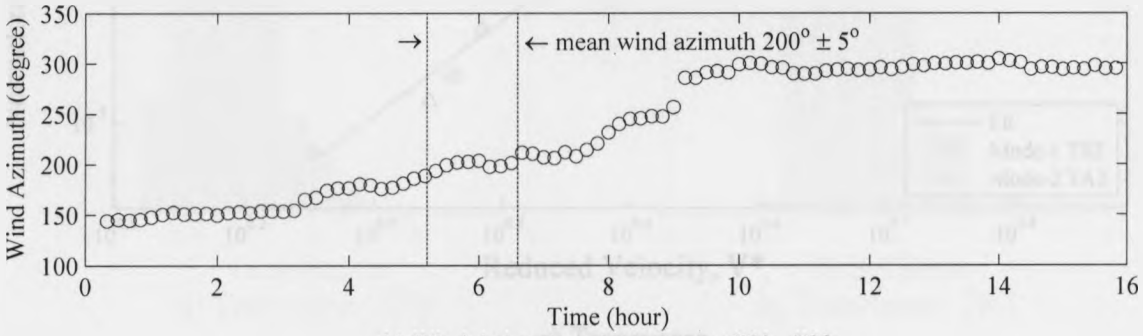

b) Wind Azimuth at Anemometer P31 - P32

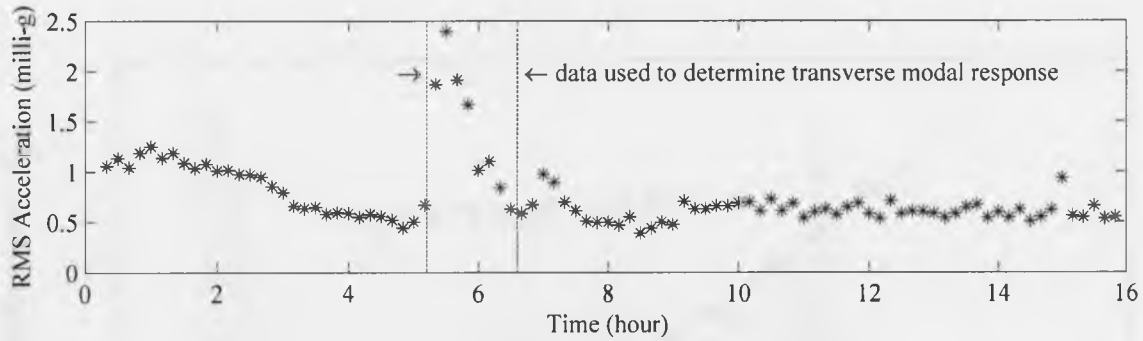

c) Transverse Midspan RMS Accelerations

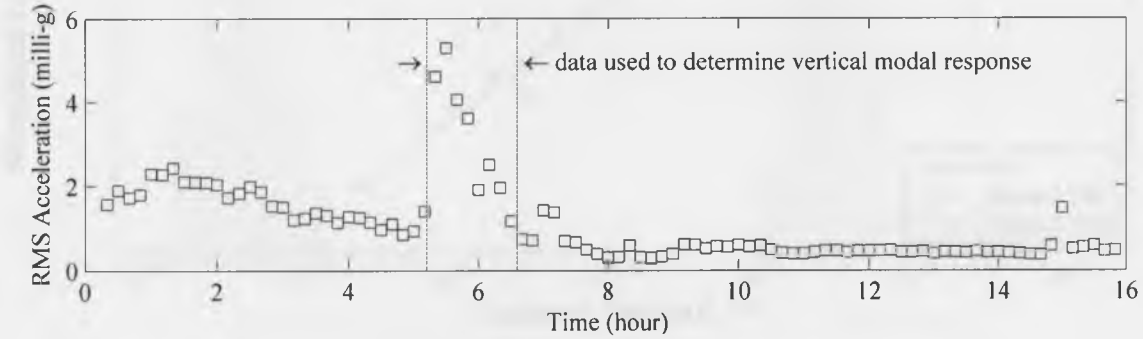

d) Vertical Midspan RMS Accelerations

Figure 3.12 – Ten-Minute Statistical Summaries Computed Using Hurricane Noel Wind and Acceleration Time Histories

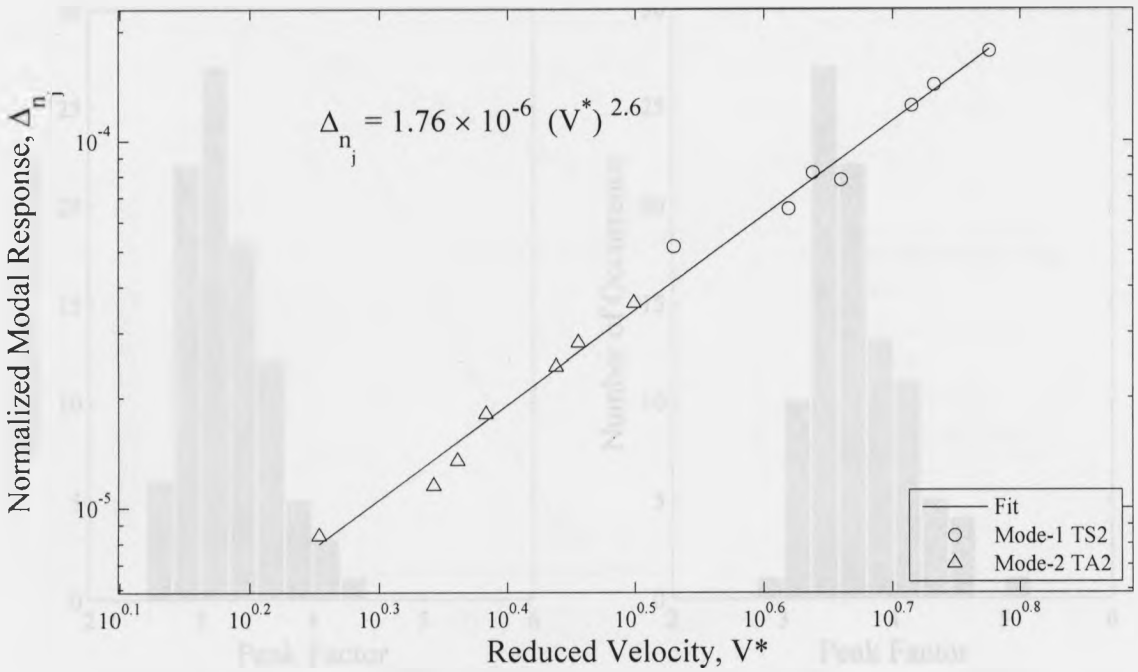

a) Transverse

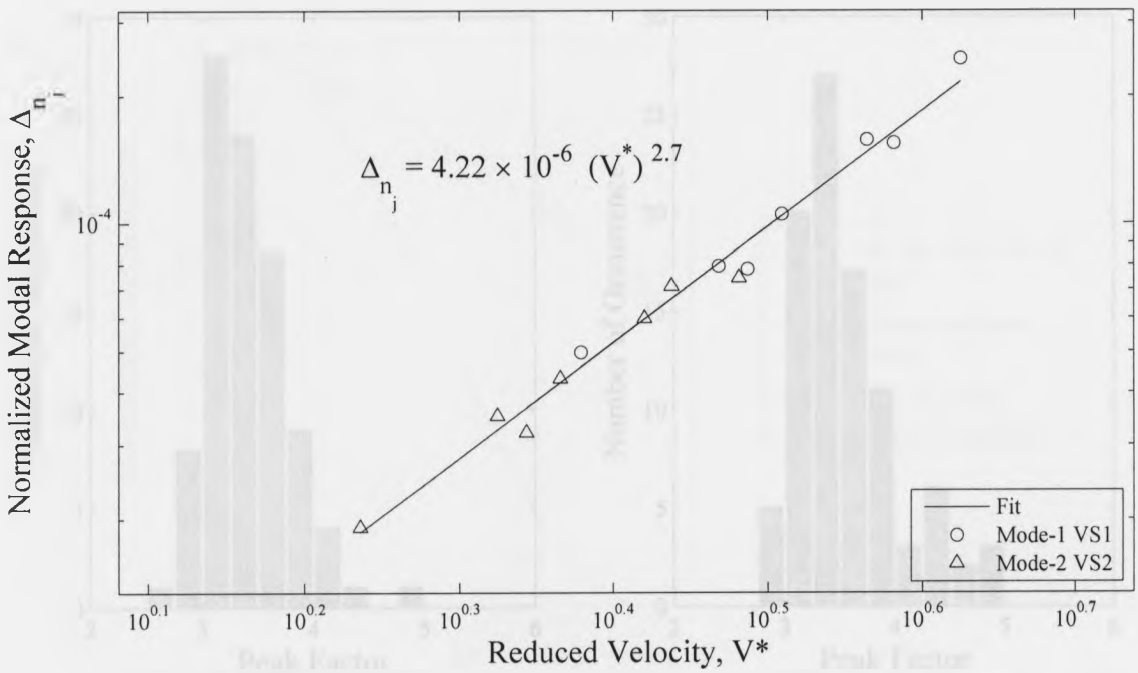

b) Vertical

Figure 3.13 – Variation of Normalized Modal Accelerations – Hurricane Noel Ten-Minute Time History Datasets

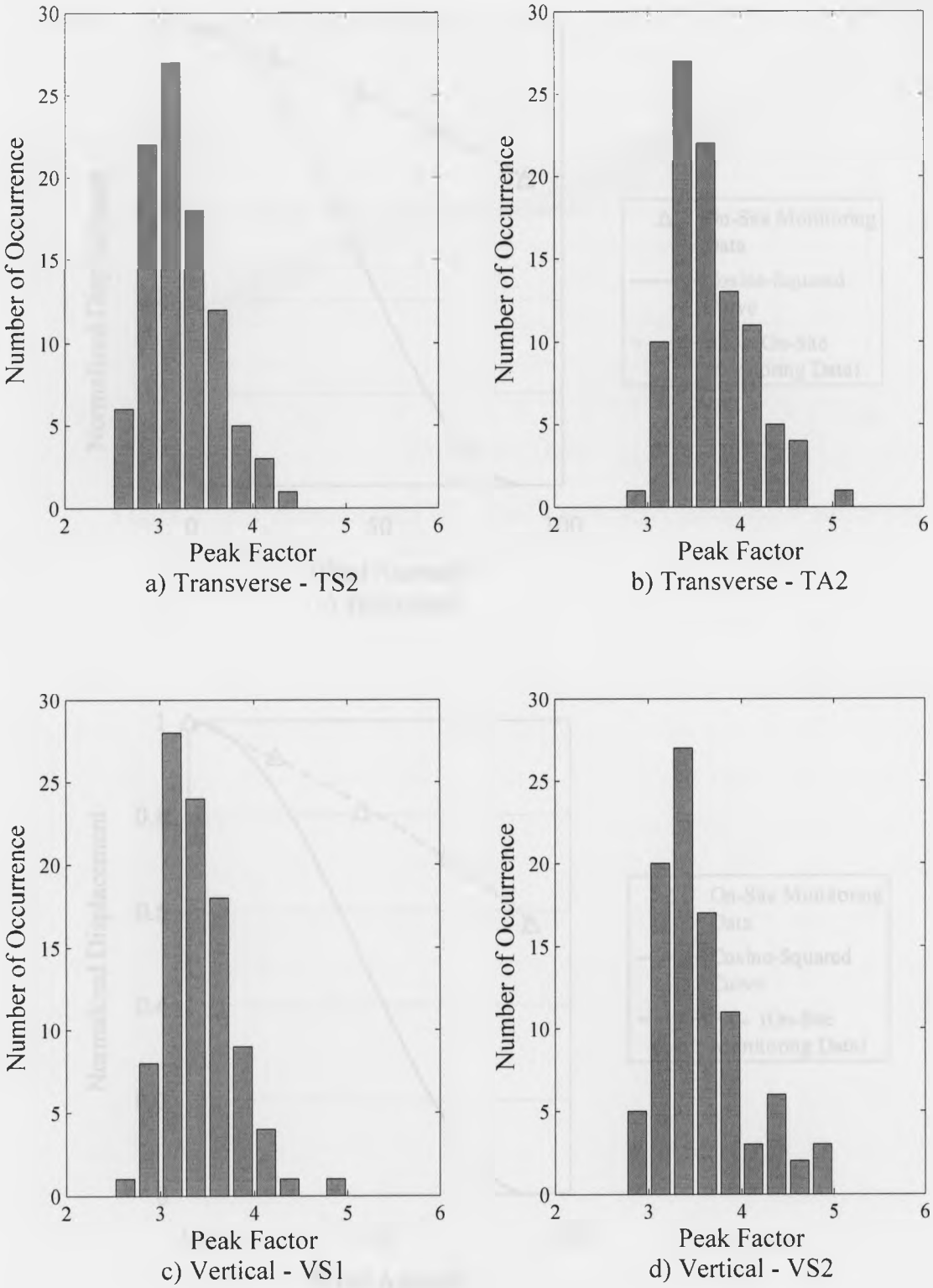

Figure 3.14 – Peak Factors from Hurricane Noel Data

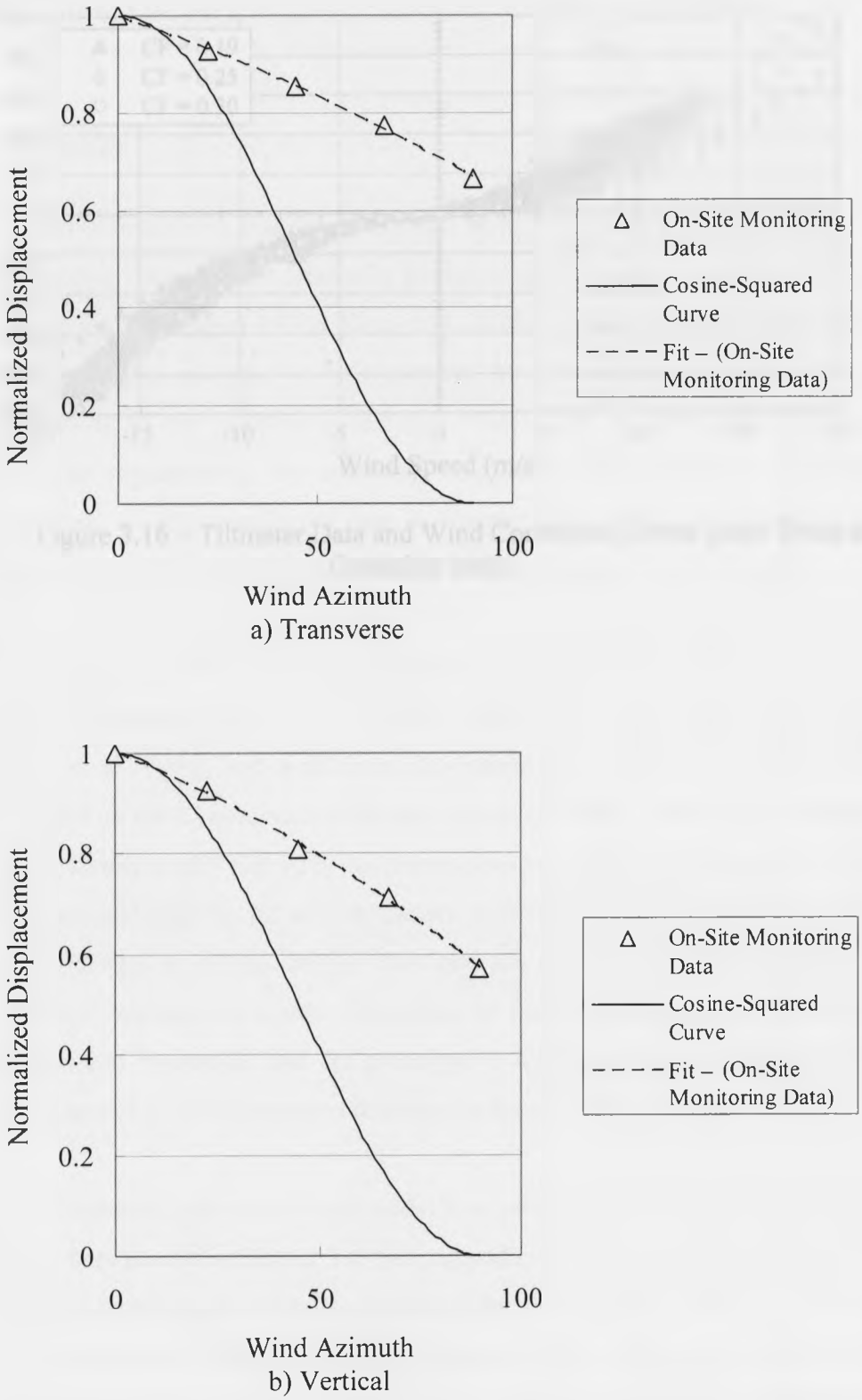

Figure 3.15 – Variation of Normalized Displacement with Wind Azimuth

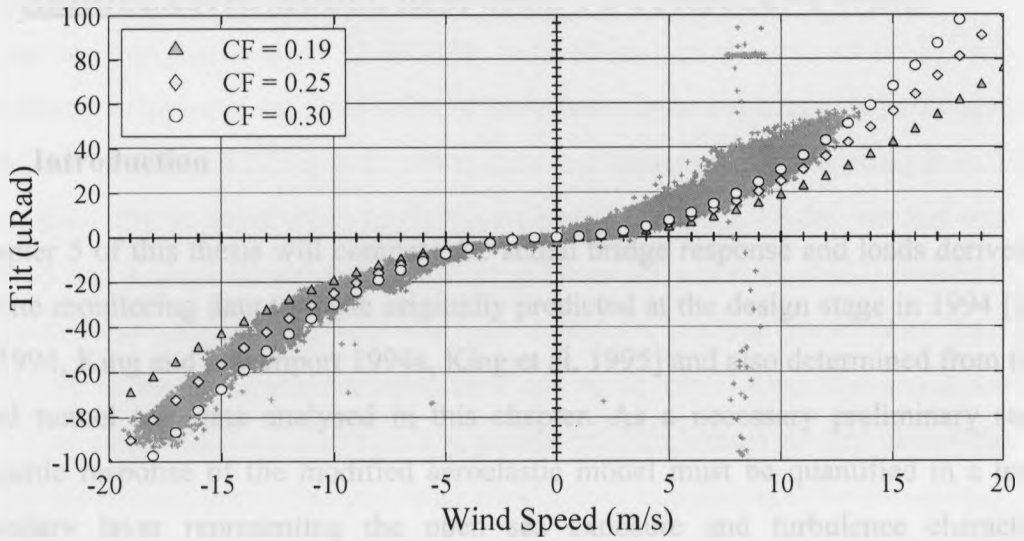

Figure 3.16 – Tiltmeter Data and Wind Correction Curves [after Bruce and Croasdale 2001]

4. AEROELASTIC MODEL RESPONSE TO TURBULENT WIND

4.1 Introduction

Chapter 5 of this thesis will compare the actual bridge response and loads derived using on-site monitoring data to those originally predicted at the design stage in 1994 [King et al. 1994, King and Davenport 1994a, King et al. 1995] and also determined from the new wind tunnel test data analysed in this chapter. As a necessary preliminary step, the dynamic response of the modified aeroelastic model must be quantified in a turbulent boundary layer representing the open sea exposure and turbulence characteristics established using on-site monitoring data in Chapter 2. In particular the mode shapes, frequencies and damping estimates must be determined for the modified model.

The full-aeroelastic model of the Confederation Bridge tested at the Boundary Layer Wind Tunnel Laboratory (BLWTL) in 1994 [King et al. 1994, King and Davenport 1994a, King et al. 1995] had a different instrumentation than the on-site monitoring system installed on the Confederation Bridge [Montreuil 1999a, 1999b]. For example, the original wind tunnel model had three accelerometers attached to the bridge deck whereas the Confederation Bridge has 42 accelerometers. It has been shown in Chapter 3 that only eight accelerometers at critical bridge locations are required to fully characterize the dynamic bridge response in winds. Therefore, to make a credible comparison of the responses between the model and the prototype it was necessary to retest the existing model with a layout of accelerometers that mimics their location on site.

Another modification to the aeroelastic model was necessary to simulate more closely the marine spans between Piers 30 and 33. The generalized masses of the end cantilevers of the two drop-in spans were not fully accounted for in the model tested in 1994 and so new generalized masses were attached to the spines of the cantilevers of the aeroelastic model. This could impact model frequencies and mode shapes of the cantilevers which are essential for the derivation of wind loads.

Very little was known about the prototype damping and so a low value of 0.13% of critical was originally used to identify instabilities and a value of 0.63% of critical, considered to be more representative of prestressed concrete structures, was used for the remainder of the tests [King et al. 1994, King and Davenport 1994a, King et al. 1995]. In developing the original wind loads, aerodynamic damping of the vertical modes was ignored and a quasi-steady approximation [Davenport and King 1982] was assumed for the transverse modes. The rationale was based on section model tests that showed instability in the vertical direction only [King et al. 1994, King and Davenport 1994]. This was considered a conservative approach in the absence of any knowledge of the variation of aerodynamic damping with wind speeds and azimuths for the bridge.

No efforts were made in 1994 to develop a numerical model of the wind tunnel model, rather, the numerical models of the prototype for the navigation and marine spans, provided by JMI-Stanley were used to derive the wind loads [King and Davenport 1994, King et al. 1995]. This is not unexpected; however, it does provide an opportunity to derive equivalent full-scale wind loads using numerical model of the aeroelastic model, which will be the first initiative.

It was shown in Chapter 3 that the variation of the bridge displacement with wind azimuth does not follow the conventional cosine-squared relationship which raises the question whether wind tunnel model follows the same trend.

In Chapter 5, the frequencies and mode shapes determined from the modified wind tunnel model and the numerical model of the aeroelastic model will be used to compute wind loads for comparison with those predicted at the design stage and using on-site monitoring data. The damping estimates will be necessary to determine the damping correction required for the equivalent full-scale loads predicted in various wind tunnel investigations.

As described in Chapter 2, the Confederation Bridge has six anemometers installed atop light standards at different elevations above the bridge deck. Some are located at the mid-

point of the continuous span, where the girder depth is smallest, and others are close to the piers, where the girder depth is largest. Five anemometers are located on the north side of the bridge and one has been recently installed on the south side. The wind data presented in Chapter 2 and the dynamic bridge response presented in Chapter 3 were recorded by the anemometers located on the north side of the bridge. The velocities recorded at these anemometers may be influenced by the presence of the bridge for certain wind directions, especially where winds approach from the south side or along the longitudinal centreline of the bridge; however, this has never been quantified. For example, the anemometers on the downstream side might record higher wind speeds than on the upstream side. Furthermore, the anemometers at locations where girder depth is large (particularly if the anemometer is located near the bridge deck) might indicate higher wind speeds for certain wind directions and reduced values for others. Similarly for winds not perpendicular to the bridge axis, the variable depth of the girder may also be a factor. Since the bridge authority Strait Crossing Bridge Limited (SCBL) relies on these anemometers to regulate traffic on the bridge and make decisions regarding the need for bridge inspection and traffic restrictions after strong wind events, the indicated wind speeds could be biased for certain wind azimuths.

4.1.1 Research Objectives

The objective of the present study is to retest the modified Confederation Bridge aeroelastic model for a wide range of wind speeds and azimuths to determine the following:

i) The dynamic bridge responses, in terms of RMS accelerations and normalized modal accelerations. These are necessary to derive the equivalent full-scale wind loads for the Confederation Bridge in Chapter 5.

ii) The variation of the bridge response with wind azimuth. This will be compared to the assumed cosine-squared relationship to investigate its accuracy.

iii) The effect of the bridge on the wind speeds recorded by the various anemometers for the 16-point compass wind directions. The quantification of the effect of wind direction on wind speed will improve decisions concerning the need for bridge closure during a severe wind event and subsequent inspection after the event.

iv) The variation of the aerodynamic damping with wind speed and azimuth to study its general behaviour and to validate the assumptions made regarding the transverse and vertical aerodynamic damping at the design stage in 1994.

Other activities to be conducted before testing in the wind tunnel include:

v) Modeling of the boundary layer flow regime based on the roughness length established using on-site monitoring data in Chapter 2 to ensure that the wind tunnel boundary layer characteristics matches that at the bridge site.

vi) Determining the dynamic characteristics of the wind tunnel model such as frequencies, mode shapes and structural damping that will be required to compute the equivalent full-scale wind loads in Chapter 5.

vii) Developing numerical model using the structural analysis software ALGOR [Logan 2001]. The ALGOR model frequencies and modes shapes will be compared to the experimentally determined frequencies and mode shapes and, if validated, the ALGOR model will be used to compute the equivalent full-scale wind loads in Chapter 5.

4.1.2 Chapter Organization

The original full-aeroelastic model of the Confederation Bridge tested at the BLWTL in 1994 is modified to match a typical marine span. The frequencies and mode shapes are determined experimentally and subsequently compared to the values determined from an ALGOR model. The structural damping for the fundamental vibration modes is estimated

using free vibration and autocorrelation techniques. The boundary layer wind and turbulence intensity profiles and the wind spectra measured in the wind tunnel are compared to the profiles and spectra derived analytically from the Power Law and Engineering Sciences Data Unit [ESDU 1974, 1993a, 1993b, 1993c]. The test programme included measurements of mean, root-mean-square (RMS), maximum and minimum values of the various responses for the eighteen test configurations. The statistical summaries of the RMS accelerations measured at the critical locations of the model are plotted versus wind speed at deck height and the time histories from the accelerometers are used to compute the dynamic modal responses. The variation of the normalized modal accelerations with wind azimuth, in the transverse and vertical directions, is determined and compared to the conventional cosine-squared relationship. The accelerometer time histories are used to estimate the total damping of the model. The variation of the aerodynamic damping with wind speed and azimuth are also presented. Finally, data from hot-film anemometers, representing three actual anemometer locations on the Confederation Bridge, are used to determine normalized polar plots for the upstream/downstream wind speeds in the 16-point compass directions.

4.2 Modifications to the Existing Model

The original Confederation Bridge model had two different sets of piers representing the height of the navigation and marine spans with deck elevations of 60.3 and 40.8 m, respectively, above Mean Sea Level [King et al. 1994, 1995]. The instrumented spans of the prototype bridge are the marine spans between Piers 30 and 33; therefore, marine span piers that reduce the deck elevation to 40.8 m were used. The different depths of Piers 31 and 32 were not modelled; however, the model incorporated typical substrate stiffness of the bedrock into the design of the piers. This was accomplished by matching displacements at the pier top due to unit load in the longitudinal and transverse directions and unit moment about the vertical axis, for the aeroelastic model and prototype [King et al. 1994].

The model, shown in Figure 4.1, is essentially as described by King et al. [1994]. Three contiguous spans of the full-scale bridge are modelled. The central span is a continuous frame and the side spans each have a drop-in segment at midspan between the cantilevers. The stiffness of the superstructure in all the three spans is modelled; however masses of the end cantilevers of the two drop-in spans were not fully taken into account in the 1994 study. This could impact model frequencies and mode shapes of the cantilevers which are essential for the derivation of wind loads. Generalized masses for the end cantilevers were therefore calculated for the first symmetric mode of vibration. The general deflection equation for a cantilever beam subjected to a unit distributed load was normalized with respect to the maximum deflection at the cantilever tip and used as a shape function to determine the generalized masses. The resulting masses (each 42.1 grams) were cut out of brass and glued to the spine of the cantilevers, shown in Figure 4.1.

4.3 Frequencies and Mode Shapes

Table 4.1 compares the model frequencies observed in 1995 at the BLWTL [King et al. 1995] and those from in the present study. The frequencies and mode shapes were determined outside the wind tunnel before testing by gently striking the instrumented model to induce each mode of vibration. The eight 2009 aeroelastic model frequencies have variabilities that are less than 1.5% of their mean values and so are considered accurate. The eighth modal frequency of 54.9 Hz is approximately 2 Hz in full-scale. As described in Chapter 3, frequencies less than 1 Hz are sensitive to wind excitation for the Confederation Bridge, therefore, this eighth mode was not considered for further analysis. The five model frequencies reported by King et al. [1995] are within 3% of the corresponding 2009 aeroelastic model frequencies, which shows the model is still intact. The addition of the generalized masses does not seem to impact significantly the aeroelastic model frequencies observed in 2009. The slight difference between the 2009 and 1995 aeroelastic model frequencies could be attributable to the different techniques and data analysis software used to compute these values. The 1995 aeroelastic frequencies were simply read from the acceleration power spectra [Dafoe 2009]. The

spectral peaks are sensitive to the sampling frequency and number of data points used to derive the power spectrum [Bendat and Piersol 2000]. Therefore, for the present investigation, a more accurate frequency estimate was determined based on the second moment of the spectrum as [Gomes and Vickery 1975]:

$$f_j = \left[\frac{\sum f_i^2 S_x(f_i)}{\sum S_x(f_i)} \right]^{1/2} \qquad [4\text{-}1]$$

where f_j is the j^{th} mode natural frequency, $S_x(f_i)$ is the spectral density for the i^{th} frequency and i is the i^{th} data point in the spectrum. Equation [4-1] gives a weighted average frequency which is more accurate compared than those values read from the spectral peaks of the acceleration power spectrum. These frequencies will be used to derive the modal dynamic responses in Sections 4.8 and subsequently the derivation of equivalent full-scale wind loads in Chapter 5.

A beam-element model was created using ALGOR [Logan 2001] for the full-aeroelastic model of the bridge. The ALGOR model is described in detail in Appendix 4A. As shown in Table 4.1, the ALGOR model frequencies are within 3% of 2009 aeroelastic model frequencies for the first five modes and within 7% for the eight modes shown. The ALGOR model frequencies are consistently high with respect to 2009 aeroelastic model values. This indicates the ALGOR model is slightly stiff, likely due to the idealization of the varying cross-section of the deck spine as discrete changes of the cross-section in ALGOR.

The mode shapes were determined experimentally using the technique of relative acceleration measurements [King et al. 1988, 1994, 2007, King and Davenport 1994c]. This involved measuring the accelerations caused by random impacts at the various locations along the length of the model when vibrating at the natural frequency corresponding to each mode of interest. The ratio of accelerations recorded simultaneously at different locations equals the ratio of displacements at these locations.

Therefore, the measured modal accelerations, at different bridge locations, normalized with respect to the maximum modal acceleration at the given frequency give the normalized modal displacements, i.e., the mode shape.

These observed mode shapes are superimposed upon those computed using the ALGOR model in Figures 4.2a to d and e to f for the symmetric and asymmetric modes of vibration, respectively. The horizontal axis in each figure is the horizontal distance along the model from Pier 31, at x = 0 m, towards Pier 32, so x = 0.5 m (or 125 m in full-scale) is the midspan between Piers 31 and 32, x = 1 m (or 250 m in full-scale) is Pier 32 and x = 1.38 m (or 345 m in full-scale) or -0.38 m (or -95 m in full-scale) is the tip of the cantilever. The solid lines are the shapes predicted by the ALGOR model and the open circle markers are the values observed from the aeroelastic model. The measured mode shapes are in excellent agreement with those of the ALGOR model suggesting that a significant number of modes can be modelled adequately. The mode shapes determined using the ALGOR model can therefore be used to compute the equivalent full-scale wind loads in Chapter 5.

4.4 Structural Damping Estimates

The structural damping for the fundamental vibration modes of the Confederation Bridge aeroelastic model was also estimated using free vibration [Chopra 2007] and autocorrelation techniques [Ochi 1990]. Table 4.2 lists mean damping ratios and variability ranges for the first two transverse and first two vertical modes of vibration computed using each technique. Both methods give similar mean damping values for the asymmetric modes; however, the damping values computed using the autocorrelation method are slightly smaller for the symmetric modes. In general the damping ratios are very low and are less than 0.24% of critical for the four modes shown. In Chapter 3, it was shown that use of the autocorrelation technique over estimated the prototype damping. However, the method gives estimates very close to the free vibration test results for the aeroelastic model. The free vibration method is generally recommended for reliable structural damping estimates [Chopra 2007 and Tedesco 2005]. The natural

frequencies of the aeroelastic model are widely spaced, 2.5 Hz to 3 Hz apart, whereas the prototype frequencies are closely spaced, 0.054 Hz to 0.43 Hz apart. This provides flexibility in setting wider filters when using the autocorrelation method on the aeroelastic model data, thus reducing spectral leakage, a phenomenon that artificially introduces secondary frequency effects [Brigham 1974].

The damping for the Confederation Bridge, estimated using the on-site monitoring data as described in Chapter 3, range from 1.5% to 3.9% for the fundamental modes of vibration. However, these values represent the total damping, i.e., the sum of structural and aerodynamic damping components. The total and aerodynamic damping for the Confederation Bridge aeroelastic model will be estimated using wind tunnel test data in Section 4.10. The total damping estimates for the aeroelastic model and the prototype are necessary to determine a damping correction for the equivalent full-scale wind loads predicted from the wind tunnel test results in Chapter 5.

4.5 Modeling of the Flow Regime

Modeling the natural wind by a turbulent boundary layer flow developed over a long upstream fetch of simulated model terrain has been adequately described in the literature [e.g., ASCE 1999]. The modeling of upstream flow regime in the wind tunnel to match the site requires accurately reproducing the mean wind profile, the longitudinal and vertical turbulence intensities and the scale of turbulence. Based on the wind tunnel tests conducted in 1994 and the turbulence intensity values determined from the on-site monitoring data analysis, a target turbulence intensity of 8% at the deck height of 40.8 m was achieved using the bare wind tunnel floor without spires at the test section inlet. The total length of the working section upstream of the model in the high speed test section of BLWT II is 30.48 m which, for the geometric scale 1:250, represents approximately 7.62 km of upwind fetch for the prototype. This length ensures that the boundary layer will fully develop [Davenport et al. 1967].

Multi-component (longitudinal and vertical) hot wire measurements of the variation of the mean wind speed and turbulence intensity at different elevations were made at the midspan portion of the model. The velocity profile for the upwind exposure is shown in Figure 4.3. The normalized mean wind speed $V(h)/V_{ref}$ is plotted on the right side of the figure using the scale given at the bottom. The corresponding longitudinal and vertical local turbulence intensities $\sigma(h)/V(h)$ are plotted on the left side of the figure using the scale given at the top. The data obtained in the wind tunnel are plotted as open triangle, circle and square markers for the mean velocity, longitudinal turbulence intensity and vertical turbulence intensity, respectively. The variation of the mean wind velocity profile is compared with two theoretical profiles, ESDU 82026 [ESDU 1993a] and a power law [Simiu and Scanlan 1978], which are widely accepted forms of defining the variation of wind velocity with height. The theoretical profiles are defined using roughness length z_o = 0.0002 m (α = 0.08, z_{ref} = 54 m) based on on-site anemometer data collected during the Hurricane Noel event as described in Chapter 2. Both theoretical velocity profiles match the wind tunnel data well in the region between the top of the pier and the top of the deck, elevations 26.8 and 40.8 m, respectively. Similarly, the local longitudinal and vertical turbulence intensities predicted using ESDU 85020 [ESDU 1993b] for the roughness length of z_o = 0.0002 m are in very close agreement with the wind tunnel data, particularly in the region between the pier top and the top of the deck. Good agreement between the theoretical profiles and the experimental values demonstrate that the wind tunnel is accurately simulating the velocity profile and turbulence characteristics of open sea exposures.

Measured power spectra, normalized by the variance, σ^2, of the longitudinal and vertical component of turbulence at deck level at the bridge centreline are shown in Figure 4.4. The horizontal axis of these graphs is the reduced frequency, fB/V. The "range of the practical interest" shown represents the lower and upper limits of the normalized bridge frequencies that are significant for the bridge response and the derivation of wind loads i.e., 0.34 to 0.94 Hz. The solid line represents the ESDU 74031 [ESDU 1974] wind spectrum based on the open-sea roughness length of 0.0002 m. To the left of the range of practical interest (i.e., low reduced frequencies) the observed and predicted spectra do not

match particularly well. To the right of this range the observed spectra also tend to deviate from the ESDU spectra. This is likely due to electrical noise which gets amplified at low spectral density values, S(f), and higher frequencies, f. For the range of practical interest the two spectra overlap for both the longitudinal and vertical wind components.

Thus the observed wind tunnel velocity profile and turbulence intensity profiles are close to those predicted using the site-based roughness length estimated from the Hurricane Noel data. It is therefore likely that the loads obtained from the wind tunnel modeling will correspond closely to those observed in full-scale investigation provided the loads are corrected to account for the actual full-scale damping.

4.6 Outline of the Wind Tunnel Test Programme

The testing of the aeroelastic model was comprised of measurements of mean, root-mean-square (RMS), maximum and minimum values of the various responses over a period of time corresponding to approximately an hour in full-scale for a range of wind speeds. The data were low-pass filtered at 40 Hz since the frequencies of interest are less than 30 Hz or 1 Hz in full-scale. Eighteen test wind azimuths were examined including the 16-point compass directions, i.e. 0°, 22.5° ... in 22.5° increments, plus two additional wind azimuths of 10° and 350°. The full aeroelastic model was tested at mean full-scale wind speeds from 4 m/s to 40 m/s at the deck height. The velocity scaling, shown in Table 4.3, of 0.1106:1 or 1:9.04, is based upon the fundamental modal frequencies shown in Table 4.2.

Resistance to deformation in a cantilever bridge is due primarily to elastic, rather than gravitational forces as in the case with suspension bridges where the "geometric stiffness" of the deflected cable under load is an important portion of the overall stiffness of the bridge. In cantilever bridges it is therefore not essential that Froude Number ($F_r = gL/V^2$) scaling be strictly enforced. (In this, g is the acceleration due to gravity, L is a characteristic length dimension and V is the mean wind speed [Davenport and King 1982, Tanaka 1992]). The benefit of Non-Froude scaled models is that a greater range of

wind tunnel speeds can be used, with the resulting benefits of better flow conditions, higher signal-to-noise ratios of the instrumentation and overall, a better-conditioned experiment [King et al. 2003]. This works very well with bridges that are not cable-supported, such as the Confederation Bridge. Therefore, Froude scaling was not used for the design of the Confederation Bridge aeroelastic model [King et al. 1994].

Table 4.3 lists the Non-Froude scaling parameters for the modified aeroelastic model of the Confederation Bridge. These parameters ensure similitude of the geometric, dynamic and material properties of the model and prototype. All the parameters listed are derived from the length, velocity (or time) and density (or mass) scales, which are the fundamental similitude requirements. For the modified aeroelastic model, the length and density scales did not change; however, the velocity scale changed to 1:9.04 and was determined based on frequencies measured from the on-site monitoring data for the instrumented spans between Piers 30 and 33. This change impacts the scale values for all parameters that depend on the velocity scale. In particular, the acceleration scale parameter, λ_a, decreased from 5.62 to 3.059. Other parameters affected by this change are the elastic stiffness, force, force per unit length, bending and torsional moments and warping stiffness. The structural damping of the prototype was not modelled and kept low to identify instabilities such as vortex shedding, galloping and flutter [King et al. 1994]. To account for the prototype damping, a damping correction originally proposed by Davenport [1967] was applied to the wind tunnel responses, which will be discussed briefly in Section 4.8 and in detail in Chapter 5.

4.7 Model Instrumentation

Figure 4.5 shows the location of the different instrumentation attached to the model during wind tunnel testing. The location of the accelerometers was chosen to match closely the onsite monitoring instrumentation on the prototype to facilitate direct comparisons of the model-scale and full-scale responses and, as described in Chapter 5, to compute and compare the wind loads. Ten accelerometers were glued to the bridge deck, and transverse accelerometers were attached at the top of Piers 31 and 32.

Transverse and vertical accelerometers were attached at mid- and quarter-point of the continuous span, the midpoint of the drop-in span and also at the tip of the cantilever as shown.

Three hot-film anemometers were calibrated prior to the test. Two were installed on the upstream side i.e., North and one on the downstream side, to examine the influence of bridge on wind speeds during the test. The location of the instruments within a span is consistent with the Pier 31-32, Pier 20 – North and Pier 20 – South anemometers as described in Chapter 2; however, distance between the Pier 20 and Pier 31-32 anemometers, 2.83 km, was not modelled for obvious reasons. Thus, an instrument representing the Pier 31-32 anemometer was located midway between Pier 31 and Pier 32, 12.85 m above the bridge deck. Similarly two hot-film anemometers representing the Pier 20 – North and Pier 20 – South anemometers were installed 6 m above the bridge deck, -41.67 m and -83.33 m from Pier 32, respectively. Pier 32 will be considered equivalent to Pier 20 when referring to the Pier 20 North and South anemometers subsequently.

Two deflection transducers were used to measure midspan deflections in the transverse and vertical directions. The tilts at the top of Piers 31 and 32 were also inferred from the transverse deflection transducers as shown.

The aeroelastic model was also instrumented with strain gauges at the pier bases to measure longitudinal and transverse bending moments and torsion. Strain gauges at the midspan of the continuous span and pier faces were used to determine wind-induced longitudinal and transverse bending moments only. The strain gauges were attached to the model and calibrated before determining frequencies, mode shapes and structural damping to ensure the dynamic properties of the aeroelastic model did not change during testing.

A full set of response plots for all wind azimuths for all the instruments is shown in Appendix 4C. The data from the accelerometers are reported as equivalent full-scale

accelerometer data. The statistical summaries and time histories from the accelerometers are used to determine the total and modal dynamic responses in the following sections.

4.8 Dynamic Response of the Bridge

The statistical summaries of the accelerometers and wind data are used to determine RMS acceleration plots in the transverse and vertical directions at the mid- and quarter-point of the continuous span, the cantilever tip, and the mid-point of the drop-in span as shown in Figure 4.6. These are the total dynamic responses, R_{t_d}, measured in the wind tunnel for winds normal to the bridge axis (i.e., at a wind azimuth of 0°) and are similar to the total dynamic responses for the prototype as described earlier in Section 3.4 as:

$$R_{t_d} \cong \sqrt{\sum_j R_{r_j}^2} \qquad [4\text{-}2]$$

The figure shows the general trend is the same as observed for the prototype, Figure 3.7. The wind tunnel responses have less variability, likely due to the stationarity of the wind speed and direction during the test.

The transverse accelerometers show maximum RMS accelerations of approximately 16 milli-g recorded at the cantilever tip for a wind speed of 40 m/s, Figure 4.6b. The mid-points of the continuous and drop-in spans, Figures 4.6a and b, respectively, show similar transverse RMS acceleration magnitudes of approximately 12 milli-g at 40 m/s. The least transverse RMS acceleration of 8 milli-g is observed at the quarter point of the continuous span, Figure 4.6c. The vertical accelerometers follow a similar trend. The cantilever tip has the maximum RMS acceleration of approximately 40 milli-g for a wind speed of 40 m/s. The mid-point of the continuous span shows a vertical RMS acceleration of 23 milli-g, and the mid-point of the drop-in span shows a vertical RMS acceleration of 38 milli-g at 40 m/s. The quarter-point shows the least vertical RMS acceleration of 14 milli-g at 40 m/s. In general, the equivalent full-scale RMS accelerations from the wind tunnel model are large compared to the observed full-scale RMS accelerations presented

in Chapter 3. This is evidently due to the low damping of the aeroelastic model. Davenport [1967] has shown that the resonant or modal response is inversely proportional to the square root of total damping, which is the sum of structural and aerodynamic damping. It will be shown in Chapter 5 that the two responses become very close once the aeroelastic model response is corrected for the total prototype damping.

The modal dynamic responses were determined using acceleration time histories following the procedure presented in Section 3.4. Figures 4.7a, b, and c show power spectra derived for time history datasets corresponding to the transverse and vertical accelerations at the cantilever tip and the transverse accelerations at the quarter-point of the continuous span, respectively. The frequency peaks correspond to the fundamental modes of vibration shown in Figure 4.2. The spectral peaks for the first two transverse and two vertical mode shapes, TS1, TA1, VA1, and VS1, did not require a modal correction as they correspond to the maximum modal displacement of 1.0 at the cantilever tip as shown in Figure 4.2. However a modal correction of 0.5, read from Figures 4.2b and d, was applied to the spectral peaks for modes TS2 and VS2. The spectral peak for mode TA2 was not used to derive the modal response. This does not impact the analysis as it was shown in Section 3.4 that not all modes of vibration are required to characterize the modal response. The identified spectral peaks were isolated using a band bass filter and the resulting time histories were used to compute the maximum modal RMS accelerations. This was repeated for all the time history datasets available from the wind tunnel testing.

As discussed in Chapter 3, the maximum modal RMS accelerations and associated wind velocities were normalized to make the response independent of frequency and proportional to the reduced velocity on a log scale, Equation [3-6]. The maximum modal RMS accelerations were normalized by the width of the bridge and the square of the circular frequency, Equation [3-3], and the associated wind velocities were normalized by the cyclic frequency and width of the bridge, Equation [3-4].

Figures 4.8a and b show the normalized modal responses for the transverse and vertical modes of vibration, respectively, for wind azimuth normal to the bridge axis. Three fundamental transverse and vertical modes were used to derive these normalized modal responses. Straight lines were fitted to the data shown and those data for the seventeen other wind azimuths using the multivariate linear regression analysis [Montgomery et al. 2001]. The resulting fits for the wind azimuth normal to the bridge axis are:

$$\Delta_{n_j} = 1.027 \times 10^{-5} (V^*)^{2.3} \qquad [4\text{-}3a]$$

and

$$\Delta_{n_j} = 1.095 \times 10^{-5} (V^*)^{2.9} \qquad [4\text{-}3b]$$

for the transverse and vertical modal responses, respectively. The standard errors for the exponent are 0.013 and 0.014 and for the coefficient are 2.97 x 10^{-7} and 2.86 x 10^{-7} for the transverse and vertical modal responses, respectively. Thus the coefficient of variation of the estimated slopes is within 1% and that for the estimated coefficients is within 3%. Both are smaller than the values computed using the on-site monitoring and Hurricane Noel data presented in Chapter 3, again likely due to the ability to control the wind in the wind tunnel. The t-statistics for both the exponent and constant parameters are significantly greater than 2, demonstrating the clear significance of the reduced velocity on the normalized modal acceleration.

The vertical modal response for the aeroelastic model and prototype has the same exponent of 2.9. The transverse modal response of the aeroelastic model has an exponent of 2.3 while the exponent for the prototype is 3.1 as described in Chapter 3. No explanation is available at this point to illuminate the different behaviour in the transverse modal response for the aeroelastic model and prototype. The coefficients, 1.027 x 10^{-5} and 1.095 x 10^{-5}, for the transverse and vertical modal responses are greater than the corresponding prototype coefficients, 1.76 x 10^{-6} and 4.22 x 10^{-6}, determined in Chapter 3. The higher coefficient values suggest higher dynamic responses, which are consistent with the low aeroelastic model damping.

The "ranges of practical interest" shown in Figures 4.8a and b represent the lower and upper limits of the normalized wind velocities that are significant for the bridge response and derivation of the wind loads. For the transverse modes, the average responses of modes TS1, TA1, and TS2 are close to the fitted line but the data for modes TS1 and TA1 lie above the line while the data for mode TS2 lies below it. For the vertical modes data for all the three modes lie close to the regression line through the range of practical interest. Equations [4-3a] and [4-3b] will be used to compute equivalent full-scale wind loads based on the 2009 aeroelastic model for the Confederation Bridge in Chapter 5.

4.9 Normalized Displacement Variation with Wind Azimuth

The variation of the bridge displacement, as represented by the coefficient or intercept of the regression fits to the modal responses shown in Equation [4-3a] and [4-3b], with wind azimuth is shown in Figures 4.9a and b as open circle markers for the transverse and vertical directions. The displacements have been normalized by the maximum displacement for the 0^{o} wind azimuth, i.e., perpendicular to the bridge axis. The data points shown for the 0^{o}, 10^{o} and 90^{o} wind azimuths are the averages of two coefficients and the rest are averages of four coefficients (e.g. 22.5^{o} represents $0^{o} \pm 22.5^{o}$ and $180^{o} \pm 22.5^{o}$). The dash-dotted lines are 4^{th} order polynomial fits to the normalized coefficients that are in excellent agreement with the open circle markers and so can be used to represent the bridge response. It is generally accepted that as the angle of wind azimuth increases from 0^{o} to 90^{o}, the bridge displacement reduces proportionally to the square of the cosine of the wind azimuth angle. The derivation used to justify this assumption is presented in Appendix 3C. The present study shows the vertical displacement of the bridge almost follows this cosine-squared relationship; however, the transverse displacement does not follow this relationship as the actual normalized displacement is 0.1 to 0.18 greater as the wind angle moves from 22.5^{o} to 90^{o}.

4.10 Total and Aerodynamic Damping Estimates

The damping estimates from the wind tunnel test data inherently contain components of the structural and aerodynamic damping. The structural damping does not change; however, the aerodynamic component varies with wind speed and direction. The wind tunnel test data for the accelerometers, used to derive the modal responses in Section 4.8, were used to calculate the total (structural + aerodynamic) model damping for different wind speeds and directions for the four transverse and three vertical modes of vibration using the autocorrelation technique [Ochi 1990]. Although, this method gave higher damping estimates in Chapter 3, the method works very well for stationary stochastic processes [Ochi 1990], especially if the natural frequencies are widely spaced. This approach has been justified in Section 4.4, where the structural damping estimates using free vibration and autocorrelation techniques are almost the same. The wind tunnel data, gathered during testing of the aeroelastic model, are stationary and the frequency peaks, as shown in Figure 4.7, are widely spaced (2.5 Hz to 3 Hz apart). This legitimises the use of the method. Randomly chosen datasets were used to compute damping using the Random Decrement Method (RDM) to further justify the use of the autocorrelation method. The damping estimates were consistent with the values determined using the autocorrelation method.

The total damping estimates for four transverse and three vertical mode shapes are tabulated in Table 4.4 for the design wind speed of 30.5 m/s at a wind azimuth of 0^{o}. These damping estimates will be used to determine the damping correction for the equivalent full-scale loads computed from the 2009 wind tunnel test results in Chapter 5.

The structural damping estimates for the two transverse and vertical modes of vibration were presented in Section 4.4. These damping values were subtracted from the total model damping to obtain the aerodynamic damping estimates, ζ_j, for different wind speeds. The resulting values are plotted versus reduced velocity for the transverse and vertical modes of vibration in Figure 4.10. Figure 4.10a shows the aerodynamic damping increases linearly with wind speed for the transverse modes. Figure 4.10b shows for the

vertical modes the aerodynamic damping increases with wind speed up to a reduced velocity of 4.25 and decreases at higher wind speeds. A fourth order polynomial fits the data well as shown. The different nature of the transverse and vertical modal aerodynamic damping values is not unexpected because the aerodynamic instabilities such as vortex shedding and galloping are due to small or even negative values of aerodynamic damping associated with the vertical modes of vibration [Holmes 2007].

Figures 4.11a and b show the variation of the aerodynamic damping with wind azimuth for the transverse and vertical modes of vibration, respectively, for a range of wind speeds. Each curve in Figure 4.11 is an average of the four curves for the four quadrants. The variability associated with the fits corresponds to the variability in the data points shown in Figure 4.10. Figure 4.11a shows the transverse aerodynamic damping reaches its peak at 10° to the bridge normal, irrespective of the wind speed, and decreases as the wind azimuth moves further off the bridge normal. Figure 4.11b shows for wind azimuths between 67.5° and 90°, the aerodynamic damping does not change appreciably with wind azimuth. For wind azimuths between 22.5° and 67.5°, the aerodynamic damping decreases with an increase in wind azimuth with the exception of 15, 20 and 25 m/s curves, which show a slight increase in damping for wind azimuths between 45° and 67.5°. For wind azimuths between 0° and 45°, there is no obvious trend between the aerodynamic damping and changing wind azimuth at these wind speeds. At this point no other information is available to illuminate the variation of aerodynamic damping with wind azimuth shown in Figure 4.11.

4.11 Effect of Bridge Superstructure on Upstream and Downstream Anemometer Readings

Figure 4.12 shows wind speeds, normalized with respect to the wind of 0° azimuth, recorded by the hot-film anemometer located midway between Piers 31 and 32 on the north side of the bridge deck for the 16-point compass directions. The figure is almost symmetrical about the North/South axis, which is consistent with the location of the hot-film anemometer over a uniform section depth of 5.5 m as shown in Figure 4.5. For the

Bridge North and ± 22.5 ° azimuths, the bridge deck has no influence on the measured with speeds. This is justified since the approaching winds and the anemometer are on the same side of the bridge. On the other hand, winds approaching from the South and 180 ° ± 22.5 ° azimuths show 10% and 5% increases in the measured wind speed, respectively. This demonstrates that the flow of the wind around the bridge deck increases the velocity recorded at the downstream anemometer. For wind blowing along the bridge axis, considerable shielding is provided by the bridge deck and, on average, a 20% reduction of the measured wind speed is observed for winds from Bridge East or West. As wind azimuth moves away from the bridge axis, the influence of the bridge deck starts diminishing and almost vanishes for the 22.5 °, 150 °, 210 ° and 337.5 ° directions.

Figure 4.13a shows a similar plot for the Pier 20 anemometer located 41.67 m west of Pier 20 on the north side of the bridge, 6 m above the bridge deck, that is used for bridge operations. The superstructure depth of 10 m at the anemometer location is gradually increasing on the east side and decreasing on the west as shown in Figure 4.5. Being in close proximity to Pier 20, the anemometer readings are increased by 17 and 12% for the 315° and 337.5° azimuths, respectively. Similarly, for the 202.5° and 225° azimuths, the indicated wind speeds are increased by 30 and 24%, respectively. For the 135° and 157.5° azimuths, considerable shielding is provided by the pier which causes 14 and 21% reductions in the indicated wind speed, respectively. For the wind blowing along the bridge axis, the bridge deck reduces the actual wind speeds by 5% to 10% for the Bridge East and West, respectively.

Figure 4.13b shows a similar polar plot for the Pier 20 anemometer located 83.3 m west of Pier 20, 6 m above the bridge deck, on the south side of the bridge and is also used for bridge operations. The superstructure depth of 7 m at the anemometer location is very gradually increasing on the east side and decreasing on the west as shown in Figure 4.5. The indicated wind speeds seem unaffected by Pier 20; however, they are consistently less than the normalizing wind speed for all compass directions except for the 202.5° azimuth which is equal. The plot does not show symmetry about the North/South or East/West axis, because the anemometer is located over a tapering section of the bridge

deck, which offers a unique deck thickness and instrument location for each compass direction. For the wind blowing along the bridge axis, 20% and 30% reductions in the indicated wind speed are observed for the Bridge East and West azimuths, respectively.

The polar plots shown in Figures 4.12 and 4.13 are a tool to determine the correction required for the indicated wind speeds by the anemometers for a given wind direction. These plots would be instrumental in decision making regarding bridge inspection after a strong wind event and also for regulating traffic on the bridge under high winds.

4.12 Conclusions

The full-aeroelastic model of the Confederation Bridge originally tested at the BLWTL in 1994 [King et al. 1994, King and Davenport 1994a, King et al. 1995] has been retested in the wind tunnel with a few minor modifications. The model frequencies and mode shapes determined experimentally are compared to the values determined numerically using ALGOR. The model frequencies are also compared to the values reported by King et al. [1995]. The structural damping for the two transverse and vertical mode shapes is estimated using free vibration and autocorrelation techniques. The time histories from the accelerometers are used to determine the total damping and the variation in the aerodynamic damping with wind speed and azimuth for these modes. The statistical summaries of the accelerometers attached at the critical locations on the model deck are used to compute the RMS accelerations and a general comparison is made with the RMS accelerations determined from the on-site monitoring data in Chapter 3. The accelerometer time histories are used to determine the dynamic modal responses for the transverse and vertical mode shapes. The model displacements for the changing wind azimuth are compared to the conventionally used cosine-squared relationship. Finally, the polar plots showing wind speeds normalized with respect to the wind of zero azimuth for the Pier 31-32, Pier 20 – North and Pier 20 – South are developed.

The following conclusions are drawn:

1. The 2009 model frequencies determined from the acceleration power spectra have variabilities that are less than 1.5% of their mean values and so are considered accurate. The values reported by King et al. [1995] are within 3% of the corresponding 2009 aeroelastic model frequencies, which shows the model is still intact. The addition of masses at the end cantilever did not impact the aeroelastic model frequencies significantly as the slight difference between the 1995 and 2009 observed frequencies could be due to different techniques used to compute the frequencies.

2. The ALGOR model frequencies are within 5% of the 2009 aeroelastic model frequencies for the first five modes and 7% for all eight modes investigated. This indicates the ALGOR model is slightly stiff compared to the aeroelastic model.

3. The mode shapes predicted using the ALGOR model for the first eight modes are in very good agreement with those observed in the 2009 aeroelastic model tests. This demonstrates the potential power of the ALGOR model to accurately predict a significant number of modes. The ALGOR model will be used in Chapter 5 to derive the equivalent full-scale wind loads for the Confederation Bridge.

4. The structural damping computed using free vibration and autocorrelation techniques are in good agreement, indicating the reported values for the different vibration modes are accurate. Although autocorrelation technique overestimated prototype damping in Chapter 3, the method gives comparable damping estimates for the aeroelastic model. This is perhaps due to the widely spaced natural frequencies (2.5 Hz to 3 Hz apart) in the aeroelastic model, which permits flexibility in setting wider filters, thus reducing spectral leakage. The model structural damping values are very low (less than 0.25% of critical).

5. The autocorrelation technique was also used to estimate the total damping using the 2009 aeroelastic model test data since the method works very well for stationary processes. The total damping estimates for the aeroelastic model range from 0.25 % to 0.92% of critical for the fundamental modes of vibration at the design wind speed of 30.5 m/s. The corresponding full-scale damping values range from 1.5% to 3.9%. The low damping for the full-aeroelastic model indicates the dynamic responses will be amplified.

6. The aerodynamic damping linearly increases with increase in the wind speed for the transverse modes. For the vertical modes, a fourth order polynomial fits the observed data well, reaching its peak and then gradually decreasing with further increase in the wind speed. The different behaviour in the transverse and vertical modal aerodynamic damping is not unexpected because the aerodynamic instabilities such as vortex shedding and galloping are associated with the vertical modes of vibration.

7. The aerodynamic damping is also sensitive to wind azimuth. For the transverse modes it increases with increase in the wind azimuth up to 10^{o} and then decreases with further increase in the wind azimuth. For the vertical modes there is no obvious trend between the aerodynamic damping and wind azimuth for values less than 45^{o}. For wind azimuths between 45^{o} and 67.5^{o}, the aerodynamic damping decreases with increase in wind azimuth for wind speeds greater than 20 m/s. Wind azimuths increasing from 67.5^{o} to 90^{o} have no appreciable effect on the aerodynamic damping.

8. The wind profile measured in the wind tunnel is in good agreement with the power law [Simiu and Scanlan 1978] and ESDU 82026 [ESDU 1993a] between the pier top and deck height. The mean longitudinal and vertical turbulence intensities are also in good agreement with the values predicted using ESDU 85020 [ESDU 1993b] in the region of interest. Furthermore, the longitudinal and vertical wind spectra derived using wind tunnel data are in excellent agreement with the

theoretical spectra such as ESDU 74031 [ESDU 1974] for the fundamental frequencies of interest. The theoretical values are based on a roughness length of 0.0002 m established using Hurricane Noel wind data in Chapter 2. Validation of the experimental results with the theoretical values demonstrates that the wind tunnel tests results are representative of the velocity profiles and turbulence characteristics of an open sea exposure.

9. It is commonly accepted that the bridge displacement reduces as the wind azimuth moves away from normal to the bridge axis following a cosine-squared relationship. The present study shows that the vertical displacement of the model can be represented by a cosine-squared relationship; however, the transverse displacements are underestimated using this relationship.

10. In general, the observed RMS accelerations from the wind tunnel model are large compared to the observed RMS accelerations from the on-site monitoring data, which is entirely consistent with the relatively low total damping of the wind tunnel aeroelastic model.

11. The wind speeds normalized with respect to the speed at zero wind azimuth for the 16-point compass directions of the Pier 31 – 32 anemometer show that the wind approaching from Bridge South is influenced by the bridge deck and is increased up to 10%. For the wind blowing along the bridge axis, the effect of the bridge deck reduces the speed by 20%. The Pier 20 – North anemometer is in close proximity to Pier 20 and so is significantly influenced by its presence. For the 202.5°, 225°, 315°, 337.5° azimuths, a 12% - 30% increase and for the 135 ° and 157.5 ° sectors, a 14 to 21% decrease in the wind speed is observed. The Pier 20 - South anemometer is not influenced by the pier; however, the indicated wind speeds are consistently smaller than the normalizing wind speed for almost all compass directions. Thus the proposed plots can effectively be used to correct the indicated wind speed by any of the three anemometers for a given wind azimuth.

4.13 References

American Society of Civil Engineers 1999. *Wind Tunnel Studies of Buildings and Structures,* ASCE Manuals and Reports on Engineering Practice No. 67.

Bendat, J. S., and Piersol, A. G. 2000. *Random Data Analysis and Measurement Procedures,* Third Edition, John Wiley and Sons, Inc. New York, USA.

Chopra, A. K. 2007. *Dynamics of Structures – Theory and Applications to Earthquake Engineering,* Third Edition, Pearson Prentice Hall, New Jersey, USA.

Dafoe, G. 1999. *Personal Communication,* Boundary Layer Wind Tunnel Laboratory, University of Western Ontario.

Davenport, A. G. 1967. The Application of the Boundary Layer Wind Tunnel to the Prediction of Wind Loading, *International Research Seminar: Wind Effects on Buildings and Structures,* Ottawa, Canada, pp. 201-230.

Davenport, A. G., and King, J. P. C. 1982. *A Study of Wind Effects for the Sunshine Skyway Bridge, Tampa, Florida – Concrete Alternate,* BLWT-SS24-1982, Boundary Layer Wind Tunnel Laboratory, University of Western Ontario.

Engineering Sciences Data Units, 1974. *Characteristics of Atmospheric Turbulence near the Ground, Part II: Single Point Data for Strong Winds (Neutral Atmosphere),* ESDU Report 74031, ESDU International.

Engineering Sciences Data Units, 1993a. *Strong Winds in the Atmospheric Boundary Layer, Part I: Mean Hourly Wind Speeds,* ESDU Report 82026, ESDU International.

Engineering Sciences Data Units, 1993b. *Strong Winds in the Atmospheric Boundary Layer, Part II: Discrete Gust Speeds,* ESDU Report 83045, ESDU International.

Engineering Sciences Data Units, 1993c. *Characteristics of Atmospheric Turbulence near the Ground, Part II: Single Point Data for Strong Winds (Neutral Atmosphere),* ESDU Report 85020, ESDU International.

Gomes, L., and Vickery, B. J. 1977. On the Prediction of Extreme Wind Speeds from the Parent Distribution, *Journal of Industrial Aerodynamics,* 2: 21-36.

King, J. P. C., Ho, E., and Davenport, A. G. 1988. *A Study of Wind Effects for the Helgelands Bridge, Norway – Cable-Stayed Alternate,* BLWT-SS17-1988, Boundary Layer Wind Tunnel Laboratory, University of Western Ontario.

King, J. P. C., and Davenport, A. G. 1993. The Treatment of Wind Effects for the Northumberland Strait Crossing, *Canadian Society for Civil Engineering Annual Conference,* Fredericton, New Brunswick, Canada, pp. 405-414.

King, J. P. C., Mikitiuk, M. J., Davenport, A. G., and Isyumov, N. 1994. *A Study of Wind Effects for the Northumberland Straits Crossing,* BLWT-SS8-1994, Boundary Layer Wind Tunnel Laboratory, University of Western Ontario (Parts of this report have been published in King and Davenport 1993, 1994b and King 1999).

King, J. P. C., and Davenport, A. G. 1994a. *The Estimation of Dynamic Wind Load Coefficients for the Northumberland Straits Crossing, PEI,* BLWT-IR-N62-16-1994, Boundary Layer Wind Tunnel Laboratory, University of Western Ontario (parts of the report have been published in King and Davenport 1994b and King 1999).

King, J. P. C., and Davenport, A. G. 1994b. P.E.I. Fixed Link – The Treatment of Wind Effects for the Northumberland Strait Crossing, *Fourth International Conference on Short and Medium Span Bridges,* Halifax, Nova Scotia, Canada.

King, J. P. C., and Davenport, A. G. 1994c. *A Study of Wind Effects for The Kwang Ahn Grand Bridge, Pusan, Korea,* BLWT-SS28-1994, Boundary Layer Wind Tunnel Laboratory, University of Western Ontario.

King, J. P. C., Crooks, G. J., and Davenport, A. G. 1995. *The Northumberland Straits Crossing, Prince Edward Island Testing of Marine Span Aeroelastic Model and Analysis of Dynamic Wind Loads,* BLWT-SS24-1995, Boundary Layer Wind Tunnel Laboratory, University of Western Ontario.

King, J. P. C. 1999. Integrating Wind Tunnel Tests of Full-Aeroelastic Models into the Design of Long Span Bridges, *Proceedings of the Tenth International Conference on Wind Engineering (ICWE),* Copenhagen, Denmark, pp. 927-934.

King, J. P. C. 2003. *The Aerodynamics of Long Span Bridges, PhD Thesis,* Department of Civil and Environmental Engineering, University of Western Ontario, London, Ontario, Canada.

King, J. P. C., Terres-Nicoli, J., Jeong, U., and Kong, L. 2007. *A Study of Wind Effects for the 3rd Millennium Bridge, Zaragoza, Spain,* BLWT-SS6-2007-issue 1, Boundary Layer Wind Tunnel Laboratory, University of Western Ontario.

Logan, D. L., 2001. *A First Course in the Finite Element Method Using ALGOR,* Second Edition, Brooks/Cole, CA, USA.

Montgomery, D. C., Peck, E. A., and Vining, G. G. 2001. *Introduction to Linear Regression Analysis,* Wiley Series in Probability and Mathematical Statistics, New York, USA.

Montreuil, M. A. 1999a. *Confederation Bridge Monitoring Project Slow-Speed Data Logger System,* Technical Manual, Preliminary Version, Thermal Technology Centre, National Research Council Canada.

Montreuil, M. A. 1999b. *Confederation Bridge Monitoring Project High-Speed Data Logger System,* Technical Manual, Preliminary Version, Thermal Technology Centre, National Research Council Canada.

Simiu, E., and Scanlan, R. H. 1996. *Wind Effects on Structures, Fundamentals and Applications to Design,* John Wiley and Sons, In., New York, USA.

Tanaka, H. 1992. Similitude and Modelling in Bridge Aerodynamics, *Proc. Aerodynamics of Large Bridges,* Balkema, Rotterdam.

Tedesco, J. W., McDougal, W. G., and Ross, C. A. 1998. *Structural Dynamics – Theory and Applications,* Addison Wesley, California, USA.

Table 4.1 – Comparison of Model Frequencies

Mode	Mean Aeroelastic Model Frequencies (2009) (Hz)	Range of Variability % of Mean	Mean Model Frequencies BLWTL (1995) (Hz)	Percent Difference w.r.t. 2009 Model Frequencies	Analytical ALGOR Model Frequencies (2009) (Hz)	Percent Difference w.r.t. 2009 Aeroelastic Model Frequencies
TS1	9.4	1.4	9.1	-3.2	9.7	+2.8
TA1	12.2	1.3	11.9	-2.3	12.6	+3.6
VA1	15.7	1.3	15.4	-1.7	15.8	+1.0
TS2	16.1	0.6	15.8	-1.9	16.8	+4.6
VS1	18.1	0.9	18.6	+3.0	19.3	+6.9
VS2	20.6	1.0	-	-	22.0	+6.5
TA2	29.1	1.2	-	-	29.9	+2.5
TA3	54.9	0.9	-	-	58.1	+5.8

Table 4.2 – Structural Damping Estimates

Mode	Frequency (Hz)	Damping as Ratio of Critical			
		Free Vibration Test		Autocorrelation	
		Mean	Range*	Mean	Range*
TS1	9.4	0.0013	0.0010 ~ 0.0015	0.0010	0.0005 ~ 0.0015
TA1	12.2	0.0024	0.0020 ~ 0.0025	0.0024	0.0020 ~ 0.0025
VA1	15.7	0.0021	0.0020 ~ 0.0025	0.0021	0.0015 ~ 0.0025
VS1	18.1	0.0010	0.0010 ~ 0.0010	0.0008	0.0005 ~ 0.0010

* Note: Range values reported to nearest 0.0005

Table 4.3 – Aeroelastic Scale Parameters – Non-Froude Scale

PARAMETER	SIMILITUDE REQUIREMENT	VALUE
Length*	$\lambda_L = L_m/L_p$	4.000E-03
Density	$\lambda_\rho = \rho_m/\rho_p$	1.000E+00
Velocity**	$\lambda_V = V_m/V_p$	1.106E-01
Mass per Unit Length	$\lambda_{m/L} = \lambda_\rho \lambda_L^2$	1.600E-05
Mass	$\lambda_m = \lambda_\rho \lambda_L^3$	6.400E-08
Mass Moment of Inertia per Unit Length	$\lambda_{I/L} = \lambda_m \lambda_L^2$	2.560E-10
Mass Moment of Inertia	$\lambda_I = \lambda_m \lambda_L^3$	1.024E-12
Time	$\lambda_T = T_m/T_p = \lambda_L/\lambda_V$	3.616E-02
Acceleration	$\lambda_a = a_m/a_p = \lambda_V/\lambda_T$	3.059E+00
Damping	$\lambda_\zeta = \zeta_m/\zeta_p$	1.000E+00
Elastic Stiffness	$\lambda_{EI} = \lambda_{GC} = \lambda_V^2 \lambda_L^4$	3.133E-12
	$\lambda_{EA} = \lambda_V^2 \lambda_L^2$	1.958E-07
Force per Unit Length	$\lambda_{F/L} = \lambda_V^2 \lambda_L = \lambda_L^3/\lambda_T^2$	4.895E-05
Force	$\lambda_F = F_m/F_p = \lambda_V^2 \lambda_L^2$	1.958E-07
Bending and Torsional Moment	$\lambda_{BM} = \lambda_V^2 \lambda_L^3$	7.831E-10
Warping Stiffness	$\lambda_{CwE} = \lambda_V^2 \lambda_L^6$	5.012E-17

* Length Scale = 1 : 250

** Velocity Scale = 1 : 9.04

Table 4.4 – Total Damping Estimates for the Fundamental Modes of Vibration

Mode Type	Transverse Mode				Vertical Mode		
Mode Shape	TS1	TA1	TS2	TA2	VA1	VS1	VS2
Frequency f_j (Hz)	9.4	12.2	16.1	29.1	15.7	18.1	20.6
ζ_{tm_j} (%)	0.63	0.52	0.52	0.25	0.92	0.76	0.6

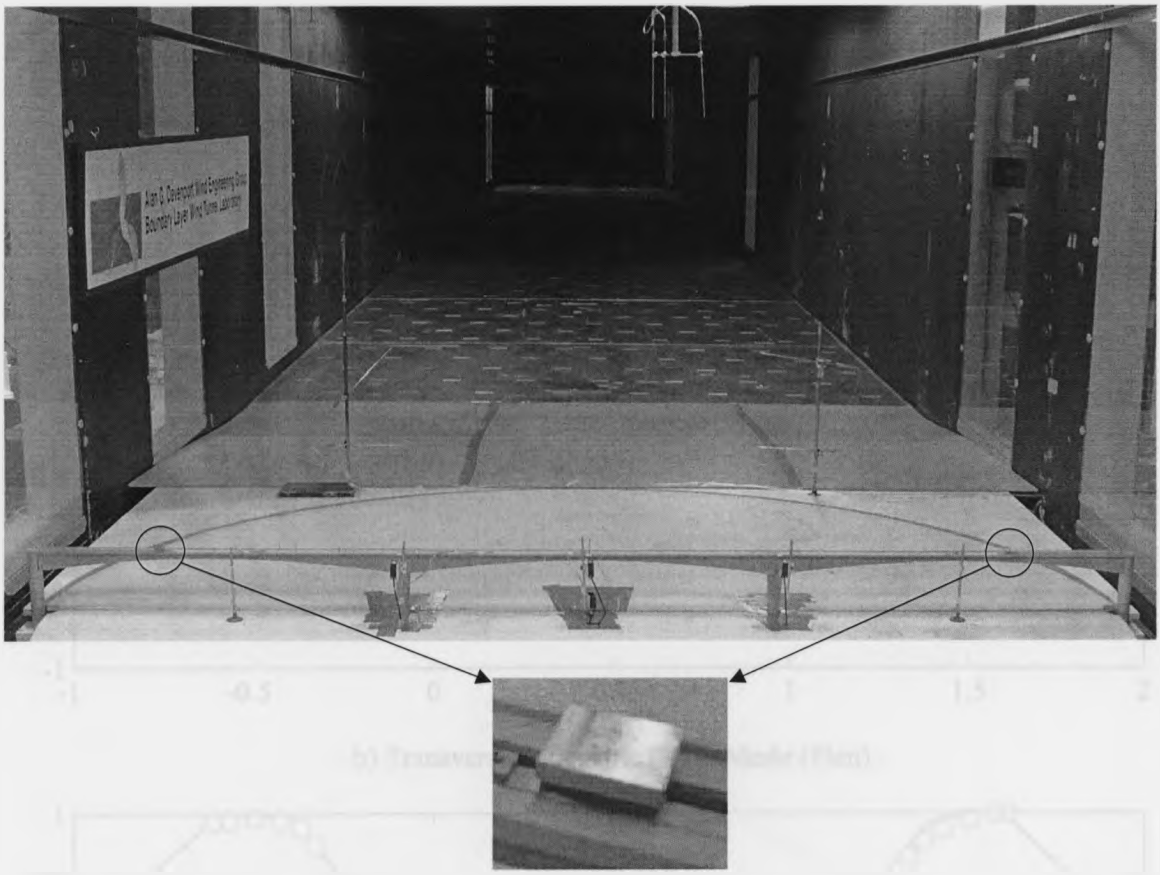

Figure 4.1 – Confederation Bridge Model with Adjusted Pier Heights and Cantilever Masses

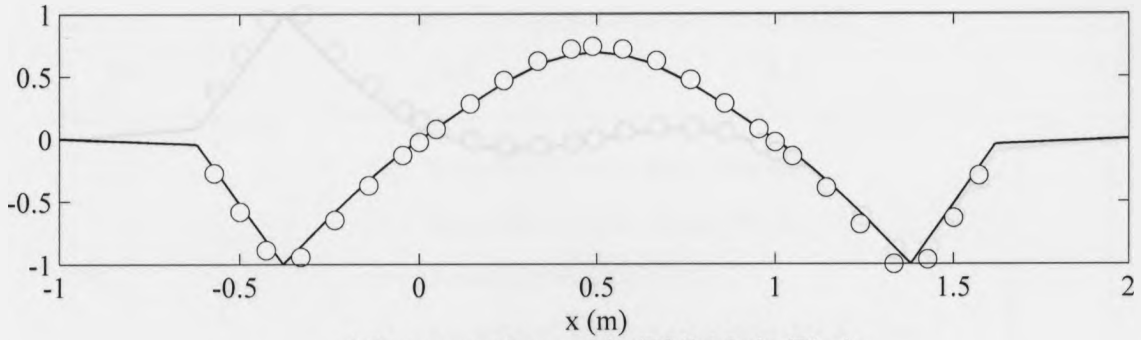

a) Transverse Symmetric (TS1) Mode (Plan)

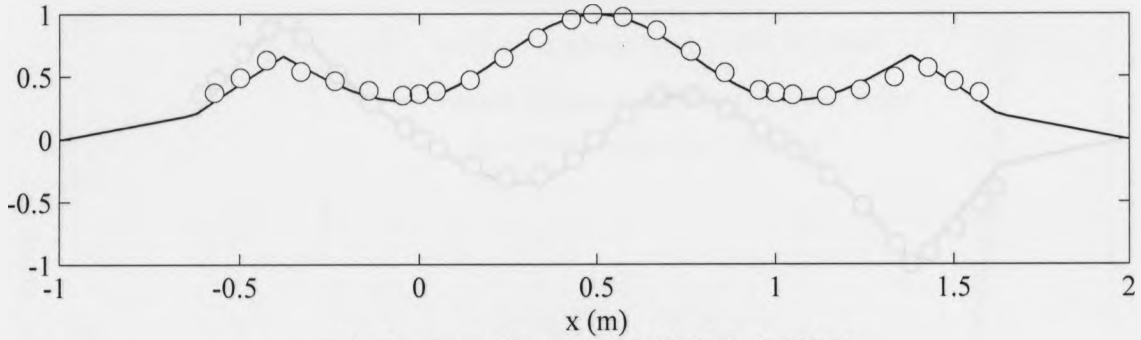

b) Transverse Symmetric (TS2) Mode (Plan)

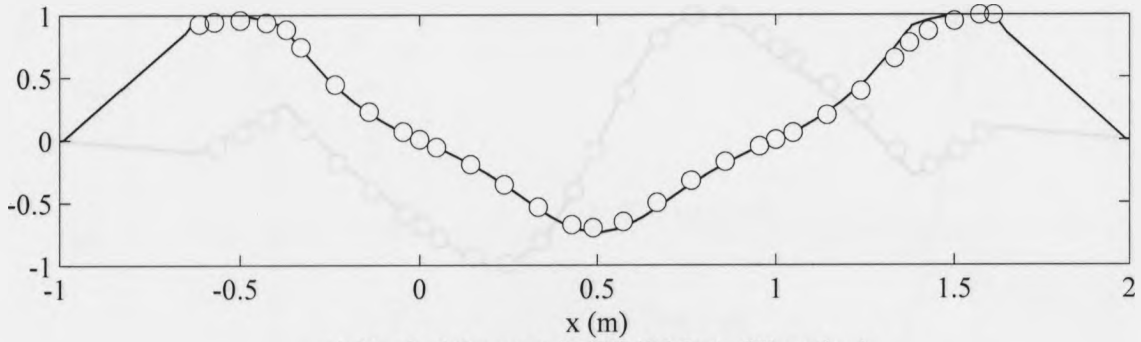

c) Vertical Symmetric (VS1) Mode (Elevation)

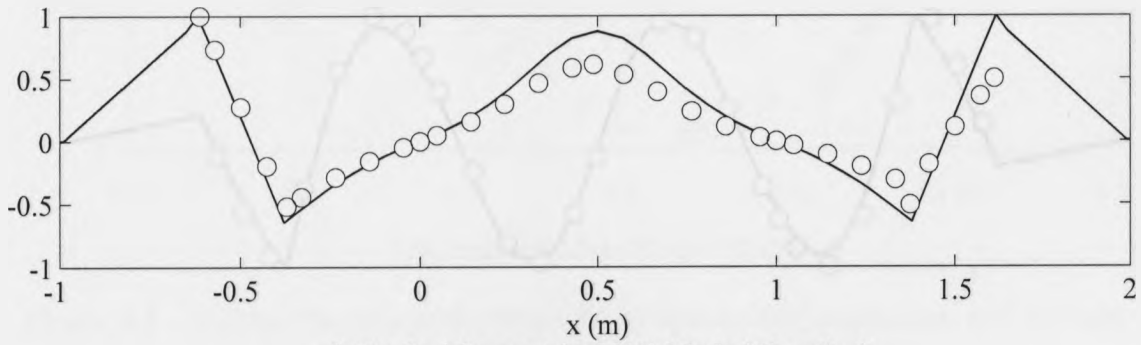

d) Vertical Symmetric (VS2) Mode (Elevation)

Figure 4.2a-d – Comparison of the Fundamental Symmetric Modes of Vibration

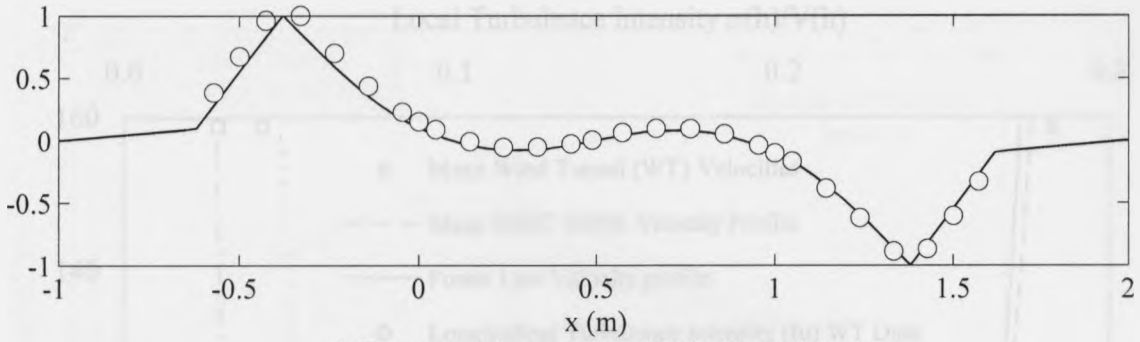

e) Transverse Asymmetric (TA1) Mode (Plan)

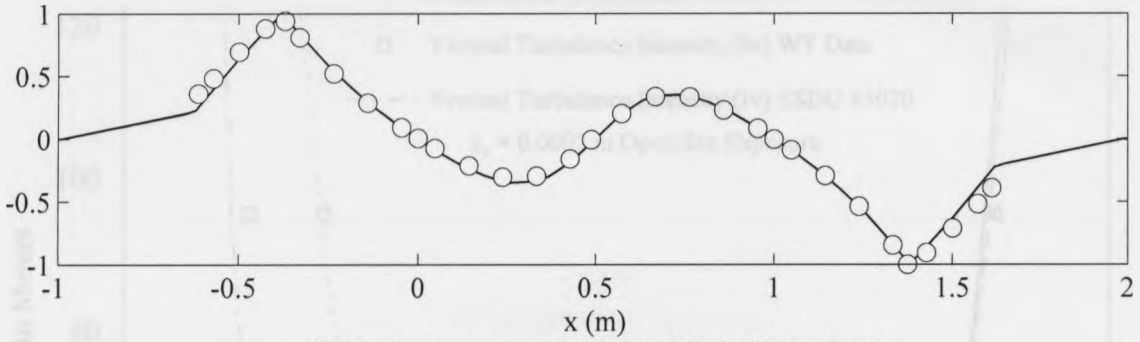

f) Vertical Asymmetric (VA1) Mode (Elevation)

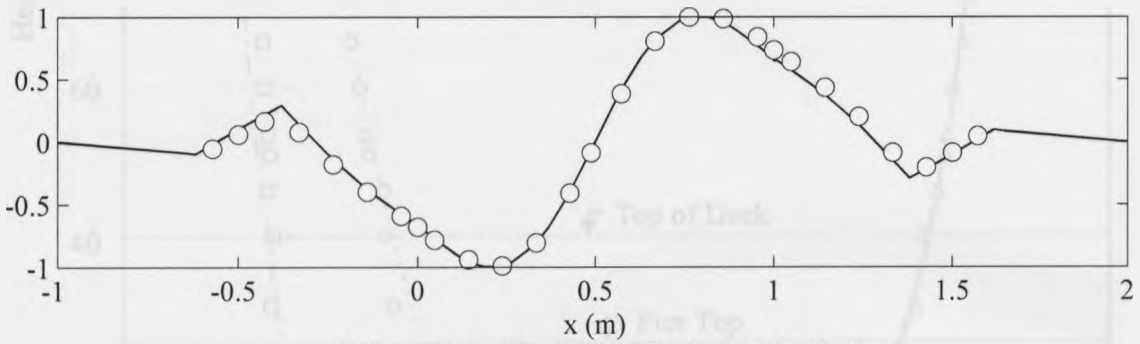

g) Transverse Asymmetric (TA2) Mode (Plan)

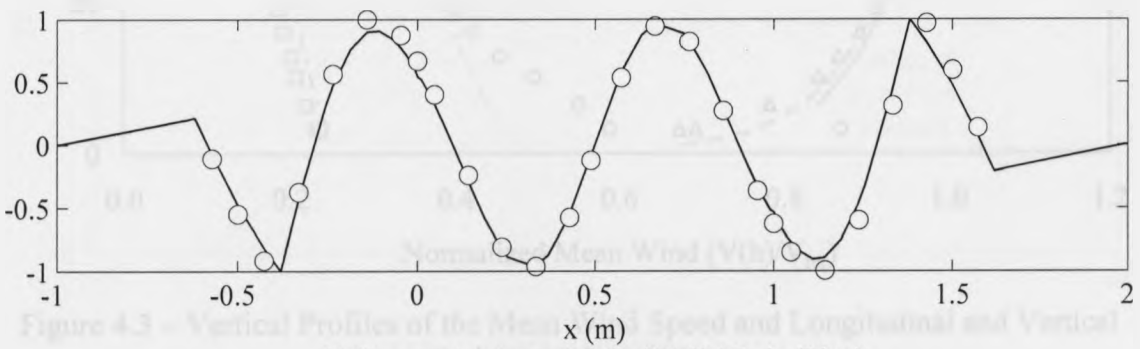

h) Transverse Asymmetric (TA3) Mode (Plan)

Figure 4.2e-h – Comparison of the Fundamental Asymmetric Modes of Vibration

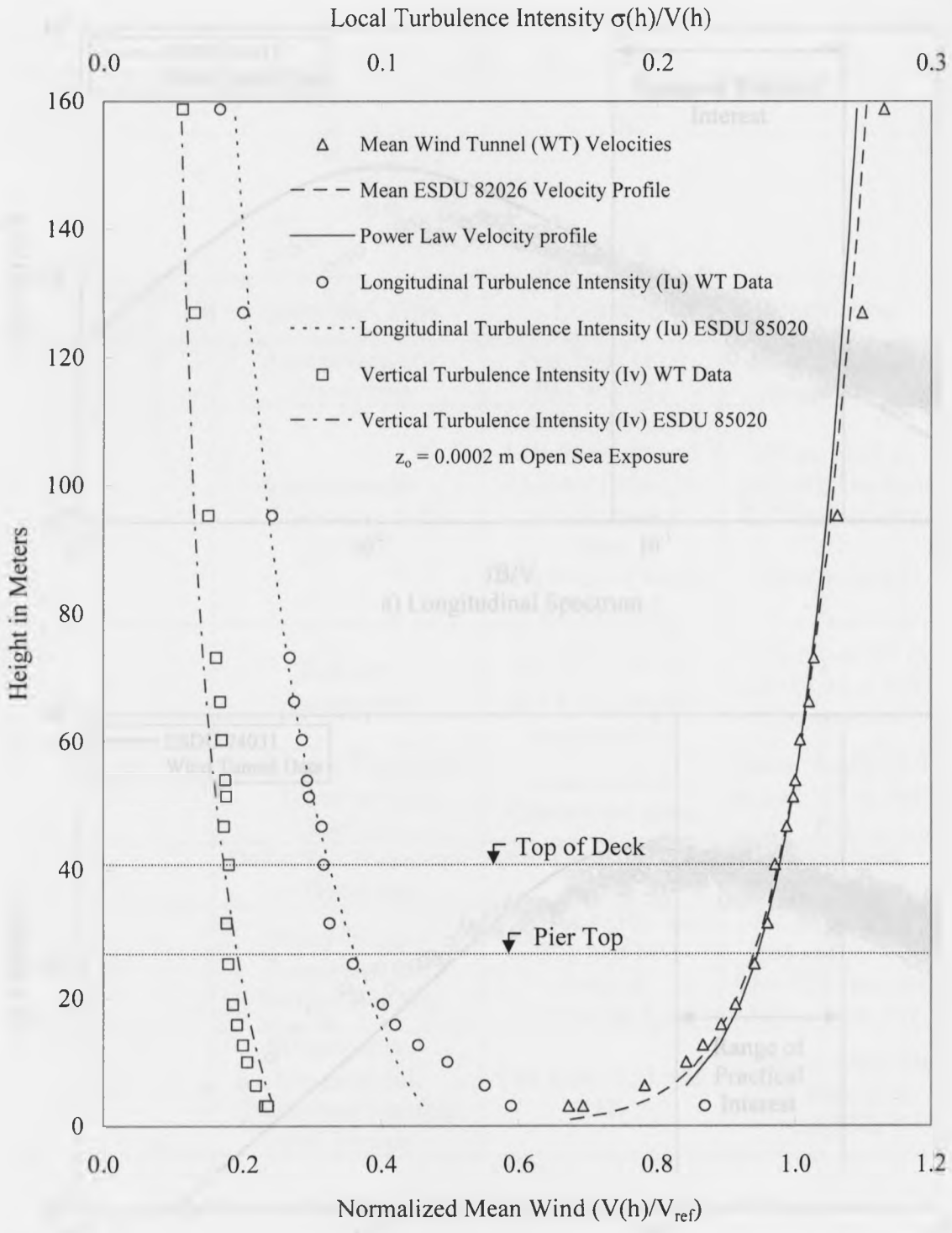

Figure 4.3 – Vertical Profiles of the Mean Wind Speed and Longitudinal and Vertical Turbulence Intensities

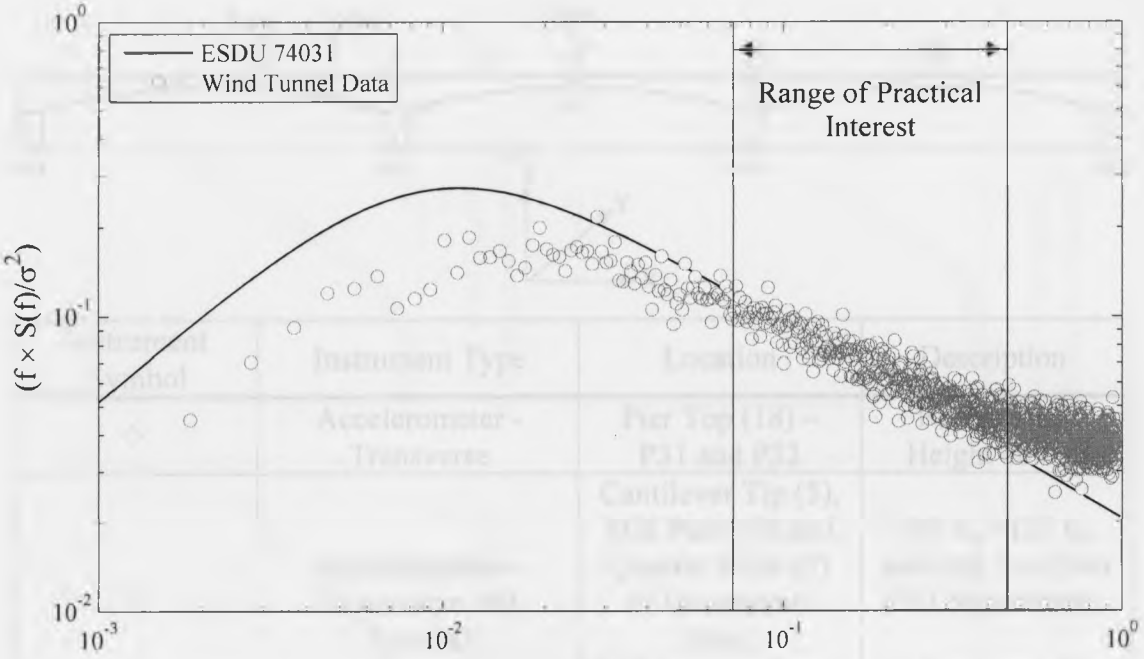

a) Longitudinal Spectrum

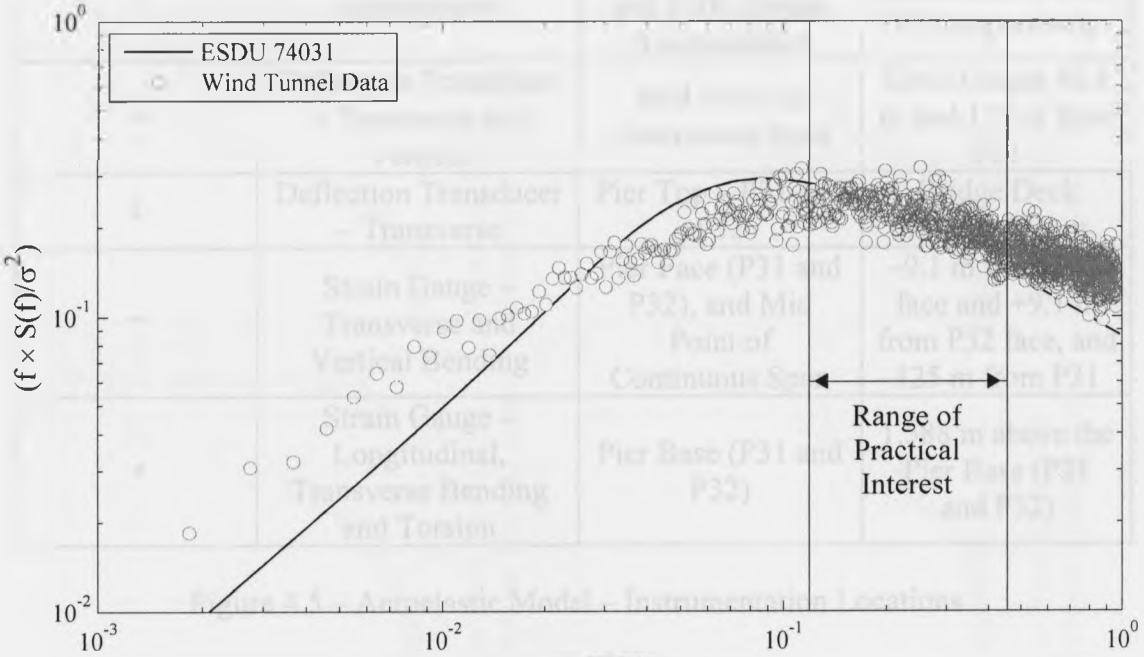

b) Vertical Spectrum

Figure 4.4 – Normalized Spectra with respect to the Variance of the Longitudinal and Vertical Components of the Wind

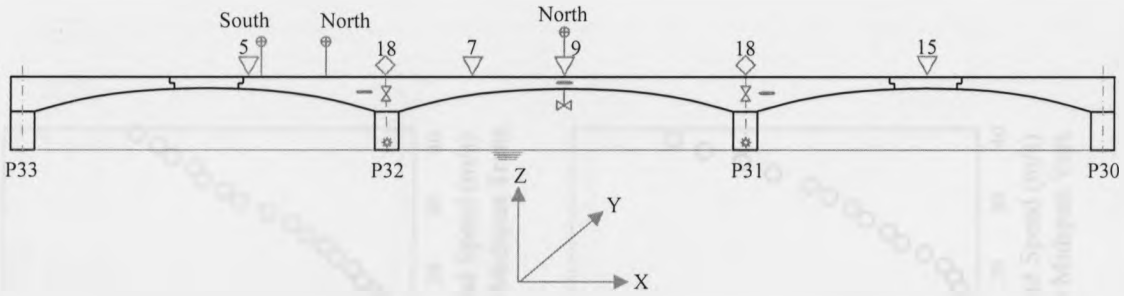

Instrument Symbol	Instrument Type	Location	Description
◇	Accelerometer - Transverse	Pier Top (18) – P31 and P32	Bridge Deck Height 40.8 m
▽	Accelerometer – Transverse and Vertical	Cantilever Tip (5), Mid Point (9) and Quarter Point (7) of Continuous Span. Mid Point of Drop-in Span (15)	-95 m, +125 m, and +62.5 m from P32 respectively. 125 m from P31
⊕	Hot-wire Anemometer	Consistent with P31-P32, P20N, and P20S Bridge Anemometers	+125 m, -41.67 m, and -83.33 m from P32 respectively
⋈	Deflection Transducer – Transverse and Vertical	Mid Point of Continuous Span	Deck Height 40.8 m and 125 m from P31
⧖	Deflection Transducer – Transverse	Pier Top – P31 and P32	Bridge Deck Height 40.8 m
–	Strain Gauge – Transverse and Vertical Bending	Pier Face (P31 and P32), and Mid Point of Continuous Span	-9.1 m from P31 face and +9.1 m from P32 face, and 125 m from P31
✡	Strain Gauge – Longitudinal, Transverse Bending and Torsion	Pier Base (P31 and P32)	1.588 m above the Pier Base (P31 and P32)

Figure 4.5 – Aeroelastic Model – Instrumentation Locations

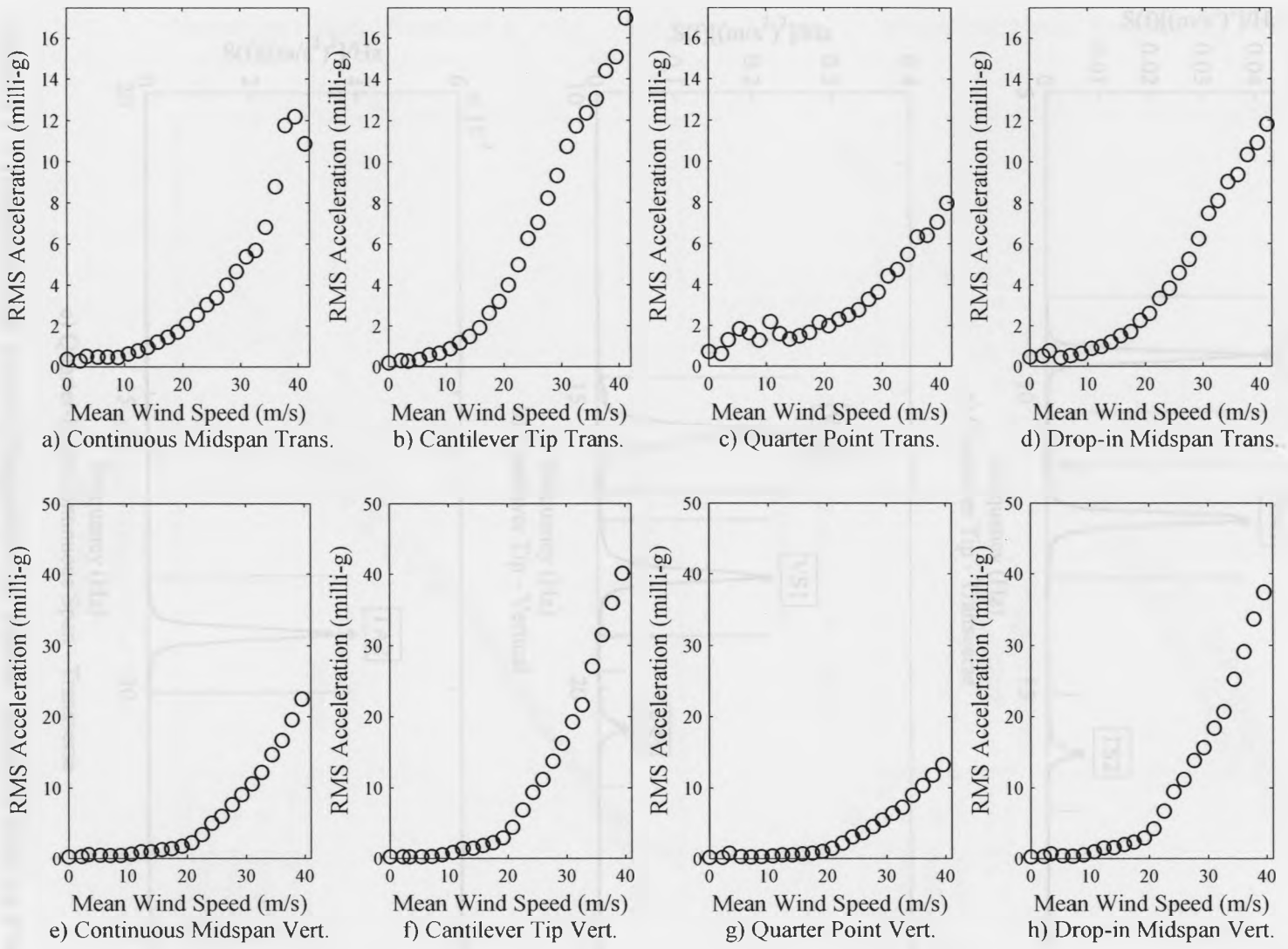

Figure 4.6 – Observed RMS Accelerations – Total Dynamic Response

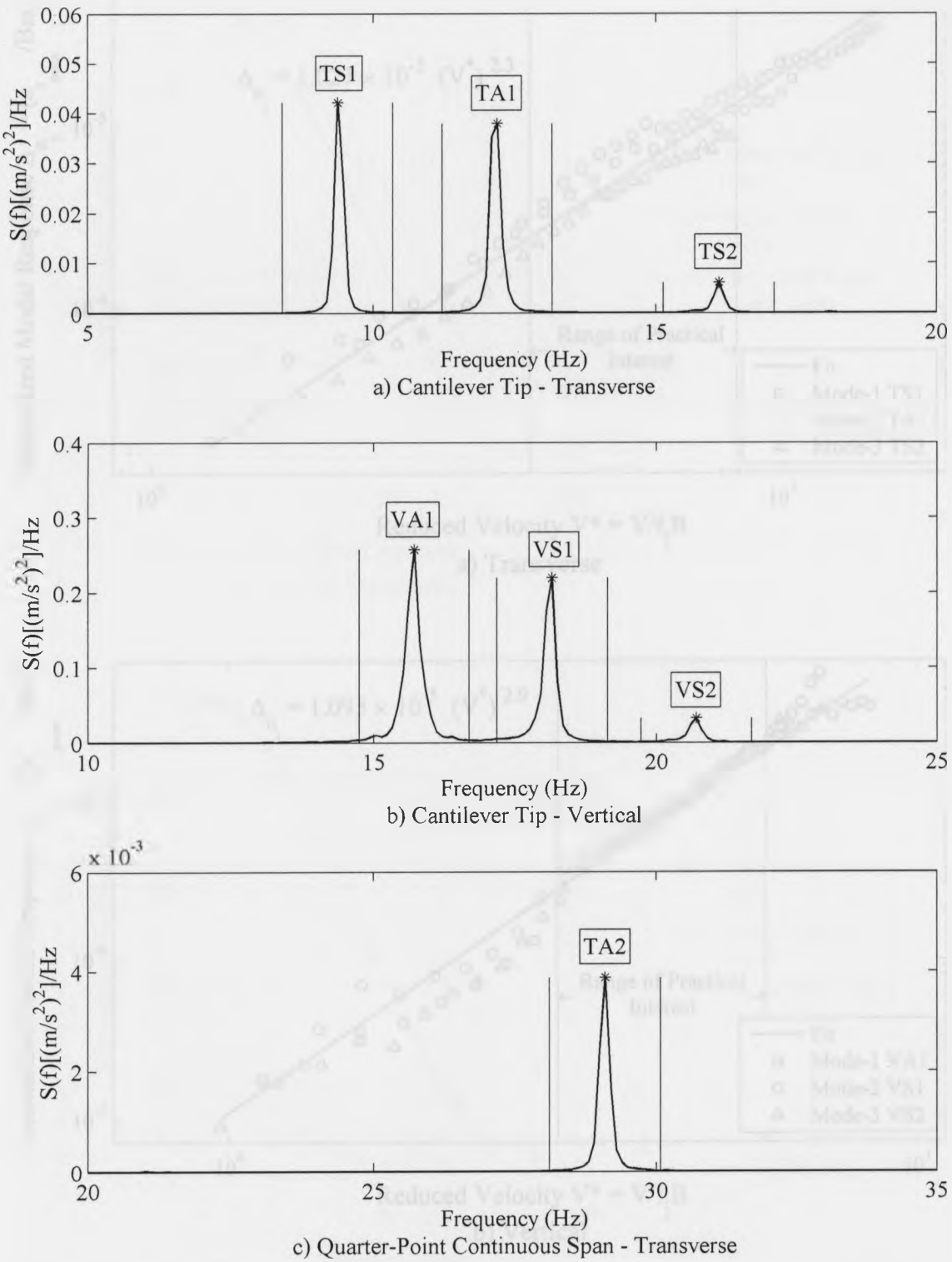

Figure 4.7 – Transverse and Vertical Frequencies of Interest Identified from the Power Spectra at the Cantilever Tip

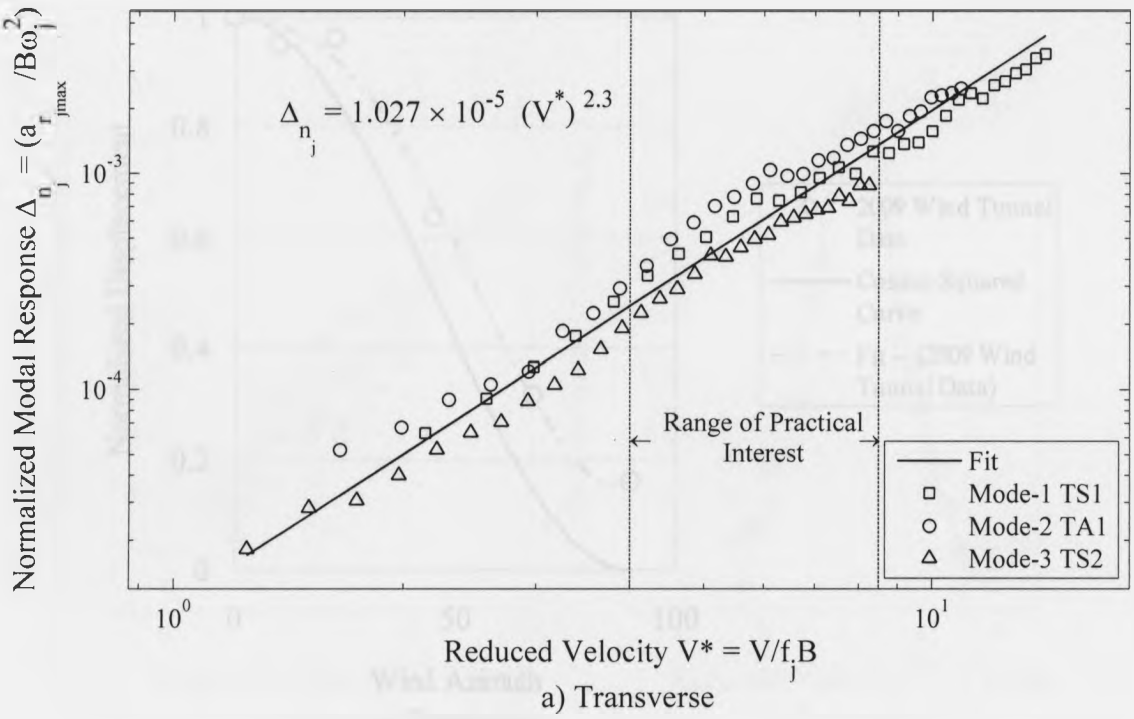

a) Transverse

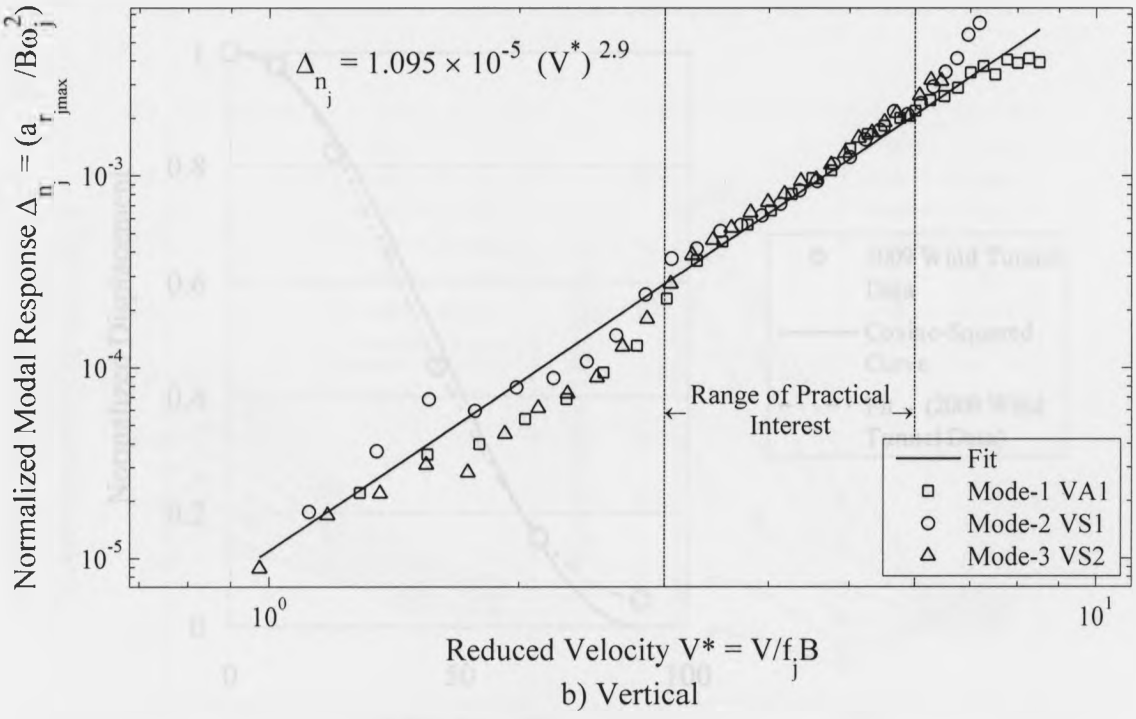

b) Vertical

Figure 4.8 – Variation of Transverse and Vertical Modal Responses

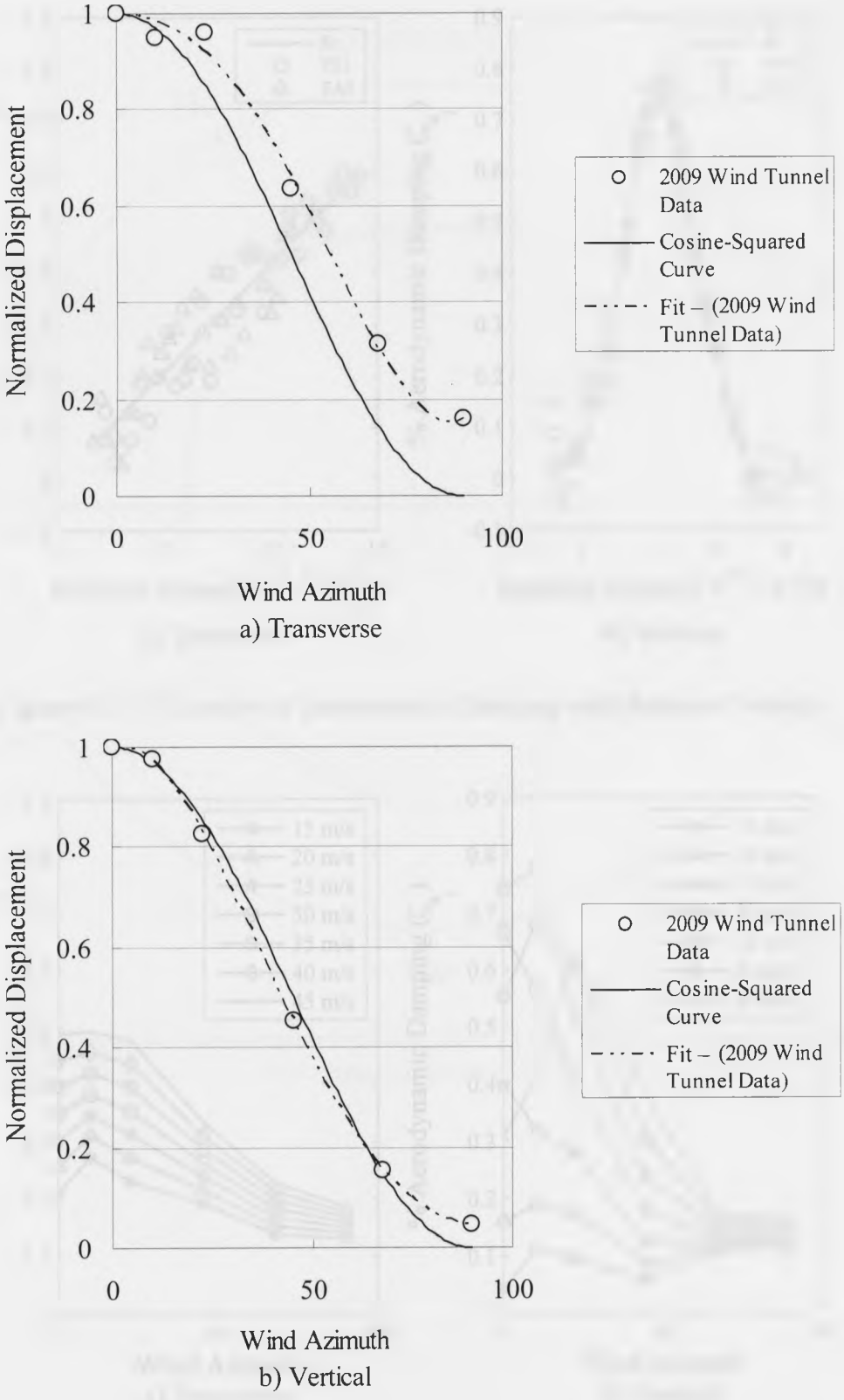

Figure 4.9 – Variation of Normalized Displacement with Wind Azimuth

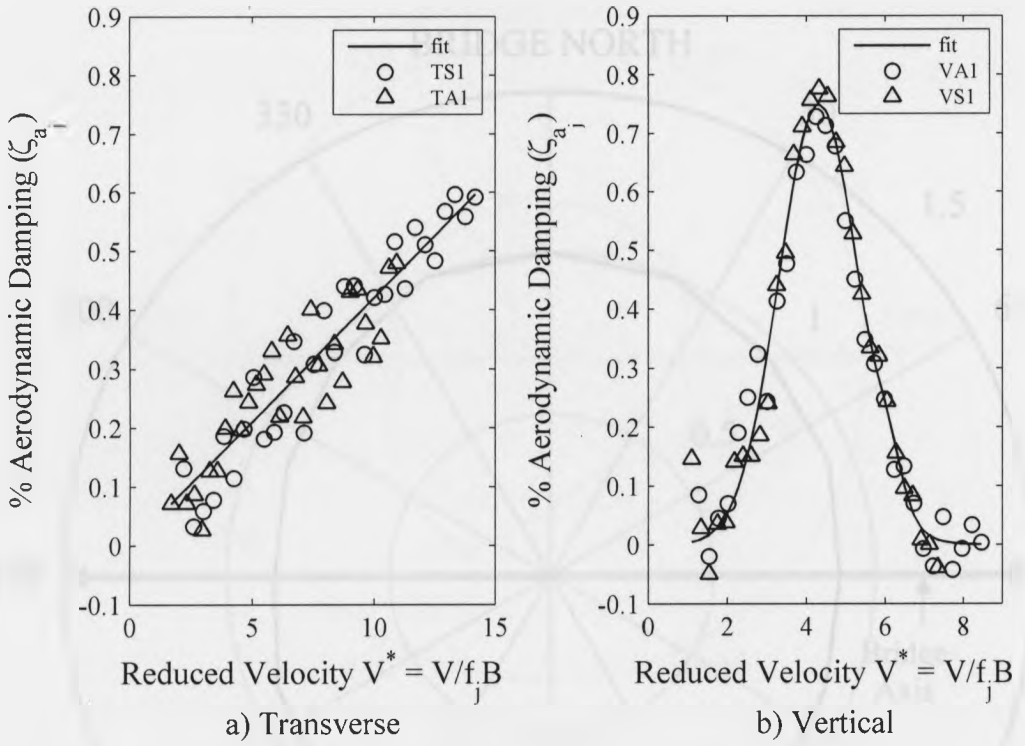

Figure 4.10 – Variation of Aerodynamic Damping with Reduced Velocity

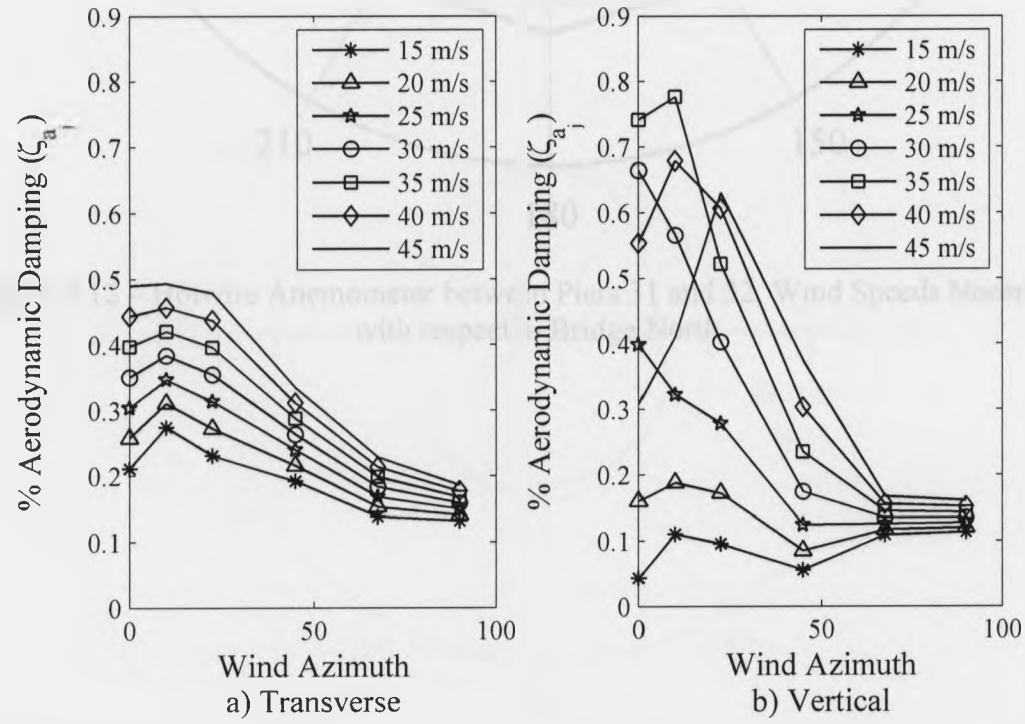

Figure 4.11 – Variation of Aerodynamic Damping with Wind Azimuth

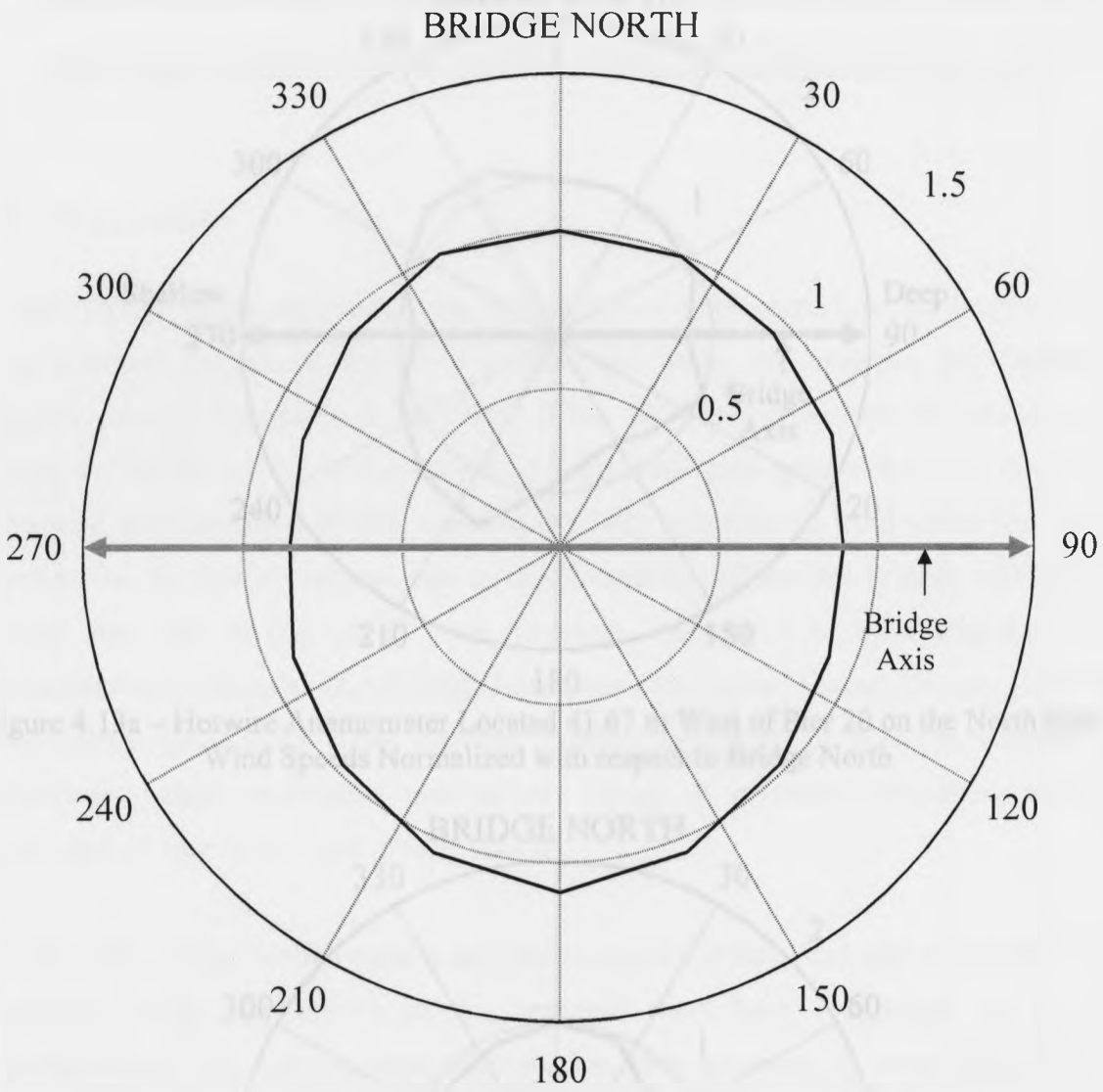

Figure 4.12 – Hotwire Anemometer between Piers 31 and 32, Wind Speeds Normalized with respect to Bridge North

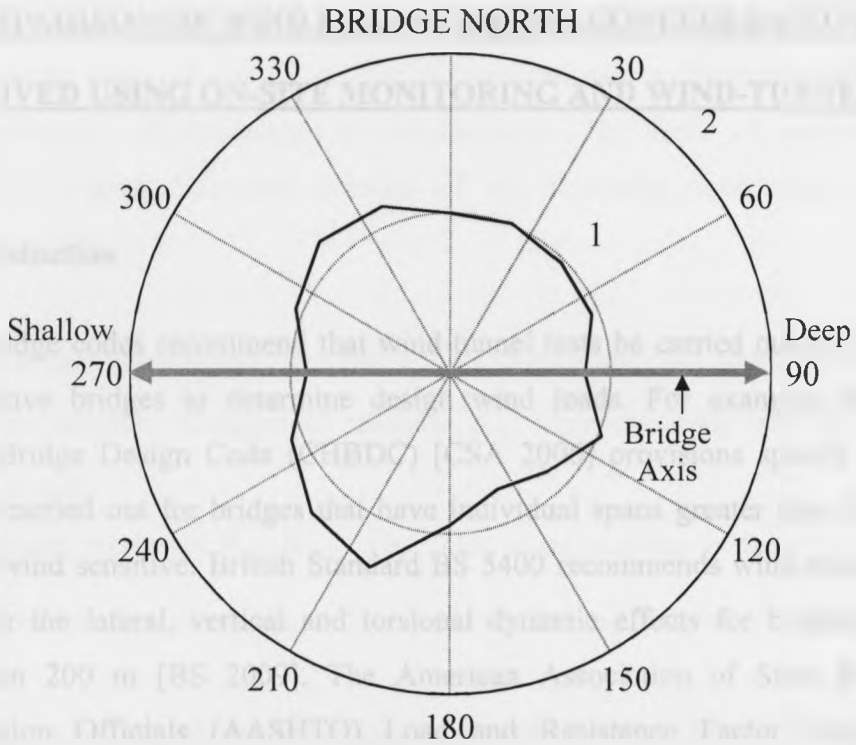

Figure 4.13a – Hotwire Anemometer Located 41.67 m West of Pier 20 on the North Side, Wind Speeds Normalized with respect to Bridge North

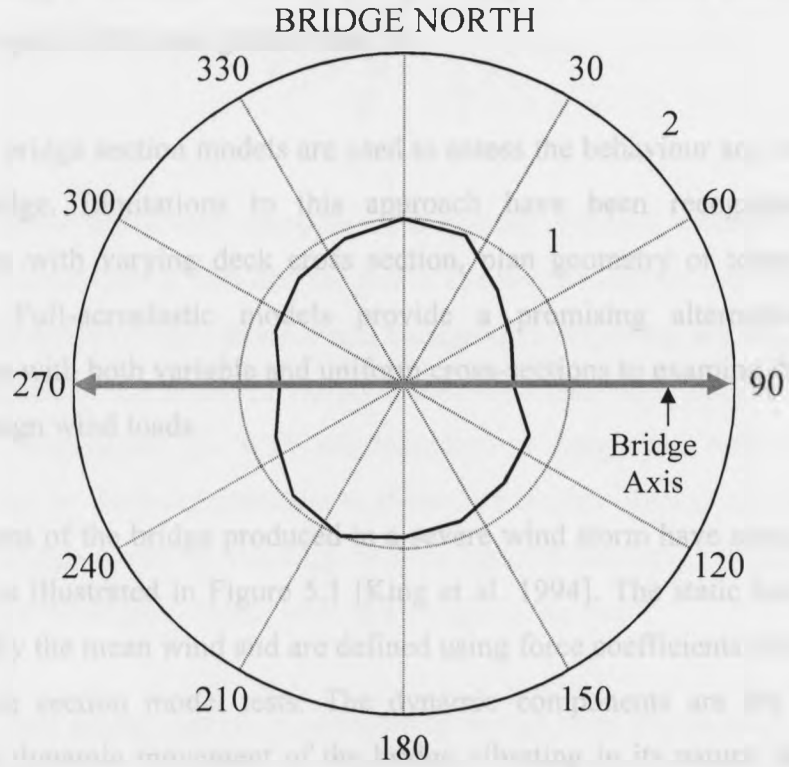

Figure 4.13b – Hotwire Anemometer Located 83.3 m West of Pier 20 on the South Side, Wind Speeds Normalized with respect to Bridge North

5. COMPARISON OF WIND LOADS FOR THE CONFEDERATION BRIDGE DERIVED USING ON-SITE MONITORING AND WIND-TUNNEL DATA

5.1 Introduction

Modern bridge codes recommend that wind tunnel tests be carried out for long-span or wind-sensitive bridges to determine design wind loads. For example, the Canadian Highway Bridge Design Code (CHBDC) [CSA 2006] provisions specify wind-tunnel testing be carried out for bridges that have individual spans greater than 125 m or are otherwise wind sensitive. British Standard BS 5400 recommends wind-tunnel testing to account for the lateral, vertical and torsional dynamic effects for bridges with spans greater than 200 m [BS 2009]. The American Association of State Highway and Transportation Officials (AASHTO) Load and Resistance Factor Design (LRFD) Specification [AASHTO 2004] requires in-depth evaluation of potential aeroelastic instabilities using wind-tunnel tests of any bridge or structural component with a span/depth or span/width ratio greater than 30.

Traditionally, bridge section models are used to assess the behaviour and wind loads of a long-span bridge. Limitations to this approach have been recognized for bridge superstructures with varying deck cross section, plan geometry or tower height [e.g., King 1999]. Full-aeroelastic models provide a promising alternative for bridge superstructures with both variable and uniform cross-sections to examine the wind effects and derive design wind loads.

The load actions of the bridge produced in a severe wind storm have static and dynamic components, as illustrated in Figure 5.1 [King et al. 1994]. The static load components are produced by the mean wind and are defined using force coefficients that are generally measured from section model tests. The dynamic components are the inertial loads caused by the dynamic movement of the bridge vibrating in its natural modes; usually only the lowest modes are significant.

The bridge response due to the combined effect of the static and dynamic wind loads can be expressed in terms of a wide variety of structural actions including forces, bending moments, stresses, displacements or accelerations. The form of such responses is illustrated in Figure 5.2a and consists of the following three main components [Davenport 1988]:

- the mean, time-average response, $\bar{R}$, due to the static load component
- a non-resonant background response, R_b, varying slowly and irregularly with time; and
- resonant responses, $R_{r_1}, R_{r_2}, \ldots R_{r_j}$, due to oscillations with varying amplitudes in natural vibration modes 1, 2, … j, also called modal dynamic effects

Combining the background and resonant responses, the total dynamic bridge response, R_{t_d}, can be expressed as:

$$R_{t_d} = \sqrt{R_b^2 + \sum_j R_{r_j}^2} \qquad [5\text{-}1]$$

Figure 5.2b shows the power spectrum of a typical response, with the logarithm of frequency on the horizontal axis and the power spectral density on the vertical axis. The relative contributions of the resonant and background responses are dependant on the natural frequencies of the modes of vibration. Resonant behaviour tends to dominate with lower natural frequencies (as with tall buildings or long span bridges) due to the increased energy in the wind spectrum at these frequencies. Background behaviour can dominate as bridge spans or building heights become shorter (hence higher natural frequencies) and therefore coincide with less energy in the wind.

The Confederation Bridge has twice experienced design wind events since it was opened to traffic in 1998. The November 7, 2001 storm, and Hurricane Noel that passed the bridge on November 4, 2007, recorded maximum ten-minute mean wind speeds of 30.5

and 33.2 m/s, respectively, at the deck height of 40.8 m as described in Chapter 2. The wind azimuth was normal to the bridge axis for the November 2001 storm and 20° to the normal for Hurricane Noel. The originally specified design wind speed of 34.1 m/s at this elevation is a ten-minute mean wind speed considering winds from all directions [King et al. 1994]. If only winds normal to the bridge axis are considered, a specified design wind speed of 30.5 m/s at the deck level was suggested [King et al. 1994]. The bridge is actually designed to resist a factored wind load that is 1.9 times the specified wind load and so corresponds to a wind speed that is 38% greater than the specified design wind speed. Nevertheless, the bridge owner Strait Crossing Bridge Limited (SCBL) has questioned whether the passage of the two wind events caused the design wind loads to be exceeded [SCBL 2008].

A methodology was developed that uses full-aeroelastic model test data to derive wind loads for the design of the Confederation Bridge [King et al. 1994]. In the present study, this methodology will be used to derive wind loads from the on-site monitoring data presented in Chapter 3. The full-scale bridge response computed from the monitoring data will be compared to the equivalent full-scale response determined by wind tunnel testing at the time of bridge design in 1994. Equivalent full-scale wind loads will also be computed using data from the 2009 wind-tunnel tests presented in Chapter 4. The bridge response derived using the 2009 wind-tunnel loads will also be compared to the responses derived using the on-site monitoring data and 1994 wind tunnel model tests to examine the appropriateness of wind loads used for the bridge design.

5.1.1 Research Objectives

The on-site monitoring data will be used for the first time to compute full-scale static and dynamic wind loads for the Confederation Bridge. The equivalent full-scale static force coefficients determined from the section model tests in 1994 will be compared to the full-scale coefficients determined from the in-place monitoring data, to validate the wind-tunnel section model test results. The dynamic load effects due to wind derived using aeroelastic wind-tunnel models, tested in 1994 and 2009, and on-site monitoring data will

be compared to investigate the sensitivity of the methodology and results obtained for the dynamic wind loads used for the design of the Confederation Bridge.

The peak bending moments used for the bridge design will be compared to the peak bending moments predicted using loads derived from the in-place monitoring data to investigate if the bridge has actually been subjected to its design moments since its completion in 1997. The variation of the bridge deflections with wind azimuth is traditionally assumed to follow a cosine-squared relationship. The normalized deflections from the on-site monitoring data and the 2009 wind tunnel test results will be compared to the cosine-squared relationship to investigate if the relationship stands valid.

The Hurricane Noel dataset analysed in Chapter 3 will also be used to compute the dynamic wind loads. The resulting load effects will be compared to the predictions made using the 2009 wind tunnel test results, in Appendix 5B, to investigate the severity of the wind event.

5.1.2 Chapter Organization

The flow diagram in Figure 5.3 gives an overview of the methodology for computing wind loads using data from the on-site monitoring and 2009 wind tunnel investigations. The on-site monitoring data from Chapter 3 yield both static and dynamic bridge responses, whereas the 2009 wind-tunnel study presented in Chapter 4 primarily yields the dynamic response. The static bridge response is indicated by the mean transverse pier tilt which is a function of the mean horizontal wind velocity. The total dynamic bridge response is expressed as the accelerations at various points of the superstructure and is quantified from the observed background and resonant accelerations. The static response reported in Chapter 3 will be used to compute static force coefficients that will be compared to the original static force coefficients used for the bridge design [JMI-Stanley 1995]. The modal response of the wind tunnel model, presented in Chapter 4, will be used to estimate dynamic wind loads appropriate for the as-tested model damping. The computed loads will be adjusted to reflect actual damping of the prototype bridge and

then will be used to predict total dynamic response for comparison with the observed response presented in Chapter 3.

The total dynamic response will also be predicted using the 1994 dynamic wind loads used for the bridge design [King et al. 1994, JMI-Stanley 1995]. Comparison between the full-scale observed response and the equivalent full-scale responses predicted using 1994 and 2009 wind tunnel loads will determine the suitability of wind loads used for the design of the Confederation Bridge.

The wind loads derived from the on-site monitoring data and the 2009 and 1994 wind tunnel tests will also be used to predict RMS bending moments at the midspan and pier face cross-sections for the Confederation Bridge. Comparison between the RMS bending moments predicted using wind loads based on in-place monitoring data and the 2009 and 1994 wind tunnel tests will further investigate the suitability of the original design wind loads.

Finally, peak bending moments using the static and dynamic wind loads will be computed and compared to the peak design bending moments at the midspan and pier faces to investigate the severity of wind loading experienced since its completion in 1997.

5.2 Wind Loads from the On-Site Monitoring Data

5.2.1 Overall Methodology

The analyses of the measured static and dynamic bridge responses have been presented in Chapter 3. A parabolic fit to the tiltmeter data will be used to determine the static wind loads in Section 5.2.2. Regression analyses of the modal responses will be used to derive the dynamic wind loads adopting the methodology presented in Section 5.2.3. The observed dynamic bridge responses at critical locations, presented as statistical summaries of the observed accelerometer data, will be compared to the responses predicted using the derived loads to check the latter for computing error in Appendix 5A.

5.2.2 Static Wind Loads

The horizontal winds applied to the superstructure and pier shafts of the Confederation Bridge cause the tops of the piers to deflect laterally, which is measured by tiltmeters attached to the pier shafts at water level [Brown 2007]. The measured mean tilts are due to the mean wind load acting over a 250 m length of bridge, including a single pier. Bruce and Croasdale [2001] developed the following empirical relationship between the tilt recorded at the Pier 31 tiltmeters and the wind speed measured at an anemometer located on the bridge deck close to Pier 31:

$$\overline{T} = k\overline{V}^2 \qquad [5\text{-}2]$$

where:

- $\overline{T}$ is the mean pier tilt at water level in μRad
- k is an empirically derived calibration factor that represents the drag coefficients, geometric properties and stiffnesses of the bridge superstructure, and
- $\overline{V}$ is the ten-minute mean wind velocity in m/s of the transverse component of the wind at the anemometer height

The methodology to compute static drag coefficients using Bruce and Croasdale's [2001] tiltmeter data is as follows:

i) Equation [5-2] is normalized using the reference wind velocity pressure, q, where

$$q = \frac{1}{2}\rho\overline{V}^2 \qquad [5\text{-}3]$$

and ρ is the air density. Using Equation [5-3] to eliminate the velocity term from Equation [5-2], the normalized mean pier tilt can be expressed as

$$\frac{\bar{T}}{q} = \frac{2k}{\rho} \qquad [5\text{-}4]$$

For $k = 0.25$ $(\mu Rad - sec^2/m^2)$ [Bruce and Croasdale 2001] and $\rho = 1.25$ $(kg\text{-}m^{-3})$, the normalized mean pier tilt is

$$\frac{\bar{T}}{q} = 0.4 \ \mu Rad/Pa \qquad [5\text{-}4a]$$

ii) It is assumed that the relative magnitude of the drag coefficient for different depths of the superstructure is accurately represented by the 1994 section model tests. Normalized values of the static drag coefficients, that vary with the depth of the superstructure, are determined by regression analysis of data corresponding to the four discrete depths investigated in the 1994 wind tunnel study. The fit has the form:

$$C'_d = a\,D^b + c \qquad [5\text{-}5]$$

where:

- C'_d is the drag coefficient normalized with respect to the static drag coefficient, C_d, at midspan
- D is the concrete box girder depth in m, and
- a, b, and c are parameters estimated by regression analysis

Experimentally determined drag coefficients are available for the girder section at midspan, the quarter point, the cantilever tip and pier face. Regression analysis yields

$$C'_d = 0.138D^{1.23} + 0.123 \qquad [5\text{-}5a]$$

The fit, shown in Figure 5.4, is excellent. Using Equation [5-5a], the normalized drag coefficients for the continuous span and two cantilevers, including two half drop-in spans, were then determined as shown in Figure 5.5. The normalized drag coefficient has a maximum value of 3.62 at the piers and reduces to 1.0 at midspan.

iii) For each node of the numerical model, the normalized static force, F'_d, is calculated as

$$F'_d = C'_d \, q' \, B \qquad [5\text{-}6]$$

where:

- q' is a unit wind pressure of 1 Pa, and
- B is the width of the bridge deck (or pier) in metres.

Using Equation [5-6], each node of the ALGOR bridge model, described in Appendix 3A, was loaded with the normalized static force, F'_d, that varied along the bridge length in proportion to the normalized drag coefficients shown in Figure 5.5.

iv) ALGOR analysis was carried out and the normalized mean pier tilt at the water level was determined to be

$$\frac{\overline{T}'}{C'_d q'} = 0.69 \ \mu\text{Rad/Pa} \qquad [5\text{-}7]$$

v) Using Equations [5-4] and [5-7] the effective drag coefficient at midspan can be determined as

$$C_d = \frac{\overline{T}}{q} \Big/ \frac{\overline{T}'}{C'_d q'} \qquad [5\text{-}8]$$

From Equations [5-4a] and [5-7], Equation [5-8] yields $C_d = 0.58$.

This drag coefficient value is compared to the static drag coefficient used for design in Table 5.1. The drag coefficients from the 1994 wind-tunnel investigation used to design the bridge are within 1% of those determined using the on-site monitoring data.

5.2.3 Dynamic Wind Loads

The dynamic wind load contribution due to oscillation in the j^{th} natural mode in the loading model originally proposed by King and et al. [1994] can be expressed as

$$W_{dyn_j}(x) = \pm q_{ref}\, C_e\, B\, C_{dyn_j}\, a_j(x) \qquad [5\text{-}9]$$

where:

- $W_{dyn_j}(x)$ is the j^{th} mode dynamic wind load, with units force/length, that varies with location along the span, x, according to the shape of mode j for a given wind speed as shown in Figure 5.1
- q_{ref} is the reference velocity pressure at 10 metres elevation
- C_e is the exposure coefficient
- B is the width of the bridge
- C_{dyn_j} is the j^{th} mode dynamic load coefficient and is quantified using wind tunnel measurements
- $a_j(x)$ is the modal load distribution function for mode j, which simply is the mode shape scaled to have a maximum displacement of 1.0

Equation [5-9] can be expressed to conform to the methodology used in the present study to derive the dynamic wind loads as

$$W_{dyn_j}(x) = \pm L_j a_j(x) \qquad [5\text{-}10]$$

where L_j is the "maximum modal load", i.e. the magnitude of the maximum dynamic wind load, with units force/length, in mode j for a given wind speed. Comparing Equations [5-9] and [5-10]

$$L_j = \pm q_{ref} C_e B C_{dyn_j} \qquad [5\text{-}11]$$

Figure 5.6 shows a power spectrum derived from data recorded by accelerometer at a critical bridge location that capture the dynamic movements of the bridge. The mean square resonant responses of the first and second vertical symmetric modes of vibration (i.e., VS1 and VS2) are shown as R_{r1}^2 and R_{r2}^2 respectively. Together they provide (46.5 + 50.5 =) 97% of the total dynamic response, so the non-resonant background response provides only 3%. Investigation of the acceleration power spectra at different bridge locations has shown that the fundamental modes of vibration contain more than 95% of the energy and the contribution of non-resonant background response is less than 5%. Given this absence of non-resonant background response, $R_b^2 \cong 0$, Equation [5-1] for the total dynamic response simplifies to

$$R_{t_d} \cong \sqrt{\sum_j R_{r_j}^2} \qquad [5\text{-}12]$$

Thus the total and modal responses determined from the power spectra in Chapter 3 can be used to compute the equivalent dynamic wind loads. Table 5.2 summarizes results of the on-site monitoring data analysis from Chapter 3 used to compute maximum modal loads, L_j, for the design wind speed of 30.5 m/s approaching from the bridge north. The chosen wind speed is also the maximum observed wind speed normal to the bridge axis

during the November 2001 wind storm. The regression parameters β and α characterize the normalized modal response, Δ_{n_j}, as a function of the reduced velocity, V^* (= V/f_jB), as

$$\Delta_{n_j} = \beta\left(V_j^*\right)^{\alpha} \qquad [5\text{-}13]$$

Four transverse and three vertical frequencies are identified from the power spectra in Chapter 3 that correspond to the fundamental modes of vibration. Using Equation [5-13], for each frequency in Table 5.2, the normalized modal response is determined and used to obtain the maximum modal displacement, $\Delta_{j_{max}}$, in (m) as

$$\Delta_{j_{max}} = \Delta_{n_j} B \qquad [5\text{-}14]$$

where B is the width of the bridge. Figure 5.7 shows the modal load distribution functions, $a_j(x)$, (i.e. normalized mode shapes) obtained using the ALGOR numerical model, each of which corresponds to one of the significant modes of vibration observed in the prototype responses. The ALGOR static analysis for each load case yields a set of modal displacement coefficients, $I_j(x)$, defined as the displacement at deck location x, due to the application of the unit modal load distribution functions. These coefficients are compared to determine the absolute maximum modal displacement as

$$I_{j_{max}} = \max\{\text{abs}[I(x)]\} \qquad [5\text{-}15]$$

where $I_{j_{max}}$ is the maximum modal displacement coefficient for mode j due to the unit maximum modal load. It has units [length]/[force/length]. Using Equations [5-14] and [5-15], the ratio of the maximum modal displacement for a given wind velocity to the maximum modal displacement coefficient gives the maximum modal load, L_j:

$$L_j = \frac{\Delta_{j_{max}}}{I_{j_{max}}} \qquad [5\text{-}16]$$

The resulting maximum modal loads are shown in Table 5.2 for four horizontal and three vertical modal load distributions.

As a final step, the computed maximum modal loads need to be checked for computational error. Accordingly, the maximum modal loads were used to determine the modal response at critical bridge locations. The responses were summed as root sum of squares using Equation [5-12]. The observed and predicted bridge responses at critical bridge locations agreed closely, indicating the calculations are internally consistent. Details of this check are presented in Appendix 5A.

5.3 Wind Loads from Model-Scale Bridge Data

Following the procedure described in Section 5.2.3, the dynamic wind loads are computed using 2009 wind tunnel test data for a mean full-scale wind speed of 30.5 m/s normal to the bridge axis. The salient quantities are summarized in Table 5.3. The variables β and α have been described in the previous section and are determined from the wind tunnel data analysis presented in Chapter 4. These are used to determine maximum modal displacements, $\Delta_{j_{max}}$, for the seven identified modes of vibration. Figure 5.8 shows modal load distribution functions, $a_j(x)$, derived from the ALGOR model, used to determine maximum modal displacement coefficients, $I_{j_{max}}$. Using Equation [5-16], the maximum modal loads, L_j, are computed, which are appropriate for the as-tested model damping.

Davenport [1981] has shown that the resonant response is inversely proportional to the square root of total damping, which is the sum of structural and aerodynamic damping. The structural damping is constant for each mode; however, aerodynamic damping varies with reduced velocity. For simplicity, a representative value of reduced velocity

corresponding to wind speed of 30.5 m/s is chosen to apply a damping correction to the maximum modal loads. Thus, the maximum modal loads that would be expected given the actual prototype damping, L_{cj}, can be expressed as

$$L_{cj} = L_j \frac{\sqrt{\zeta_{m_j} + \zeta_{am_j}}}{\sqrt{\zeta_{p_j} + \zeta_{ap_j}}} \qquad [5\text{-}17]$$

where:

- ζ_{am_j} is the j^{th} mode aerodynamic damping for the model at wind speed 30.5 m/s
- ζ_{ap_j} is the j^{th} mode aerodynamic damping for the prototype at the same wind speed
- ζ_{m_j} is the j^{th} mode structural damping for the model
- ζ_{p_j} is the j^{th} mode structural damping for the prototype

Equation [5-17] can be further simplified as

$$L_{cj} = L_j \frac{\sqrt{\zeta_{tm_j}}}{\sqrt{\zeta_{tp_j}}} \qquad [5\text{-}18]$$

where:

- ζ_{tm_j} is the j^{th} mode total damping for the model
- ζ_{tp_j} is the j^{th} mode total damping for the prototype

The model and prototype damping (ζ_{tm_j} and ζ_{tp_j}) estimates are shown in Table 5.3, which represents the total damping, and have previously been determined in Chapters 4 and 3 respectively. Using Equation [5-18], damping correction is applied to each

maximum modal load and the resulting values are tabulated. These loads will be used to predict equivalent full-scale bridge response and be compared to the responses predicted using loads derived from the on-site monitoring data and the 1994 wind tunnel test results in the next section.

5.4 Comparison

The full-scale observed RMS accelerations will be compared to the equivalent full-scale RMS accelerations predicted using 2009 and 1994 wind tunnel loads. Bending moments are critical for the bridge design, therefore, RMS and peak bending moments predicted using loads derived from the on-site monitoring data and the wind tunnel tests will also be compared. The variation of the normalized displacements with wind azimuth for the prototype and wind tunnel model has been discussed in Chapters 3 and 4 respectively. These will be compared in Section 5.4.2.

5.4.1 RMS Accelerations

Figure 5.9 compares RMS accelerations observed in the prototype to those predicted from the wind tunnel based loadings. The open circles are the RMS accelerations derived from the on-site monitoring data. Large RMS accelerations at low wind speeds are either due to traffic on the bridge or electrical noise. The solid lines are the RMS accelerations predicted using loads derived from the on-site monitoring data in Section 5.2. The broken lines with markers (+) are the equivalent RMS accelerations predicted using loads derived from the 2009 wind-tunnel test results in Section 5.3. Both the solid and broken lines are in excellent agreement at all bridge locations. For the vertical RMS accelerations, the two curves are indistinguishable. The damping estimates for the prototype, available from the on-site monitoring data, play a crucial role in better predicting the equivalent RMS accelerations. Good agreement suggests the proposed methodology can be used to compute wind loads using on-site monitoring or wind-tunnel data.

The asterisks are the RMS accelerations predicted using the original 1994 wind tunnel loads, assuming the damping of the bridge to be 0.63% of critical, used for the bridge design. The solid squares are the RMS accelerations predicted using 1994 design loads adjusted to the prototype damping ranging from 1.5% to 3.9% of critical shown in Table 5.3. The solid squares are in close agreement with the observed values and the 2009 wind tunnel predictions for the transverse RMS accelerations. The vertical RMS accelerations predicted using the 1994 design loads, shown as solid squares, are conservative with respect to the observed values and the 2009 wind tunnel predictions particularly for the two midspans and cantilever locations.

The full-aeroelastic model tested in 1994 had a viscous damper attached at the midpoint of the continuous span that was intended to ensure the damping was 0.63% of critical. Therefore, no damping adjustment was made for the vertical symmetric mode (VS1). All other modal loads were adjusted to 0.63% damping [King et al. 1994] using methodology similar to that presented in Section 5.2, however, ignoring aerodynamic damping. Due to non-linear behaviour of the viscous damper, it is believed that the damper was not effective for full-scale wind speeds less than 32 m/s. The range of observed wind speeds, shown by the open circles in Figure 5.9, is between 0 and 31 m/s. For this range, the effect of the liquid damper is believed to be negligible and so the structural damping for mode VS1 is only 0.15% of critical [King et al. 1994]. Using Equation [5-18], a damping correction was applied to the VS1 modal load and the corresponding vertical RMS accelerations are shown as inverted solid triangles in Figure 5.9. These points lie above the observed and 2009 wind tunnel vertical RMS accelerations, indicating the predicted loads are still conservative, but markedly less conservative.

5.4.2 Bending Moments

5.4.2.1 RMS Bending Moments

To make a credible comparison of the loads derived from the in-place monitoring data, and the 2009 and 1994 wind tunnel test data, these loads were used to predict RMS bending moments at midspan and pier faces for the prototype.

Figure 5.10 compares RMS bending moments at the midspan and pier faces, in the transverse and vertical directions, predicted using four different sets of dynamic wind loads. The solid lines are the RMS moments predicted using loads determined in Section 5.2 from the on-site monitoring data. The broken lines with markers are the RMS moments predicted using 2009 wind tunnel loads determined in Section 5.3. The asterisks are the RMS moments based on the 1994 wind tunnel loads adjusted to 0.63% damping used for the bridge design. The inverted triangles are the RMS moments predicted using 1994 design loads corrected to the prototype damping ranging from 1.5% to 3.9% of critical shown in Table 5.3. For the damping correction, the 1994 design loads were considered to have 0.63% damping except for mode VS1, which was assumed to have 0.15% damping for wind speeds less than 32 m/s as described in the discussion of Figure 5.9.

The transverse RMS moments predicted using loads derived from the on-site monitoring data and the 2009 wind tunnel model test results agree very well as shown in Figures 5.10a, b and c. The agreement for the vertical RMS moments, Figures 5.10d, e and f is excellent: the curves lie on top of each other. The asterisks indicate that the vertical RMS moments predicted using the 1994 design loads are conservative with respect to the loads derived from the on-site monitoring data and the 2009 wind tunnel test results, whereas the transverse RMS moments agree more closely. The inverted triangles indicate that the transverse RMS moments predicted using 1994 design loads corrected to the prototype damping are in good agreement with the RMS moments predicted using loads derived from the on-site monitoring data and the 2009 wind tunnel test results; however, the

vertical RMS moments are conservative. The degree of conservatism in the 1994 wind tunnel loads will be quantified next.

Table 5.4 compares RMS moments predicted for a mean wind speed of 30.5 m/s using loads derived from the in-place monitoring data and from the 2009 and 1994 wind tunnel investigations. The derived loads from the on-site monitoring data and the 2009 wind tunnel test results are based on four transverse and three vertical modal loads each. The 1994 wind tunnel loads considered only two modal loads in each direction, which were based on the energy contained in the spectral peaks for these modes. The higher modal loads were not required to produce the required equivalent full-scale RMS moments and so were not included in the loading model [King and Davenport 1994]. In addition, a transverse point load of 185 kN is applied at the pier face in conjunction with the Transverse Symmetric (TS1) and Asymmetric (TA1) distributed loads to obtain the correct pier base moment [JMI-Stanley 1995].

Values shown in right 3rd column in Table 5.4 are the RMS moments predicted using the various wind tunnel loads normalized using the RMS moments derived from the on-site monitoring data. The transverse and vertical RMS moments predicted using the 2009 wind tunnel loads are within 5% of the values derived from the on-site monitoring data. The transverse and vertical RMS moments predicted using the 1994 design loads assuming 0.63% damping are within 40% and 161% of the on-site monitoring values respectively. In the absence of realistic estimates of the prototype damping, the designer always uses a conservative value. If the 1994 design loads are adjusted to realistic prototype damping, ranging from 1.5% to 3.9% of critical for the different modes, the resulting transverse RMS moments are within 6% and the vertical RMS moments are between 28% - 58% of the RMS moments derived from the on-site monitoring data. Thus the knowledge of prototype damping is crucial for estimating dynamic wind loads based on wind tunnel tests. The relatively high vertical RMS moments could be due to higher vertical turbulence intensity present during the 1994 wind tunnel tests.

5.4.2.2 Peak Bending Moments

Davenport [1962, 1979, 1988] has shown that the peak response, $\hat{R}$, can be expressed as

$$\hat{R} = \overline{R} + g R_{t_d} \qquad [5\text{-}19]$$

where $\overline{R}$ is the mean response, and g is a statistical peak factor, usually in the range 3 – 5. Table 5.5 compares peak bending moments predicted using loads derived from the in-place monitoring data and the 2009 wind tunnel test results for a mean wind speed of 30.5 m/s normal to the bridge axis, as occurred during the November 2001 storm, with the peak bending moments predicted using the design loads. The mean bending moments are available from the 2009 wind tunnel test results. The dynamic wind loads from the on-site monitoring data are used to determine RMS bending moments. A mean peak factor of 3.47 is determined from the analysis of the on-site monitoring data in Chapter 3. Using Equation [5-19], peak bending moments are computed for the transverse and vertical directions.

The force coefficients determined from the section model tests [JMI-Stanley 1995] are used to compute design mean bending moments and the dynamic force coefficients determined from the full-aeroelastic model test [JMI-Stanley 1995] are used to compute design RMS bending moments. A peak factor of 3.5 was recommended for the bridge design [King et al. 1994]. Using Equation [5-19] design peak bending moments are computed for the transverse and vertical directions.

The peak bending moments due to the specified design wind loads are 11% – 19% higher in the transverse direction and 67% - 96% higher in the vertical direction compared to the peak bending moments resisted by the bridge during November 2001 storm. These are specified or unfactored peak bending moments. The higher percentage difference in the vertical peak moments is due to the higher modal damping assumed for mode VS1 for wind speeds less than 32 m/s as described in the discussion of Figure 5.9. Hence one

concludes that the bending moments created during the passage of November 2001 storm approached, but did not exceed, those due to the specified design wind loads.

5.4.3 Normalized Displacement versus Wind Azimuth

Figure 5.11 shows the variation of normalized displacement with wind azimuth. Zero wind azimuth corresponds to winds blowing normal to the bridge axis and 90^{o} corresponds to winds parallel to the bridge axis. The normalized bridge displacement reduces as the wind azimuth moves away from the bridge normal. This relationship is conventionally assumed to follow a cosine – squared relationship [Appendix 3C] as shown by the solid lines. The curves with open triangle markers correspond to the normalized bridge deflections determined using loads derived from the in-place monitoring data. Figure 5.11 shows the cosine-squared relationship underestimates bridge deflections, computed using loads derived from the in-place monitoring data, both in the transverse and vertical directions. The relatively high bridge deflections at quartering winds determined from the on-site monitoring data could be attributed to several factors. The wave action and/or ice in the strait can excite the bridge under high winds irrespective of the wind azimuth. The bridge alignment is not a straight line and so winds along the bridge axis for the New Brunswick Marine Spans will be 7^{o} normal to the PEI Marine Spans and therefore the combined effect of the 65 spans of the bridge will always have some residual response. Finally the indicated wind azimuths in Figure 5.11 vary within 22.5^{o} and so it is very unlikely for the wind azimuth to be perfectly stationary.

The cosine – squared relationship underestimates the wind tunnel bridge deflections in the transverse direction; however, it simulates the bridge deflections reasonably well in the vertical direction. The slightly elevated bridge deflections in the transverse direction could be due to the influence of the bridge deck; however this requires further investigation. Thus, one concludes the cosine – squared relationship should not be used for skew wind azimuths as the relationship could give unconservative estimates of the associated forces and displacements for the Confederation Bridge.

5.5 Summary and Conclusions

The derivation of wind loads from the on-site monitoring data for the Confederation Bridge has been accomplished for the first time. The dynamic load effects derived using loads from the on-site monitoring data are compared to the load effects derived using loads from the 1994 and 2009 wind tunnel test results. The peak bending moments used for the bridge design are compared to the peak bending moments derived partly from the 2009 wind tunnel test results (i.e., mean component) and partly from the on-site monitoring data (i.e., dynamic component). The data suggest that the bridge has not been subjected to its specified (i.e., unfactored) wind force effects since it was opened to traffic in 1997, even in the November 2001 storm.

The following conclusions can be drawn:

1. The static load coefficients developed using on-site monitoring tiltmeter data are within 1% of the static loads used for the bridge design thus validating the 1994 wind tunnel test results.

2. Comparison of the dynamic load effects derived using loads from the on-site monitoring data and the 2009 and 1994 wind tunnel test results clearly demonstrates the following:

    i) The dynamic load effects predicted using 2009 wind tunnel loads are within 5% of the values predicted using loads from the on-site monitoring data. The damping estimates available from the on-site monitoring data have been essential to accurately predicting the equivalent load effects. Good agreement between the load effects predicted using loads derived from the on-site monitoring data and the 2009 wind tunnel test results validates the methodology used for the derivation of dynamic wind loads.

    ii) The transverse and vertical dynamic load effects predicted using 1994 wind tunnel loads used for the bridge design, are within 40% and 161% of the values

predicted using loads from the on-site monitoring data, respectively. The wind tunnel predictions are conservative, especially in the vertical direction, due to the low damping assumed for the model during the 1994 wind tunnel tests (i.e. 0.63% for all modes except VS1 that had a damping of 0.15% for wind speeds less than 32 m/s).

iii) The dynamic load effects predicted using 1994 design loads rectified to the correct prototype damping are 6% greater in the transverse direction and 28% - 58% greater in the vertical direction than the load effects derived from the on-site monitoring data. The 1994 design loads adjusted to prototype damping predict transverse load effects that are in good agreement with the full-scale values. The vertical load effects due to the 1994 design loads are conservative, but markedly less conservative than those obtained for the originally assumed damping.

3. Comparison of the peak bending moments for a mean wind speed of 30.5 m/s normal to the bridge, as occurred during the November 2001 storm, with the values predicted using the 1994 design loads shows the peak bending moments specified (i.e. unfactored) for the bridge design are 11% - 19% higher in the transverse direction and 67% - 96% higher in the vertical direction compared to the bending moments induced by the November 2001 storm. The data suggest that the bridge has not been subjected to its specified (i.e., unfactored) wind force effects since it was opened to traffic in 1997, even in the November 2001 storm.

4. The variation of the bridge deflection with wind azimuth reduces as wind azimuth moves away from the bridge normal; nevertheless it does not follow the conventional cosine-squared relationship. The normalized bridge deflections computed from the in-placed monitoring data show greater deflections for skew wind azimuths in the transverse and vertical directions than predicted by the cosine-squared relationship. The normalized transverse deflections from the wind tunnel data analysis are also greater than predicted by the cosine-squared

relationship, but the normalized vertical deflections almost follow the cosine-squared curve. The difference in the behaviour between the deflections computed from the on-site monitoring data and 2009 wind tunnel test results is not well understood and requires further investigation. However, the cosine-squared relationship is not a conservative approach to be used for bridges similar to the Confederation Bridge when subjected to skew wind azimuths.

5.6 References

AASHTO 2004. *AASHTO LRFD Bridge Design Specification,* American Association of State Highway and Transportation Officials.

Brown, T. G. 2007. Ice Force Monitoring, *Confederation Bridge Engineering Summit Proceedings,* Charlottetown, PEI, Canada. pp. 224-254.

Bruce, J. R., and Croasdale, K. R. 2001. *Confederation Bridge Ice Force Monitoring Joint Industry Project Annual Report,* IFN Engineering Ltd. Report Number 00-1-001, 40 p.

BS 2009. *Design Manual for Roads and Bridges,* BD 37/01 Volume 1, Section 3, Part 14, Loads for Highway Bridges. BS 5400. British Standard Institution London.

CHBDC. 2006. *Canadian Highway Bridge Design Code. A National Standard of Canada,* Canadian Standards Association CAN/CSA – S6 – 06.

Davenport, A. G. 1964. Note on the Distribution of the Largest Value of a Random Function with Application to Gust Loading, *Proceedings of the Institution of Civil Engineers,* Paper No. 6739, Vol. 28, pp. 187-196.

Davenport, A. G. 1979. The Influence of Turbulence on the Aeroelastic Responses of Tall Structures to Wind, *IAHR/IUTAM Symposium,* Karlsruhe, Germany, pp. 681-695.

Davenport, A. G. 1981. Reliability of Long Span Bridges under Wind Loading, *3rd International Conference on Structural Safety and Reliability (ICOSSAR),* Norway, pp. 679-694.

Davenport, A. G. 1988. The Response of Tension Structures to Turbulent Wind: The Role of Aerodynamic Damping, *1st International Oleg Kerensky Memorial Conference on Tension Structures,* London, England, Session 4: pp. D1-D7.

JMI-Stanley. 1995. *Design Criteria Northumberland Strait Crossing Project,* Jean Muller International, Stanley Joint Venture Inc.

King, J. P. C., Mikitiuk, M. J., Davenport, A. G., and Isyumov, N. 1994. *A Study of Wind Effects for the Northumberland Straits Crossing,* BLWT-SS8-1994, Boundary Layer Wind Tunnel Laboratory, University of Western Ontario (Parts of this report have been published in King and Davenport 1994b and King 1999).

King, J. P. C., and Davenport, A. G. 1994a. *The Estimation of Dynamic Wind Load Coefficients for the Northumberland Straits Crossing, PEI,* BLWT-IR-N62-16-1994, Boundary Layer Wind Tunnel Laboratory, University of Western Ontario (parts of the report have been published in King and Davenport 1994b and King 1999).

King, J. P. C., and Davenport, A. G. 1994b. P.E.I. Fixed Link – The Treatment of Wind Effects for the Northumberland Strait Crossing, *Fourth International Conference on Short and Medium Span Bridges,* Halifax, Nova Scotia, Canada, pp. 1377-1388.

King, J. P. C., Crooks, G. J., and Davenport, A. G. 1995. *The Northumberland Straits Crossing, Prince Edward Island Testing of Marine Span Aeroelastic Model and Analysis of Dynamic Wind Loads,* BLWT-SS24-1995, Boundary Layer Wind Tunnel Laboratory, University of Western Ontario.

King, J. P. C. 1999. Integrating Wind Tunnel Tests of Full-Aeroelastic Models into the Design of Long Span Bridges, *Proceedings of the Tenth International Conference on Wind Engineering (ICWE),* Copenhagen, Denmark, pp. 927-934.

SCBL. 2008. *Personal Correspondence via Email Dated: 28th January 2008,* Strait Crossing Bridge Limited, Prince Edward Island, Canada.

Table 5.1 – Drag Coefficients – 1994 Design Criteria versus On-Site Monitoring

Location	Drag Coefficients		Average Difference
	1994 Design Criteria	On-Site Monitoring	
Midpoint of Continuous Span	0.58	0.58	0.63 %
Cantilever Tip	0.82	0.83	
Quarter-Point of Continuous Span	1.75	1.76	
Pier Face	2.1	2.11	

Table 5.2 – Derivation of Dynamic Wind Loads Using On-Site Monitoring Data

On-Site Monitoring Data Chapter - 3	Wind Speed V (m/s)	30.5						
	Wind Azimuth	Bridge North						
	Direction	Transverse				Vertical		
	β	1.34×10^{-6}				6.60×10^{-6}		
	α	3.06				2.94		
	Mode Shape	TS1	TA1	TS2	TA2	VA1	VS1	VS2
	Frequency f_j (Hz)	0.343	0.397	0.485	0.913	0.57	0.678	0.942
Chapter - 5	$\Delta_{j_{max}} \times 10^{-3}$ (m)	7.39	4.72	2.56	0.37	6.42	3.85	1.46
	$I_{j_{max}} \times 10^{-6}$ m/(N/m)	6.59	5.04	3.61	1.38	2.64	1.83	0.80
	L_j (kN/m)	1.12	0.94	0.71	0.27	2.43	2.10	1.83

Table 5.3 – Derivation of Dynamic Wind Loads Using 2009 Wind Tunnel Test Data

'09 Wind Tunnel Data Chapter - 4	Wind Speed V (m/s)	30.5						
	Wind Azimuth	Bridge North						
	Direction	Transverse				Vertical		
	β	1.027×10^{-5}				1.095×10^{-5}		
	α	2.3				2.9		
	Mode Shape	TS1	TA1	TS2	TA2	VA1	VS1	VS2
	Frequency f_j (Hz)	9.37	12.16	16.11	29.13	15.59	17.96	20.59
Chapter - 5	$\Delta_{j_{max}} \times 10^{-3}$ (m)	12.35	6.78	3.55	0.91	10.03	6.65	4.48
	$I_{j_{max}} \times 10^{-6}$ m/(N/m)	6.75	3.86	2.44	0.58	2.13	1.88	1.53
	L_j (kN/m)	1.83	1.76	1.46	1.57	4.71	3.54	2.92
	ζ_{tm_j} (%)	0.63	0.52	0.52	0.25	0.92	0.76	0.6
	ζ_{tp_j} (%)	2.0	1.95	1.68	1.95	3.91	2.06	1.51
	L_{c_j} (kN/m)	1.02	0.91	0.81	0.56	2.29	2.15	1.84

Table 5.4 – Comparison of RMS Bending Moments for Mean Wind Speed 30.5 m/s Normal to the Bridge Axis

Data Type	Transverse Modal Wind Loads (kN/m)				Root Mean Square (RMS) Bending Moment (kN-m x 10^3)			RMS Bending Moment Ratio with respect to Full Scale		
	TS1	TA1	TS2	TA2	Midspan	Pier 32 Face	Pier 31 Face	Midspan	Pier 32 Face	Pier 31 Face
On-Site Monitoring	1.12	0.94	0.71	0.27	2.87	6.62	6.81	1.00	1.00	1.00
Wind Tunnel '09	1.02	0.91	0.81	0.56	2.81	6.43	6.45	0.98	0.97	0.95
Wind Tunnel '94	1.78	1.08	-	-	3.91	8.54	9.53	1.37	1.29	1.40
Wind Tunnel '94	1.34	0.73	-	-	2.94	6.21	6.99	1.03	0.94	1.03
Data Type	Vertical Modal Wind Loads (kN/m)				Root Mean Square (RMS) Bending Moment (kN-m x 10^3)			RMS Bending Moment Ratio with respect to Full Scale		
	VA1	VS1	VS2	VA2	Midspan	Pier 32 Face	Pier 31 Face	Midspan	Pier 32 Face	Pier 31 Face
On-Site Monitoring	2.43	2.10	1.83	-	1.46	13.99	13.91	1.00	1.00	1.00
Wind Tunnel '09	2.29	2.15	1.84	-	1.49	13.63	13.74	1.01	0.97	0.99
Wind Tunnel '94	2.3	7.5	-	-	3.33	29.74	36.28	2.28	2.13	2.61
Wind Tunnel '94	1.33	4.56	-	-	2.02	17.95	21.96	1.38	1.28	1.58

Table 5.5 – Comparison of Peak Bending Moments Predicted for a Mean Wind Speed of 30.5 m/s Normal to the Bridge Axis

Load Type	Direction	Mean Bending Moment (kN-m x 10^3)			RMS Bending Moment (kN-m x 10^3)			Peak Bending Moment (kN-m x 10^3)		
		Midspan	Short Pier Face	Long Pier Face	Midspan	Short Pier Face	Long Pier Face	Midspan	Short Pier Face	Long Pier Face
Wind Tunnel '09 On-Site Monitoring	Transverse	8.94	38.15	38.15	2.87	6.62	6.81	18.97	61.31	61.98
Design Loads	Transverse	8.81	37.88	37.88	3.91	8.54	9.53	22.51	67.79	71.23
Ratio – Design / (WT '09 or On-Site)	Transverse	0.98	0.99	0.99	1.36	1.29	1.40	1.19	1.11	1.15
Wind Tunnel '09 On-Site Monitoring	Vertical	2.97	30.66	30.66	1.46	13.99	13.91	8.09	79.64	79.34
Design Loads	Vertical	3.19	28.85	28.85	3.33	29.74	36.28	14.85	132.94	155.83
Ratio – Design / (WT '09 or On-Site)	Vertical	1.07	0.94	0.94	2.28	2.13	2.61	1.84	1.67	1.96

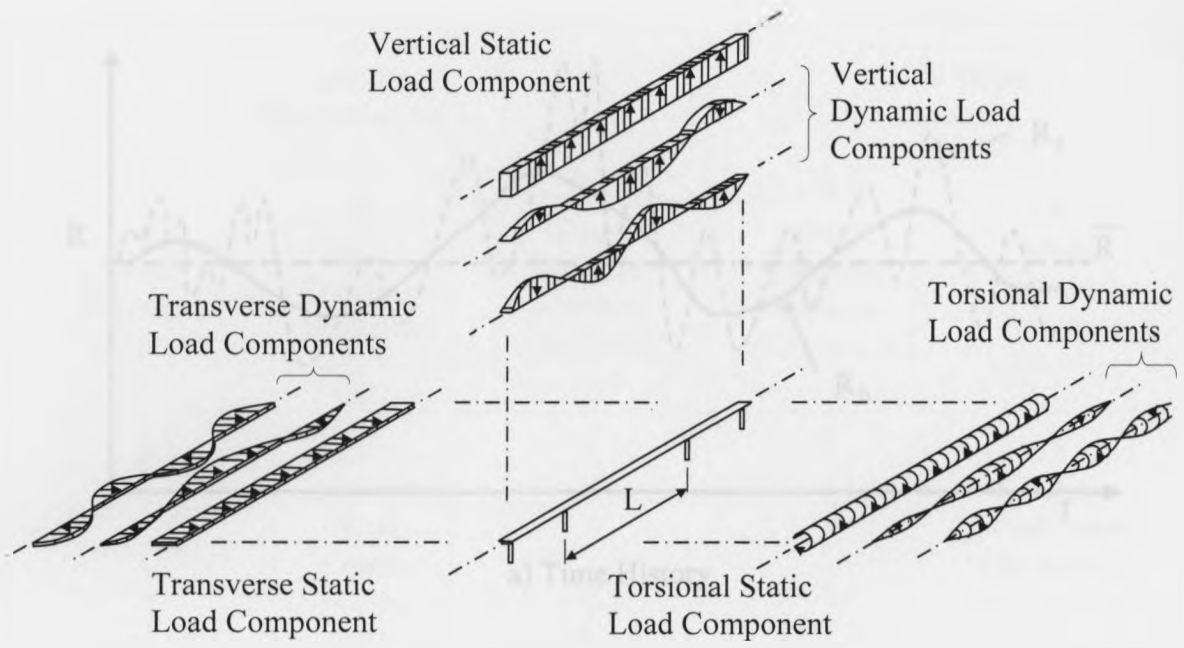

Figure 5.1 – Distributed Wind Load Components [adapted from King et al. 1994]

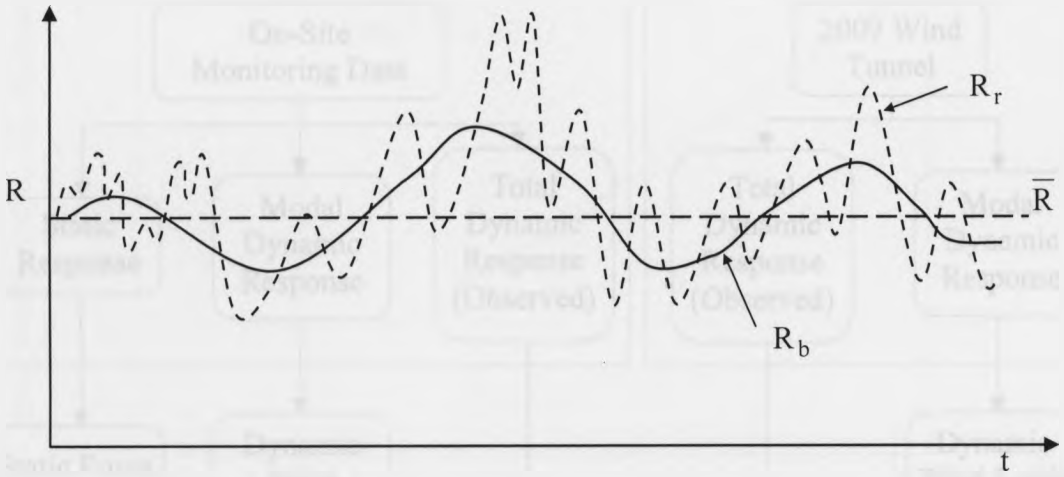

a) Time History

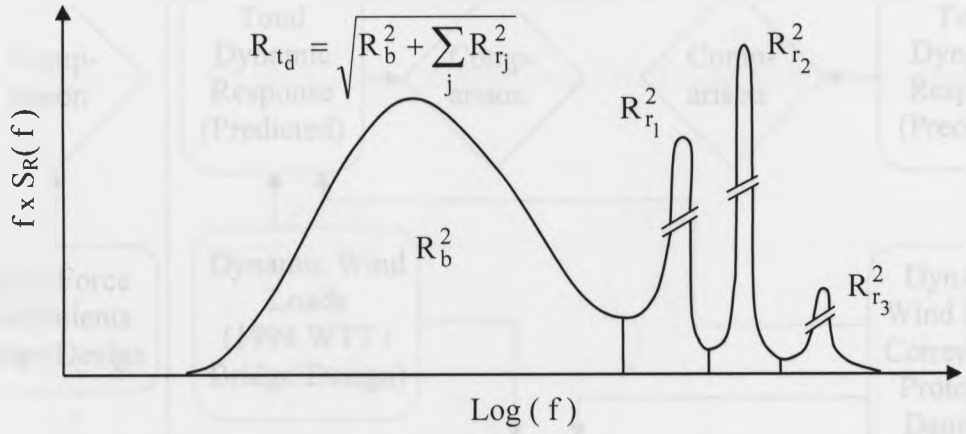

b) Power Spectrum

Figure 5.2 – Response to Wind: a) Time History; b) Power Spectrum [adapted from Davenport 1988]

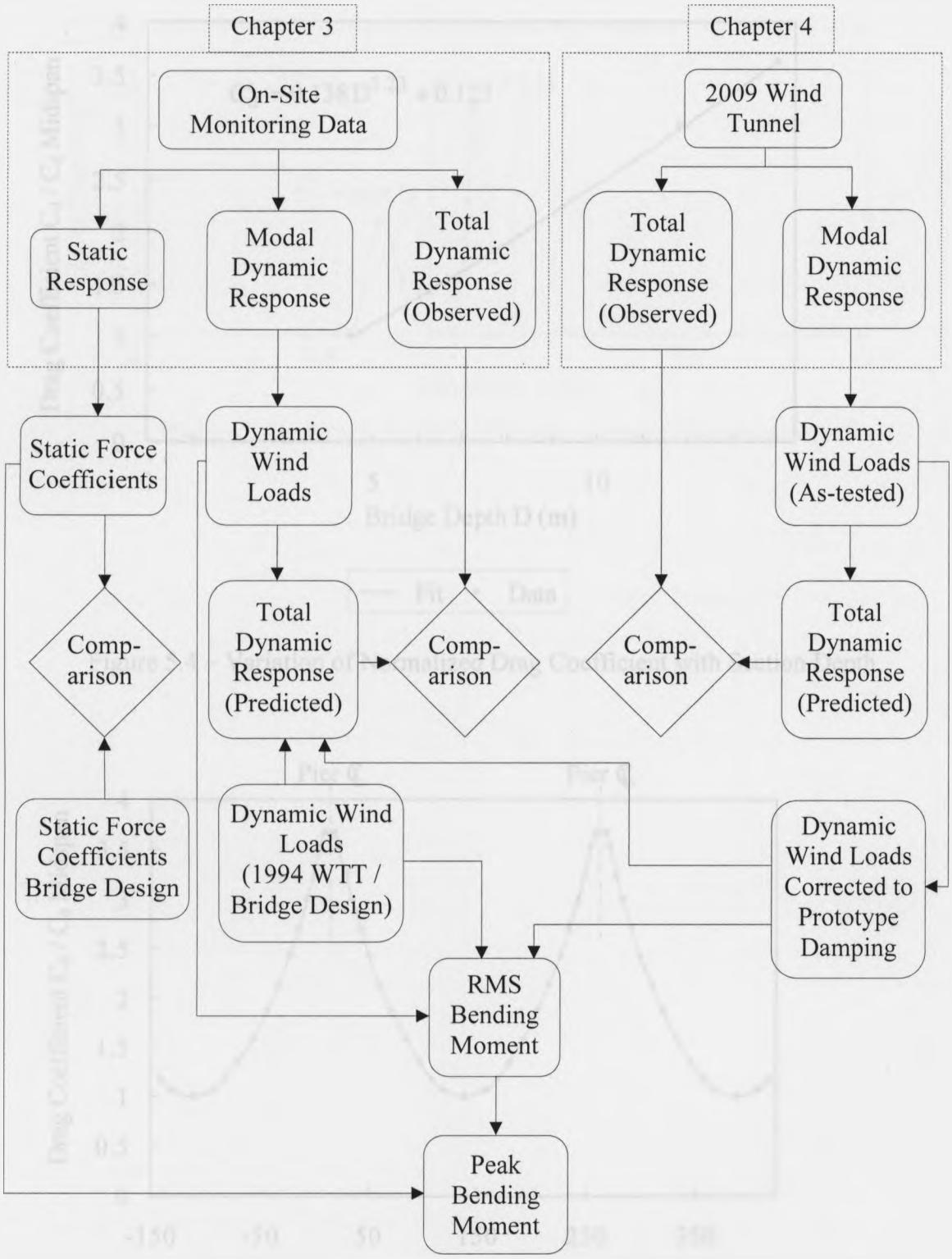

Figure 5.3 – Flow Diagram Explaining Derivation of Wind Loads Using On-Site Monitoring Data and the 1994 and 2009 Wind Tunnel Test Results

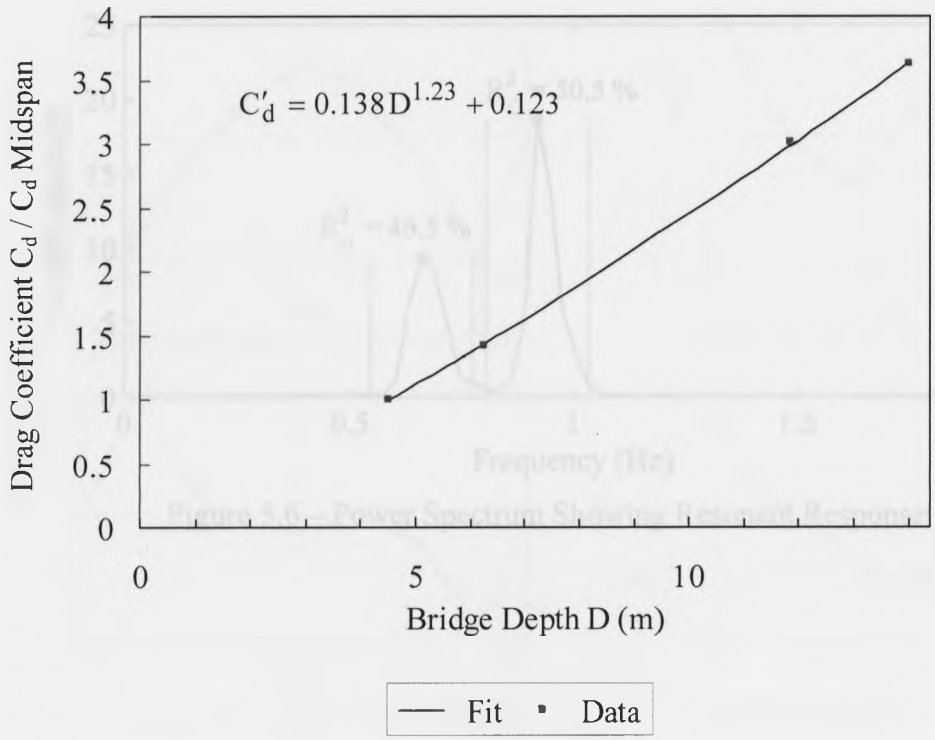

Figure 5.4 – Variation of Normalized Drag Coefficient with Section Depth

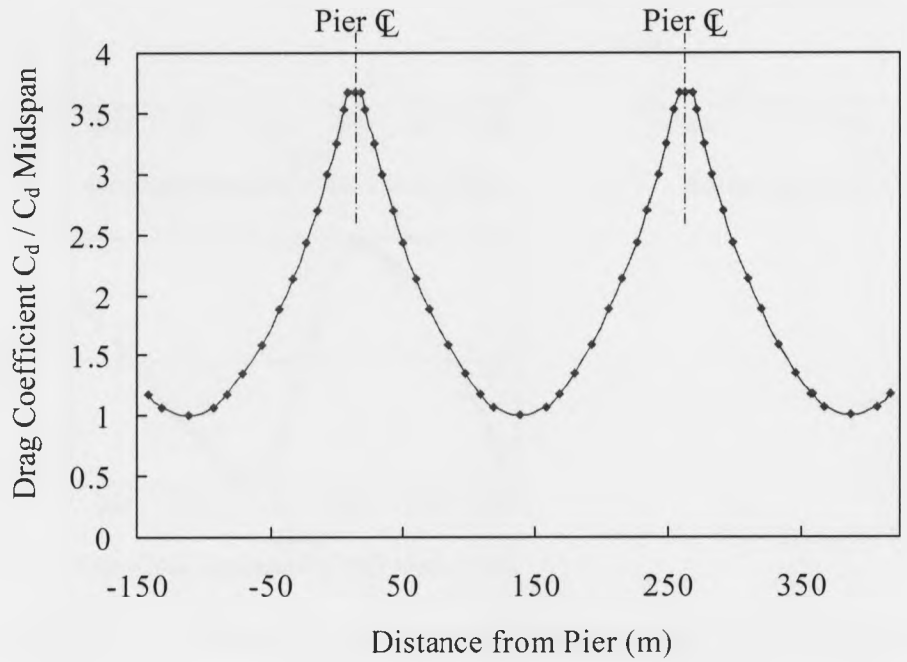

Figure 5.5 – Variation of Normalized Drag Coefficient for the Continuous Span and Two Cantilevers

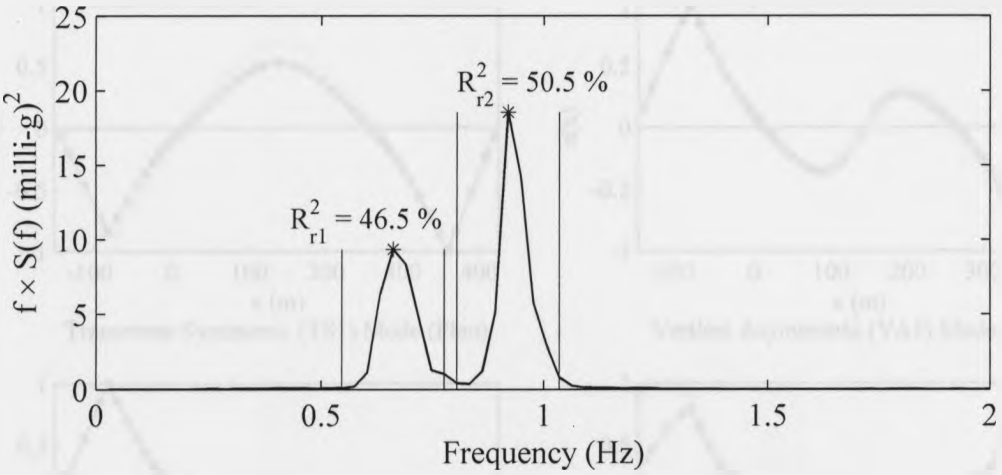

Figure 5.6 – Power Spectrum Showing Resonant Responses

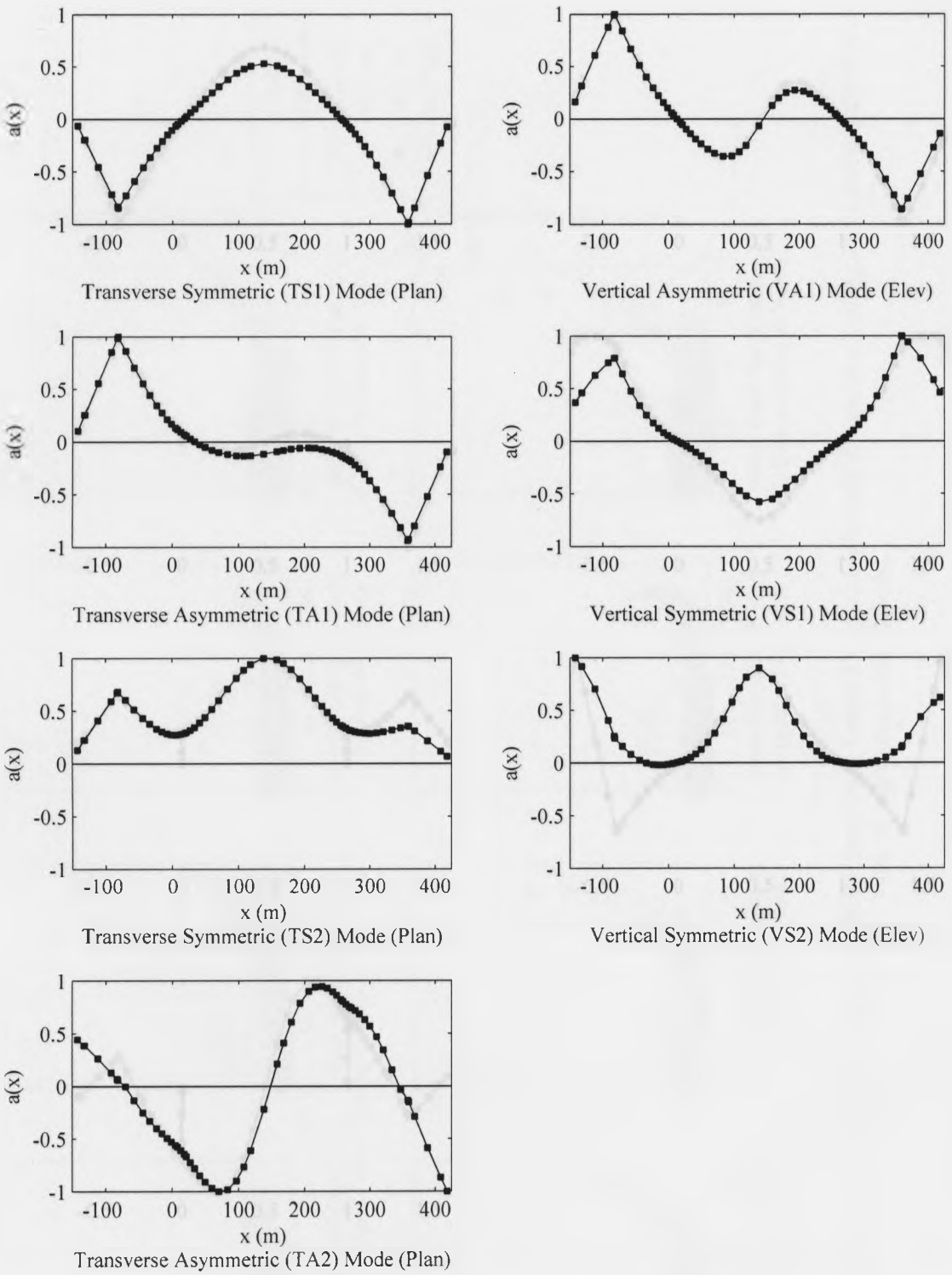

Figure 5.7 – Prototype Modal Load Distribution Functions for the Transverse and Vertical Mode Shapes

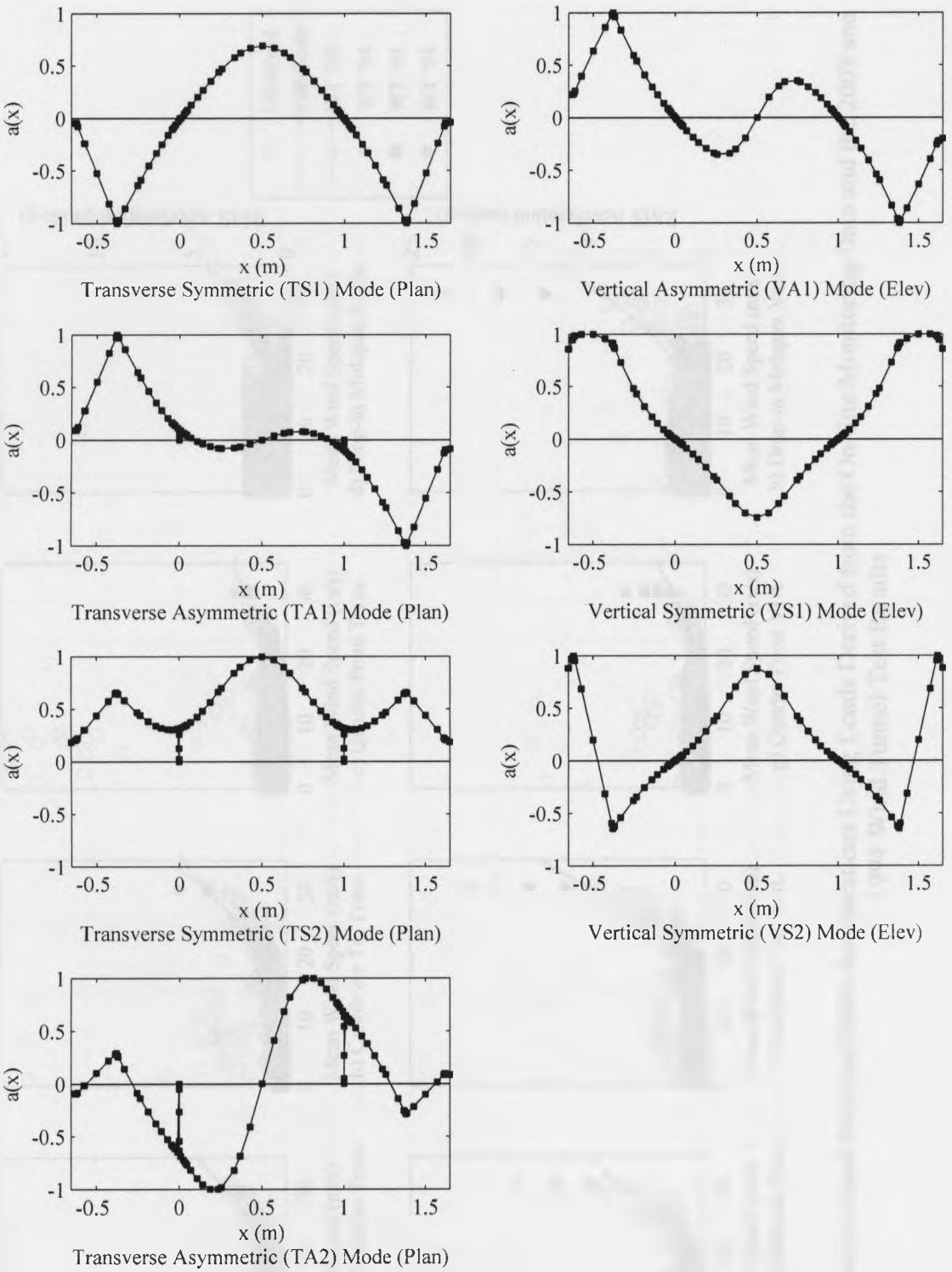

Figure 5.8 – Full-Aeroelastic Model Modal Load Distribution Functions for the Transverse and Vertical Mode Shapes

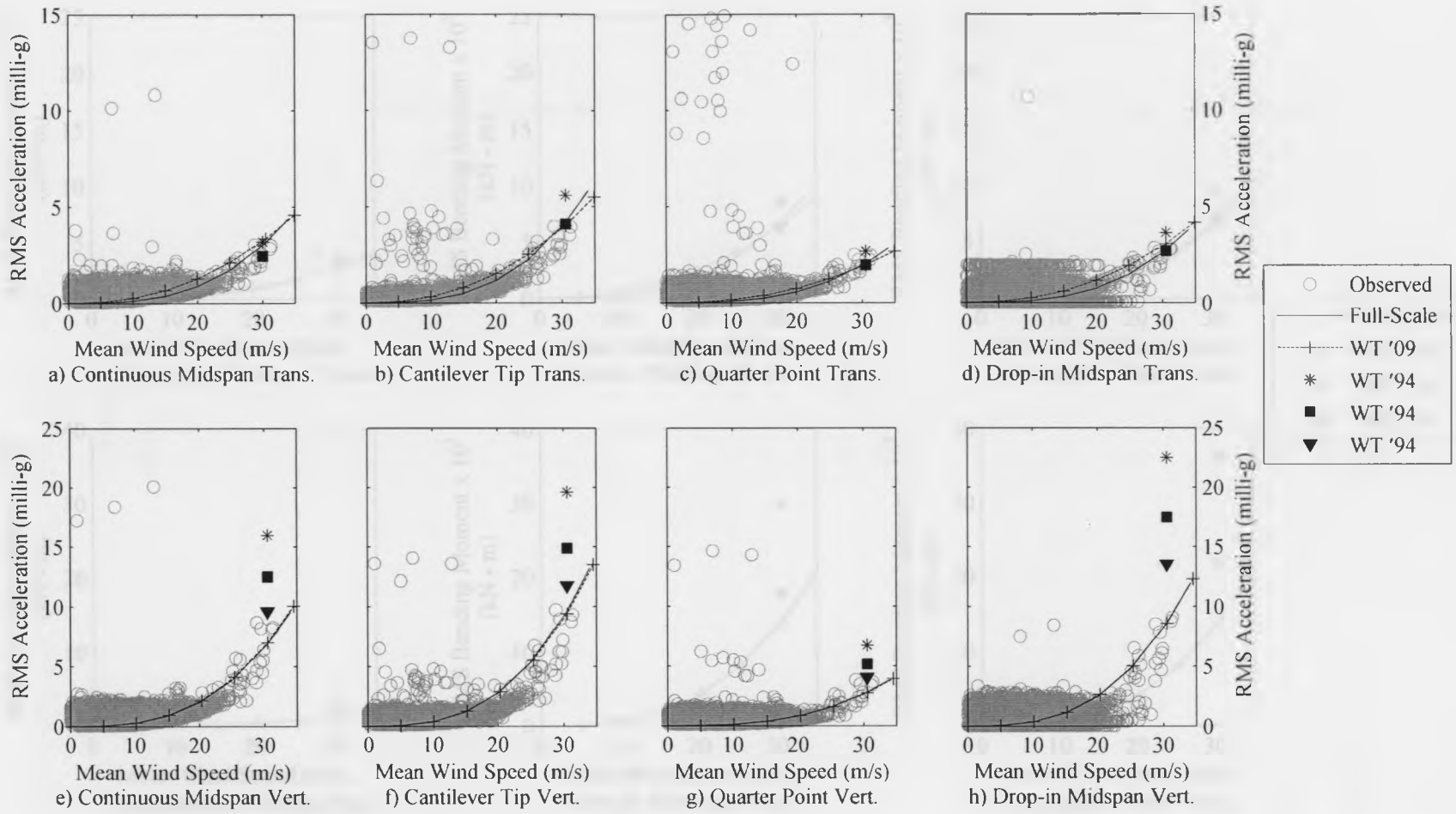

Figure 5.9 – Observed and Predicted RMS Accelerations Using Loads Derived from the On-Site Monitoring Data and the 2009 and 1994 Wind Tunnel Test Results

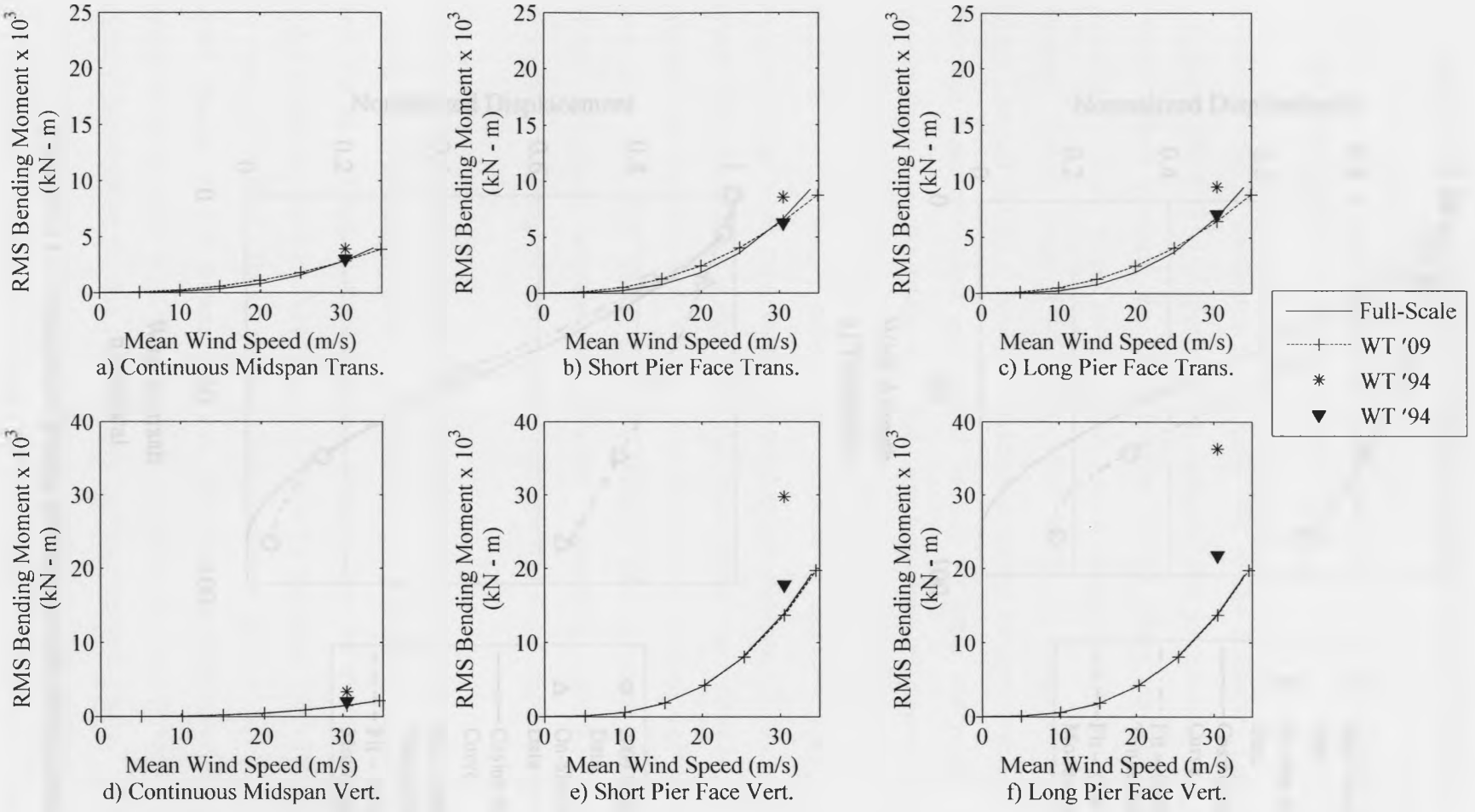

Figure 5.10 – Predicted RMS Bending Moments Using Loads Derived from the On-Site Monitoring Data and the 2009 and 1994 Wind Tunnel Test Results

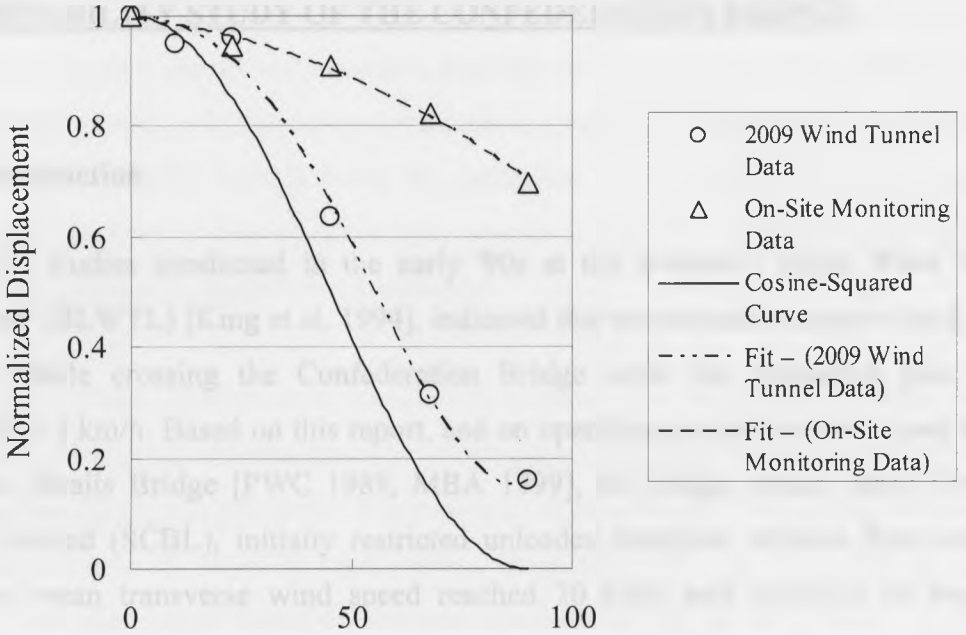

a) Transverse

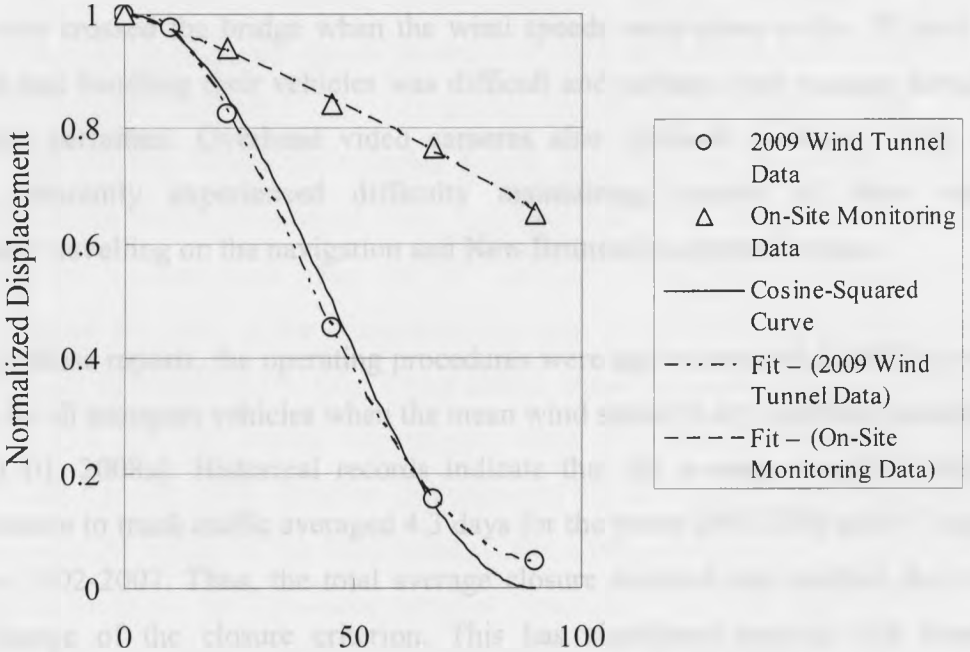

b) Vertical

Figure 5.11 – Variation of Bridge Deflection with Wind Azimuth

6. DRIVABILITY STUDY OF THE CONFEDERATION BRIDGE

6.1 Introduction

Drivability studies conducted in the early '90s at the Boundary Layer Wind Tunnel Laboratory (BLWTL) [King et al. 1994], indicated that an unloaded transport truck could overturn while crossing the Confederation Bridge when the transverse gust speed exceeded 115 km/h. Based on this report, and on operating procedures developed for the Mackinac Straits Bridge [PWC 1988, MBA 1999], the bridge owner, Strait Crossing Bridge Limited (SCBL), initially restricted unloaded transport vehicles from crossing when the mean transverse wind speed reached 70 km/h and restricted all transport vehicles from using the bridge when the mean transverse wind speed exceeded 80 km/h. In practice it proved difficult to identify and remove unloaded vehicles from the traffic stream, so the operating procedure was amended to restrict all transport vehicles from using the bridge when mean transverse wind speeds surpassed 70 km/h. On rare instances, drivers who crossed the bridge when the wind speeds were close to the 70 km/h limit indicated that handling their vehicles was difficult and perhaps their passage should not have been permitted. Overhead video cameras also captured instances where some drivers apparently experienced difficulty maintaining control of their vehicles, particularly travelling on the navigation and New Brunswick approach spans.

In light of these reports, the operating procedures were again amended in 2002 to restrict crossing by all transport vehicles when the mean wind speed in any direction exceeded 70 km/h [SCBL 2008a]. Historical records indicate that the average annual duration of bridge closure to truck traffic averaged 4.3 days for the years 1997-2001 and 8.7 days for the years 2002-2007. Thus, the total average closure duration has doubled due to this subtle change of the closure criterion. This has significant societal and economic consequences as there is no alternate route or detour for the Confederation Bridge. The primary justification for the current study is therefore to refine or verify the existing closure criteria using new empirical data to ensure that high, lightly loaded vehicles are prevented from crossing the bridge when the wind conditions are unsafe but are not

prevented unnecessarily from crossing. It is hypothesized, but has not been demonstrated experimentally, that the driver's comfort and degree of control will be enhanced as the vehicle speed is reduced. Similarly drivers have speculated that vehicle control may be enhanced if the vehicle travels down the centreline of the bridge, which requires that traffic be maintained in one direction only and so is altered on perhaps an hourly basis but there are no data to support this contention.

Cheung and Chan [2010] have developed a simulation technique to estimate the operational driving speed limits for vehicles crossing long-span bridges in general and the Confederation Bridge in particular. For example, they conclude that a high-sided vehicle is safe travelling at 28 m/s (101 km/h) with a mean cross-wind of 25 m/s (90 km/h) and an associated gust speed, based on the two examples presented in the paper, of 34 m/s (122 km/h). These proposed limits for high-sided vehicles seem excessive. Ample evidence is available to prove that high-sided vehicles roll-over at wind speeds less than these proposed limits. For example, on 10th June 2008, seven lightly loaded truck-trailers and a passenger bus were overturned on the Champlain Bridge in Montreal [CBC 2008]. The maximum mean and gust speeds recorded at the nearby Saint Hubert Airport were 24.2 m/s (87 km/h) and 30.8 m/s (111 km/h) respectively [CRIACC 2008, Weather Underground 2008b]. While the vehicles speeds are unknown, it is believed that the vehicle speed for the extreme wind event was less than the posted 22.2 m/s (80 km/h) limit. Another incident took place on 30th January 2008, when a truck-trailer was overturned near the crest of the Niagara-bound span of the Burlington Skyway Bridge [The Hamilton Spectator 2008, City News 2008]. Mean and gust speeds of 18 m/s (65 km/h) and 23.6 m/s (85 km/h), respectively, were recorded at the Hamilton Airport [Environment Canada 2008, Weather Underground 2008a]. Given that wind pressure is proportional to the square of the wind velocity, these two events clearly demonstrate that the proposed limits for the high-sided vehicles crossing the Confederation Bridge exceed the stability limits and so can not be regarded as the operational limits.

Cheung and Chan [2010] do not seem to differentiate between the stability and operational limits for the high-sided vehicles travelling across the Confederation Bridge.

The authors have implicitly used a bus model for the vehicle instability analysis and the factors of safety against roll-over are considered representative of all high-sided vehicles. These claims are based on computer simulations and are yet to be verified through field experiments.

Extensive research has been conducted to quantify acceleration limits associated with motion perceived by pedestrians on pedestrian bridges [CSA 2006, Kasperski 2006, Pimental et al. 2001], drivers on highway bridges [Oehler 1957, Wright and Green 1964, Shahanadi 1977], and office workers and residents in tall buildings [Burton et al. 2006]. Wind-tunnel studies have been conducted to determine average wind speeds that could roll-over stationary high-sided vehicles for the Bronx-Whitestone Bridge [King and Kong 2001]. There are no studies, however, that address the driver's perceptions of motion and degree of control of high-sided transport vehicles under strong wind conditions that can be used to refine the closure criteria. Despite the high cost involved, Strait Crossing Bridge Ltd (SCBL) decided to conduct a preliminary study to investigate how the wind direction and speed, vehicle speed, and travelled lane or vehicle travelling along the bridge centreline may influence the driver's perception of motion and degree of control.

6.1.1 Research Objectives

The objective of the study is to collect motion data for a lightly loaded truck-trailer and an intercity bus travelling at different speeds in different lanes under moderately high wind conditions to address the following:

i) To refine or verify the current critical wind condition (speed and direction) limits for restricting lightly loaded high-sided transport trucks and buses from crossing the Confederation Bridge.

ii) To characterize how wind direction, wind and vehicle speeds, and travelled lane or vehicle travelling along the centreline of the bridge impact the driver's perceptions of the degree of control of the test vehicles.

iii) To estimate factors of safety (FS) against roll-over of the test vehicles and to investigate if the high-sided vehicles such as buses and truck-trailers have the same stability limits, and

iv) To investigate if the stability and operational limits are same for different types of high-sided vehicles subjected to high winds.

6.1.2 Chapter Organization

This chapter describes the methodology used to collect motion data for a passenger bus and truck-trailer. The acceleration data will be used to derive the fundamental mode shapes and frequencies for the bus and an estimation of the vehicle accelerations at the driver's head level for the bus and truck-trailer. The accelerations will be correlated with the driver's anecdotal evidence of his degree of control of the vehicles for each passage. The cumulative distributions of acceleration for the different bus and truck-trailer passages will be developed and superimposed with the driver's characterization of the wind effects; the latter will serve as perception limits. Finally a crude estimate of the factors of safety against roll-over for the two vehicles will be determined.

6.2 Methodology – Field Data Acquisition System

A preliminary study of drivers' perceptions of light high-sided vehicle control on the Confederation Bridge during severe crosswinds was conducted. SCBL retained two professional driving instructors: one to drive an empty bus and the other to drive an unloaded high-sided transport truck across the bridge when the transverse wind speed exceeded a threshold value of 60 km/h. A typical truck or bus driver would not likely be as experienced as the drivers who participated in this study. The bus crossed the bridge six times under the conditions shown in Table 6.1, and the truck-trailer crossed the bridge four times under the conditions shown in Table 6.2. The bridge was closed to other traffic while these tests were conducted, with emergency personnel available in the event of an

accident. The bus crossings were at speeds of 40 km/h and 60 km/h in the travelled lane and 80 km/h along the centerline of the bridge in both the east and west directions. The truck-trailer crossed the bridge at 60 km/h along the centerline of the bridge in the east and west directions and at 50 km/h and 40 km/h in the travelled lane in the west direction only. The range of vehicle speeds chosen for the test is considered typical during high wind conditions.

The mean wind speed and 3-second gust speed for each passage, as recorded by the anemometer located at Pier 41 (close to the New Brunswick coast), is also shown in Tables 6.1 and 6.2. The wind speeds during testing could not be controlled: the mean speed varied from 67 km/h to 82 km/h, and the gust speeds varied from 83 km/h to 102 km/h. These variations are significant because the pressure exerted against an object by wind is proportional to the square of the wind speed. The wind direction remained approximately constant (WNW) for all the bus passages and the first three truck-trailer passages. The last truck-trailer passage (T4) had wind normal (NW) to the bridge axis, which is approximately NE-SW. The wind rose shown in Figure 6.1 displays the frequency of winds measured between 1998 and 2007, and indicates that the wind directions during the tests are consistent with the prevailing wind directions.

During each passage, the drivers verbally characterized the effect of the wind on the response of the vehicle, and the researcher travelling in the vehicle recorded these characterizations with the exact time stamp on the "Confederation Bridge Drivability Test Data Sheet," shown in Appendix 6B. The characterizations "Not Perceptible," "Slightly Perceptible," "Distinctly Perceptible," "Strongly Perceptible," and "Disturbing," were discussed with the drivers before the start of the test and are defined as follows:

- *Not Perceptible*: Driver cannot feel the presence of wind.
- *Slightly Perceptible*: Driver can feel the presence of wind but does not need to steer the vehicle to compensate for it.

- *Distinctly Perceptible*: Driver can feel wind striking the vehicle and needs to steer the vehicle somewhat to compensate for it. Wind gusts are audible. Passengers might feel uncomfortable due to the noise produced by the wind.

- *Strongly Perceptible*: Wind striking the vehicle is audible and pronounced, and the driver requires larger steering adjustments to accommodate it. Passengers feel uncomfortable and might not be willing to ride in the vehicle. The driver can still, with care, control the vehicle.

- *Disturbing*: Wind consistently forces the vehicle into the leeward lane and it is very difficult for the driver to control the vehicle. The driver prefers to reduce speed or stop.

Both drivers further subdivided each scale in to three sub-categories e.g. "Slightly Perceptible (easy / light)," "Slightly Perceptible (medium)," and "Slightly Perceptible (strong)."

Four wireless triaxial accelerometers were mounted on each vehicle to capture the fundamental vehicle motion in three principal (i.e., longitudinal, transverse and vertical) directions and sampled at 64 Hz. On the bus, accelerometers were mounted on the roof and the floor approximately above the middle of the front and rear axles as shown in Figure 6.2. On the truck-trailer, one accelerometer was mounted on the roof of the cab above the driver, two were attached to the trailer ceiling above the middle of the front and rear trailer axles, and one was placed on the trailer floor above the middle of the rear axle as shown in Figure 6.3. Each wireless accelerometer was calibrated before the first run and again after the last run to verify that its performance was consistent.

6.3 Vehicle Acceleration Data Analysis

The underlying assumptions in the analysis of accelerometer data for both the vehicles are as follows:

i) The average of the time histories of the front two accelerometers gives accelerations of the bus at the elevation of the driver's head. This is a reasonable assumption since the driver's head elevation was approximately midway between the floor and roof of the bus as shown in Figure 6.2.

ii) The accelerations experienced by the truck-trailer driver are derived from the time histories of the accelerometer attached to the truck cab roof. Since no accelerometer was attached on the floor of the truck cab, the ratios of the bus roof accelerations to the floor accelerations were used to estimate accelerations at the elevation of the truck driver's head.

iii) Frequencies greater than 5Hz are ignored because, as shown later, higher frequencies are not critical to the driver's perceptions of the wind effect and degree of control of the vehicle.

The steps involved in the analysis of the data are as follows:

1. The fundamental vehicle frequencies, which represent vehicle modes of vibration, are identified using power spectra derived from the time histories of accelerations for each bus or truck-trailer passage. Figure 6.4 shows acceleration time histories in the longitudinal, transverse and vertical directions of one of the four triaxial accelerometers mounted on the bus for Run B7. The longitudinal accelerations, shown in Figure 6.4a, are the least because the vehicle was travelling at a constant vehicle speed. The vertical accelerations, shown in Figure 6.4c, are the largest and approach 5 m/s^2. The transverse accelerations, shown in Figure 6.4b, lie between the longitudinal and vertical accelerations.

   Figure 6.5 shows corresponding power spectra. The longitudinal spectrum in Figure 6.5a shows no significant spectral peaks, which means the longitudinal vehicle accelerations are negligible. It will be shown later that the transverse vehicle accelerations are critical to driver's perception of the wind effect and

degree of control, and since the transverse spectrum in Figure 6.5b has no significant frequency peaks greater than 5 Hz, the higher frequencies are not considered for further analysis. The vertical spectrum in Figure 6.5c shows several jagged peaks covering a wide range of frequencies. The spectral peaks greater than 5 Hz could be due to local panel vibrations or the vehicle passing over expansion joints or manhole covers etc. Since the associated frequencies are too high to cause excessive vertical displacements, these frequency peaks are ignored. The vertical frequencies less than 5 Hz are expected to be that of suspension system and so are of interest for the present study.

2. For each spectral peak, a weighted average frequency is determined by taking second moment in the spectrum as [Gomes and Vickery 1975]:

$$f_j = \left[\frac{\sum f_i^2 S_x(f_i)}{\sum S_x(f_i)} \right]^{1/2} \qquad [6\text{-}1]$$

where f_j is the j^{th} mode natural frequency, $S_x(f_i)$ is the spectral density for the i^{th} frequency and i is the i^{th} data point in the spectrum. The spectra in Figure 6.5 show energy peaks; however, the distribution of energy is not even on both sides of the peaks; therefore, Equation [6-1] is used to estimate weighted average frequencies for the spectral peaks.

3. The identified frequencies are used to determine mode shapes for the bus following the procedure presented in Section 6.4.1. Fundamental vibration modes for the truck trailer could not be determined because the accelerometers mounted on the ceiling of the trailer recorded very high accelerations, likely due to the flexibility of the aluminum ribs of the roof, which are not representative of the accelerations experienced by the driver.

4. The vehicle accelerations at the elevation of the driver's head level in the transverse and vertical directions are used to calculate RMS accelerations averaged over two seconds and over the entire passage for each runs of each vehicles.

5. For each vehicle trip, cumulative distributions of the measured accelerations are produced using time histories for the accelerometers close to the driver's head.

6. The measured accelerations in Step (5) are fitted with exponential function of the form $y = e^{-cx}$, with acceleration along the abscissa and cumulative time on a normalized scale along the ordinate. The usefulness of these curves will be discussed in Section 6.4.2.3.

6.4 Bus Passages

In the following the derivation of mode shapes and the results of the data analysis for the six bus passages are discussed.

6.4.1 Mode Shapes

For each bus passage, modal displacements for the 12 accelerometer channels (three channels per accelerometer) were calculated using time histories for the weighted average frequencies. For a frequency to be considered as a mode, 80% coherence between two channels was warranted. The magnitude-squared coherence, C_{xy}, was calculated using the following expression [Hayes 1996, Stoica 1997]:

$$C_{xy} = \frac{(\text{abs}(S_{xy}))^2}{S_{xx}S_{yy}} \qquad [6\text{-}2]$$

where: S_{xx} and S_{yy} are the Power Spectral Densities of the variables X and Y, respectively, and S_{xy} is the Cross Spectral Density of the variables X and Y. In Equation [6-2], the variables X and Y represent the accelerometer time histories for any two channels.

To make the modal displacements representative of the bus vibration modes, twelve modal displacements were reduced to six degrees of freedom at the centroid of the accelerometers, considering the bus as a rigid body as shown in Figure 6.2. Three linear modal displacements in the longitudinal, transverse and vertical directions and three modal rotations about the longitudinal (roll), vertical (yaw) and transverse (pitch) axes were calculated. Linear modal displacements (longitudinal, transverse and vertical) are the average of the four modal displacements in the respective directions. Roll is the difference between the average roof and floor modal displacements in the transverse direction multiplied by the vertical lever arm. Yaw is the difference between the average front and rear modal displacements in the transverse direction multiplied by the longitudinal lever arm. Pitch is the difference between the average front and rear modal displacements in the vertical direction multiplied by the longitudinal lever arm. The six degrees of freedom were used to calculate new coordinates for the eight corners of the bus and plotted on two dimensional planes representing the top, back and side views. Figures 6.6 – 6.8 show roll, pitch and bounce mode shapes, respectively for Bus Passage B7. Similar results were derived for the remaining five bus passages. Each mode shape is uniquely normalized with respect to the maximum coordinate marked with an asterisk (*). The modal accelerations of the bus at the elevation of the driver's head are similar for the three modes as shown.

6.4.2 Discussion

Figures 6.9a and b show the variation of transverse accelerations (averaged over two seconds and the entire passage as shown by the solid and dotted lines, respectively) at the driver's head level for bus Runs B7 (westbound at 80 km/h, mean wind speed 80 km/h) and B6 (eastbound at 80 km/h, mean wind speed 67 km/h), respectively. For each vehicle passage at a constant vehicle speed, the driver's perception of the wind effect did not vary

significantly and an average perception limit on a scale 1 – 5 could be assigned to each vehicle run. However, instances during the travel when the driver registered a concern are shown highlighted with an asterisk (*). For example, the driver's perception, reflecting the average perception for the entire run, is markedly worse, i.e. Scale – 4, for the westbound run B7 and instances of concern are marked with an asterisk (*) i.e. 4 (strong) shown in Figure 6.9a. For the eastbound run B6, the driver's perception is significantly reduced, i.e. Scale – 2, with instances where driver registered 2 (strong) shown as asterisk (*) in Figure 6.9b. The corresponding mean and peak transverse accelerations are also markedly worse for the westbound run B7. The mean acceleration is of 29 milli-g (i.e., 0.029 times the acceleration due to gravity) for the westward run B7 and only 14 milli-g for the eastbound run B6. Thus, the average driver's perception seems to be correlated to the average acceleration experienced by the driver for each passage. In other words, the subjective measure of the driver's perception of the wind effect can be quantified in terms of the acceleration experienced by the driver. Figures 6.9a and b indicate that the bus driver tended to verbalize his perceptions while crossing the navigation spans and the New Brunswick approaches: while there is no sure explanation for this tendency, it is consistent with past observations by other drivers who reported their travelling experiences to the bridge authority (SCBL) on several occasions [SCBL 2008b].

Table 6.3a compares the observed mode shapes, frequencies, and accelerations with the associated wind speed/direction, travelled lane, and driver perception for the runs shown in Figures 6.9a and b. The fundamental roll, pitch, and bounce motions are shown in Figures 6.6 – 6.8, respectively. The magnitude of the pitch and bounce RMS accelerations are similar for both runs shown in Table 6.3a and so cannot explain why the perception during the westbound run B7 is markedly worse than that during the eastbound run B6. The higher transverse acceleration for the westbound run is due to the increased wind speed experienced during this run but may also be partially attributable to the slight head wind component of the cross wind for the westbound vehicle. The head and cross wind components are shown in Figure 6.3, which can be determined by multiplying wind speed by the sine and cosine of α, respectively.

Table 6.3b compares the westbound and eastbound runs B3 and B2 at a vehicle speed of 60 km/h, when the wind speeds were similar. Although the accelerations for the three modes are similar, the driver distinctly perceived the effect of the wind during the westbound run and only slightly perceived it during the eastbound run. This could be due to the vehicle travelling in the windward lane or to the slight head wind component of the cross wind for the westbound vehicle. The drivability study conducted at the BLWTL found the overturning tendency of light high-sided vehicles is higher travelling in the windward lane than in the leeward lane [King et al. 1994]. Figure 6.10, taken from this source, shows wind speed profiles (i.e. variation of wind speed with height) at five different locations across the bridge deck. The truck-trailer in the windward lane is subjected to higher gust speeds (profile 02) than the truck-trailer in the leeward lane (profile 04), which may explain the driver's more severe perception while travelling in the windward lane as reported in Table 6.3b.

Table 6.3c compares the westbound and eastbound runs B5 and B4 at a vehicle speed of 40 km/h, when the wind speeds were again similar. The driver's perception and transverse acceleration are again higher when travelling west. Though wind speeds are increased for both the westbound and eastbound passages at 40 km/h, compared to the corresponding passages at 60 km/h shown in Table 6.3b, the driver's perceptions and transverse accelerations are lower for the 40 km/h passages suggesting that a decrease in the vehicle speed reduces transverse accelerations and consequently the driver's perception of the wind effect for a given vehicle direction.

6.4.2.1 Bus Transverse Accelerations

Table 6.4 summarizes the transverse accelerations recorded during the rolling motion of the six bus runs. Wind direction (WNW) has a more severe effect on the driver's perception of the wind effect for all the westbound passages than for the eastbound passages. Further tests are required to understand how the driver's perception of the wind effect varies with varying wind direction. The effect of the travelled lane and head/tail wind component of the cross wind on the driver's perception of the effect of the wind is

still unclear. For example, the effect of the wind during Run B3, involving travel in the windward lane with a slight head wind component, was distinctly perceived by the driver. The effect of the wind during Run B2, however, involving travel in the leeward lane with a slight tail wind component, was only slightly perceived by the driver. The tail wind component of the cross wind is shown in Figure 6.3, which is the wind speed times the sine of α. The vehicle speeds, wind speeds and directions were similar for both passages. Was it the travelled lane or the slight head/tail wind component of the cross wind - or both - that caused the different driver's perceptions of the wind effect? If additional runs had been made where the bus travelled on the wrong side of the road, the relationship between the travelled lane, the head/tail wind component of the cross wind, and the driver's perception of the wind effect could perhaps be determined. A better understanding of this interaction is necessary for the development of rationally based bridge closure criteria.

The bus driver was asked to comment if the 70 km/h wind speed limit, currently used to restrict the high-sided vehicles, was safe before and after the test runs. The driver was uncertain before the test; however, after the study recommended that the 70 km/h limit was safe.

6.4.2.2 Distribution of Bus Accelerations

Figure 6.11 shows the distribution of the transverse acceleration at the elevation of the driver's head plotted for the three westbound runs. The vertical axis indicates the fraction of the total trip where the acceleration was greater than or equal to the value on the horizontal axis. The driver's anecdotal evidence, i.e. the average perception for the entire passage, is used to define the limits of perception shown superimposed on the plot. The solid curve corresponding to the bus travelling westbound at 80 km/h shows: the effect of the wind was strongly perceptible for 30% of the trip, at least distinctly perceived (Scale greater than 3) for 60% of the trip, and was at least slightly perceived (Scale greater than 2) for 75% of the trip. The dot-dash and dotted curves indicate that the transverse accelerations and associated driver's perceptions are worse when the vehicle travels

westbound at 60 km/h instead of 40 km/h even though the wind speeds and directions and the travelled lane for these two passages are similar.

Figure 6.12 shows a similar plot for the eastbound bus passages. As for the westbound passages, shown in Figure 6.11, the transverse accelerations are greater, and the driver's perceptions of the effect of the wind are more severe when vehicle speed is increased. The transverse accelerations shown in Figure 6.12 are, however, consistently smaller than those shown in Figure 6.11. The accelerations between the perception limits are gray areas which correspond to further subdivision of each limit into three sub-categories by the driver as explained earlier. The limits are slightly adjusted to make them consistent for the east and west bound passages. Finally, since the limits are based on the feedback provided by a single highly experienced driver, the proposed limits must be used with caution.

6.4.2.3 Exponential Fits

Figure 6.13 shows exponential functions fitted to the curves shown in Figures 6.11 and 6.12. The form of the fit is

$$T_N = e^{Ca_v} \qquad [6\text{-}3]$$

where: T_N is the normalized time, a_v is the vehicle acceleration and C is a constant determined by regression analysis. The constant determined through the fitting procedure implicitly accounts for vehicle and wind speeds and directions, and travelled lane and so could be interpolated for other wind and travelled conditions. Thus, for a given wind speed/direction and travelled conditions, the safe vehicle speed that will reduce the percentage of the travel time below the allowable driver acceleration/perception limit could be determined from the cumulative curves. These functions could be programmed into the bridge operations monitoring system, which can automatically calculate and post the safe vehicle speed, based on prevailing wind and travelled conditions. Thus

cumulative acceleration curves could be very effective in establishing an evidence-based bridge closure protocol which can be used to manage high-sided vehicles on the Confederation Bridge. To accomplish this goal, more tests covering different wind and travelled conditions and drivers with different perception levels are required. This could be a potential area of future research.

6.5 Truck –Trailer Passages

Figure 6.14a and b show the variation of transverse accelerations (averaged over two second intervals and over the entire passage, shown in solid and dotted lines, respectively) at the elevation of the driver's head for truck-trailer runs T1 (westbound at 60 km/h, mean wind speed 82 km/h) and T2 (eastbound at 60 km/h, mean wind speed 79 km/h), respectively. Instances during the travel when the driver registered a concern have again been highlighted with an asterisk (*) for the westbound passage only, as the driver expressed no concerns during the eastbound passage. Figures 6.14a and 6.9a show that under similar wind and travelled lane conditions, the average transverse acceleration and the driver's average perception are higher for the bus, which might be expected because it is travelling at a higher speed, 80 km/h, than the truck, 60 km/h. However, there are common features: perception of the wind effect (strong (*)) on the New Brunswick approaches correspond to peak accelerations with similar magnitudes (50 milli-g); and in general, higher peak accelerations are recorded at similar locations along the bridge i.e., the navigation spans and New Brunswick approaches for both passages. Figures 6.14b and 6.9b display similar trends: the transverse accelerations and driver's average perceptions are similar even though the vehicle speeds and wind speeds are different.

Table 6.5 summarizes the accelerations at the approximate elevation of the driver's head, the wind speed/direction, and the driver's perceptions for the four truck-trailer passages. The westbound and eastbound runs at 60 km/h (T1 and T2) experienced quite similar wind conditions, and the truck-trailer travelled down the bridge centerline in both cases, so the higher perceived impact during the westbound run could be due to the slight head wind component of the crosswind. Both transverse and vertical accelerations are

increased for the westbound run; however, the transverse accelerations increased more than the vertical accelerations, which again suggests that the driver's perception is sensitive to transverse vehicle accelerations and insensitive to vertical accelerations.

Table 6.5 also indicates that the transverse vehicle accelerations and associated driver perceptions can be reduced or controlled by reducing the vehicle speed for a given vehicle direction. The 60 km/h and 40 km/h westbound runs (T1 and T4, respectively) have similar wind speeds; however, T4 has lower transverse acceleration and driver perception than T1 even though the wind direction is more critical for T4 (NW - crosswind), and the vehicle is travelling in the windward lane. The 50 km/h and 40 km/h westbound runs (T3 and T4, respectively) have similar transverse accelerations and driver perceptions even though wind speeds are different (80 km/h for T4 and 71 km/h for T3). This indicates combinations of higher vehicle speed and slower wind speed (T3) or slower vehicle speed and higher wind speed (T4) can have the same effect on transverse acceleration and the associated driver's perception of the wind effect.

It is still unclear how travelled lane impacts the driver's perception of the wind effect and degree of control given the vehicle speed and direction and the wind conditions are controlled. Further tests are required for winds from the NNW and ESE sectors to investigate whether the presence of head wind component or travelling in the windward lane is responsible for more severe driver's perception. A better understanding of the vehicle, wind and travelled lane interaction with the driver's perceptions will aid in establishing acceleration-based bridge closure criteria for the high-sided vehicles under high wind conditions. A rational bridge closure criteria has the potential to reduce the duration and number of bridge closures without compromising safety of the users.

The truck-driver was also asked to comment if the 70 km/h limit, currently used to restrict the high-sided vehicles, was safe before and after the test runs. The driver was uncertain before the test; however, after the study recommended that the 70 km/h limit was safe.

6.5.1 Distribution of Truck-Trailer Accelerations

Figure 6.15 shows the distribution of the transverse accelerations at the elevation of the driver's head plotted for the four truck-trailer runs, with the driver's perception levels again superimposed. The solid curve corresponding to the tractor-trailer travelling westbound at 60 km/h shows that the effect of the wind is distinctly perceived (Scale greater than 3) for 30% of the trip and at least slightly perceived (Scale greater than 2) for 40% of the trip. The other three curves provide cumulative distributions for the other three runs. The transverse accelerations again increase with increased vehicle speed for the three westbound runs (T1, T3 and T4), where the wind speed or direction is similar. The middle curves (T3 - 50 km/h and T4 - 40 km/h) almost overlap, which indicates that the combination of higher wind speed and slower vehicle speed (T4) or slower wind speed and higher vehicle speed (T3) give rise to similar cumulative acceleration curves and similar perceptions of the effect of the wind on the control of the vehicle. The solid (T1 – 60 km/h) and dotted (T4 – 40 km/h) curves indicate that even though the wind direction is more severe for T4, and wind speeds are comparable, the reduced vehicle speed corresponds to reduced transverse vehicle accelerations and associated driver's perceptions. Thus, cumulative distributions of transverse acceleration are potentially effective to predict driver's perceptions and vehicle accelerations for different wind speeds/directions, vehicle speeds and travelled conditions. The exponential functions fitted to the curves shown in Figure 6.15 are given in Appendix 6C.

6.6 Comparison between Bus and Truck-Trailer Passages

A comparison of Tables 6.4 and 6.5 shows the transverse accelerations experienced by the truck driver for the Runs T1, T2, and T4 are greater than those experienced by the bus driver for the Runs B3, B2 and B5, respectively, when the wind direction, vehicle speed and direction of travel are similar. This might be expected because truck-trailer passages were made when the wind speeds were greater. However, anecdotal perceptions of the wind impact from the two drivers are similar, perhaps because the drivers have different perception levels or because other unmeasured factors (suspension system, seat

characteristics, articulated truck/single unit bus, etc.) mitigated the truck driver's perceptions of the transverse accelerations. The drivers' anecdotal perceptions of the wind effect during the west bound passages (T1 and B3) are markedly worst for both the vehicles compared to the east bound passages (T2 and B2) for the same vehicle speeds and wind directions. This could be due to the presence of head wind component of the cross wind for the westbound passages, which has a stronger effect on the vehicle compared to the tail wind component of the cross wind.

6.7 Nominal Factors of Safety against Vehicle Roll-Over

The drivability study for the Confederation Bridge as described in the previous sections was not designed to determine the factor of safety (FS) against roll-over of the test vehicles. However, estimates of the FS can be made using assumed mean pressure distributions around the vehicles and estimates of the dynamic overturning moment. The following significant assumptions are required in the calculation of these Factors of Safety against overturning:

i) The mean pressure distributions for stationary and moving vehicles are the same.

ii) The other modes of vibration (e.g. yaw, pitch, bounce) do not play a part in determining the roll-over potential.

iii) The measured transverse accelerations can be used to determine the dynamic moments.

iv) The vehicle mass is evenly distributed over the height of the vehicle.

Assumptions (i) and (ii) are realistic if the wind direction is at right angles to the vehicle at all times during the passage. However, the additional component of the vehicle velocity means that for nearly all cases, the relative wind angle between the vehicle and the wind is between 0^{o} and 90^{o}. The mean pressure distribution will be altered from that

of a pure cross-wind with the likely net result of reduced mean roll-over moments, but higher yawing moments. It is unclear how the interaction of roll and yaw moments will affect the ultimate roll-over of a high-sided vehicle. There is also some approximation required in the determination of the effective lateral acceleration at the centre of mass. Thus, the following procedure provides only a crude approximation of the factors of safety against roll-over of high-sided vehicles.

6.7.1 Derivation

The factor of safety against vehicle roll-over can be defined as the ratio of the stabilizing moment (M_s) to the over-turning moment (M_o).

$$FS = M_s/M_o \qquad [6\text{-}4]$$

A factor of safety of 1.0 indicates equal overturning and stabilizing moments and corresponds to the windward tire losing contact with the pavement and the initiation of roll-over as shown in Figure 6.16. The stabilizing moment is

$$M_s = GVW\ b_v/2 \qquad [6\text{-}5]$$

where GVW is the Gross Vehicle Weight and b_v is the out-to-out distance between wheels on an axle. The stabilizing moment is constant for a particular vehicle. It reduces slightly as the reactions under the wind ward lines of the wheels reduce because of the wind-induced transverse vehicle accelerations. It reduces more significantly as tipping initiates when the over-turning moment exceeds the stabilizing moment.

The overturning moment has static and dynamic components, M_{st} and M_{dy}, respectively:

$$M_o = M_{st} + M_{dy} \qquad [6\text{-}6]$$

The static component is given by:

$$M_{st} = 1/2\,\rho\,\overline{V}^2\,\overline{C}_m\,A_v\,h_v \qquad [6\text{-}7a]$$

where: ρ is density of air, $\overline{V}$ is the mean wind speed, A_v is the projected area of the vehicle exposed to the wind, h_v is the overall height of the vehicle, and $\overline{C}_m$ is the mean overturning moment coefficient. Rearranging Equation [6-7a],

$$\overline{C}_m = M_{st} \Big/ \left(\frac{1}{2}\rho\,\overline{V}^2\,A_v\,h_v\right) \qquad [6\text{-}7b]$$

Pressure tests for a passenger bus and a truck-trailer (as well as two other typical highway vehicles) were performed for the Bronx-Whitestone Bridge section model study at BLWTL in 2001 [King and Kong 2001], yielding the mean pressure coefficients for the bus and truck shown in Appendix 6D. The Bronx-Whitestone Bridge has a side barrier of approximately the same height as that of the Confederation Bridge so it is appropriate to assume that similar mean pressures will be experienced by stationary vehicles. The mean pressure coefficients multiplied by an effective moment arm can be integrated over the surface of the vehicle to yield an overturning moment coefficient, $\overline{C}_m$. The resulting overturning moment coefficients of 0.68 and 0.76 for the bus and truck-trailer, respectively, are used to calculate the static roll-over moment (M_{st}) for each vehicle passage under different travelled conditions and mean wind speeds.

The dynamic component is given by:

$$M_{dy} = GVM\,a_m\,h_m \qquad [6\text{-}8]$$

where: GVM is the Gross Vehicle Mass, a_m is the transverse GVM acceleration, and h_m is the distance from the road surface to the centre of the GVM.

For a given vehicle, the mass and centre of mass are approximately constant for all runs. The transverse vehicle acceleration, however, varies with vehicle speed, lane travelled, and wind speed and direction. Based on rocking and vertical natural frequencies, the dynamic centre of mass (h_m) is estimated to be 2.57 and 1.88 m from the road surface for the bus and truck-trailer, respectively. The instantaneous transverse vehicle accelerations at the centre of mass are estimated from the measured accelerations, which are then used to calculate dynamic roll-over moment time histories using Equation [6-8]. Since the accelerations of the trailer were based solely on the accelerometer fixed to the floor (rather than an average of the floor and roof acceleration), a nominal allowance for the increase in acceleration with height was required.

As noted above, this methodology used to compute the factors of safety against overturning are quite approximate, requiring significant assumptions and the resulting values are therefore also approximate. They crudely indicate the safety against roll-over and can give some indication of the relative safety of the bus and truck-trailer passages.

6.7.2 Discussion

Figure 6.17 shows the variation of stabilizing and over-turning moments with time for bus run B7 (vehicle speed 80 km/h, mean wind speed 80 km/h, WNW). The factor of safety against roll-over for the stationary bus, based on the mean wind speed alone, is approximately 4.9. As the bus travels across the bridge, instantaneous factors of safety reduce as the dynamic roll-over moments increase as shown. The most critical factors of safety against roll-over occur when the bus is travelling over the PEI Marine, Navigation and NB Approach spans and are as low as 2.2.

Figure 6.18 shows the variation of stabilizing and over-turning moments with time for the truck trailer run T1 (vehicle speed 60 km/h, mean wind speed 82 km/h, WNW). Since the truck-trailer roll-over is initiated by the trailer roll-over, only the weight, projected area and transverse accelerations for the trailer were used to calculate stabilizing and

over-turning moments. The factor of safety against roll-over for the stationary trailer based on the mean wind speed alone is approximately 2.6 but reduces to values as low as 1.2 when the dynamic component is included and the vehicle is travelling over the NB Approach and NB Marine spans. Although dynamic roll-over for the bus, 2.7, is two times the dynamic roll-over for the trailer, 1.4, the percentage reduction with respect to the total roll-over is the same for the two vehicles i.e., 55% and 54% for the bus and trailer, respectively. Since the acceleration at the centre of mass is estimated from a single accelerometer mounted on the floor of the trailer, the resulting factor of safety has a greater degree of uncertainty than the one determined for the bus.

A comparison of Figures 6.17 and 6.18 shows that the empty truck-trailer travelling at 60 km/h is more susceptible to roll-over than the bus travelling at 80 km/h under similar extreme wind conditions. This is so because the stabilising moment for the trailer, 121 kN-m, is almost half the value for the bus, 209 kN-m. This difference was also confirmed by observation of the response of the vehicles crossing the bridge through overhead cameras during the test. Since the study was designed primarily to access the driver's perception of vehicle control under high wind conditions, these crude estimates of the factors of safety should be used with caution.

Cheung and Chan [2010] have implicitly used a bus model for the vehicle instability analysis and consider their results representative of all high-sided vehicles. The factors of safety computed for the bus and truck-trailer in Figures 6.17 and 6.18 indicate that a truck-trailer is more susceptible to roll-over compared to a bus under similar travelled/wind conditions; therefore, analysis results for a bus can not be used for all high-sided vehicles. Although a factor of safety greater than 2 against roll-over was maintained at all times for the westbound bus Run 7, the driver said he would refuse to cross the bridge with passengers on board under similar wind and travelled conditions. Clearly the chosen wind and vehicle speeds for the test passage in some cases exceeded the operational driving limits for the Confederation Bridge. Therefore, the operational limits proposed by Cheung and Chan [2010] can not be considered to be the operational

driving speed limits for the Confederation Bridge as such limits are governed by the driver's perception of the wind effect on the degree of control of the vehicle.

6.8 Lessons Learned from the Full-Scale Testing

The vehicles and wireless accelerometers used in the study are shown in Figure 6.19. The specifications of the accelerometer can be found elsewhere [Micro Strain 2010]. Several problems were encountered during the full-scale test. In the case of bus, the four accelerometers could not communicate with the base station simultaneously during travel, which made it difficult to trigger them simultaneously. Therefore, the accelerometers had to be triggered with the base station located at an elevated position outside the bus while the engine was idling. It was impossible to trigger the accelerometers mounted on the truck-trailer simultaneously because three were mounted inside the trailer and the fourth was mounted on the cab roof. In spite of extensive efforts, no base station location could be found to make the four trigger at the same time. Hence the trailer and cab roof accelerometers were triggered separately and the trigger times were noted manually. Had there been a secondary base station on site, this problem could have been overcome.

Ideally, to record accelerations at the elevation of the driver's head, the accelerometers should be mounted on the driver's head or on a rigid bar hanging from the ceiling close to the driver's head or where a front-seat passenger's head would be. The accelerometers should not be mounted on flexible body parts like the aluminum ribs of the trailer ceiling shown in Figure 6.19e, which are susceptible to local panel vibrations that are not representative of the overall vehicle accelerations.

6.9 Conclusions

A preliminary study of drivers' perceptions of light high-sided vehicle control on the Confederation Bridge during severe crosswinds was conducted. A bus and a truck-trailer were instrumented with wireless accelerometers and two professional driving instructors drove the vehicles across the bridge several times under severe cross-wind conditions.

Each driver verbally characterized the effect of the wind on his driving experience on a scale of 1 to 5 (i.e., "Not Perceptible" to "Disturbing"). These perceptions were then correlated with the transverse accelerations measured at the elevation of the driver's head. A crude factor of safety was developed based on the measured dynamic responses of the vehicles and using published data from wind-tunnel pressure tests on similar vehicle types.

The main findings of the study are as follows:

1. The current procedure whereby high-sided vehicles are restricted when the wind exceeds 70 km/h in any direction was not perceived to be unsafe by the two professional driving instructors participating in this study. However, further tests under different wind conditions and involving different drivers are required to better quantify vehicle behaviour and driver's perceptions before revising the current criteria.

2. The driver's perception of the wind effect is particularly sensitive to transverse vehicle accelerations. Vertical accelerations do not influence the driver's perceptions and seem insensitive to wind speed or vehicle direction.

3. Both bus and truck-trailer runs show that transverse vehicle accelerations increase with increased vehicle speed for a given vehicle direction and wind speed and direction.

4. For the WNW and NW wind directions present during the test, the perceived severity of the wind during westbound travel was consistently worse than that during eastward travel. One explanation is that, for wind from these directions, the westward lane is the windward lane and so subjected to higher gust speeds. It is also possible that the slight headwind component of the cross wind for the westbound travel is responsible for the driver's increased perception for this case.

5. Transverse accelerations for the tractor-trailer are greater than for the corresponding bus for crossings made at the same vehicle speed and direction of travel. Anecdotal evidence from the two drivers is similar, however, suggesting that the drivers may have different perception levels.

6. Comparison of the factor of safety for the truck-trailer and bus suggests the former is more susceptible to roll-over under similar wind conditions. This is so because the stabilising moment for the trailer is almost half the value for the bus. Thus the instability limits for the two are different. Since the study was designed primarily to assess the driver's perception of the vehicle control under high wind conditions, the estimates of the factors of safety should be used with caution.

7. The instability limits causing vehicle roll-over are distinct from, and less stringent than, the operational limits. The latter are governed by the driver's perception of the wind effect and degree of control of the vehicle.

6.10 Recommendations

1. Further tests are required to investigate how the lane travelled by the vehicle (i.e. windward lane, leeward lane or bridge centreline) impacts vehicle control, when all other conditions such as vehicle speed and direction and wind conditions are controlled. This would require recording vehicle accelerations and driver anecdotal evidence for the same wind and vehicle speeds and directions travelling along the bridge centreline and also in the left and right lanes.

2. Further tests are required for winds from the NNW or ESE sectors to investigate whether the presence of a head-wind component or travelling in the windward lane more strongly influences the driver's perception. This would require collecting data while travelling in the westward lane for the eastbound passage with winds approaching from the ESE sector and vice versa.

3. Further tests should investigate the accuracy of the method for interpolating the accelerations at the driver's head. This would require measuring accelerations at the elevation of the driver's head using an accelerometer mounted on a rigid bar hanging from the ceiling.

4. In part, to account for the variable driver sensitivity to wind effects, a database of wind conditions (average and gust speed, direction) and driving direction which have been perceived to be unsafe, based on past and future anecdotal evidence, could be developed.

6.11 References

Burton, M. D., Kwok, K. C. S., Hitchcock, P. A., and Denoon, R. O. 2006. Frequency Dependence of Human Response to Wind-Induced Building Motion, *Journal of Structural Engineering*, ASCE, 132:2, pp. 296-303.

Canadian Standards Association (CSA) 2006. *Canadian Highway Bridge Design Code (CAN/CSA S6-06) and Commentary (CAN/CSA S6.1-06)*, Canadian Standards Association, Mississauga Ontario.

Canadian Broadcasting Corporation. 2008. http://www.cbc.ca/canada/montreal/story/2008/06/10/qc-weather0610.html

Centre de Ressources en Impacts et Adaptation au Climat et à ses Changements. 2008. http://www.criacc.qc.ca/climat/suivi/Evenements/Orages_et_Vents_violents_10_juin_08_e.html

Cheung, M. M. S., and Chan, B. Y. B. 2010. Operational Requirements for Long-Span Bridges under Strong Wind Events, *Journal of Bridge Engineering,* ASCE, 15:2, pp. 131-144.

City News. 2008. http://www.citytv.com/toronto/citynews/news/local/article/20220--winds-topple-tractor-trailer-on-burlington-skyway

Environment Canada. 2008. http://www.climate.weatheroffice.gc.ca/climateData/hourlydata_e.html?timeframe=1&Prov=CA&StationID=4932&Year=2008&Month=1&Day=30

Gomes, L., and Vickery, B. J. 1977. On the Prediction of Extreme Wind Speeds from the Parent Distribution, *Journal of Industrial Aerodynamics,* 2: 21-36.

Hayes, M. 1996. *Statistical Digital Signal Processing and Modeling,* John Wiley and Sons, NY, USA.

Kasperski, M. 2006. Vibration Serviceability for Pedestrian Bridges, *Proceedings of the Institution of Civil Engineers,* Structures and Buildings 159, Issue SB5, pp. 273-282.

King, J. P. C., Mikitiuk, M. J., Davenport, A. G., and Isyumov, N. 1994. *A Study of Wind Effects for the Northumberland Straits Crossing,* BLWT-SS8-1994, Boundary Layer Wind Tunnel Laboratory, University of Western Ontario (Parts of the report have been published in King and Davenport 1994).

King, J. P. C., and Davenport, A. G. 1994. P.E.I. Fixed Link – The Treatment of Wind Effects for the Northumberland Strait Crossing, *Fourth International Conference on Short and Medium Span Bridges,* Halifax, Nova Scotia, Canada, pp. 1377-1388.

King, J. P. C., and Kong, L. Z. 2001. *A study of Wind Effects for Bronx-Whitestone Bridge,* BLWT-SS25-2001, Boundary Layer Wind Tunnel Laboratory, University of Western Ontario, London, Ontario, Canada.

MBA.1999, *Wind Warning, Escort, and Closure Procedures,* Mackinac Bridge Authority.

Micro Strain 2010, http://microstrain.com/g-link.aspx

Oehler, L. T. 1957. *Vibration Susceptibilities of Various Highway Bridge Types,* Report No.272, Project 55 F-40, Michigan State Highway Department.

Pimentel, R. L., Paric, A., and Waldron, P. 2001. Evaluation of Design Requirements for Footbridges Excited by Vertical Forces from Walking, *Canadian Journal of Civil Engineering,* 28:769-777.

Public Works Canada 1988. *Investigation into the Effect of High Winds on Vehicular Traffic, Northumberland Strait Crossing Project,* PWC, December 1988.

SCBL. 2008a, *Confederation Bridge Wind Test Studies, Phase – 3 Vehicle Performance/Drivability Study,* Appendix 1, Strait Crossing Bridge Limited.

SCBL. 2008b. *Personal Correspondence via Email,* Strait Crossing Bridge Limited, Prince Edward Island, Canada.

Shahanadi, A. 1977. *Bridge Vibration Studies. Joint Highway Research Project,* Report No. JHRP – 77 – 17, Purdue University and Indiana State Highway Commission, September 1977.

Stoica, P., and Moses, R. 1997. *Introduction to Spectral Analysis,* Prentice Hall, NJ, USA.

The Hamilton Spectator. 2008. http://www.thespec.com/article/317145

Weather Underground. 2008a. http://www.wunderground.com/history/airport/CYHM/2008/1/30/DailyHistory.html?req_city=NA&req_state=NA&req_statename=NA

Weather Underground. 2008b. http://www.wunderground.com/history/airport/CYHU/2008/6/10/DailyHistory.html?req_city=NA&req_state=NA&req_statename=NA

Wright, D. T. and Green, R. 1964. *Highway Bridge Vibrations,* Part II: Report No. 5. Ontario Test Programme. Ontario Department of Highways and Queen's University. Kingston, Ontario, May 1964.

Table 6.1 – Summary of Bus Runs – Wind Direction WNW

Run No	B7	B3	B5	B6	B2	B4
Bus Speed (km/h)	80	60	40	80	60	40
Bus Direction	West			East		
Mean Wind Speed (km/h)	80	71	72	67	68	74
Maximum Gust Speed (km/h)	102	88	91	85	83	93
Head / Tail Wind Component	Head Wind Component			Tail Wind Component		
Travelled Lane	Bridge Centre-line	Windward Lane		Bridge Centre-line	Leeward Lane	

Table 6.2 – Summary of Truck-Trailer Runs

Run No	T1	T2	T3	T4
Truck-Trailer Speed (km/h)	60	60	50	40
Truck-Trailer Direction	W	E	W	W
Mean Wind Speed (km/h)	82	79	71	80
Maximum Gust Speed (km/h)	101	96	94	102
Wind Direction	WNW	WNW	WNW	NW
Head / Tail Wind Component or Cross Wind	Head Wind Component	Tail Wind Component	Head Wind Component	Cross Wind
Travelled Lane	Bridge Centreline	Bridge Centreline	Windward Lane	Windward Lane

Table 6.3 – Summary of Bus Mode, Frequency, RMS Acceleration (Driver's Head Level), Wind Speed, Wind Direction (WNW), Travelled Lane and Driver Perception

a) Relative Effect of Transverse and Vertical Accelerations Bus Speed 80 km/h Travelling Along Bridge Centreline						
Bus Direction (Run)	West (B7)			East (B6)		
Mode	Roll	Pitch	Bounce	Roll	Pitch	Bounce
Type	T	V	V	T	V	V
Frequency (Hz)	0.5	1.19	2.5	0.56	1.13	2.5
RMS Acceleration (milli-g)	29	36	27	14	33	26
Mean Wind Speed (km/h)	80			67		
Max. Gust Speed (km/h)	102			85		
Head / Tail Wind	Head Wind Component			Tail Wind Component		
Driver Perception	Strongly Perceptible			Slightly Perceptible		
Scale	Scale - 4 (strong*)			Scale - 2 (strong*)		
b) Relative Effect of Head and Tail Winds Bus Speed 60 km/h						
Bus Direction (Run)	West (B3)			East (B2)		
Mode	Roll	Pitch	Bounce	Roll	Pitch	Bounce
Type	T	V	V	T	V	V
Frequency (Hz)	0.57	1.13	2.25	0.63	1.13	2.25
RMS Acceleration (milli-g)	15	21	22	13	20	24
Mean Wind Speed (km/h)	71			68		
Max. Gust Speed (km/h)	88			83		
Head / Tail Wind	Head Wind Component			Tail Wind Component		
Travelled Lane	Windward Lane			Leeward Lane		
Driver Perception	Distinctly Perceptible			Slightly Perceptible		
Scale	Scale - 3 (strong*)			Scale - 2		
c) Relative Effect of Head and Tail Winds Bus Speed 40 km/h						
Bus Direction (Run)	West (B5)			East (B4)		
Mode	Roll	Pitch	Bounce	Roll	Pitch	Bounce
Type	T	V	V	T	V	V
Frequency (Hz)	0.75	1.63	2.5	0.63	1.63	2.69
RMS Acceleration (milli-g)	11	21	14	9	22	13
Mean Wind Speed (km/h)	72			74		
Max. Gust Speed (km/h)	91			93		
Head / Tail Wind	Head Wind Component			Tail Wind Component		
Travelled Lane	Windward Lane			Leeward Lane		
Driver Perception	Distinctly Perceptible			Slightly Perceptible		
Scale	Scale - 3 (easy*)			Scale - 2 (easy*)		

* further subdivision of the scale by the driver e.g. 4(easy), 4, 4(strong). T – Transverse, V – Vertical.

Table 6.4 – Summary of Transverse RMS Accelerations for All Bus Runs: Wind Direction WNW – Roll Mode

Run No	B7	B3	B5	B6	B2	B4
Bus Speed (km/h)	80	60	40	80	60	40
Bus Direction	West			East		
Frequency (Hz)	0.5	0.56	0.75	0.56	0.63	0.63
RMS Acceleration (milli-g) (Driver's Head Level)	29	15	12	14	13	9
Mean Wind Speed (km/h)	80	71	72	67	68	74
Maximum Gust Speed (km/h)	102	88	91	85	83	93
Head / Tail Wind Component	Head Wind Component			Tail Wind Component		
Travelled Lane	Centre line	Windward Lane		Centre line	Leeward Lane	
Driver Perception	Strong	Distinct		Slightly Perceptible		
Scale	Scale–4 (strong*)	Scale–3 (strong*)	Scale–3 (easy*)	Scale -2 (strong*)	Scale–2	Scale–2 (easy*)

* Further subdivision of the scale by the driver e.g. 2 (easy), 2, 2 (strong).

Table 6.5 – Summary of Transverse and Vertical RMS Accelerations for All Truck-Trailer Runs

Run No	T1	T2	T3	T4
Truck-Trailer Speed (km/h)	60	60	50	40
Truck-Trailer Direction	W	E	W	W
Mean Wind Speed (km/h)	82	79	71	80
Maximum Gust Speed (km/h)	101	96	94	102
Wind Direction	WNW	WNW	WNW	NW
RMS Accelerations (milli-g) (Transverse) (Driver's Head Level)	26	16	19	19
RMS Accelerations (milli-g) (Vertical)	40	33	37	36
Head / Tail Wind Component or Cross Wind	Head Wind Component	Tail Wind Component	Head Wind Component	Cross Wind
Travelled Lane	Bridge Centreline	Bridge Centreline	Windward Lane	Windward Lane
Driver Perception	Distinctly Perceptible	Slightly Perceptible	Slightly Perceptible	Slightly Perceptible
Scale	Scale – 3 (strong*)	Scale – 2 (medium*)	Scale – 2 (strong*)	Scale – 2 (strong*)

* Further subdivision of the scale by the driver e.g. 2 (light), 2 (medium), 2 (strong).

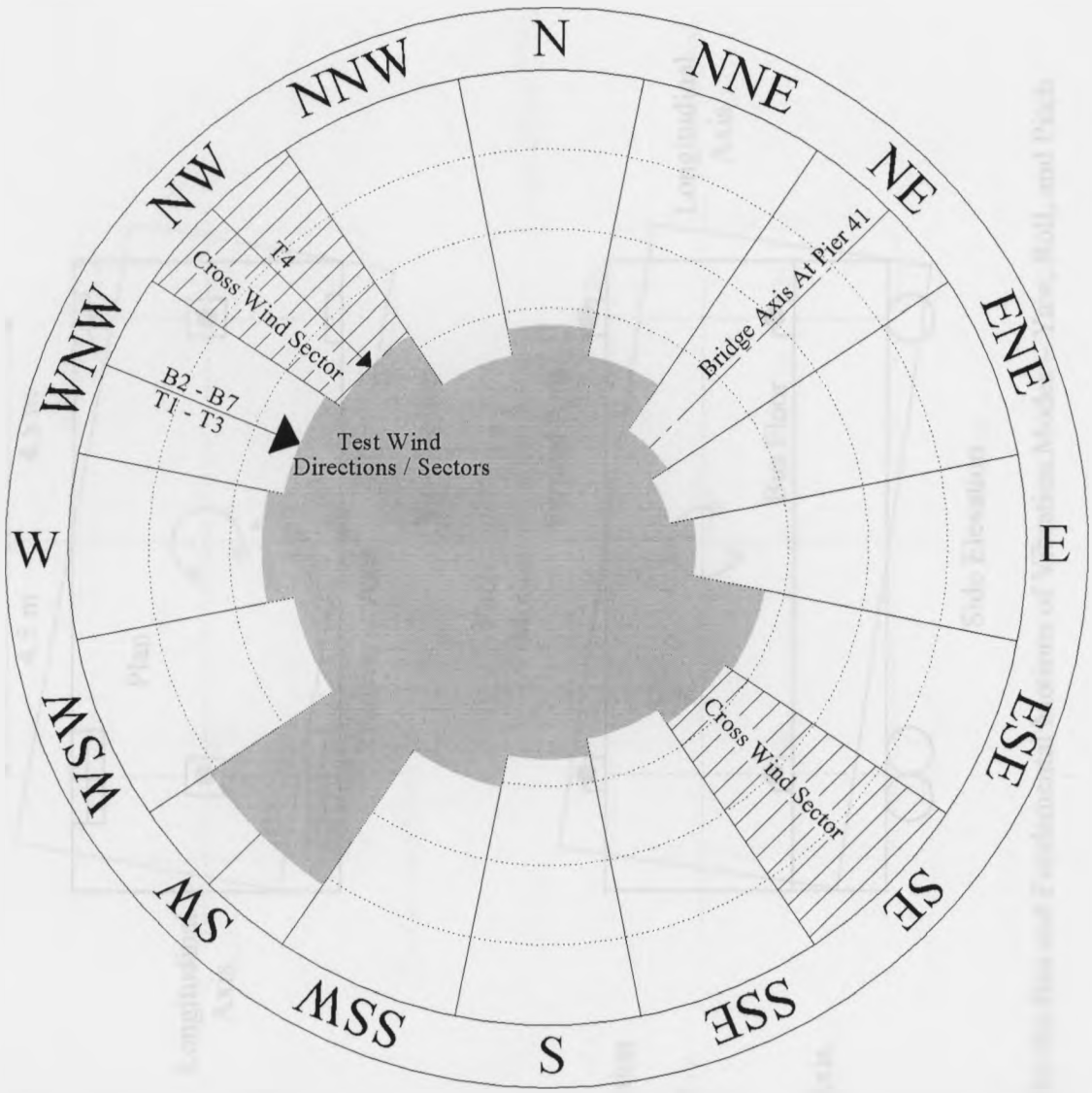

Figure 6.1 – Test Wind Directions Shown on the Wind Rose – Shaded region represents relative frequency of wind speeds measured between 1998 to 2007

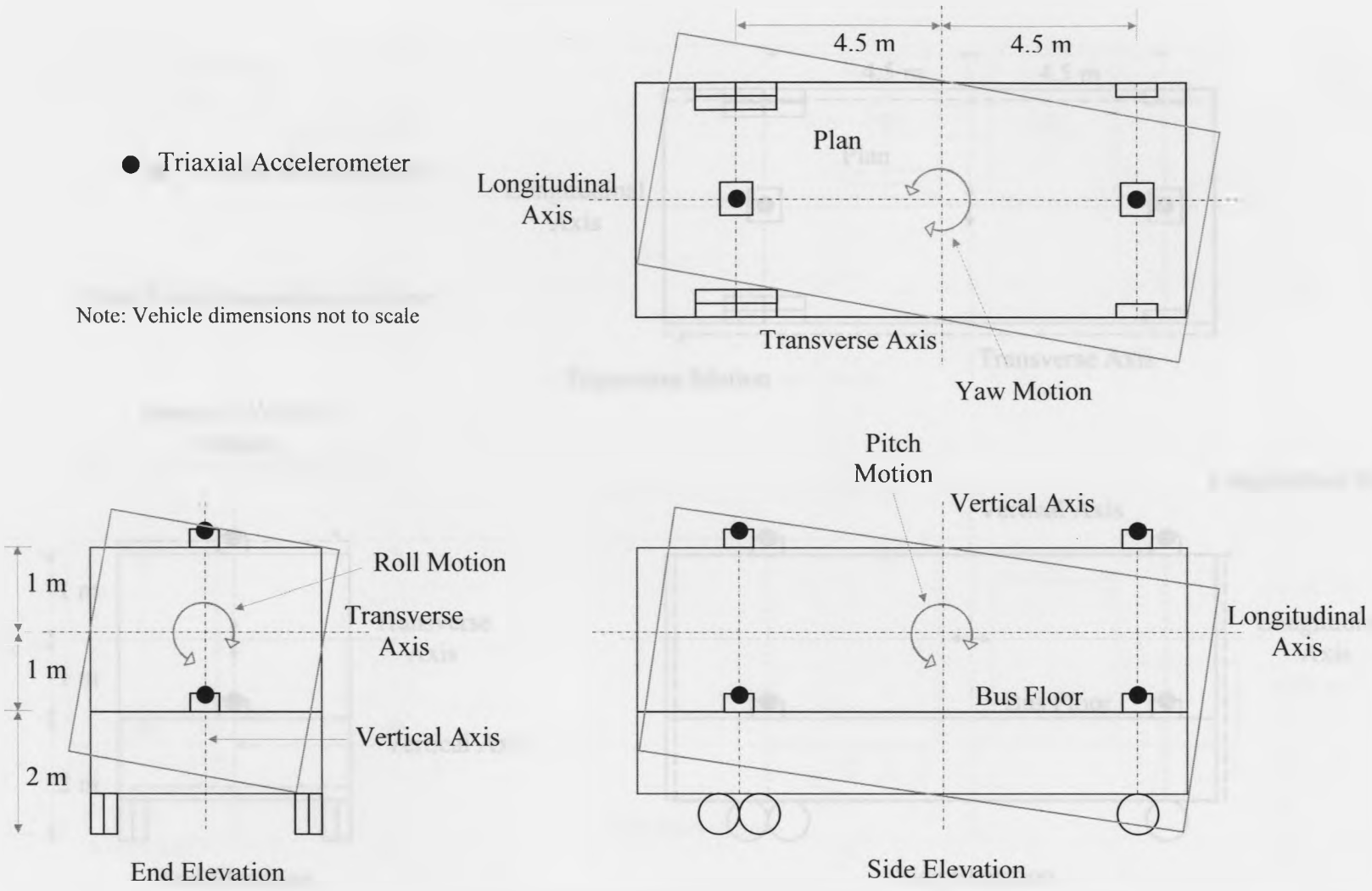

Figure 6.2a – Instrument Layout for the Bus and Fundamental Motions of Vibration Modes – Yaw, Roll, and Pitch

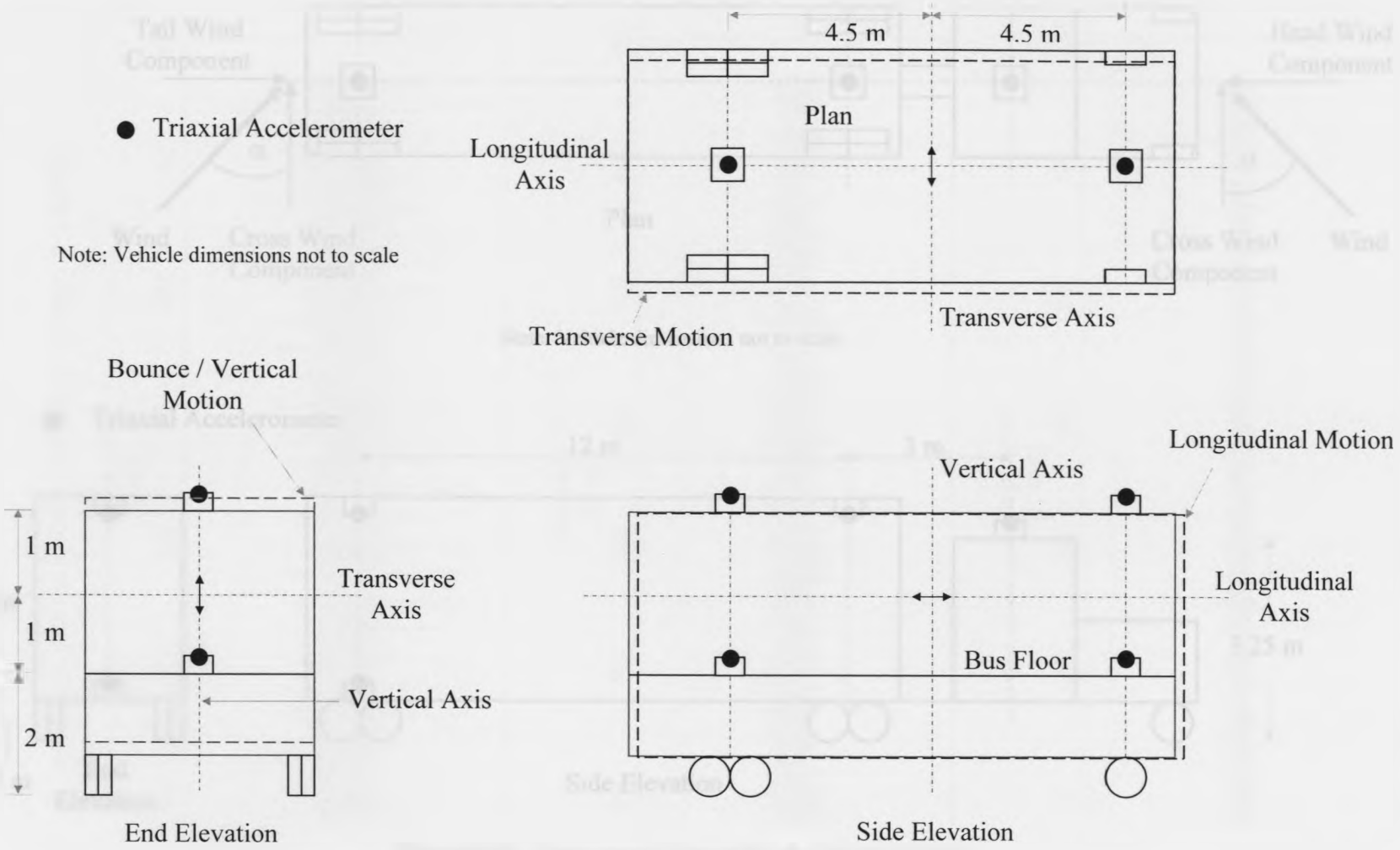

Figure 6.2b – Instrument Layout and Longitudinal, Transverse and Vertical Motions of the Bus

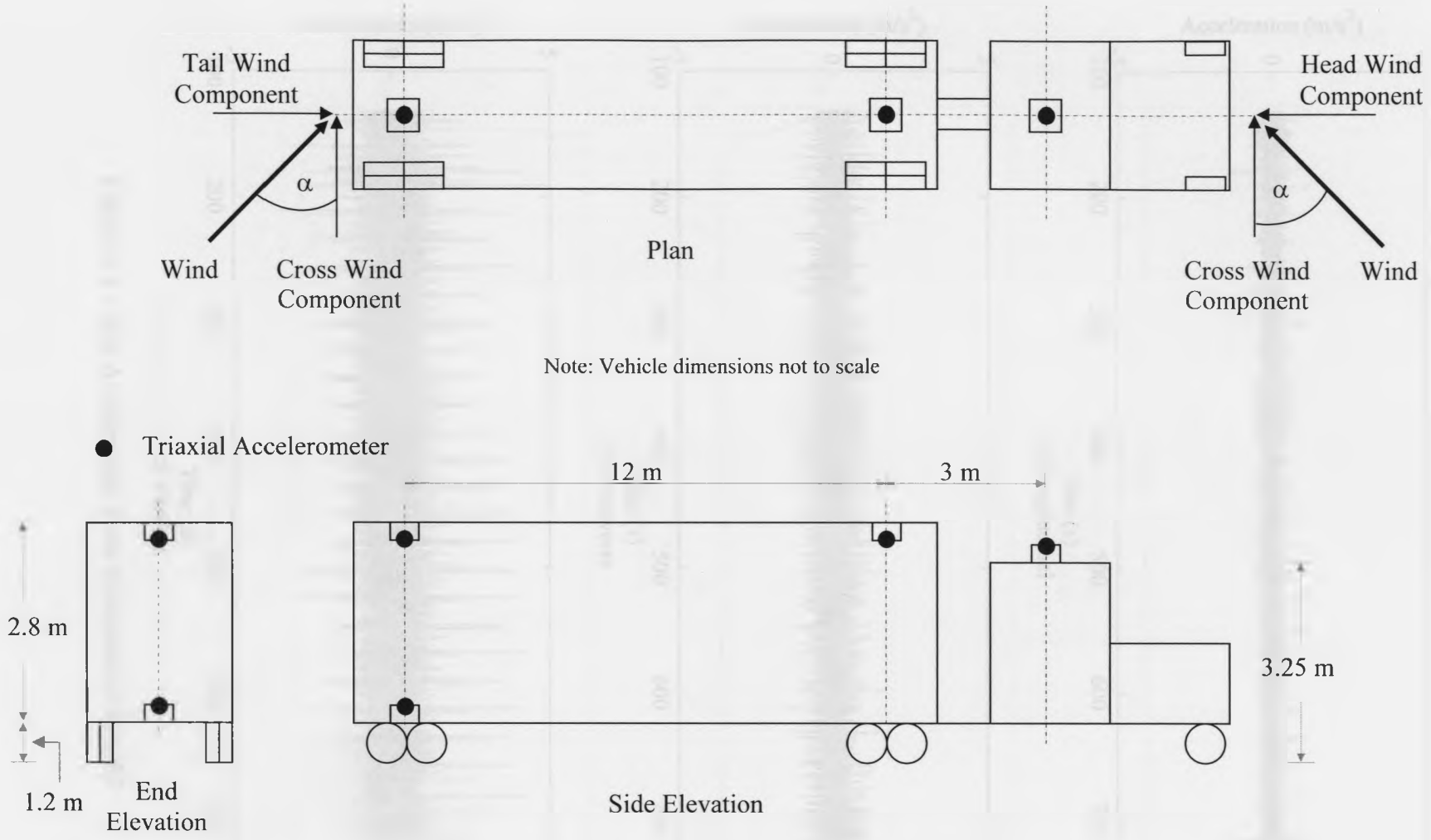

Figure 6.3 – Instrument Layout for the Truck-Trailer

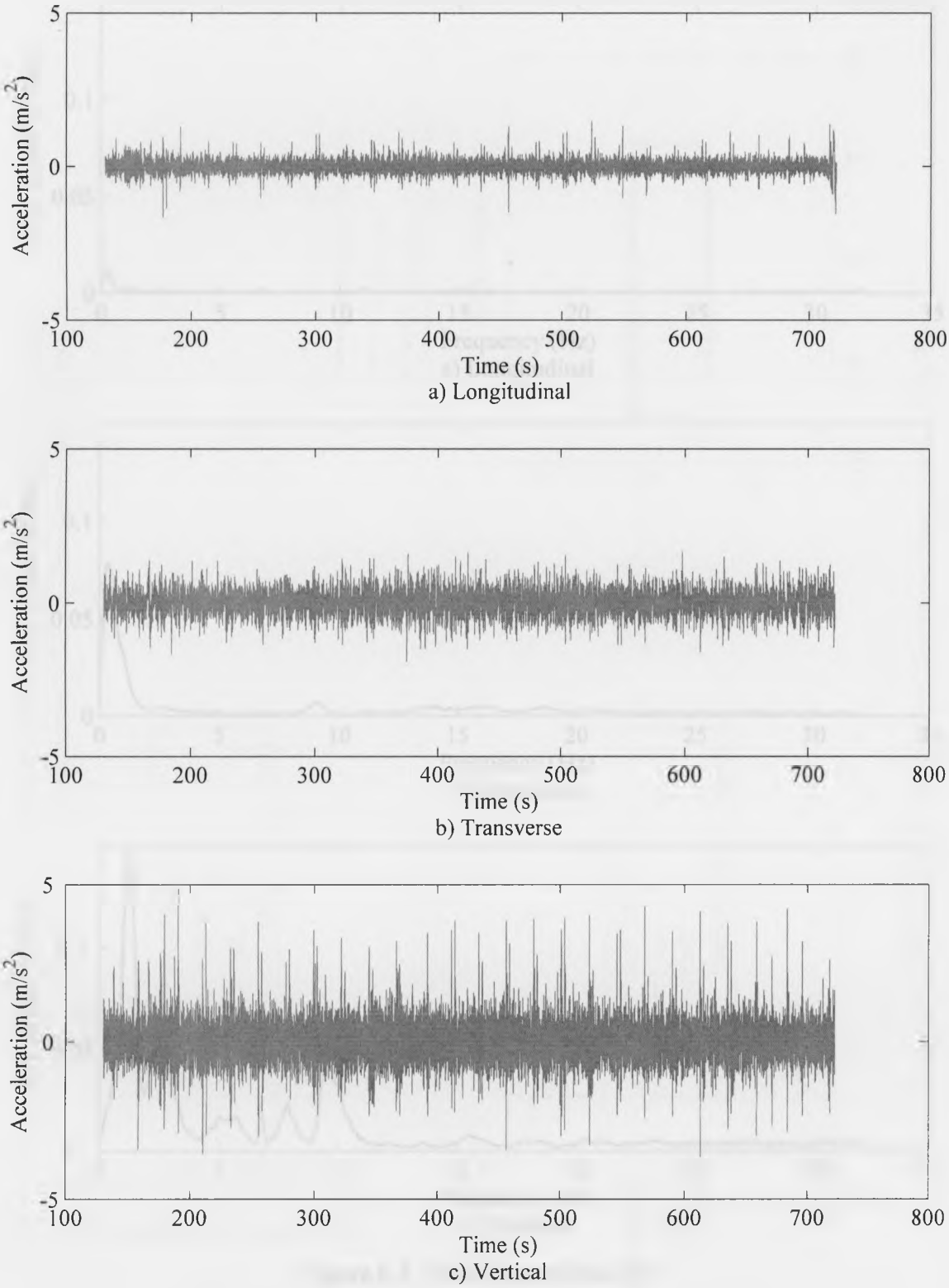

Figure 6.4 – Bus Acceleration Time Histories for Run B7

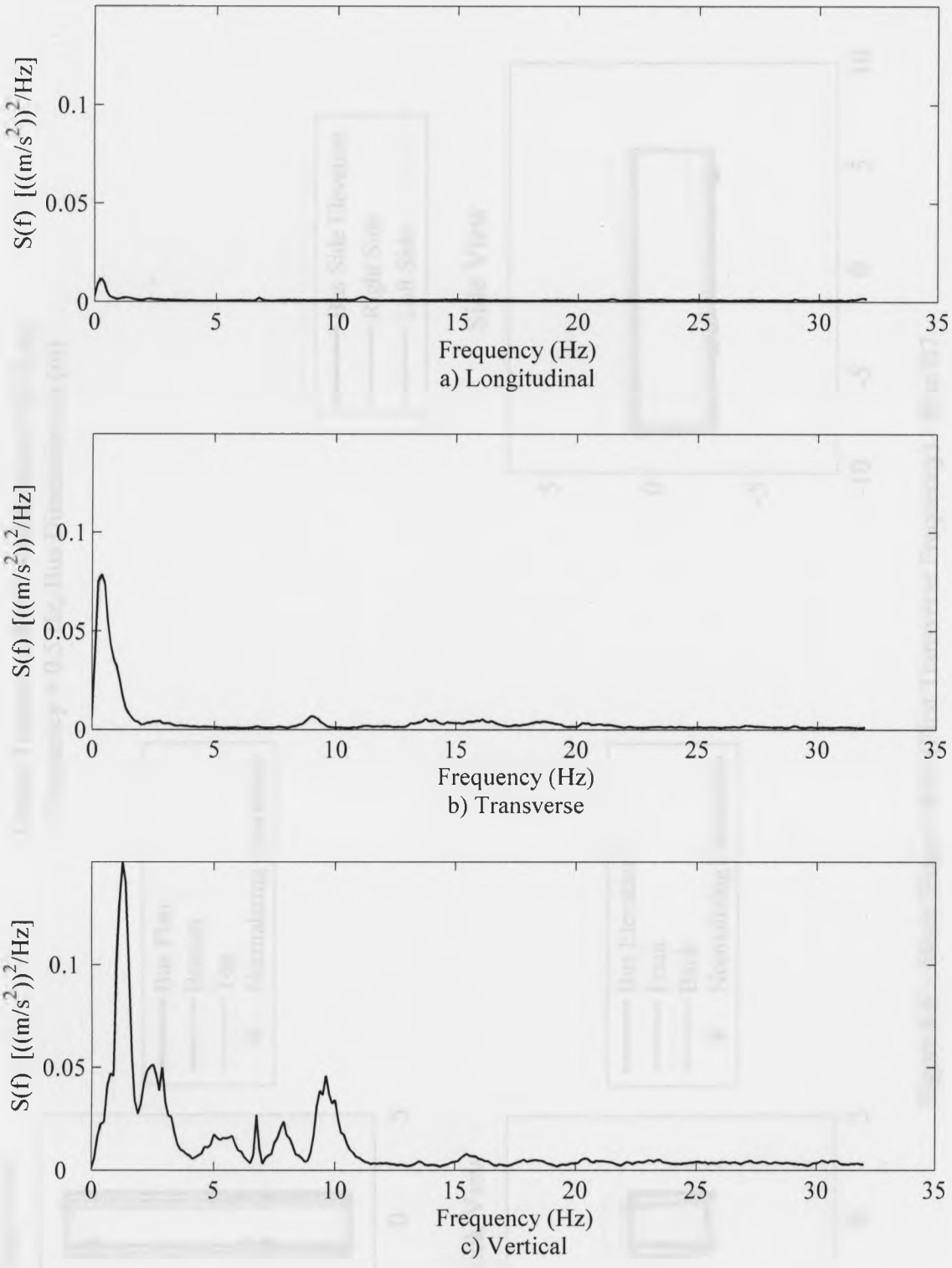

Figure 6.5 – Bus Spectra Run B7

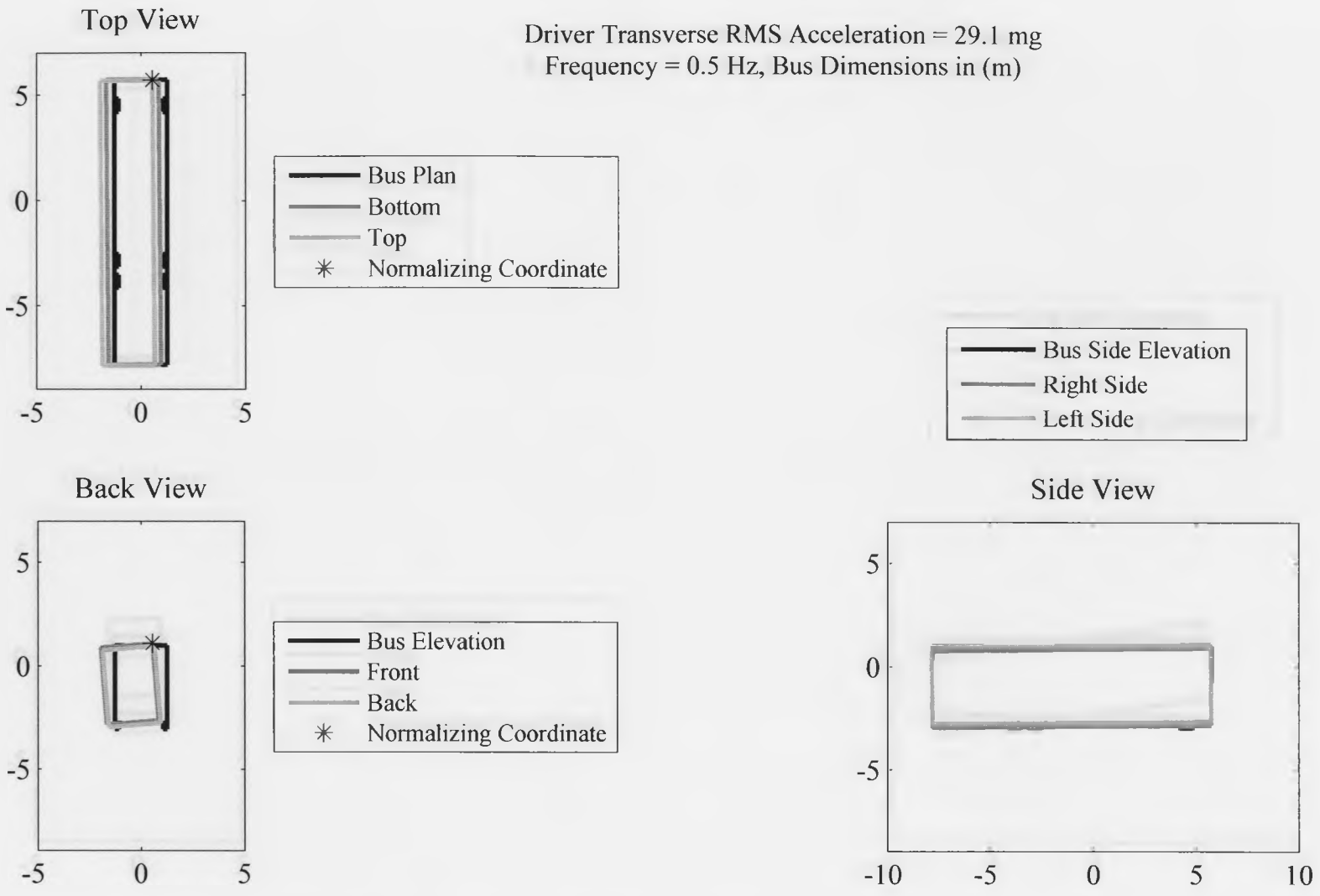

Figure 6.6 – Mode Shape – Roll (First Transverse Frequency) – Run B7

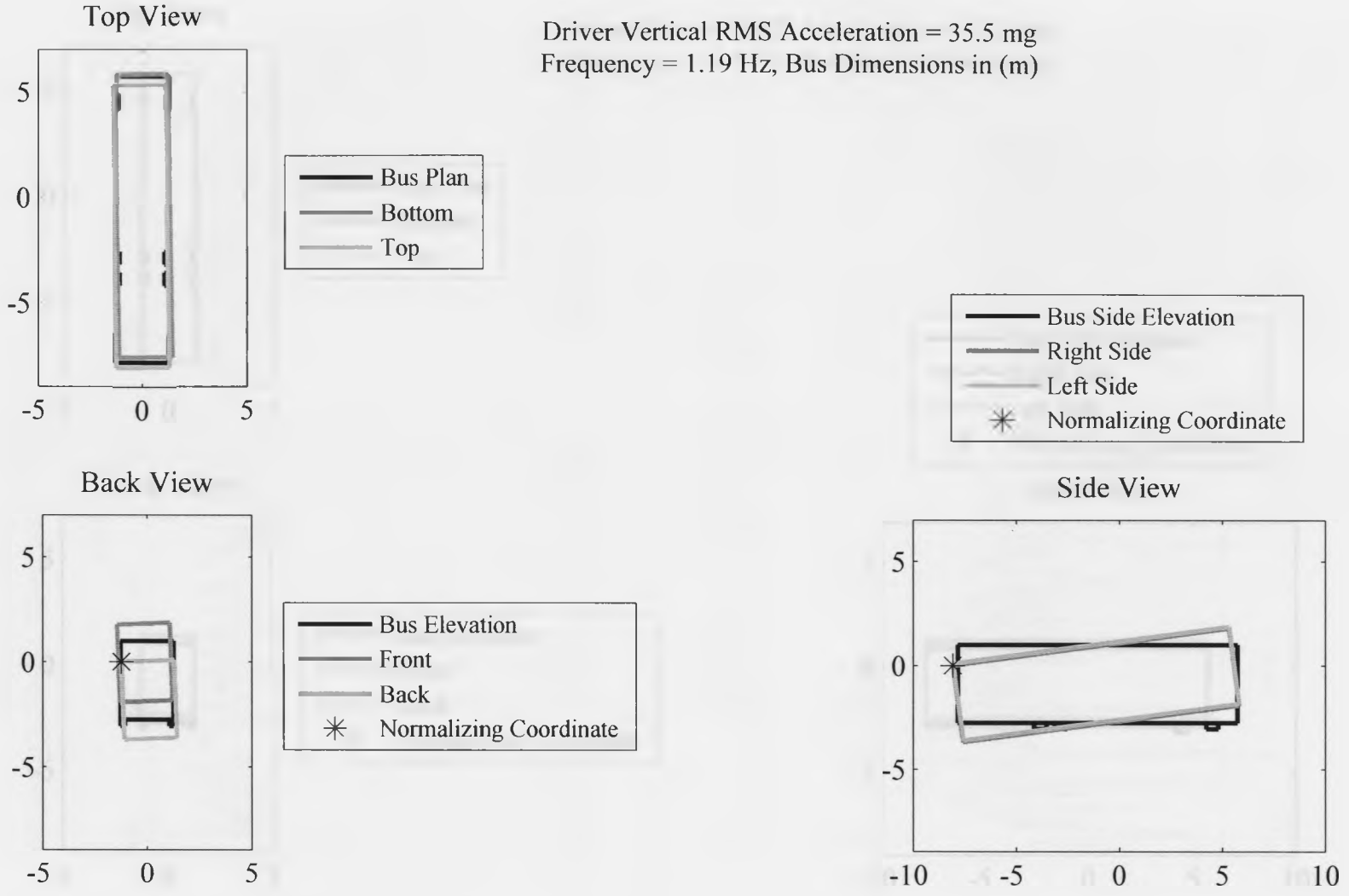

Figure 6.7 – Mode Shape – Pitch (First Vertical Frequency) – Run B7

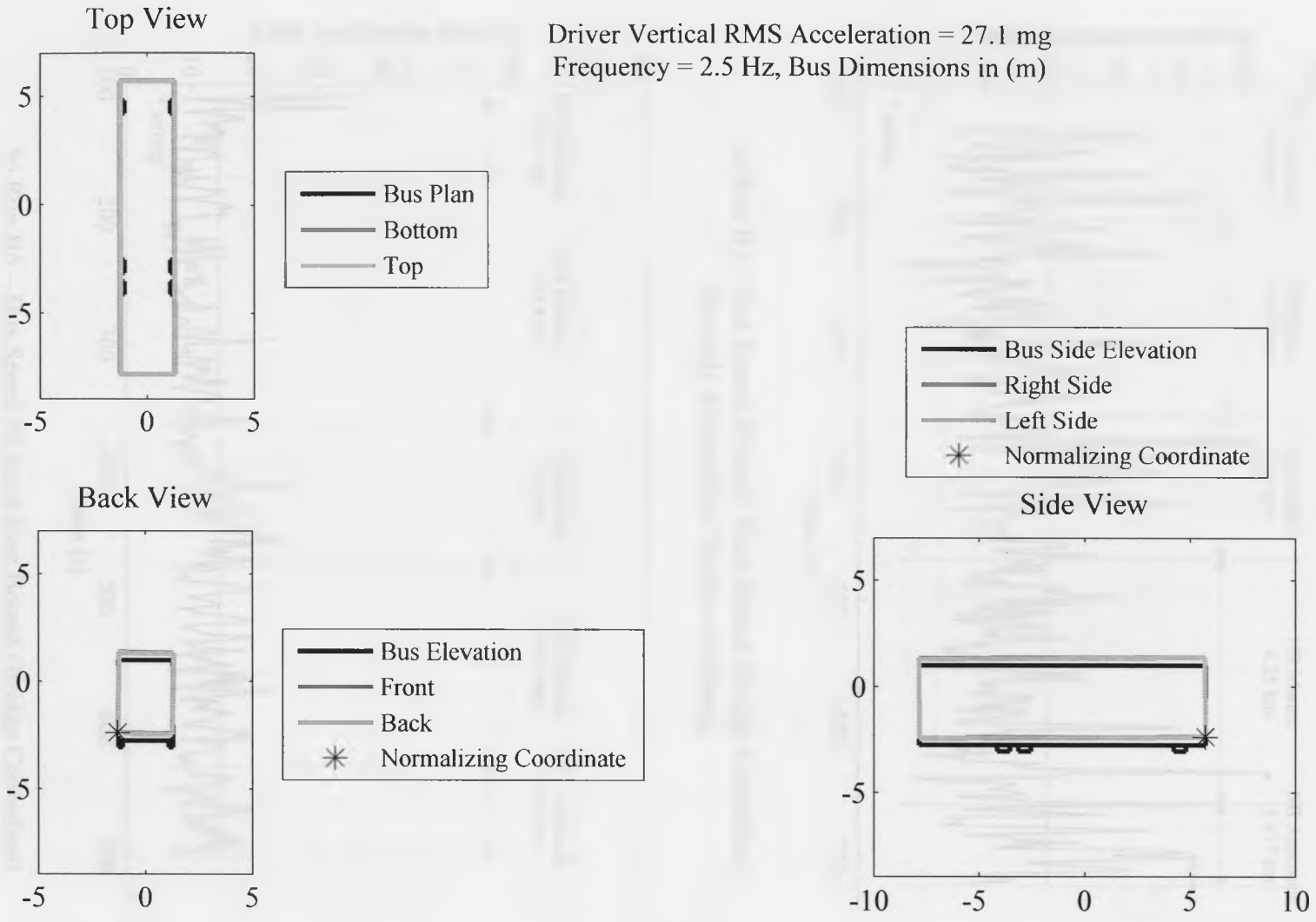

Figure 6.8 – Mode Shape – Bounce (Second Vertical Frequency) – Run B7

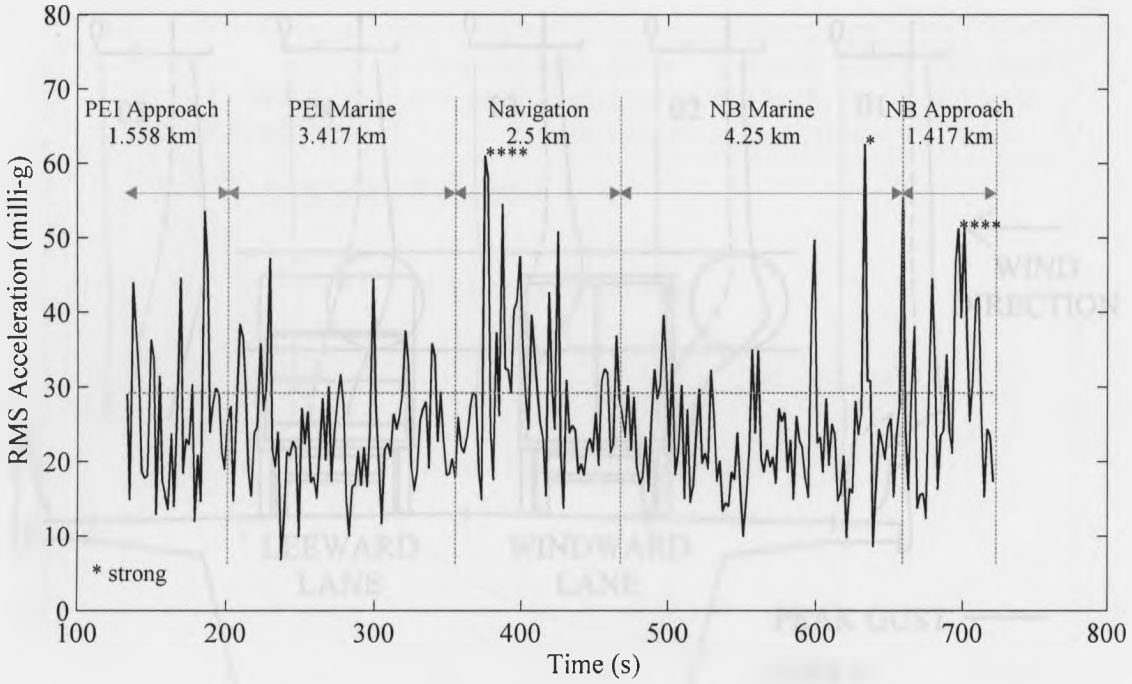

a) Run B7 – Bus Speed 80 km/h West Bound (Bridge Centreline)
Strongly Perceptible / Scale – 4 (strong)

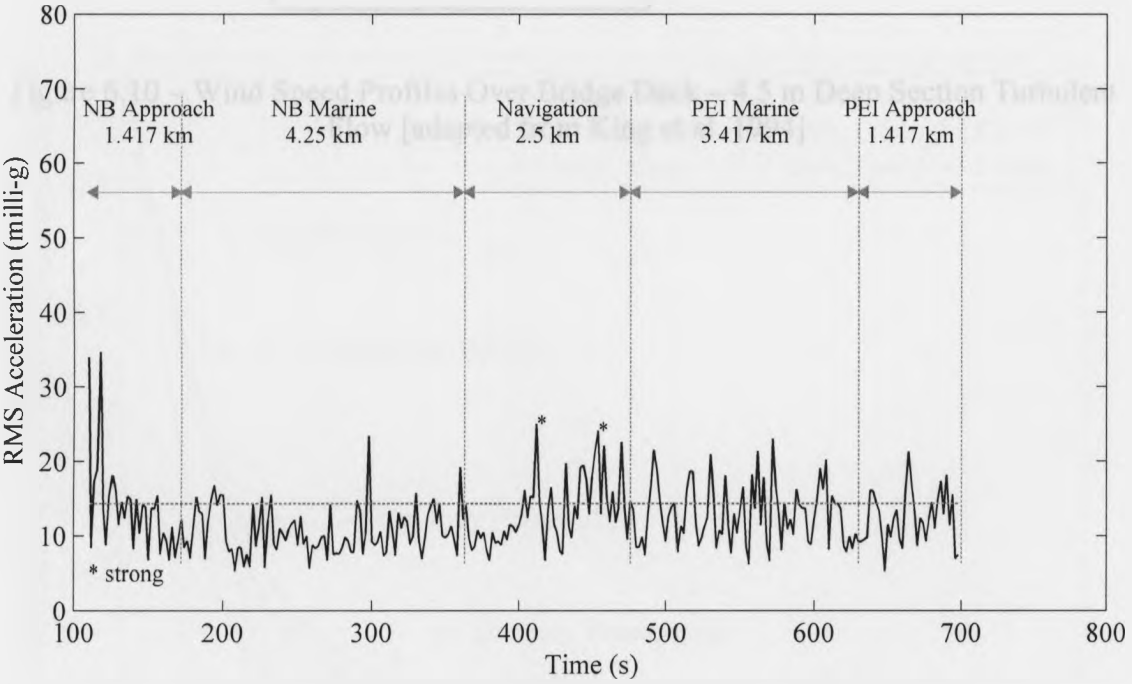

b) Run B6 – Bus Speed 80 km/h East Bound (Bridge Centerline)
Slightly Perceptible / Scale – 2 (strong)

Figure 6.9 – Transverse Two-Second RMS Accelerations at the Driver's Head Level

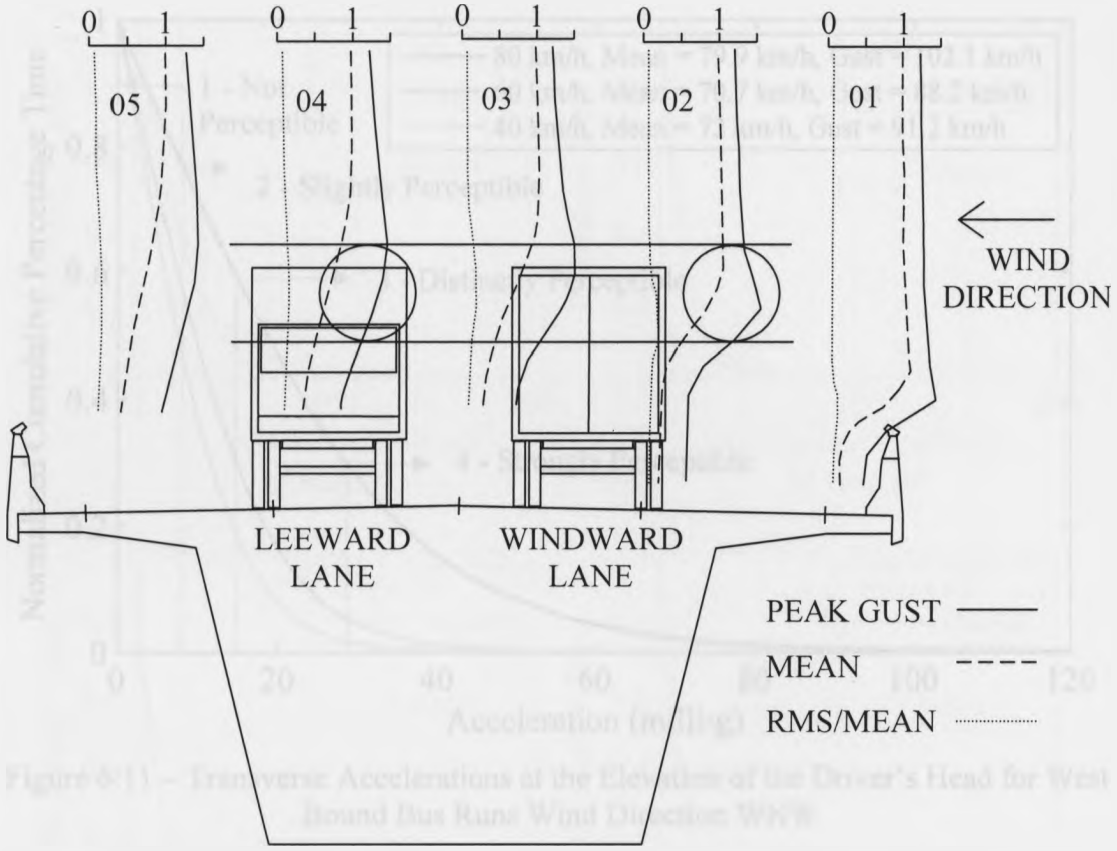

Figure 6.10 – Wind Speed Profiles Over Bridge Deck – 4.5 m Deep Section Turbulent Flow [adapted from King et al. 1994]

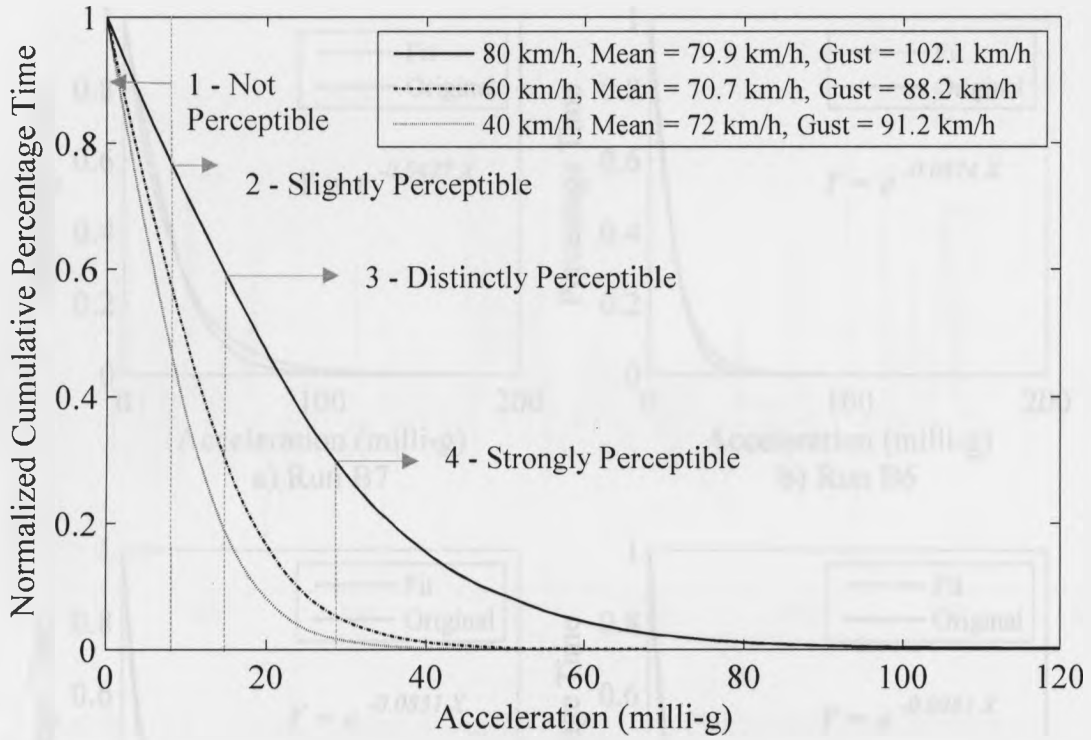

Figure 6.11 – Transverse Accelerations at the Elevation of the Driver's Head for West Bound Bus Runs Wind Direction WNW

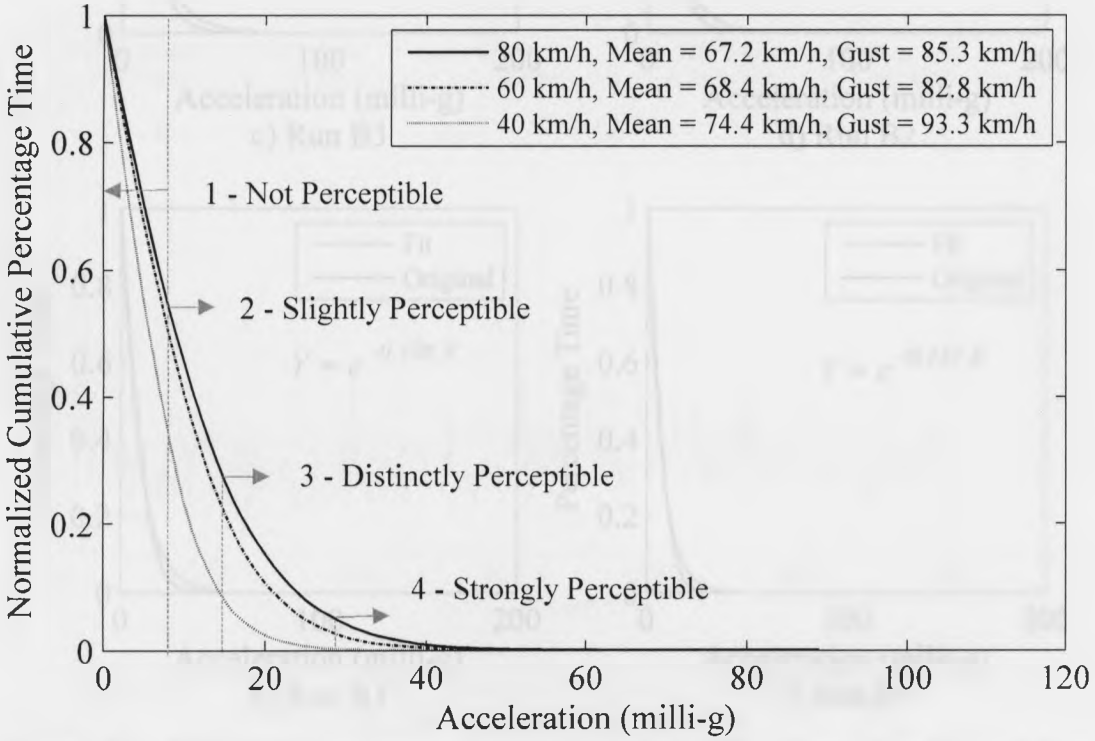

Figure 6.12 – Transverse Accelerations at the Elevation of the Driver's Head for East Bound Bus Runs Wind Direction WNW

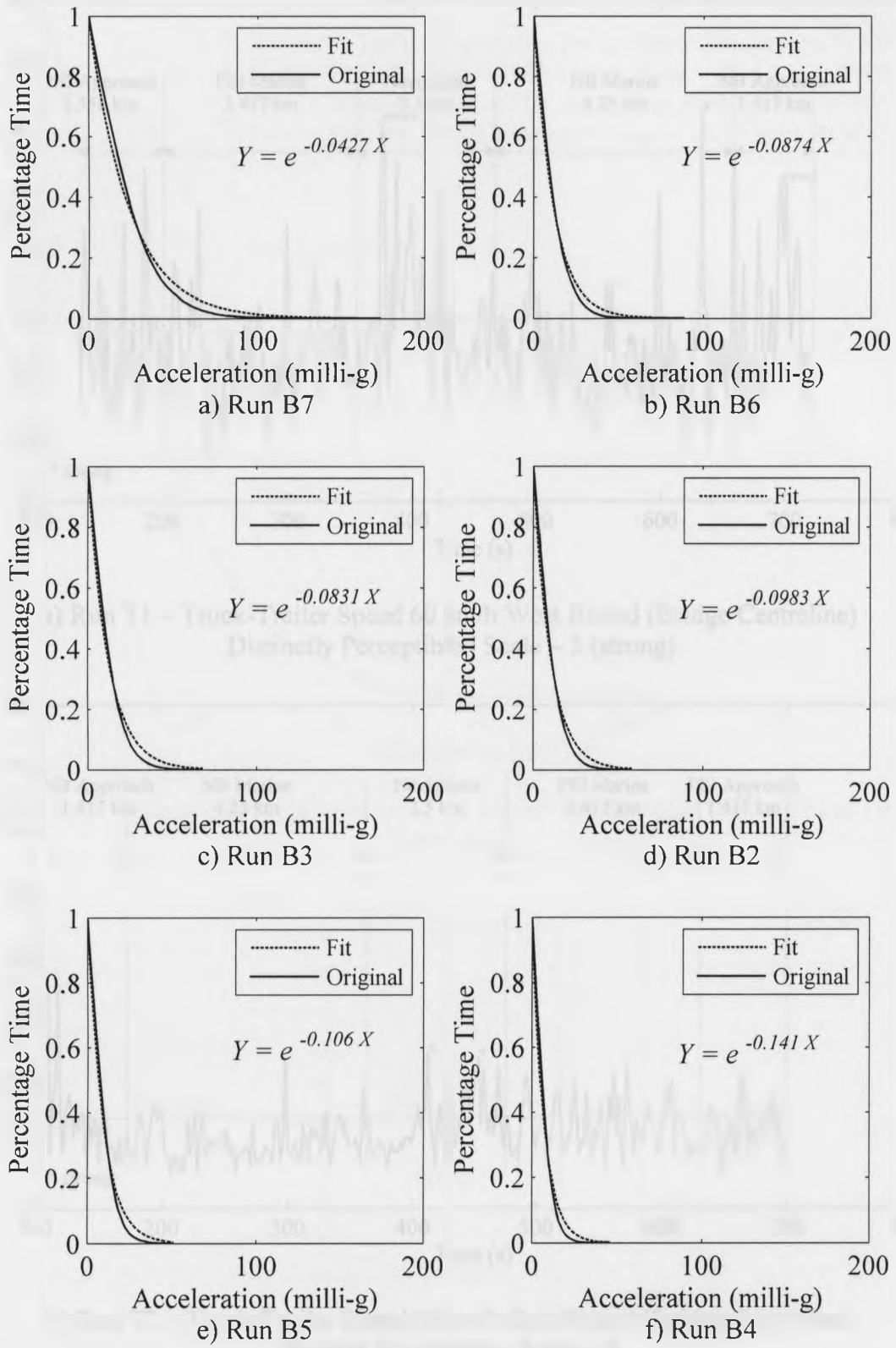

Figure 6.13 – Fits to the Transverse Accelerations at the Elevation of the Driver's Head for the East and West Bound Bus Runs Wind Direction WNW

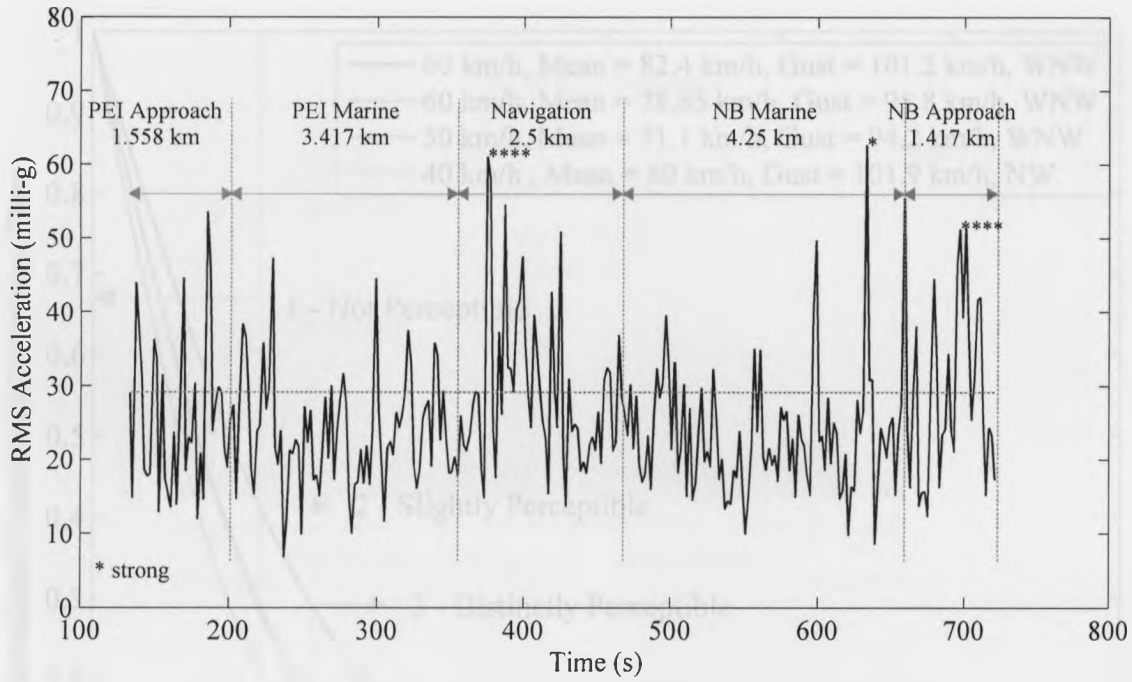

a) Run T1 – Truck-Trailer Speed 60 km/h West Bound (Bridge Centreline)
Distinctly Perceptible / Scale – 3 (strong)

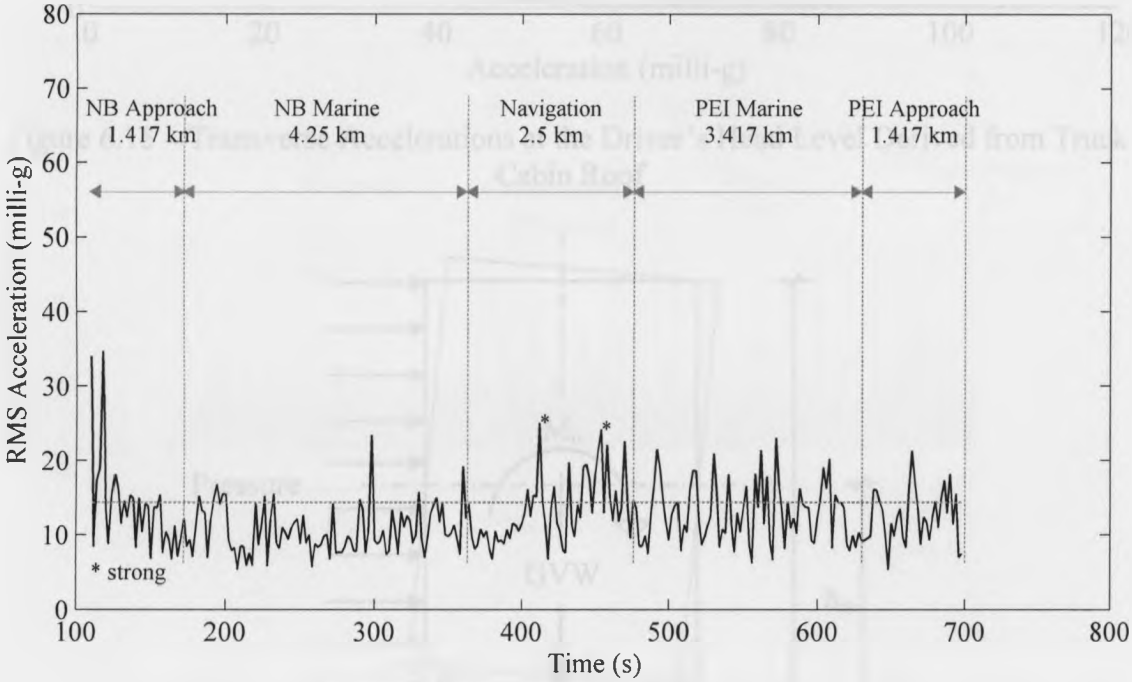

b) Run T2 – Truck-Trailer Speed 60 km/h East Bound (Bridge Centreline)
Slightly Perceptible / Scale – 2

Figure 6.14 – Transverse Two-Second RMS Accelerations at the Driver's Head Level

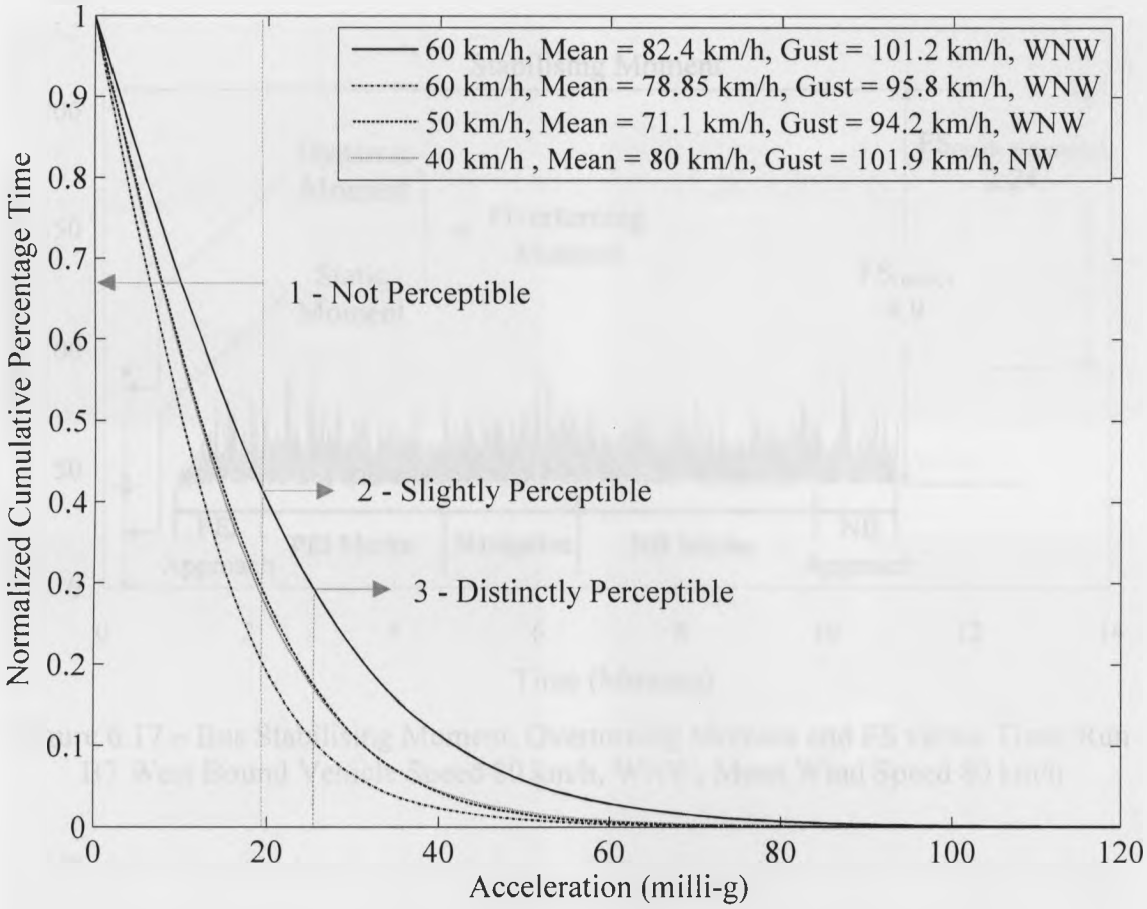

Figure 6.15 – Transverse Accelerations at the Driver's Head Level Derived from Truck Cabin Roof

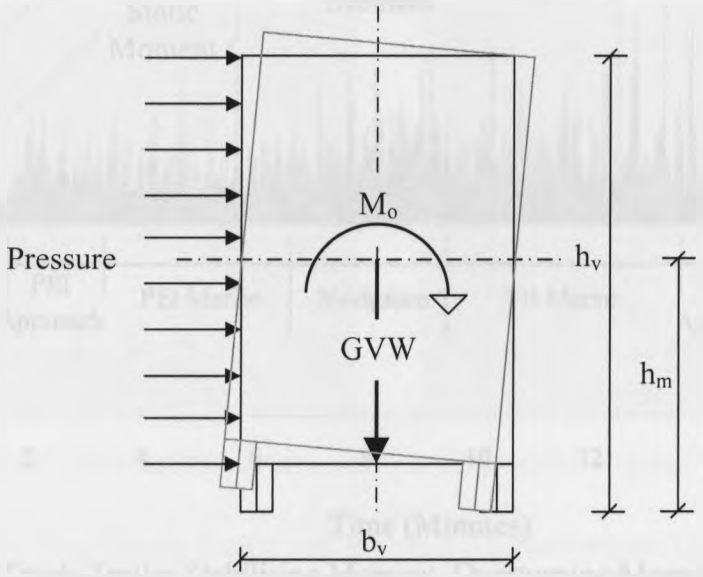

Figure 6.16 – Definition of Factor of Safety

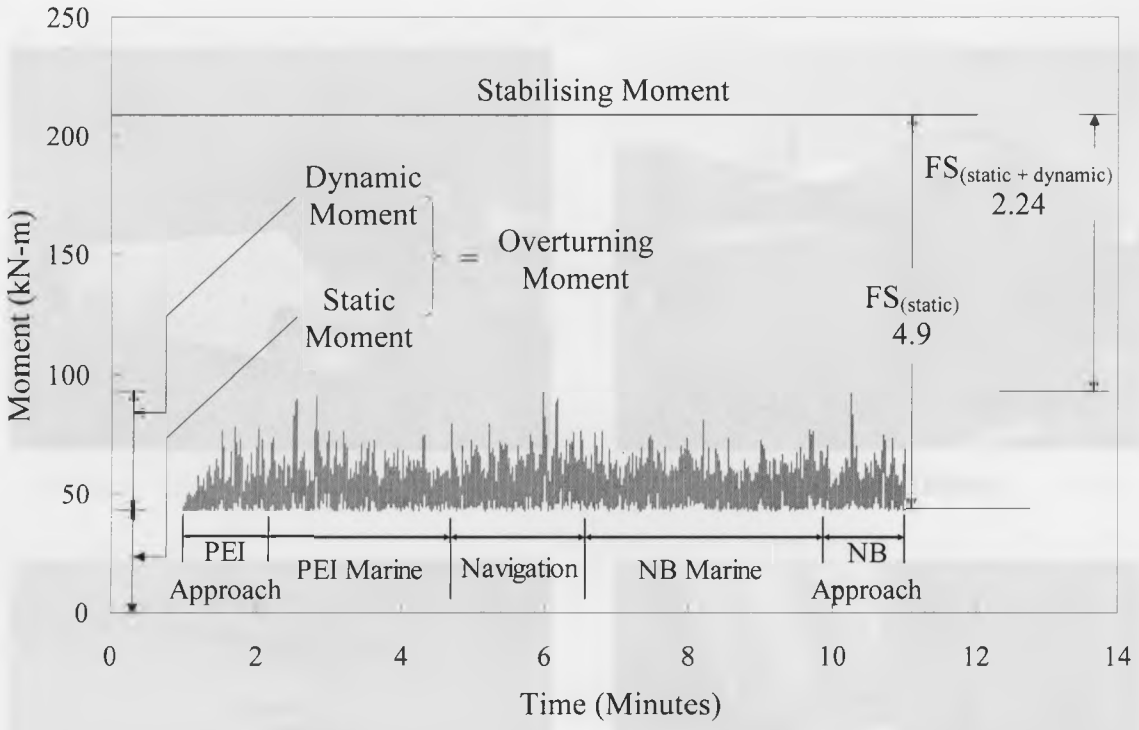

Figure 6.17 – Bus Stabilising Moment, Overturning Moment and FS versus Time: Run B7 West Bound Vehicle Speed 80 km/h, WNW, Mean Wind Speed 80 km/h

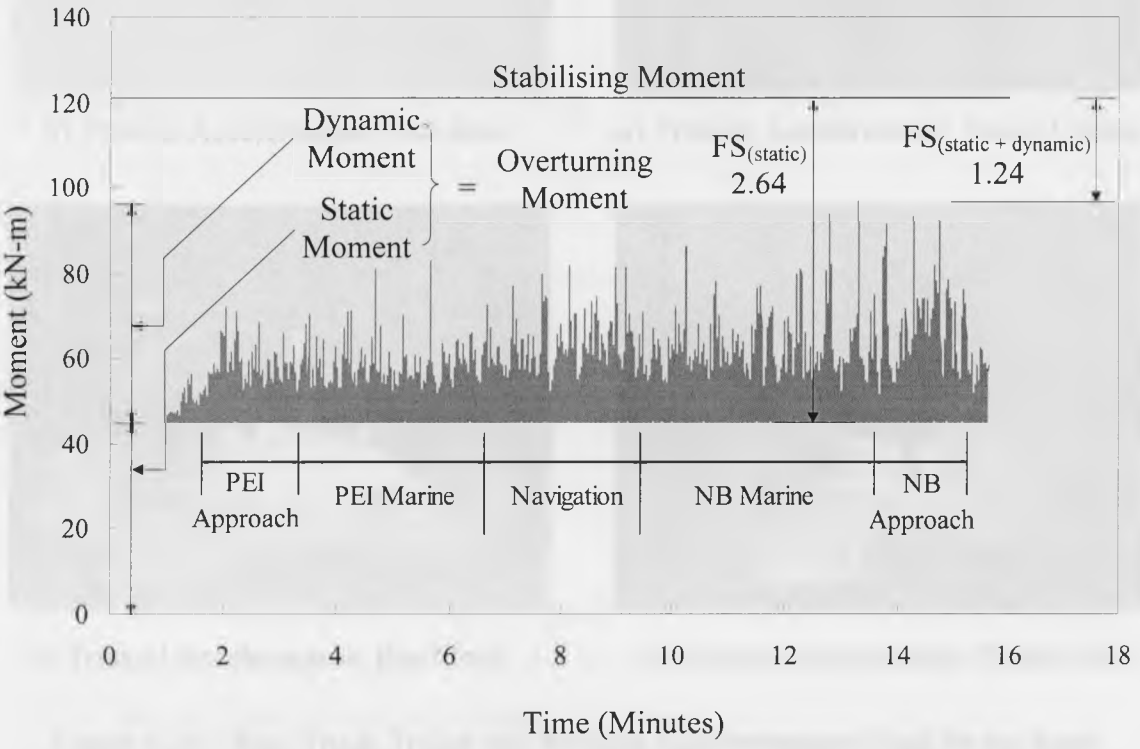

Figure 6.18 – Truck-Trailer Stabilising Moment, Overturning Moment and FS vs. Time: Run T1 West Bound Vehicle Speed 60 km/h, WNW, Mean Wind Speed 82 km/h

a) Bus

d) Truck-Trailer

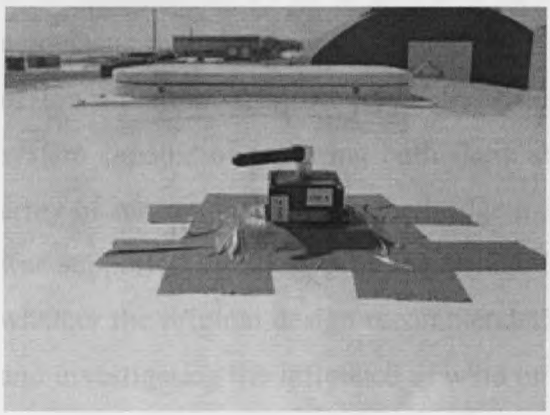

b) Triaxial Accelerometer Bus Roof

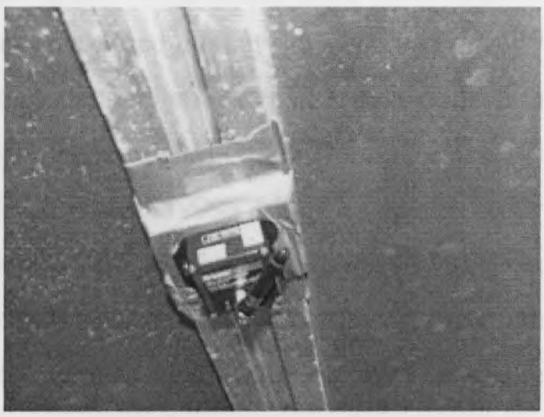

e) Triaxial Accelerometer Trailer Ceiling

c) Triaxial Accelerometer Bus Floor

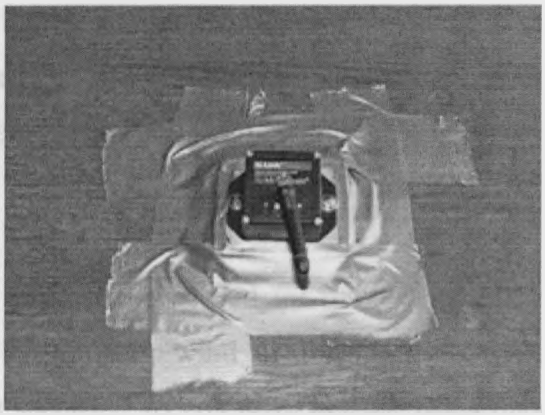

f) Triaxial Accelerometer Trailer Floor

Figure 6.19 – Bus, Truck-Trailer and Wireless Accelerometers Used for the Study

7. SUMMARY, CONCLUSIONS AND RECOMMENDATIONS

The Confederation Bridge is a 13 km long precast concrete structure which has been in service since 1997. The main superstructure is comprised of 43 – 250 m spans in an alternating rigid frame/cantilevered drop-in span arrangement [Tadros 1997]. The Boundary Layer Wind Tunnel Laboratory (BLWTL) was involved with the structural design of the Confederation Bridge defining wind effects on the bridge and on vehicles that cross it [King et al. 1994, King and Davenport 1994a, King et al. 1995]. Given the variable geometry of the structure, particularly the box girder depth that ranges from 4.5 m at midspan to 14 m at the face of the piers, the wind loads were derived from aeroelastic model test results using novel procedures. Recognising the scale and novelty of the structure, the owners of the bridge implemented an extensive data collection system capable of capturing both static and high-speed dynamic data from an extensive array of sensors installed on the bridge in 1997 [Montreuil 1999a &b]. The present study was supported by Strait Crossing Bridge Limited (SCBL) with the intention of verifying whether the original design recommendations based on model-scale studies was accurate and investigating the influence of wind on lightly loaded high-sided vehicles. The on-site monitoring data are used for the first time to compute full-scale wind loads for the Confederation Bridge in particular and the methodology can be generalized to apply to any long-span bridge. The problem of driving light high-sided vehicles across the bridge under high wind conditions has also been addressed. The vehicle-wind interaction and its influence on driver's vehicle control have been studied for the first time. The primary objectives of the study were threefold, namely:

i) To validate the 100-year wind speed originally specified for the design of the Confederation Bridge [King et al. 1994], using wind data from the on-site monitoring programme. The originally specified speeds were derived using data from land-based weather stations and so required manipulation to be extrapolated to a structure located in the middle of the strait.

ii) To investigate the accuracy of the wind loads originally derived, using aeroelastic wind tunnel models, for the design of the Confederation Bridge [King et al. 1994, King and Davenport 1994a, King et al. 1995], using on-site monitoring data and new wind tunnel test data.

iii) To study the impact of extreme winds on the drivers' control of light high-sided vehicles, including buses, crossing the Confederation Bridge, as the basis for a rational refinement of current bridge closure policies.

7.1 Summary

The anemometer data have been organized systematically, for the first time, to build a complete wind database for the Confederation Bridge. Analysis of the on-site monitoring wind data collected between 1998 and 2007 from the anemometer located between Piers 31 and 32 indicates that the harsh marine environment has affected both the quality and quantity of the data collected: only 40% to 50% of the ten-year dataset is archived and accurate. The missing data have been replenished using data from the reliable and accurate anemometer near Pier 20, after minor adjustment necessary due to the 2.83 km distance between the two anemometers. The complete dataset is used to determine the 10-minute mean wind speeds for various return periods, which are compared to the values originally recommended by King et al. [1994]. Unique data collected during the passage of Hurricane Noel for an 18-hour period have been used to derive wind spectra, which are compared to the widely used theoretical spectrum reported by the Engineering Sciences Data Unit [ESDU 1974].

A comprehensive database of statistics and time histories of the available accelerometer and tiltmeter data from the on-site monitoring programme has been developed for the first time. The statistical summaries of the accelerometer data obtained between 1998 and 2006 have been analysed to determine dynamic responses that have been compared to the responses predicted using accelerometer data collected during the Hurricane Noel event. The time histories for both the 1998-2006 and Hurricane Noel datasets have been used to

identify bridge frequencies, which have been compared to the frequencies computed analytically using ALGOR and reported by Londoño [2006]. The total bridge damping for the various mode shapes, estimated using Hurricane Noel time histories, have been compared to the damping estimates reported by Londoño [2006] and Brown and Bruce [1997]. The peak factors have been also computed using Hurricane Noel data and have been compared to the peak factor used for the bridge design [JMI-Stanley 1995]. The variation in the transverse and vertical bridge displacements with wind azimuth has been compared to the conventional cosine-squared relationship shown in Appendix 3C.

To make a credible comparison of the responses between the wind tunnel model and the prototype, the original full-aeroelastic model of the Confederation Bridge [King et al. 1994, King and Davenport 1994a, King et al. 1995] was retested in the wind tunnel with a layout of accelerometers that mimicked their location on-site. A few modifications were made to the aeroelastic model before testing. The model frequencies determined experimentally have been compared to the values determined numerically using ALGOR and the values reported by King et al. [1995]. The structural damping for the various modes of vibration has been estimated using free vibration and autocorrelation techniques [Ochi 1990]. The time histories from the accelerometers have been used to determine the total damping and the variation in the aerodynamic damping with wind speed and azimuth for the fundamental mode shapes. The accelerometer time histories have been used to determine the dynamic responses for the transverse and vertical modes of vibration. The model transverse and vertical displacements for the changing wind azimuth have been compared to the conventional cosine-squared relationship. Finally, data from hot-film anemometers, representing three actual locations of anemometers Pier 31-32, Pier 20-North and Pier 20-South on the Confederation Bridge, have been used to determine normalized polar plots for the upstream/downstream wind speeds in the 16-point compass directions.

The derivation of wind loads from the on-site monitoring data for the Confederation Bridge has, for the first time, validated the methodology developed for the derivation of wind loads using wind tunnel aerodynamic model test data in 1994 [King et al. 1994,

King and Davenport 1994a, King et al. 1995]. The static load coefficients from the tiltmeter data have been compared to the coefficients used for the bridge design in 1994 [JMI-Stanley 1995]. The dynamic load effects derived using loads from the on-site monitoring data have been compared to the load effects derived using loads from the 1994 and 2009 wind tunnel test results. The peak bending moments used for the bridge design have been compared to the peak bending moments derived partly from the 2009 wind tunnel test results (i.e., mean component) and partly from the on-site monitoring data (i.e., dynamic component).

The challenge of driving light high-sided vehicles across the bridge under high wind conditions has been investigated. A preliminary study of drivers' perceptions of light high-sided vehicle control on the Confederation Bridge during severe crosswinds has been conducted. A bus and a truck-trailer were instrumented with wireless accelerometers and two professional driving instructors drove the vehicles across the bridge several times under high wind conditions. Each driver verbally characterized the effect of the wind on his driving experience on a scale of 1 to 5 (i.e., "Not Perceptible" to "Disturbing"). The drivers' perceptions of the wind effect on controlling the vehicle under different travelled and wind conditions have been correlated with the vehicle/driver acceleration data. A quantitative estimate of the factor of safety against roll-over has been developed based on the measured dynamic responses of the vehicles and using published data from wind tunnel pressure tests on similar vehicle types [King and Kong 2001].

7.2 Conclusions

The following major conclusions are drawn from the study:

1. The methodology developed for the derivation of dynamic wind loads, originally based on wind tunnel tests of an aerodynamic model carried out in 1994 [King et al. 1994, King and Davenport 1994a, King et al. 1995], has been validated for the first time using on-site monitoring data for the Confederation Bridge. The dynamic load effects predicted using 2009 wind tunnel loads adjusted to the prototype damping

are within 5% of the values predicted using loads determined from the on-site monitoring data.

2. The 1994 methodology [King et al. 1994] used to map land-based anemometer data to the middle of the strait has been validated. Analysis of the on-site monitoring wind data indicates that the 10-minute mean wind speed with a 100-year return period at an elevation of 40.8 m above MSL is 33.6 m/s. This value is within 1.5% of the original specified design wind speed of 34.1 m/s.

3. The static force coefficients derived based on section model tests carried out in 1994 [King et al. 1994] have been validated using on-site monitoring tiltmeter data. The static load coefficients estimated using tiltmeter data reported by Bruce and Croasdale [2001] are within 1% of the static loads originally used for the bridge design [JMI-Stanley 1995].

4. The damping estimates available from the on-site monitoring data are essential for accurate prediction of the wind loads and load effects. The dynamic load effects predicted using 1994 design loads corrected to the prototype damping are 6% greater in the transverse direction and 28% -58% greater in the vertical direction than the load effects derived from the on-site monitoring data. The 1994 design loads predict transverse load effects that are in good agreement with the full-scale values. The vertical load effects due to the 1994 design loads are conservative, but markedly less conservative than those obtained using the smaller damping value originally assumed.

5. The drivability study found that the perceived vehicle control improves as vehicle speed reduces under similar wind and travelled lane conditions. The current bridge operation procedure that restricts high-sided vehicles from crossing the bridge when the wind exceeds 70 km/h in any direction was not perceived to be unsafe by either of the professional driving instructors who participated in the study.

6. The driver's perceptions of the wind effect seem most strongly correlated to the transverse vehicle accelerations. Both bus and truck-trailer runs show that transverse vehicle accelerations increase with increased vehicle speed for a given vehicle direction and wind direction.

7. The factors of safety against roll-over for the bus and truck-trailer suggest the truck-trailer is more susceptible to roll-over under similar wind conditions. The minimum factors of safety against roll-over for the bus and the trailer during various passages were 2.2 and 1.2, respectively, even though the bus speed was 25% greater and all other conditions (travelled lane, wind speed and direction) were the same. This is attributed to the stabilising moment for the bus being almost twice that for the trailer. Since the study was designed primarily to access the driver's perception of the vehicle control under high wind conditions, these factors of safety are preliminary and should be used with caution.

Other conclusions are:

8. The most severe wind event that the bridge has been subjected to was the November 7, 2001 storm where the 10-minute mean wind speed at the marine span deck elevation, 40.8 m above MSL, was 30.5 m/s normal to the bridge axis. This is equivalent to the originally specified design wind event. However, the transverse force effects caused by this storm were 84 to 90% of those caused by the 1994 specified design loads, and the vertical force effects are 51 to 60% of those caused by the 1994 specified design loads.

9. The passage of Hurricane Noel on November 4, 2007 recorded a maximum ten-minute mean wind speed of 33.2 m/s at the marine span deck elevation, which is the maximum observed wind speed that the bridge has been subjected to to-date. The corresponding wind azimuth was 200^{o} with respect to Bridge North or 20^{o} off normal to the longitudinal axis of the bridge. The design wind speed for the Confederation Bridge [King et al. 1994] considering all wind azimuths is 34.1 m/s

at the deck elevation of the marine span, so the actual wind speed approached the specified design value during this event. However, the transverse and vertical force effects caused by this storm were only 71 to 80% and 38 to 47%, respectively, of those caused by the specified design loads, because the wind was not normal to the bridge axis.

10. The Random Decrement Method (RDM) [Cole 1973] gives better damping estimates than Autocorrelation [Ochi 1990] for the on-site monitoring data. The total damping values determined using the data collected during the Hurricane Noel event are 1.8% to 4.7% of critical, except for the first vertical asymmetric mode (VA1) which is 7%, when computed using the Autocorrelation method and only half as large, 3.9% of critical, when computed using RDM. The damping estimates reported by Londoño [2006] for the fundamental modes of vibration range from 1.3% to 3.8% of critical and are in close agreement with those determined using RDM. The structural damping estimates by Brown and Bruce [1997] range from 5.5% to 7.7% of critical for the three transverse modes of vibration and are the largest of all the reported values.

11. Though based on experience, the specified peak factor of 3.5 used for the design of the Confederation Bridge in 1994 [King et al. 1994, JMI-Stanley 1995] has been validated using on-site monitoring data. The peak factors determined using accelerations recorded during the Hurricane Noel event range between 2.5 to 5 for wind speeds greater than 15 m/s. The mean peak factor of 3.47 is within 1% of the peak factor of 3.5 originally recommended in 1994 for the bridge design.

12. The present extensive arrangement of accelerometers is not required to determine the wind-induced response of the Confederation Bridge. Only eight accelerometers (four transverse and four vertical) at critical bridge locations are necessary to fully characterize the total and modal dynamic responses of the bridge due to wind. The data from 76 accelerometers attached to the Confederation Bridge were analysed

and most of the accelerometers were found to provide redundant information concerning behaviour during an extreme wind event.

13. The current data sampling, both for the Slow Speed and High Speed Data Loggers, is inadequate for monitoring the wind response of the Confederation Bridge. It has been shown that a ten-minute accelerometer time history sampled at 125 Hz or 20 Hz yields similar acceleration power spectra provided the number of spectral averages is same. Thus lowering the sampling frequency to 20 Hz could enable the duration of the time history record to be increased 4 to 5 times without compromising the accuracy of the acceleration power spectrum. In spite of strenuous efforts, the time histories collected from the Slow Speed Data Logger (SSDL) between 1998 and 2007 could not yield a wind power spectrum because the time histories are too short, have missing data points, and have been sampled at a very low frequency of 1 Hz. The analysis of the Hurricane Noel wind data indicate that a minimum of 2 Hz sampling frequency for 2 to 3 hours duration is essential to derive a reliable wind power spectrum.

14. It is an accepted assumption that wind pressures normal to a surface, and the associated forces and deflections, are proportional to the square of the cosine of the angle between the wind azimuth and the line normal to the bridge axis. The on-site monitoring data indicate this is not the case for the Confederation Bridge, as the bridge modal displacements for winds blowing along the bridge axis were 55% to 65% of that observed for winds blowing normal to the bridge axis. The cosine – squared relationship underestimates the wind tunnel bridge deflections in the transverse direction; however, it simulates the bridge deflections reasonably well in the vertical direction. The difference in the behaviour between the deflections computed from the on-site monitoring data and 2009 wind tunnel test results is not well understood and requires further investigation.

7.3 Recommendations for Future Research

The main recommendations for future research are as follows:

1. The results of the present study can be used to develop a condition assessment tool for the short- and long-term management of the Confederation Bridge. An efficient post-event assessment procedure can be implemented, using charts and a simple computer programme, where the user could input the wind speed and direction of a severe wind event, as recorded by the anemometers currently mounted on the bridge, and the corresponding force effects at critical bridge locations could be computed for comparison to the design force effects to decide whether an immediate structural inspection and/or traffic load restrictions were necessary.

2. The on-site monitoring system should be reconfigured to avoid data loss. The current High Speed Data Logger programming that stops collection of time history data when the instantaneous wind speed drops below 15 m/s is unsatisfactory and should be changed as it can create gaps in, and so ruin, the time history record. The High Speed Data Loggers, once triggered, should collect accelerometer time history data without interruption for the entire wind event as continuous data collected for an extended period provide more accurate results and offer more flexibility in the analysis.

3. Further vehicle tests covering different wind and travelled lane conditions and drivers with different perception levels are required to develop a methodology to assess the severity of a wind storm and so be able to rapidly and rationally determine an operational response i.e., partial or complete bridge closure that could be implemented to regulate traffic on the bridge. The development of evidence-based closure protocols has the potential to reduce the duration and number of bridge closures without compromising safety of the users.

Other recommendations are:

4. Further vehicle tests are required for winds from the NNW or ESE sectors to investigate whether the presence of a head-wind component or travelling in the windward lane more strongly influences the driver's perception. This would require collecting data while travelling in the westward lane for the eastbound passage with winds approaching from the ESE sector and vice versa.

5. Further vehicle tests should investigate the accuracy of the method for interpolating the accelerations at the driver's head. This would require measuring accelerations at the elevation of the driver's head using an accelerometer mounted on a rigid bar hanging from the ceiling of the cab. The driver should also wear an accelerometer on his/her head so that the actual accelerations of the head could be known.

6. In part, to account for the variable driver sensitivity to wind effects, a database of wind conditions (average and gust speed, direction) and driving direction which have been perceived to be unsafe, based on past and future anecdotal evidence, could be developed. Eventually, this could lead to the development of an operations decision assistance tool.

7.4 References

Brown, T. G., and Bruce, J. R. 1997. *Confederation Bridge Ice Force Monitoring Joint Industry Project Annual Report*, IFN Engineering Ltd.

Bruce, J. R., and Croasdale, K. R. 2001. *Confederation Bridge Ice Force Monitoring Joint Industry Project Annual Report,* IFN Engineering Ltd. Report Number 00-1-001, 40 p.

Cole, A. H. 1973. *On-line Failure Detection and Damping Measurement of Aerospace Structures by Random Decrement Signatures*, CR-2205, NASA.

Engineering Sciences Data Units. 1974. *Characteristics of Atmospheric Turbulence near the Ground, Part II: Single Point Data for Strong Winds (Neutral Atmosphere)*, ESDU Report 74031, ESDU International.

JMI-Stanley. 1995. *Design Criteria Northumberland Strait Crossing Project*, Jean Muller International, Stanley Joint Venture Inc.

King, J. P. C., Mikitiuk, M. J., Davenport, A. G., and Isyumov, N. 1994. *A Study of Wind Effects for the Northumberland Straits Crossing,* BLWT-SS8-1994, Boundary Layer Wind Tunnel Laboratory, University of Western Ontario, London (Parts of this report have been published in King 1999).

King, J. P. C. and Davenport, A. G. 1994a. *The Estimation of Dynamic Wind Load Coefficients for the Northumberland Straits Crossing, PEI,* BLWT-IR-N62-16-1994, Boundary Layer Wind Tunnel Laboratory, University of Western Ontario (parts of the report have been published in King and Davenport 1994b and King 1999).

King, J. P. C., and Davenport, A. G. 1994b. P.E.I. Fixed Link – The Treatment of Wind Effects for the Northumberland Strait Crossing, *Fourth International Conference on Short and Medium Span Bridges*, Halifax, Nova Scotia, Canada.

King, J. P. C., Crooks, G. J., and Davenport, A. G. 1995. *The Northumberland Straits Crossing, Prince Edward Island Testing of Marine Span Aeroelastic Model and Analysis of Dynamic Wind Loads*, BLWT-SS24-1995, Boundary Layer Wind Tunnel Laboratory, University of Western Ontario, London (Parts of this report have been published in King 1999).

King, J. P. C. 1999. Integrating Wind Tunnel Tests of Full-Aeroelastic Models into the Design of Long Span Bridges, *Proceedings of the Tenth International Conference on Wind Engineering (ICWE),* Copenhagen, Denmark, pp 927-934.

King, J. P. C., and Kong, L. Z. 2001. *A study of Wind Effects for Bronx-Whitestone Bridge,* BLWT-SS25-2001, Boundary Layer Wind Tunnel Laboratory Research Report, University of Western Ontario, London, Ontario, Canada.

Londoño, N. A. 2006. *Use of Vibration Data for Structural Health Monitoring of Bridges*, Department of Civil and Environmental Engineering, Carleton University, Ottawa, Canada.

Montreuil, M. A. 1999a. *Confederation Bridge Monitoring Project Slow-Speed Data Logger System,* Technical Manual, Preliminary Version, Thermal Technology Centre, National Research Council Canada.

Montreuil, M. A. 1999b. *Confederation Bridge Monitoring Project High-Speed Data Logger System,* Technical Manual, Preliminary Version, Thermal Technology Centre, National Research Council Canada.

Ochi, M. K. 1990. *Applied Probability and Stochastic Processes in Engineering and Physical Science*, John Wiley and Sons, New York, NY, USA.

Tadros, G. 1997. The Confederation Bridge: An Overview. *Canadian Journal of Civil Engineering,* 24: 850-866.

APPENDIX 2A: ANOMALIES IN THE DATA FROM THE HANDAR AND R. M. YOUNG ANEMOMETERS

Figure 2A.1a shows a typical wind power spectrum obtained using a four-hour time history dataset sampled at 2 Hz from the R. M. Young anemometer during the passage of Hurricane Noel. Figure 2A.1b shows the wind power spectrum derived using data, for the same duration and time, from the Handar unit, which is atypical. This is likely due to the numerous "drop-offs" in the time history records for wind speed from the Handar unit, shown in Figure 2.14. Given the anomalies in the data from the Handar anemometer, analysis of the data from the R. M. Young anemometer is only presented in Chapter 2.

The time histories from R. M. Young unit also had several missing data points. For example, the first six and a half hours of data (1199 x 40 = 47960 data points) had 39 missing data points i.e., one point missing after every 1199 data points. Compared to the total number of data points, the missing points are small in number and are interspersed at a regular interval and therefore, could be replaced for example, by using linear interpolation. Generally the impact of this procedure was negligible; for example, Figure 2A.2a shows the power spectra obtained using the original dataset and the set with added interpolated points for the 10 to 14 hours interval in the storm are nearly identical. However, during the last four hours of the storm (hours 14 – 18), 42% of the data points are missing and the power spectra obtained using original dataset and the set with interpolated data are clearly different as shown in Figure 2A.2b. Thus, after this detailed examination of all the sub-datasets, the initial 14 hours of data were used to derive wind spectra in Chapter 2 and the last four hours of data were not analysed further.

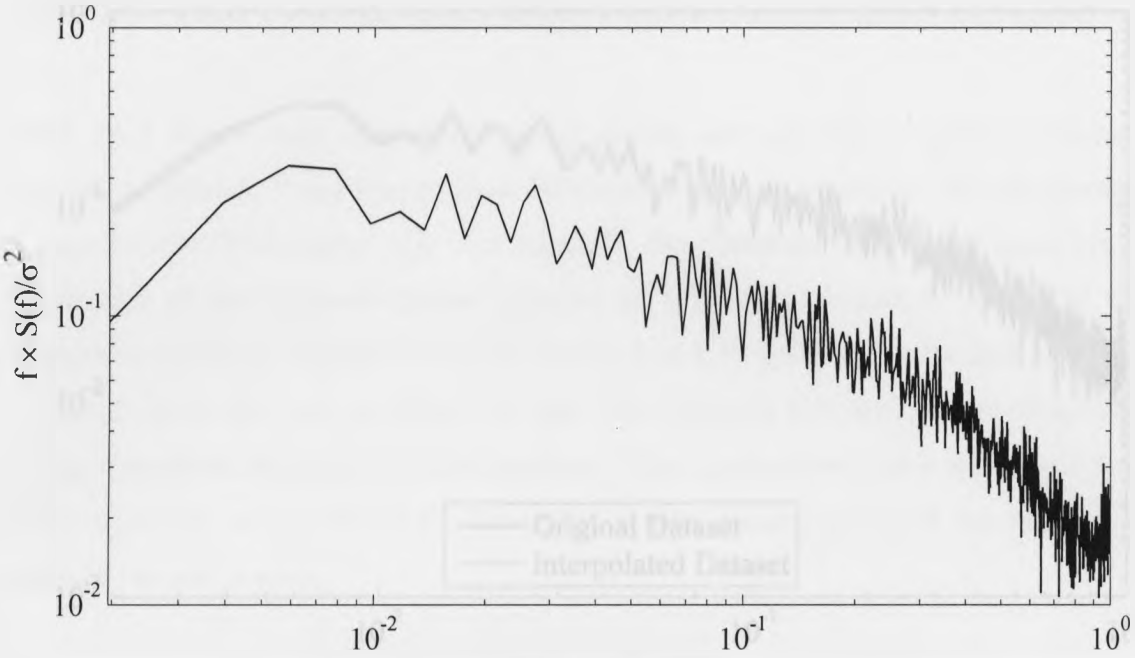

a) R. M. Young Anemometer

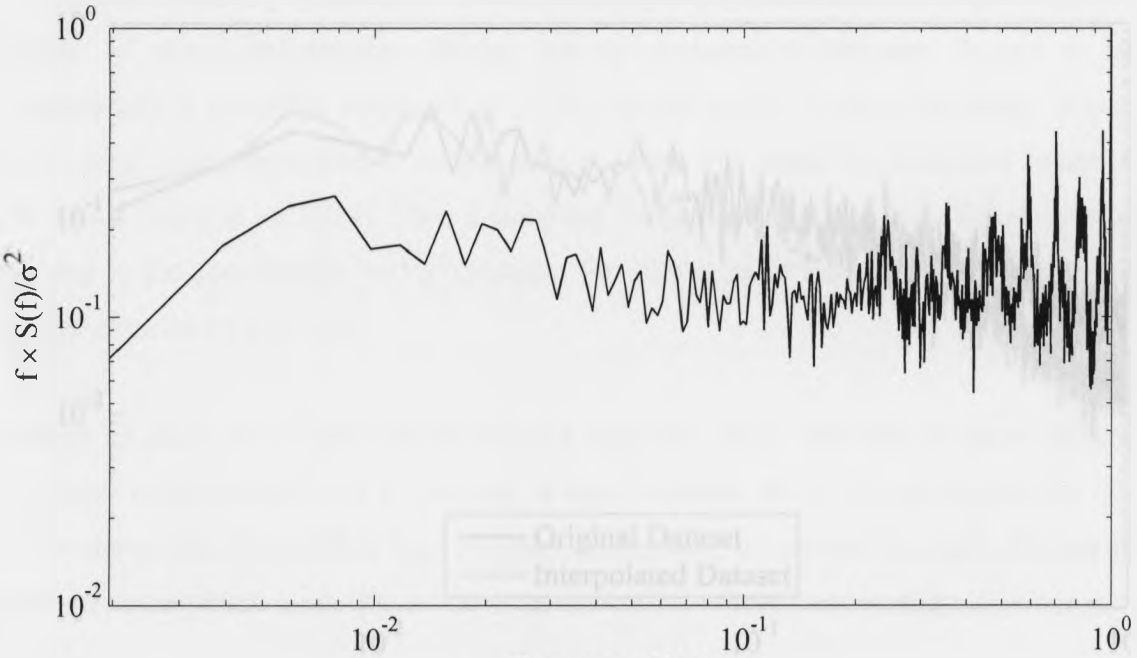

b) Handar Anemometer

Figure 2A.1 – Power Spectra Derived Using Hurricane Noel Data

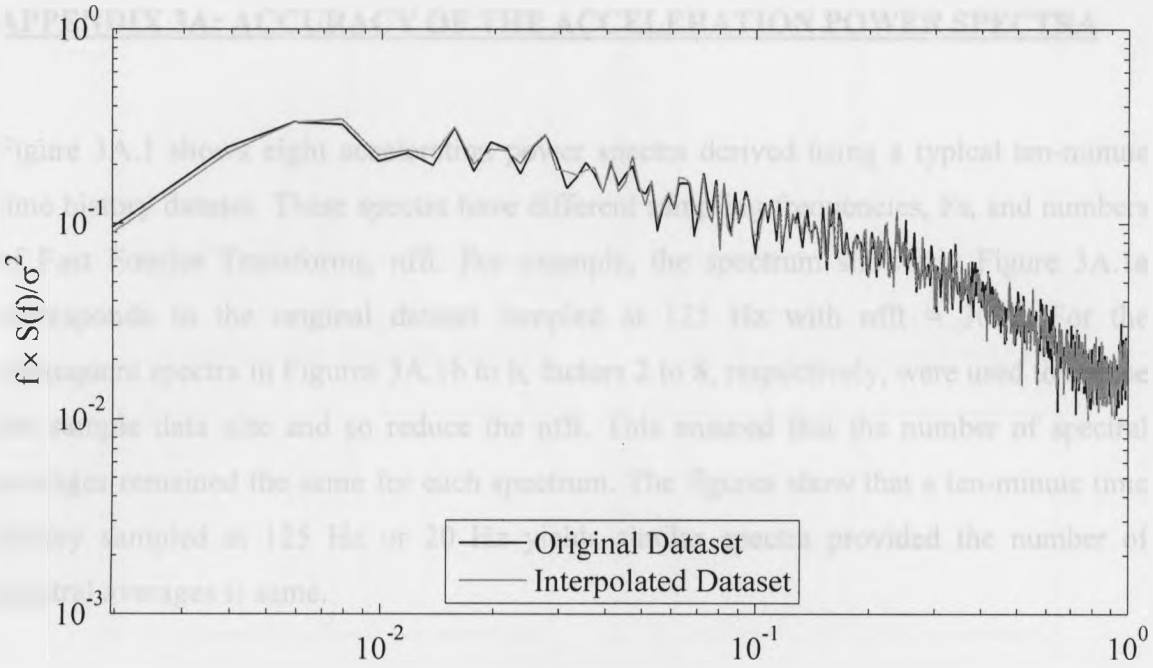

a) 10^{th} - 14^{th} Hour from R. M. Young Anemometer

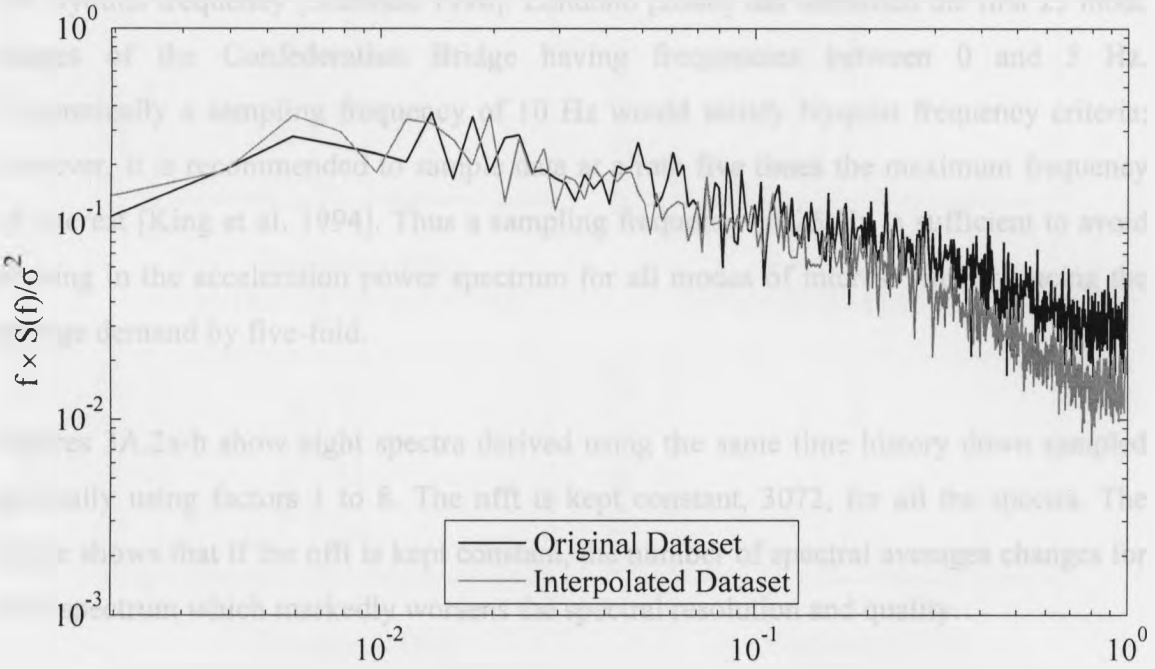

a) 14^{th} - 18^{th} Hour from R. M. Young Anemometer

Figure 2A.2 – Comparison between Power Spectra Derived Using Original and Interpolated Datasets

APPENDIX 3A: ACCURACY OF THE ACCELERATION POWER SPECTRA

Figure 3A.1 shows eight acceleration power spectra derived using a typical ten-minute time history dataset. These spectra have different sampling frequencies, Fs, and numbers of Fast Fourier Transforms, nfft. For example, the spectrum shown in Figure 3A.1a corresponds to the original dataset sampled at 125 Hz with nfft = 3072. For the subsequent spectra in Figures 3A.1b to h, factors 2 to 8, respectively, were used to reduce the sample data size and so reduce the nfft. This ensured that the number of spectral averages remained the same for each spectrum. The figures show that a ten-minute time history sampled at 125 Hz or 20 Hz yields similar spectra provided the number of spectral averages is same.

One could argue that reducing sampling frequency increases the risk of aliasing, a phenomenon that impacts the power spectrum if the sampling frequency is less than twice the Nyquist frequency [Shannon 1998]. Londoño [2006] has identified the first 25 mode shapes of the Confederation Bridge having frequencies between 0 and 5 Hz. Theoretically a sampling frequency of 10 Hz would satisfy Nyquist frequency criteria; however, it is recommended to sample data at a rate five times the maximum frequency of interest [King et al. 1994]. Thus a sampling frequency of 25 Hz is sufficient to avoid aliasing in the acceleration power spectrum for all modes of interest while reducing the storage demand by five-fold.

Figures 3A.2a-h show eight spectra derived using the same time history down sampled gradually using factors 1 to 8. The nfft is kept constant, 3072, for all the spectra. The figure shows that if the nfft is kept constant, the number of spectral averages changes for each spectrum which markedly worsens the spectral resolution and quality.

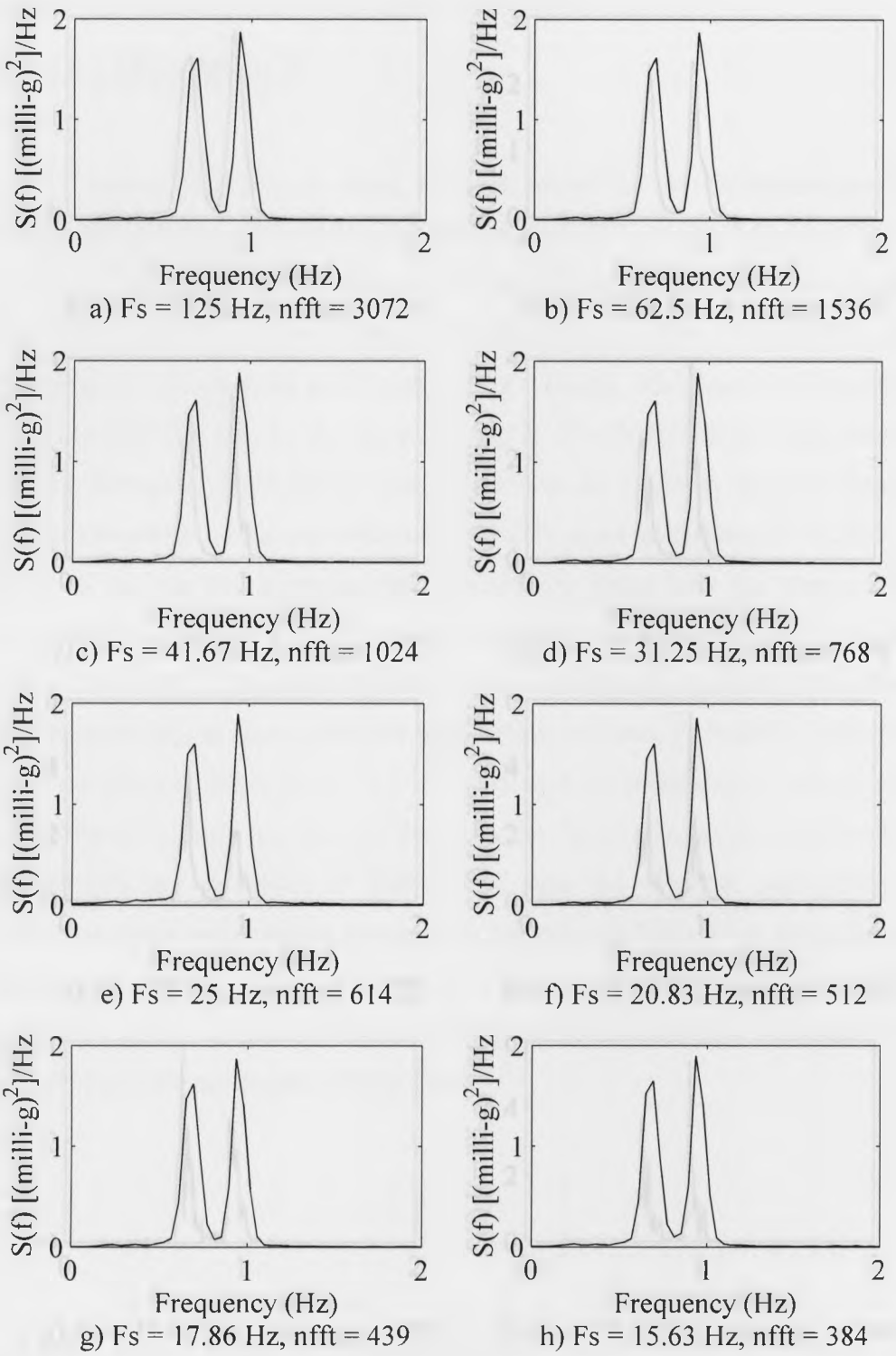

Figure 3A.1 – Acceleration Power Spectra Derived Using Typical Ten-Minute Time History: Number of Spectral Averages = 24

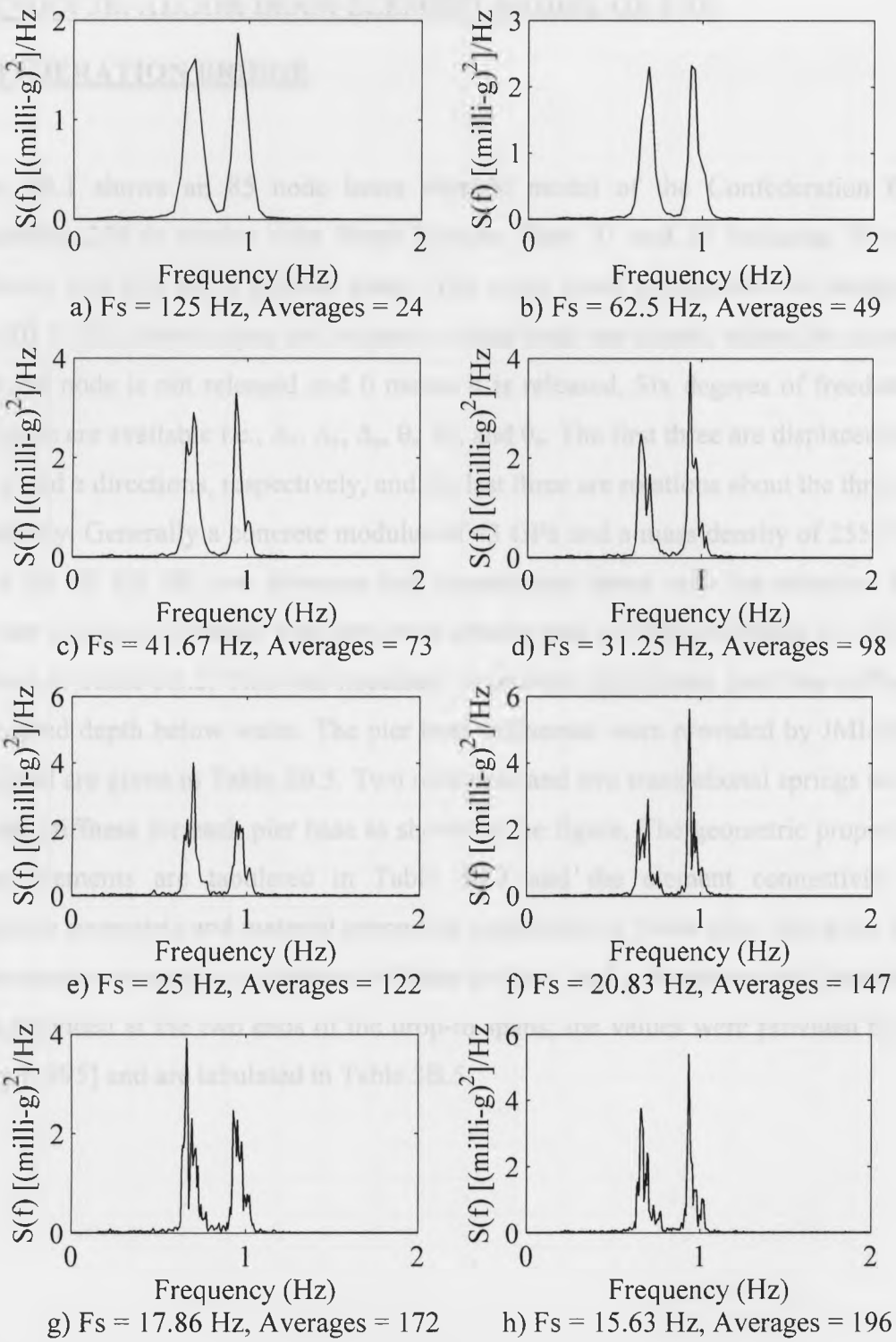

Figure 3A.2 – Acceleration Power Spectra Derived Using Typical Ten-Minute Time History: Number of Fast Fourier Transform (nfft) = 3072

APPENDIX 3B: ALGOR BEAM ELEMENT MODEL OF THE CONFEDERATION BRIDGE

Figure 3B.1 shows an 85 node beam element model of the Confederation Bridge representing 250 m marine span frame between Piers 31 and 32 including 95 m end cantilevers and two 60 m drop-in spans. The nodal point coordinates are tabulated in Table 3B.1. The drop-in span end releases at each node are shown, where the numeral 1 means the node is not released and 0 means it is released. Six degrees of freedom at a given node are available i.e., Δ_x, Δ_y, Δ_z, θ_x, θ_y, and θ_z. The first three are displacements in the x, y and z directions, respectively, and the last three are rotations about the three axes, respectively. Generally a concrete modulus of 43 GPa and a mass density of 2550 kg/m^3 is used for all but the two elements that connect pier bases with the structure above. These are fictitious elements with zero mass density and an elastic modulus of 1000 GPa as shown in Table 3B.2. This was necessary to provide appropriate pier base stiffness at the required depth below water. The pier base stiffnesses were provided by JMI-Stanley [1995] and are given in Table 3B.5. Two rotational and two translational springs are used to model stiffness for each pier base as shown in the figure. The geometric properties of various elements are tabulated in Table 3B.3 and the element connectivity with appropriate geometric and material properties is provided in Table 3B.4. Since the bridge is a continuous structure, equivalent stiffness in the y and z directions and about the x-axis is provided at the two ends of the drop-in spans; the values were provided by JMI-Stanley [1995] and are tabulated in Table 3B.5.

Table 3B.1 – Nodal Point Coordinates

Node	Boundary Condition Codes						Nodal Point Coordinates (m)		
	Tx	Ty	Tz	Rx	Ry	Rz	X	Y	Z
1	0	0	0	0	0	0	-70.5	-2	0
2	0	0	0	0	0	0	-57.25	-2.596	0
3	0	0	0	0	0	0	-44	-3.309	0
4	0	0	0	0	0	0	-33.75	-3.964	0
5	0	0	0	0	0	0	-23.5	-4.636	0
6	0	0	0	0	0	0	-15.5	-5.194	0
7	0	0	0	0	0	0	-7.5	-5.781	0
8	0	0	0	0	0	0	-1.25	-6.26	0
9	0	0	0	0	0	0	5	-6.76	0
10	0	0	0	0	0	0	8	-7	0
11	0	0	0	0	0	0	18	-7	0
12	0	0	0	0	0	0	21	-6.76	0
13	0	0	0	0	0	0	27.25	-6.265	0
14	0	0	0	0	0	0	33.5	-5.781	0
15	0	0	0	0	0	0	41.5	-5.194	0
16	0	0	0	0	0	0	49.5	-4.636	0
17	0	0	0	0	0	0	59.75	-3.964	0
18	0	0	0	0	0	0	70	-3.309	0
19	0	0	0	0	0	0	83.25	-2.596	0
20	0	0	0	0	0	0	96.5	-2	0
21	0	0	0	0	0	0	108	-1.789	0
22	0	0	0	0	0	0	118	-1.618	0
23	0	0	0	0	0	0	138	-1.494	0
24	1	0	0	0	0	0	-142	-1.789	0
25	0	0	0	0	0	0	-132	-1.618	0
26	0	0	0	0	0	0	-112	-1.494	0
27	0	0	0	0	0	0	-92	-1.618	0
28	0	0	0	0	0	0	-83	-1.773	0
29	0	0	0	0	0	0	-82	-1.789	0
30	0	0	0	0	0	0	13	-14	0
31	0	0	0	0	0	0	13	-7	0
32	0	0	0	0	0	0	158	-1.618	0
33	0	0	0	0	0	0	168	-1.789	0
34	0	0	0	0	0	0	179.5	-2	0
35	0	0	0	0	0	0	192.8	-2.596	0
36	0	0	0	0	0	0	206	-3.309	0
37	0	0	0	0	0	0	216.2	-3.964	0
38	0	0	0	0	0	0	226.5	-4.636	0
39	0	0	0	0	0	0	234.5	-5.194	0
40	0	0	0	0	0	0	242.5	-5.781	0
41	0	0	0	0	0	0	248.8	-6.265	0

Table 3B.1 – Nodal Point Coordinates - Continued

Node	Boundary Condition Codes						Nodal Point Coordinates (m)		
	Tx	Ty	Tz	Rx	Ry	Rz	X	Y	Z
42	0	0	0	0	0	0	255	-6.759	0
43	0	0	0	0	0	0	258	-7	0
44	0	0	0	0	0	0	263	-7	0
45	0	0	0	0	0	0	268	-7	0
46	0	0	0	0	0	0	271	-6.76	0
47	0	0	0	0	0	0	277.2	-6.26	0
48	0	0	0	0	0	0	283.5	-5.781	0
49	0	0	0	0	0	0	291.5	-5.194	0
50	0	0	0	0	0	0	299.5	-4.636	0
51	0	0	0	0	0	0	309.8	-3.964	0
52	0	0	0	0	0	0	320	-3.309	0
53	0	0	0	0	0	0	333.2	-2.596	0
54	0	0	0	0	0	0	346.5	-2	0
55	0	0	0	0	0	0	358	-1.789	0
56	0	0	0	0	0	0	359	-1.773	0
57	0	0	0	0	0	0	368	-1.618	0
58	0	0	0	0	0	0	388	-1.494	0
59	0	0	0	0	0	0	408	-1.618	0
60	1	0	0	0	0	0	418	-1.789	0
61	0	0	0	0	0	0	263	-14	0
62	0	0	0	0	0	0	13	-21	0
63	0	0	0	0	0	0	13	-28	0
64	0	0	0	0	0	0	13	-35	0
65	0	0	0	0	0	0	13	-43	0
66	1	1	1	1	1	1	13	-60.5	0
67	0	0	0	0	0	0	263	-21	0
68	0	0	0	0	0	0	263	-28	0
69	0	0	0	0	0	0	263	-35	0
70	0	0	0	0	0	0	263	-50.6	0
71	1	1	1	1	1	1	263	-68.1	0
72	1	1	1	1	1	1	-142	-11.79	0
73	1	1	1	1	1	1	-142	-1.789	10
74	1	1	1	1	1	1	-152	-1.789	0
75	1	1	1	1	1	1	418	-11.79	0
76	1	1	1	1	1	1	418	-1.789	10
77	1	1	1	1	1	1	428	-1.789	0
78	1	1	1	1	1	1	13	-43	-10
79	1	1	1	1	1	1	3	-43	0
80	1	1	1	1	1	1	23	-43	0
81	1	1	1	1	1	1	13	-43	10
82	1	1	1	1	1	1	263	-50.6	-10

Table 3B.1 – Nodal Point Coordinates - Concluded

Node	Boundary Condition Codes						Nodal Point Coordinates (m)		
	Tx	Ty	Tz	Rx	Ry	Rz	X	Y	Z
83	1	1	1	1	1	1	253	-50.6	0
84	1	1	1	1	1	1	273	-50.6	0
85	1	1	1	1	1	1	263	-50.6	10

Table 3B.2 – Material Properties

Material Index	Modulus E (GPa)	Poisson Ratio ν	Mass Density (kg/m^3)	Weight Density (N/m^3)
1	43	0.2	2550	25000
2	1000	0.2	0	0

Table 3B.3 – Area Properties

Section Index	Areas	Torsion	Flexural Inertias	
	(m^2)	(m^4)	(m^4)	(m^4)
	A	J	I_2	I_3
1	67	960	480	480
2	21.21	221	138.5	526.7
3	20.54	207.7	134.3	466.5
4	19.63	190.2	129.8	392.5
5	18.62	171.2	122.7	320.5
6	17.53	151	116.2	252
7	16.34	129.6	109.2	190.7
8	14.75	104.6	99.6	134.8
9	13.13	80.24	90.18	89.13
10	11.85	59.31	83.5	54.56
11	10.75	45.5	76.76	36.4
12	9.74	37.69	69.39	27.29
13	9.153	31.88	64.94	21.05
14	78.16	464900	70.73	27.55
15	14.71	201	108	108
16	15.6	185	94	136
17	16.5	150	59	183
18	19.43	100000	10000000	1000000
19	10000000	100000	2.444	2.444

Table 3B.4 – Element Connectivity Data

Element Number	Node		Section Index	Material Index	Release Codes	
	I	J			I - End	J - End
1	2	1	10	1	0	0
2	3	2	9	1	0	0
3	4	3	8	1	0	0
4	5	4	7	1	0	0
5	6	5	6	1	0	0
6	7	6	5	1	0	0
7	8	7	4	1	0	0
8	9	8	3	1	0	0
9	10	9	2	1	0	0
10	11	12	2	1	0	0
11	12	13	3	1	0	0
12	13	14	4	1	0	0
13	14	15	5	1	0	0
14	15	16	6	1	0	0
15	16	17	7	1	0	0
16	17	18	8	1	0	0
17	18	19	9	1	0	0
18	19	20	10	1	0	0
19	20	21	11	1	0	0
20	21	22	12	1	0	0
21	22	23	13	1	0	0
22	24	25	12	1	0	0
23	25	26	13	1	0	0
24	27	26	13	1	0	0
25	28	27	12	1	0	0
26	29	28	14	1	100011	0
27	1	29	11	1	0	0
28	32	23	13	1	0	0
29	33	32	12	1	0	0
30	34	33	11	1	0	0
31	35	34	10	1	0	0
32	36	35	9	1	0	0
33	37	36	8	1	0	0
34	38	37	7	1	0	0
35	39	38	6	1	0	0
36	40	39	5	1	0	0
37	41	40	4	1	0	0
38	42	41	3	1	0	0
39	43	42	2	1	0	0
40	45	46	2	1	0	0

Table 3B.4 – Element Connectivity Data Concluded

Element Number	Node		Section Index	Material Index	Release Code	
	I	J			I - End	J - End
41	46	47	3	1	0	0
42	47	48	4	1	0	0
43	48	49	5	1	0	0
44	49	50	6	1	0	0
45	50	51	7	1	0	0
46	51	52	8	1	0	0
47	52	53	9	1	0	0
48	53	54	10	1	0	0
49	54	55	11	1	0	0
50	55	56	14	1	100011	0
51	56	57	12	1	0	0
52	57	58	13	1	0	0
53	59	58	13	1	0	0
54	60	59	12	1	0	0
55	30	62	17	1	0	0
56	62	63	16	1	0	0
57	63	64	15	1	0	0
58	64	65	1	1	0	0
59	61	67	17	1	0	0
60	67	68	16	1	0	0
61	68	69	15	1	0	0
62	69	70	1	1	0	0
63	30	31	18	1	0	0
64	10	31	18	1	0	0
65	31	11	18	1	0	0
66	43	44	18	1	0	0
67	44	45	18	1	0	0
68	61	44	18	1	0	0
69	65	66	19	2	0	0
70	70	71	19	2	0	0

Table 3B.5 – Boundary Elements

Element Number	I	J	Linear	Rotational	Spring Rate (MN/m)
71	24	72	1	0	18.46
72	24	73	1	0	16.28
73	24	74	0	1	118700
74	60	75	1	0	18.46
75	60	76	1	0	16.28
76	60	77	0	1	118700
77	65	78	0	1	240900
78	65	79	0	1	240900
79	65	80	1	0	3104
80	65	81	1	0	3104
81	70	82	0	1	240900
82	70	83	0	1	240900
83	70	84	1	0	3104
84	70	85	1	0	3104

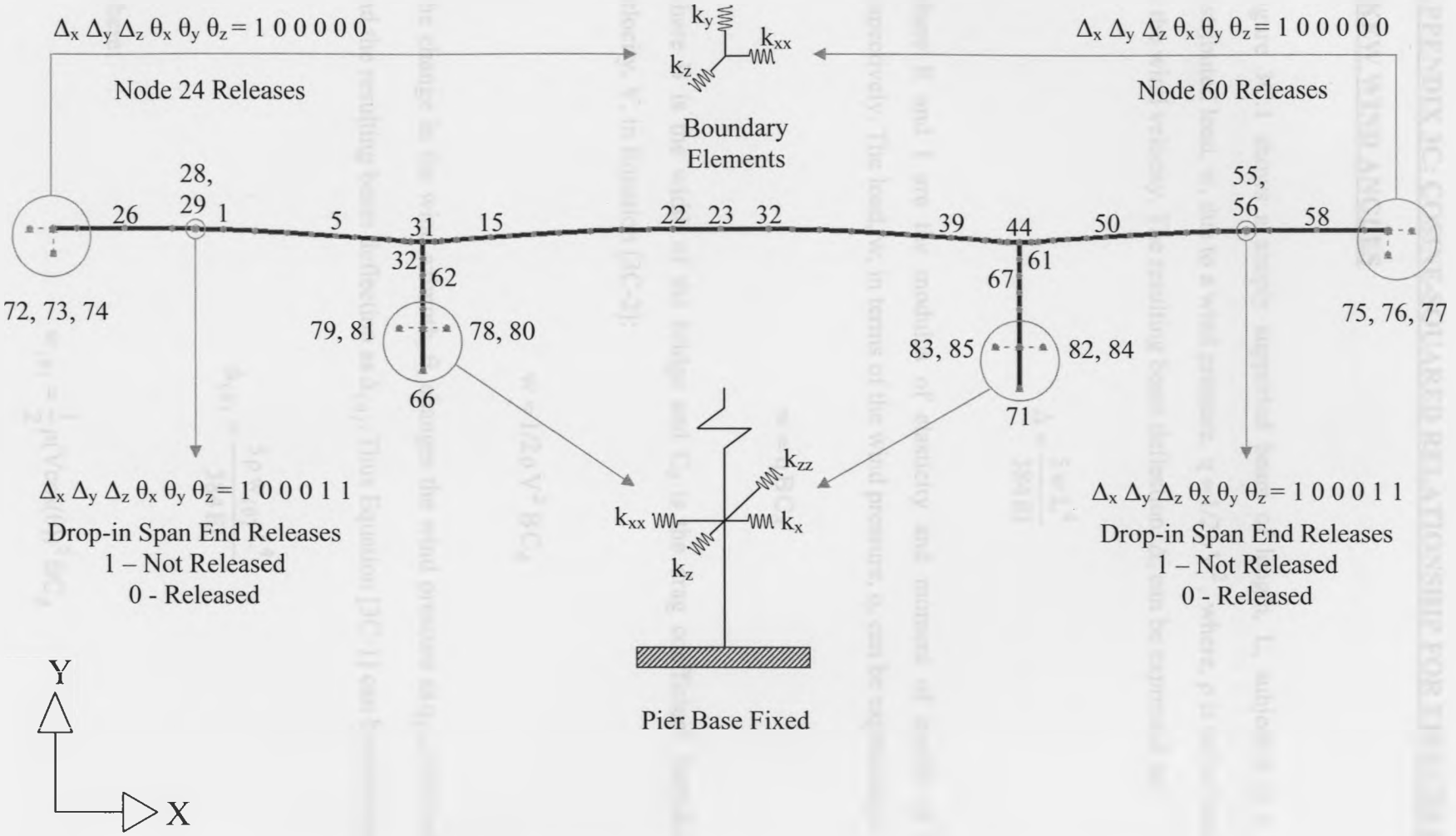

Figure 3B.1 – ALGOR Beam Element Model of the Confederation Bridge (Prototype)

APPENDIX 3C: COSINE-SQUARED RELATIONSHIP FOR EFFECTS DUE TO SKEW WIND ANGLES

Figure 3C.1 shows a simply supported beam of length, L, subjected to a uniformly distributed load, w, due to a wind pressure, $q = 1/2\rho V^2$, where, ρ is the air density and V is the wind velocity. The resulting beam deflection, Δ, can be expressed as:

$$\Delta = \frac{5 w L^4}{384 EI} \qquad [3C\text{-}1]$$

where E and I are the modulus of elasticity and moment of inertia of the beam, respectively. The load, w, in terms of the wind pressure, q, can be expressed as:

$$w = q B C_d \qquad [3C\text{-}2]$$

where B is the width of the bridge and C_d is the drag coefficient. Introducing wind velocity, V, in Equation [3C-2]:

$$w = 1/2\rho V^2 B C_d \qquad [3C\text{-}3]$$

The change in the wind azimuth, θ, changes the wind pressure as $q_{(\theta)}$, the load as $w_{(\theta)}$, and the resulting beam deflection as $\Delta_{(\theta)}$. Thus Equation [3C-1] can be rewritten as:

$$\Delta_{(\theta)} = \frac{5\rho w_{(\theta)} L^4}{384 EI} \qquad [3C\text{-}4]$$

where:

$$w_{(\theta)} = \frac{1}{2}\rho(V\cos(\theta))^2 B C_d \qquad [3C\text{-}5]$$

Thus

$$\Delta_{(\theta)} = \frac{5\rho B C_d L^4}{768 EI} V^2 \cos^2(\theta) \qquad [3C\text{-}6]$$

For $\theta = 0^o$, Equation [3C-5] gives maximum deflection, and for $\theta = 90^o$, Equation [3C-6] yields zero.

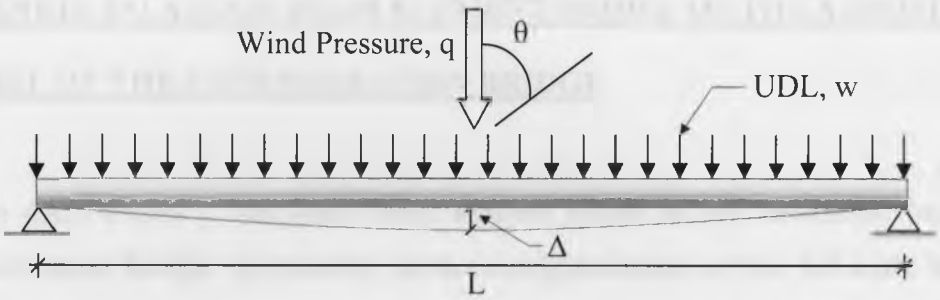

Figure 3C.1 – Simply Supported Beam Subjected to Uniformly Distributed Load (UDL), w, due to Wind Pressure, q

APPENDIX 4A: ALGOR BEAM ELEMENT MODEL OF THE AEROELASTIC MODEL OF THE CONFEDERATION BRIDGE

Figure 4A.1 shows a 106 node beam element model of the aeroelastic model of the Confederation Bridge representing three contiguous spans of the full-scale bridge each 250 m long. The nodal coordinates are tabulated in Table 4A.1. The central span is a continuous frame and the side spans have a drop-in segment each at midspan between the cantilevers. The equivalent pier and deck stiffnesses are provided using Aluminum and the material properties are given in Table 4A.2. The links connecting the drop-in spans with the cantilevers were also modelled as aluminum members. A shell element model of the link in ALGOR was used to determine the link stiffnesses in various directions that were used to determine the geometric properties of the equivalent aluminum element. The geometric properties of the different types of elements used for the numerical model are tabulated in Table 4A.3 and the element connectivity with appropriate geometric and material properties is provided in Table 4A.4.

Table 4A.1 – Nodal Point Coordinates

Node	Boundary Condition Codes						Nodal Point Coordinates (cm)		
	Tx	Ty	Tz	Rx	Ry	Rz	X	Y	Z
1	1	1	1	1	1	1	0	0	0
2	0	0	0	0	0	0	0	0.63	0
3	0	0	0	0	0	0	0	4	0
4	0	0	0	0	0	0	0	10	0
5	0	0	0	0	0	0	0	15.37	0
6	0	0	0	0	0	0	100	17.02	0
7	0	0	0	0	0	0	0.95	17.66	0
8	0	0	0	0	0	0	2.6	17.68	0
9	0	0	0	0	0	0	3.625	17.72	0
10	0	0	0	0	0	0	4.45	17.72	0
11	0	0	0	0	0	0	4.6	17.75	0
12	0	0	0	0	0	0	6.95	17.75	0
13	0	0	0	0	0	0	10.8	17.85	0
14	0	0	0	0	0	0	14.1	17.96	0
15	0	0	0	0	0	0	18.7	17.96	0
16	0	0	0	0	0	0	23.6	18.06	0
17	0	0	0	0	0	0	25.45	18.06	0
18	0	0	0	0	0	0	33.1	18.12	0
19	0	0	0	0	0	0	36.83	18.12	0
20	0	0	0	0	0	0	42.7	18.12	0
21	0	0	0	0	0	0	50	18.12	0
22	0	0	0	0	0	0	93.05	17.75	0
23	0	0	0	0	0	0	89.2	17.85	0
24	0	0	0	0	0	0	95.4	17.75	0
25	0	0	0	0	0	0	66.9	18.12	0
26	0	0	0	0	0	0	63.17	18.12	0
27	0	0	0	0	0	0	57.3	18.12	0
28	0	0	0	0	0	0	99.05	17.66	0
29	0	0	0	0	0	0	97.4	17.68	0
30	0	0	0	0	0	0	95.55	17.72	0
31	0	0	0	0	0	0	76.4	18.06	0
32	0	0	0	0	0	0	74.55	18.06	0
33	0	0	0	0	0	0	96.38	17.72	0
34	0	0	0	0	0	0	81.3	17.96	0
35	0	0	0	0	0	0	85.9	17.96	0
36	0	0	0	0	0	0	0	17.02	0
37	0	0	0	0	0	0	100	0.63	0
38	0	0	0	0	0	0	100	4	0
39	0	0	0	0	0	0	100	15.37	0
40	1	1	1	1	1	1	100	0	0
41	0	0	0	0	0	0	100	10	0

Table 4A.1 – Nodal Point Coordinates - Continued

Node	Boundary Condition Codes						Nodal Point Coordinates (cm)		
	Tx	Ty	Tz	Rx	Ry	Rz	X	Y	Z
42	0	0	0	0	0	0	-6.95	17.75	0
43	0	0	0	0	0	0	-10.8	17.85	0
44	0	0	0	0	0	0	-4.6	17.75	0
45	0	0	0	0	0	0	-33.1	18.12	0
46	0	0	0	0	0	0	-36.83	18.12	0
47	0	0	0	0	0	0	-0.95	17.66	0
48	0	0	0	0	0	0	-2.6	17.68	0
49	0	0	0	0	0	0	-4.45	17.72	0
50	0	0	0	0	0	0	-23.6	18.06	0
51	0	0	0	0	0	0	-25.45	18.06	0
52	0	0	0	0	0	0	-3.625	17.72	0
53	0	0	0	0	0	0	-18.7	17.96	0
54	0	0	0	0	0	0	-14.1	17.96	0
55	0	0	0	0	0	0	-37.19	18.12	0
56	0	0	0	0	0	0	-37.87	18.12	0
57	0	0	0	0	0	0	-38	18.12	0
58	0	0	0	0	0	0	-38.69	18.12	0
59	0	0	0	0	0	0	-42.7	18.12	0
60	0	0	0	0	0	0	-50	18.12	0
61	0	0	0	0	0	0	-57.1	18.12	0
62	0	0	0	0	0	0	-61.11	18.12	0
63	0	0	0	0	0	0	-61.8	18.12	0
64	0	0	0	0	0	0	-61.93	18.12	0
65	0	0	0	0	0	0	-62.61	17.94	0
66	0	0	0	0	0	0	-64.91	17.94	0
67	0	0	0	0	0	0	-98.96	17.94	0
68	0	0	0	0	0	0	-100	17.94	0
69	1	1	1	1	1	1	-100	0	0
70	0	0	0	0	0	0	123.6	18.06	0
71	0	0	0	0	0	0	125.5	18.06	0
72	0	0	0	0	0	0	133.1	18.12	0
73	0	0	0	0	0	0	136.8	18.12	0
74	0	0	0	0	0	0	161.8	18.12	0
75	0	0	0	0	0	0	161.9	18.12	0
76	0	0	0	0	0	0	138	18.12	0
77	0	0	0	0	0	0	138.7	18.12	0
78	0	0	0	0	0	0	102.6	17.68	0
79	0	0	0	0	0	0	103.6	17.72	0
80	0	0	0	0	0	0	104.5	17.72	0
81	0	0	0	0	0	0	162.6	17.94	0
82	0	0	0	0	0	0	164.9	17.94	0

Table 4A.1 – Nodal Point Coordinates - Concluded

Node	Boundary Condition Codes						Nodal Point Coordinates (cm)		
	Tx	Ty	Tz	Rx	Ry	Rz	X	Y	Z
83	0	0	0	0	0	0	200	17.94	0
84	1	1	1	1	1	1	200	0	0
85	0	0	0	0	0	0	114.1	17.96	0
86	0	0	0	0	0	0	118.7	17.96	0
87	0	0	0	0	0	0	199	17.94	0
88	0	0	0	0	0	0	161.1	18.12	0
89	0	0	0	0	0	0	157.1	18.12	0
90	0	0	0	0	0	0	104.6	17.75	0
91	0	0	0	0	0	0	107	17.75	0
92	0	0	0	0	0	0	137.2	18.12	0
93	0	0	0	0	0	0	110.8	17.85	0
94	0	0	0	0	0	0	101	17.66	0
95	0	0	0	0	0	0	142.7	18.12	0
96	0	0	0	0	0	0	150	18.12	0
97	0	0	0	0	0	0	137.9	18.12	0
98	0	0	0	0	0	0	19.19	17.97	0
99	0	0	0	0	0	0	19.68	17.98	0
100	0	0	0	0	0	0	20.17	17.99	0
101	0	0	0	0	0	0	20.66	18	0
102	0	0	0	0	0	0	21.15	18.01	0
103	0	0	0	0	0	0	21.64	18.02	0
104	0	0	0	0	0	0	22.13	18.03	0
105	0	0	0	0	0	0	22.62	18.04	0
106	0	0	0	0	0	0	23.11	18.05	0

Table 4A.2 – Material Properties

Material Index	Aluminium Modulus E x 10^9 (dyn / cm^2)	Poisson Ratio ν	Mass Density (g/cm^3)	Weight Density (dyn/cm^3)
1	689	0.33	2.7	2650

Table 4A.3 – Area Properties

Section Index	Areas	Torsion	Flexural Inertias	
	(cm^2)	(cm^4)	(cm^4)	(cm^4)
	A	J	I_2	I_3
1	0.574	0.047	0.029	0.027
2	3.018	1.833	1.086	1.086
3	3.018	4.833	1.886	5.690
4	0.990	0.114	0.042	0.160
5	0.965	0.109	0.041	0.148
6	0.911	0.100	0.038	0.124
7	0.860	0.092	0.036	0.105
8	0.732	0.071	0.031	0.065
9	0.593	0.049	0.027	0.032
10	0.453	0.028	0.022	0.013
11	0.358	0.016	0.017	0.007
12	0.712	0.071	0.042	0.042
13	11.40	20.69	10.34	10.34
14	2.58E-07	5.01E-05	8.17E-08	2.80E-08

Table 4A.4 – Element Connectivity Data

Element Number	Node		Section Index	Material Index	Release Codes	
	I	J			I - End	J - End
1	1	2	1	1	0	0
2	2	3	1	1	0	0
3	3	4	1	1	0	0
4	4	5	1	1	0	0
5	5	36	2	1	0	0
6	36	7	3	1	0	0
7	7	8	4	1	0	0
8	8	9	5	1	0	0
9	9	10	5	1	0	0
10	10	11	6	1	0	0
11	11	12	6	1	0	0
12	12	13	7	1	0	0
13	13	14	8	1	0	0
14	14	15	8	1	0	0
15	16	17	9	1	0	0
16	17	18	10	1	0	0
17	18	19	10	1	0	0
18	19	20	11	1	0	0
19	20	21	11	1	0	0

Table 4A.4 – Element Connectivity Data Continued

Element Number	Node		Section Index	Material Index	Release Code	
	I	J			I - End	J - End
20	22	23	7	1	0	0
21	24	22	6	1	0	0
22	25	26	10	1	0	0
23	27	21	11	1	0	0
24	28	29	4	1	0	0
25	26	27	11	1	0	0
26	30	24	6	1	0	0
27	31	32	9	1	0	0
28	29	33	5	1	0	0
29	34	31	9	1	0	0
30	32	25	10	1	0	0
31	33	30	5	1	0	0
32	23	35	8	1	0	0
33	35	34	8	1	0	0
34	6	28	3	1	0	0
35	37	38	1	1	0	0
36	39	6	2	1	0	0
37	40	37	1	1	0	0
38	41	39	1	1	0	0
39	38	41	1	1	0	0
40	42	43	7	1	0	0
41	44	42	6	1	0	0
42	45	46	10	1	0	0
43	47	48	4	1	0	0
44	49	44	6	1	0	0
45	50	51	9	1	0	0
46	48	52	5	1	0	0
47	53	50	9	1	0	0
48	51	45	10	1	0	0
49	52	49	5	1	0	0
50	43	54	8	1	0	0
51	54	53	8	1	0	0
52	36	47	3	1	0	0
53	46	55	11	1	0	0
54	55	56	11	1	0	0
55	57	58	11	1	0	0
56	58	59	11	1	0	0
57	59	60	11	1	0	0
58	60	61	11	1	0	0
59	61	62	11	1	0	0
60	62	63	11	1	0	0

Table 4A.4 – Element Connectivity Data Continued

Element Number	Node		Section Index	Material Index	Release Code	
	I	J			I - End	J - End
61	64	65	12	1	0	0
62	65	66	12	1	0	0
63	66	67	12	1	0	0
64	67	68	13	1	0	0
65	68	69	13	1	0	0
66	70	71	9	1	0	0
67	72	73	10	1	0	0
68	76	77	11	1	0	0
69	78	79	5	1	0	0
70	79	80	5	1	0	0
71	81	82	12	1	0	0
72	83	84	13	1	0	0
73	85	86	8	1	0	0
74	86	70	9	1	0	0
75	87	83	13	1	0	0
76	88	74	11	1	0	0
77	89	88	11	1	0	0
78	90	91	6	1	0	0
79	73	92	11	1	0	0
80	71	72	10	1	0	0
81	93	85	8	1	0	0
82	94	78	4	1	0	0
83	77	95	11	1	0	0
84	75	81	12	1	0	0
85	91	93	7	1	0	0
86	95	96	11	1	0	0
87	80	90	6	1	0	0
88	6	94	3	1	0	0
89	96	89	11	1	0	0
90	92	97	11	1	0	0
91	82	87	12	1	0	0
92	15	98	9	1	0	0
93	98	99	9	1	0	0
94	99	100	9	1	0	0
95	100	101	9	1	0	0
96	101	102	9	1	0	0
97	102	103	9	1	0	0
98	103	104	9	1	0	0
99	104	105	9	1	0	0
100	105	106	9	1	0	0
101	106	16	9	1	0	0

Table 4A.4 – Element Connectivity Data Concluded

Element Number	Node		Section Index	Material Index	Release Code	
	I	J			I - End	J - End
102	56	57	14	1	0	0
103	63	64	14	1	0	0
104	74	75	14	1	0	0
105	97	76	14	1	0	0

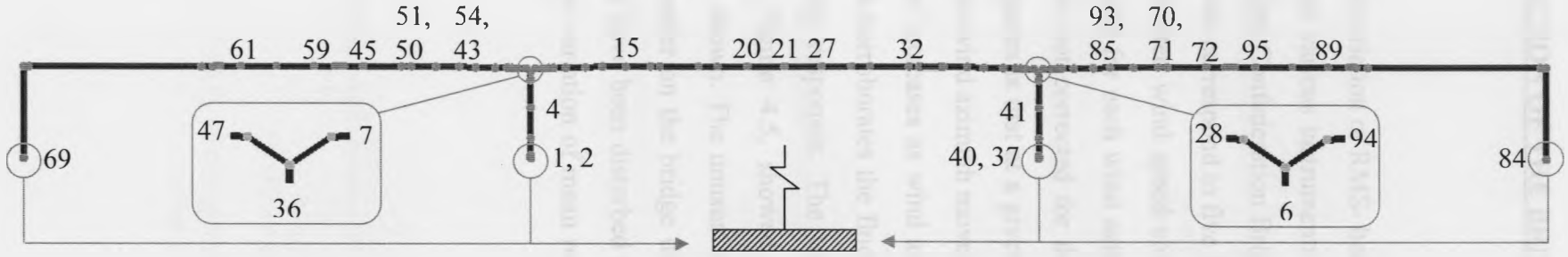

Figure 4A.1 – ALGOR Beam Element Model of the Confederation Bridge (Wind Tunnel Model)

APPENDIX 4B: VARIATION OF THE BRIDGE RESPONSE WITH WIND AZIMUTH

Figures 4B.1- 7 show the variation of RMS- bending moment, acceleration and deflection with wind azimuth for the various instruments that were located at different sections of the aeroelastic model of the Confederation Bridge during testing as shown in Figure 4.5. The five curves in each plot correspond to five different wind speeds from 10 to 30 m/s at 5 m/s interval. Each indicated wind speed could vary within 1 m/s as the wind speed increment was not identical for each wind azimuth. These responses represent as-tested measurements and so are not corrected for the prototype damping. One distinguished feature common to all figures is that at a given location and for a given wind speed the bridge response reduces as wind azimuth moves away from normal to the bridge axis, i.e., from 0^{o} to 90^{o}, and again increases as wind azimuth moves towards the bridge normal, i.e., 180^{o} and so on. This corroborates the findings presented in Chapters 3 and 4 based on the normalized modal responses. The transverse deflection transducers at three locations, described in Figure 4.5, showed erratic displacements for certain wind azimuths and so are not shown. The unusual behaviour was observed likely due to the thin depth of the side barrier on the bridge deck chosen to point the laser light of the transducers, which could have been disturbed for certain wind azimuths during testing. Figures 4B.8-11 show the variation of mean response with wind azimuth which follows the same trend.

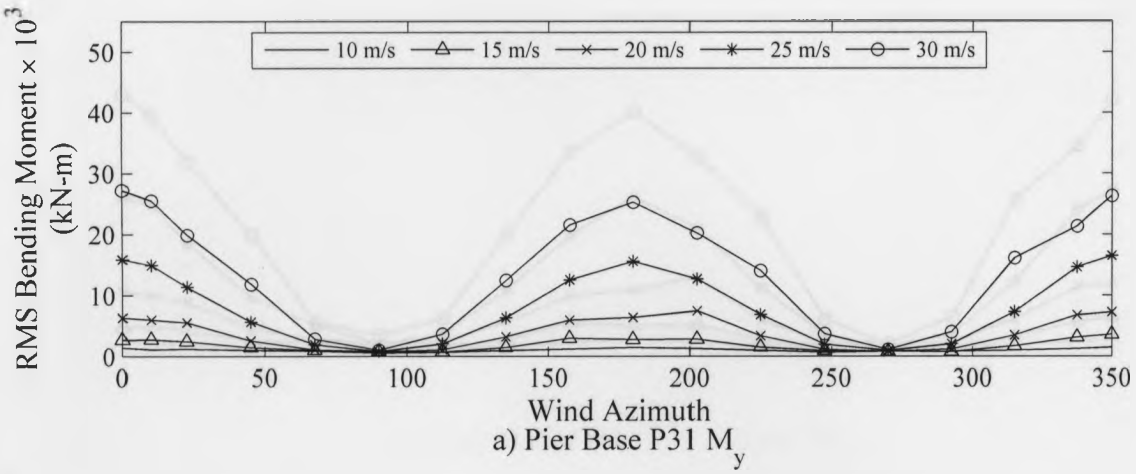

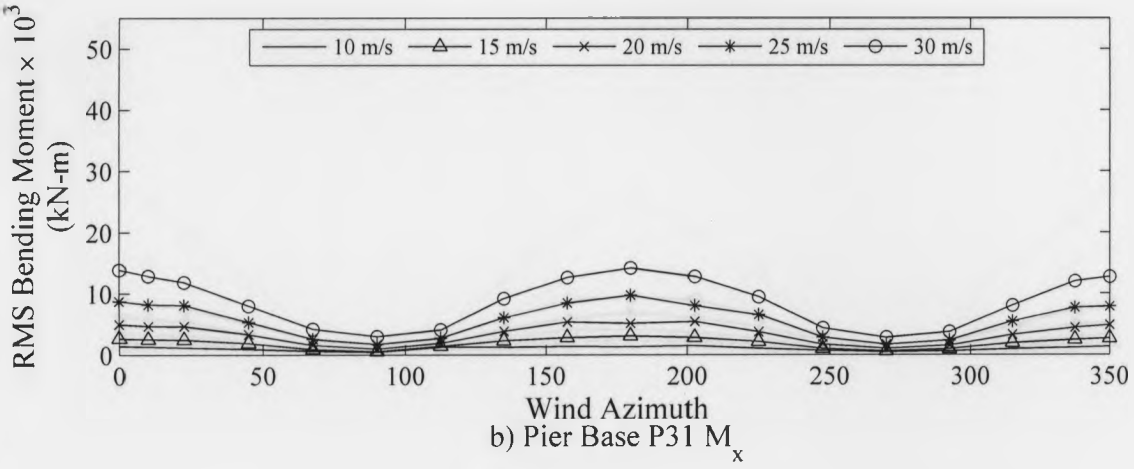

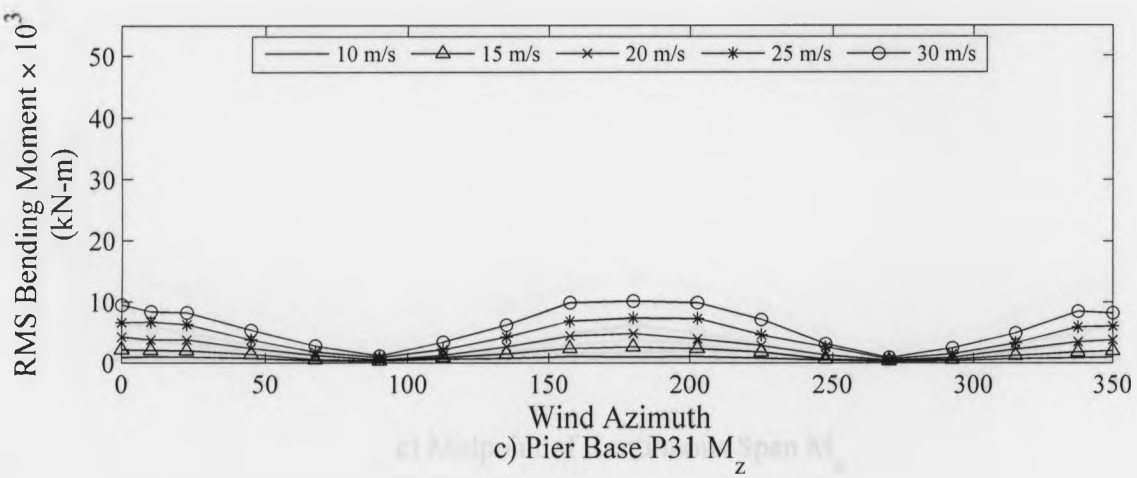

Figure 4B.1 – Variation of RMS Bending Moment with Wind Azimuth at the Base of Pier 31

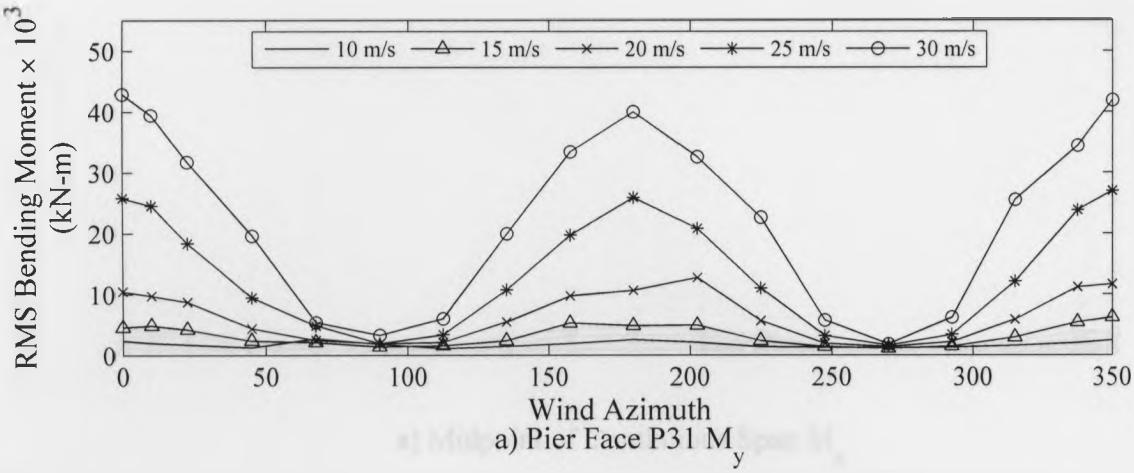

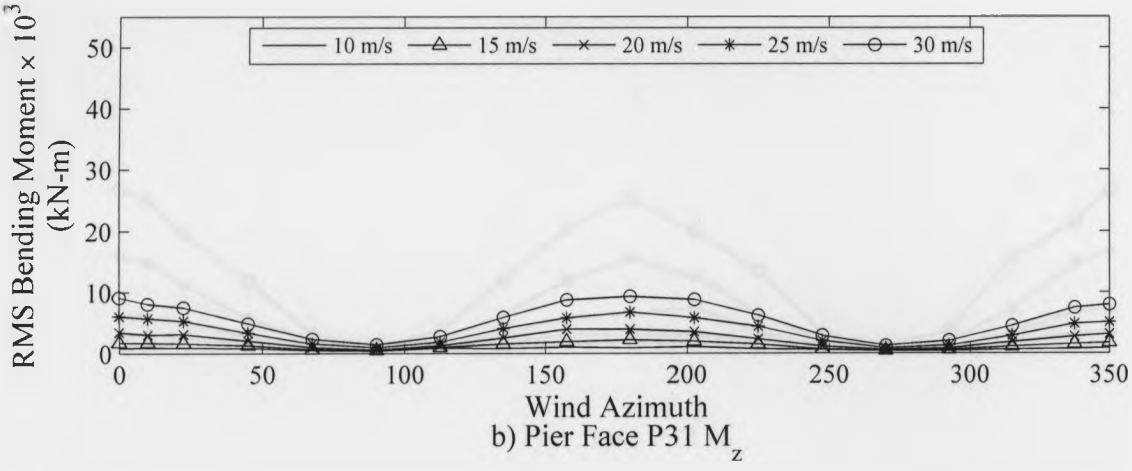

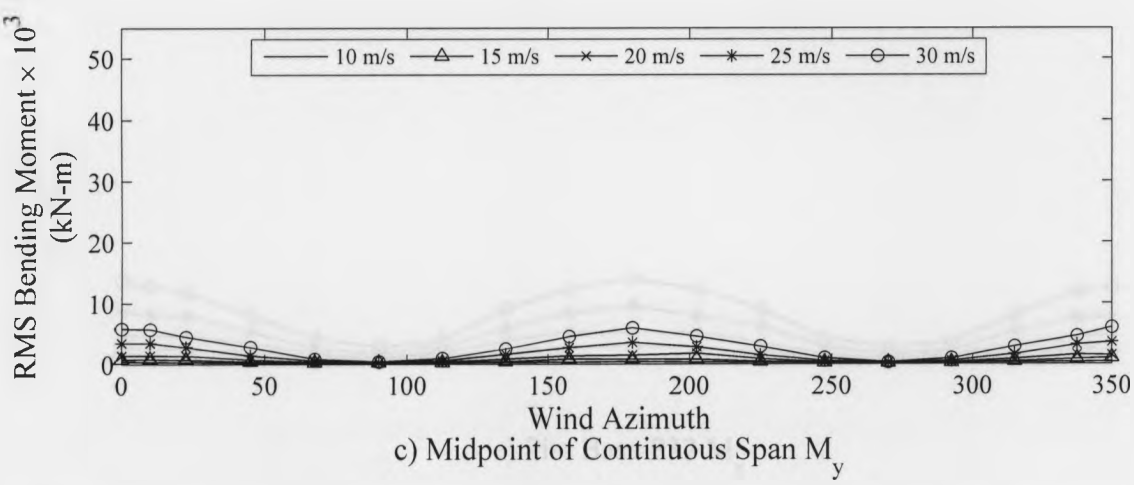

Figure 4B.2 – Variation of RMS Bending Moment with Wind Azimuth at the Face of Pier 31 and Midpoint of the Continuous Span

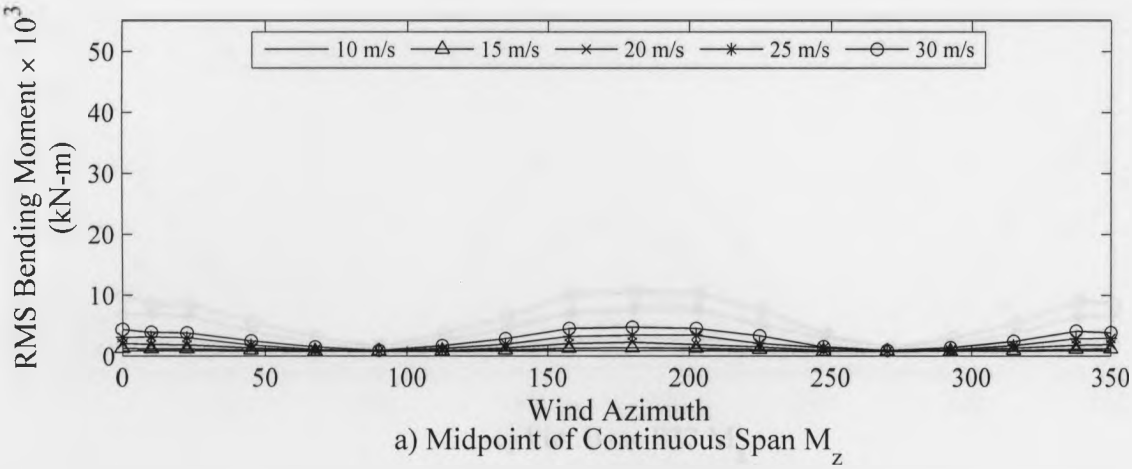

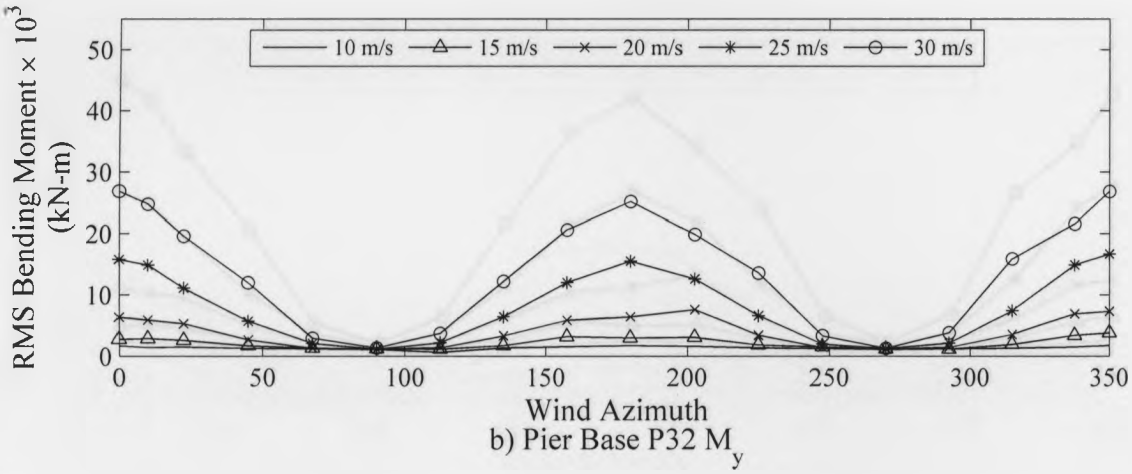

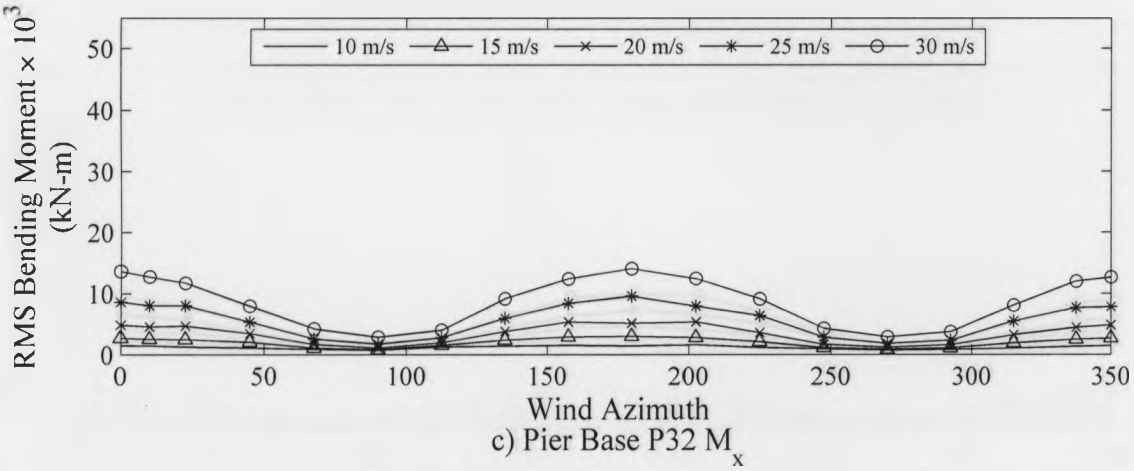

Figure 4B.3 – Variation of RMS Bending Moment with Wind Azimuth at the Midpoint of Continuous Span and Base of Pier 32

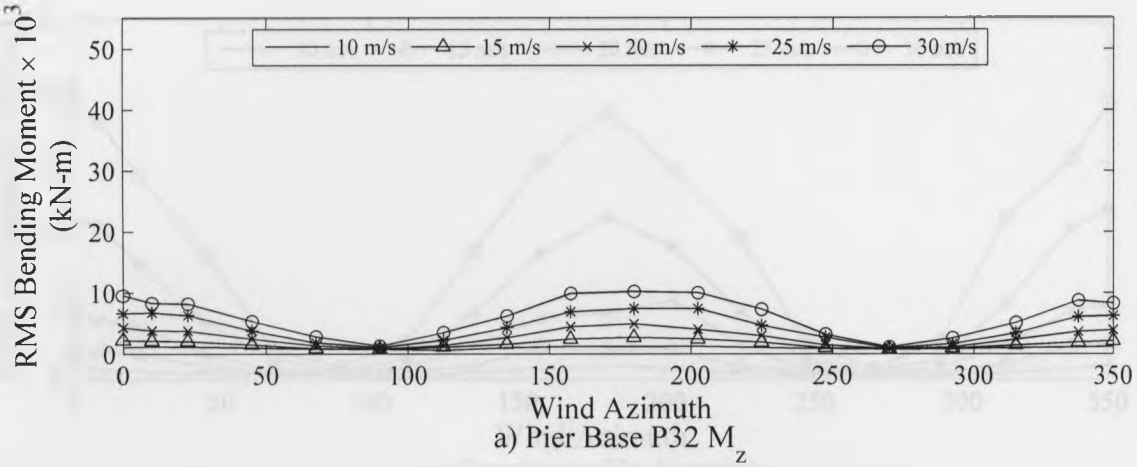

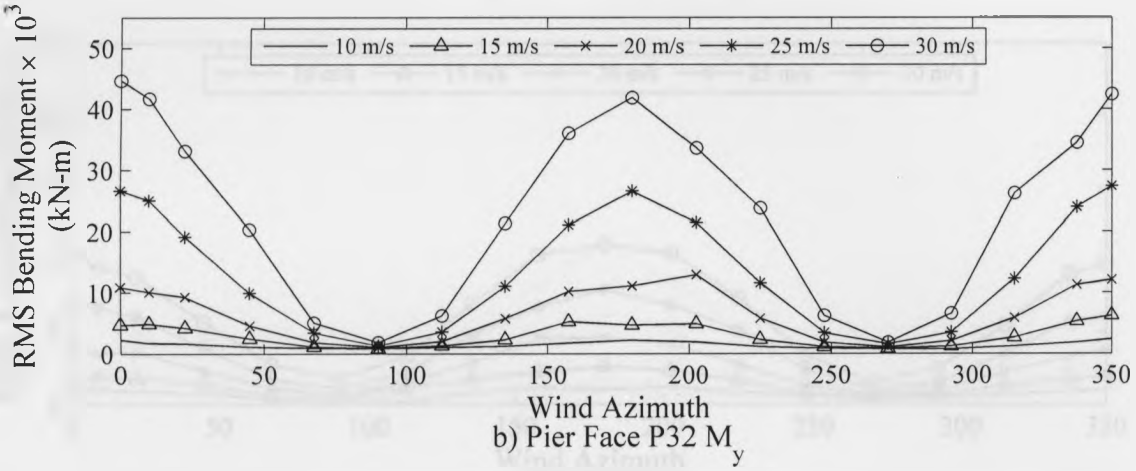

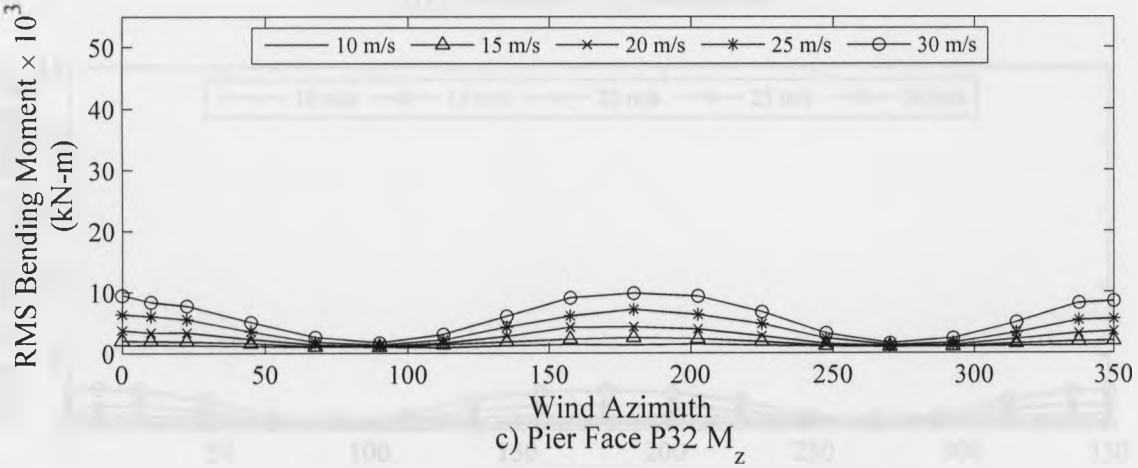

Figure 4B.4 – Variation of RMS Bending Moment with Wind Azimuth at the Base and Face of Pier 32

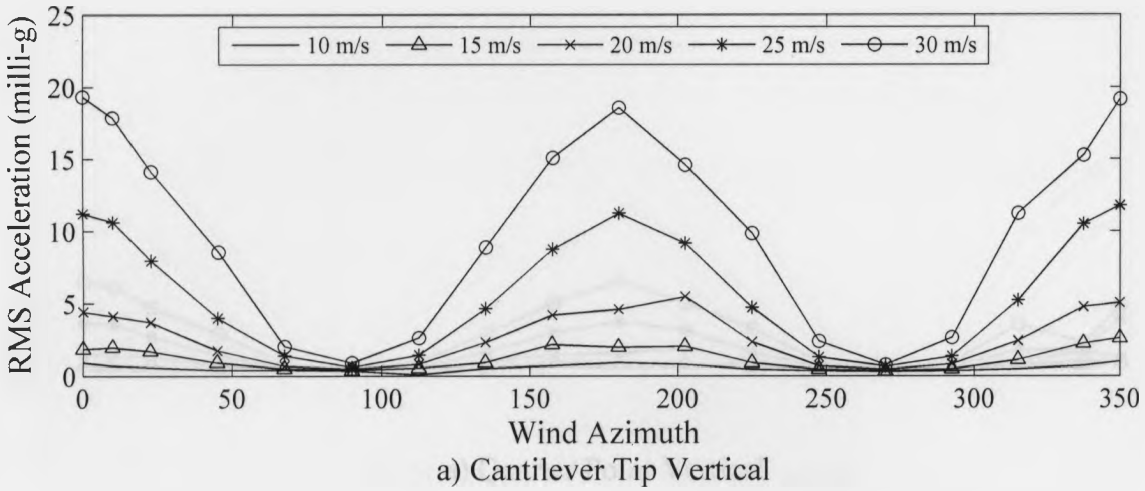

a) Cantilever Tip Vertical

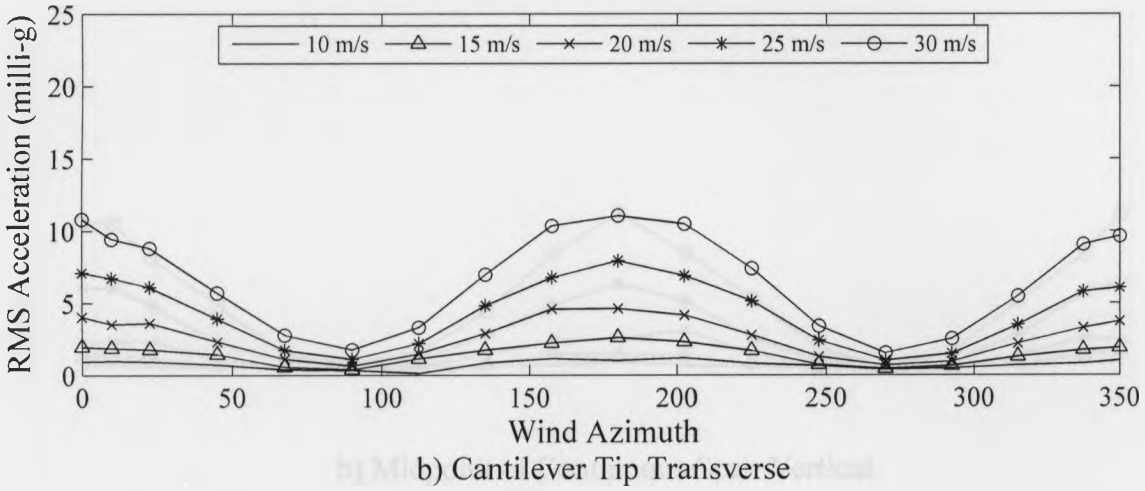

b) Cantilever Tip Transverse

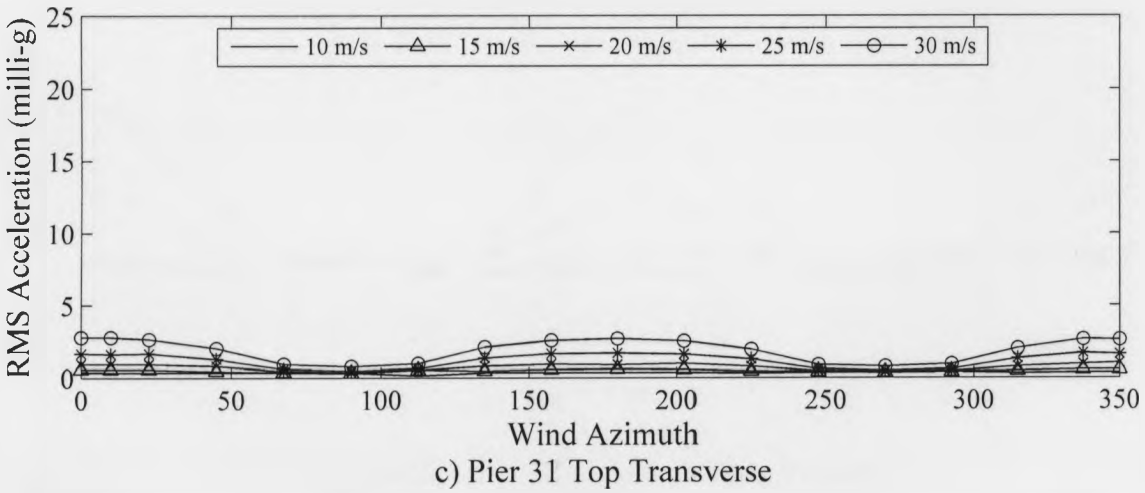

c) Pier 31 Top Transverse

Figure 4B.5 – Variation of RMS Acceleration with Wind Azimuth at the Cantilever Tip and Top of Pier 31

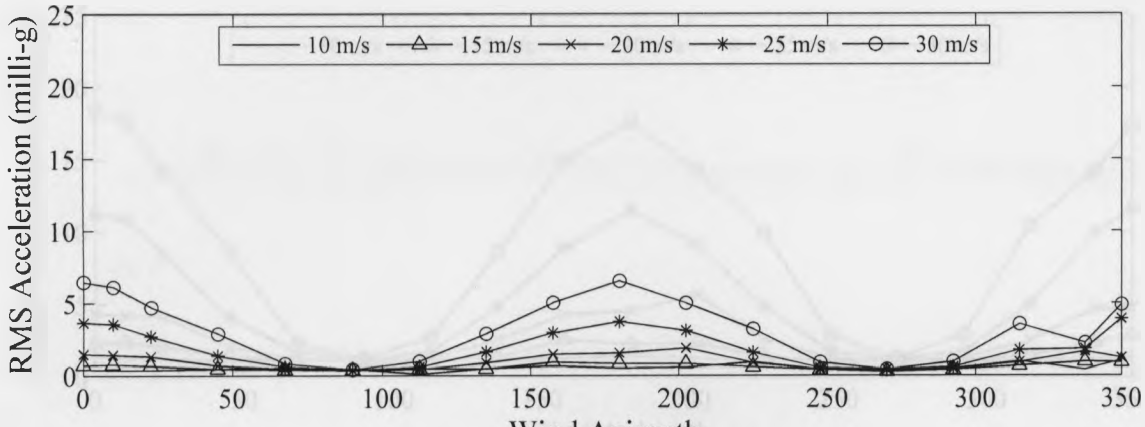

a) Quarter Point Vertical

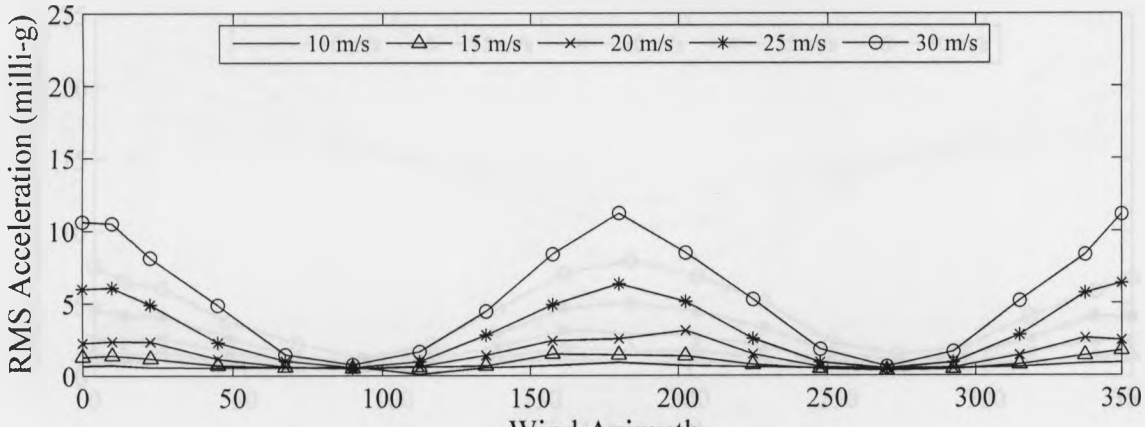

b) Midpoint of Continuous Span Vertical

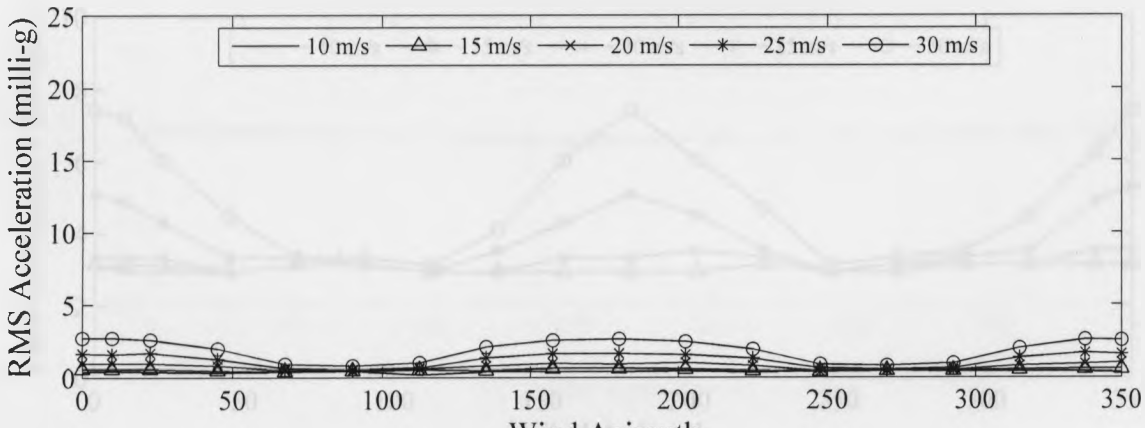

c) Pier 32 Top Transverse

Figure 4B.6 – Variation of RMS Acceleration with Wind Azimuth at the Quarter- and Mid-point of the Continuous Span and Top of Pier 32

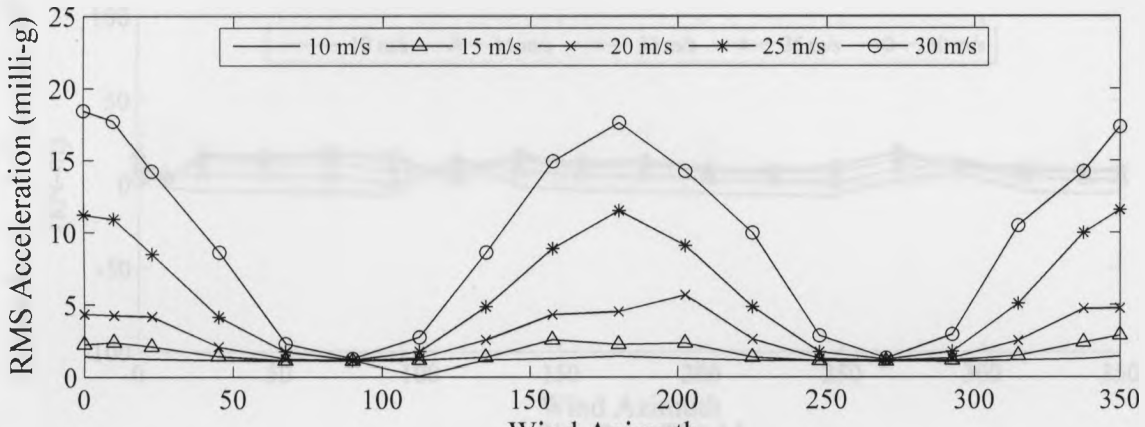

a) Midpoint of Drop-in Span Vertical

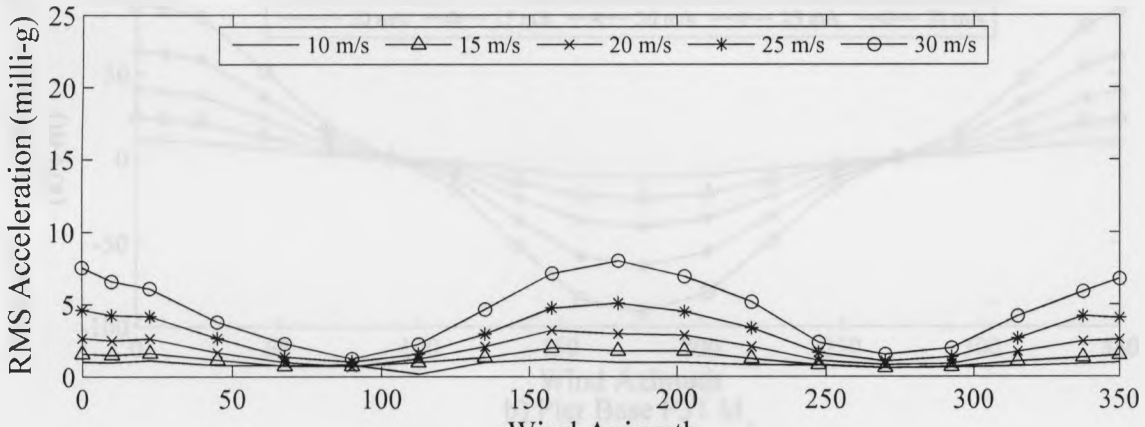

b) Midpoint of Drop-in Span Transverse

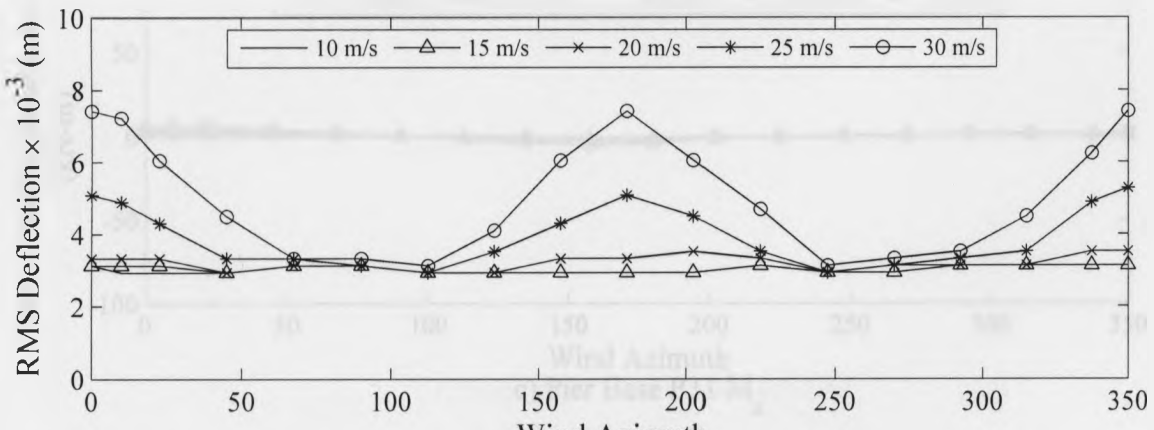

c) Midpoint of Continuous Span Vertical

Figure 4B.7 – Variation of RMS Acceleration and Deflection with Wind Azimuth at the Midpoint of Drop-in and Continuous Spans, Respectively

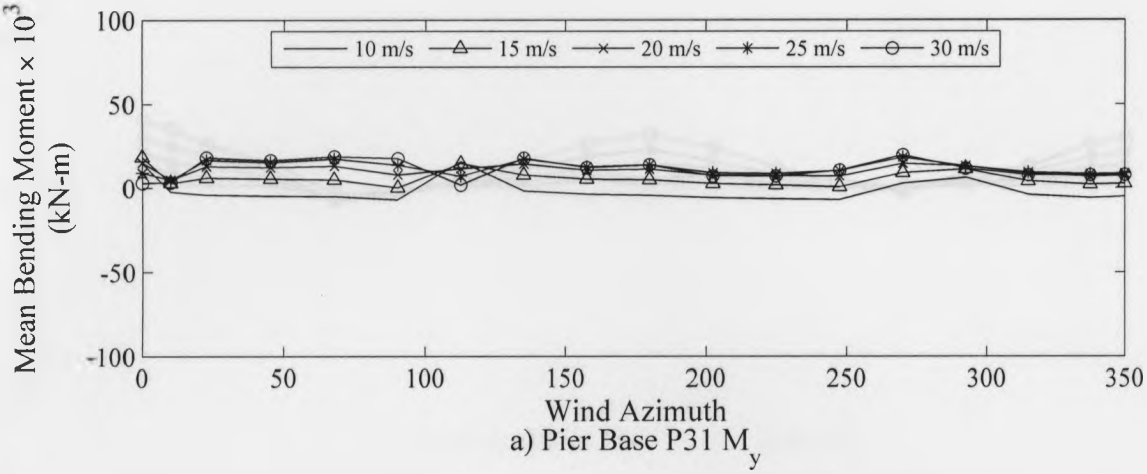

a) Pier Base P31 M_y

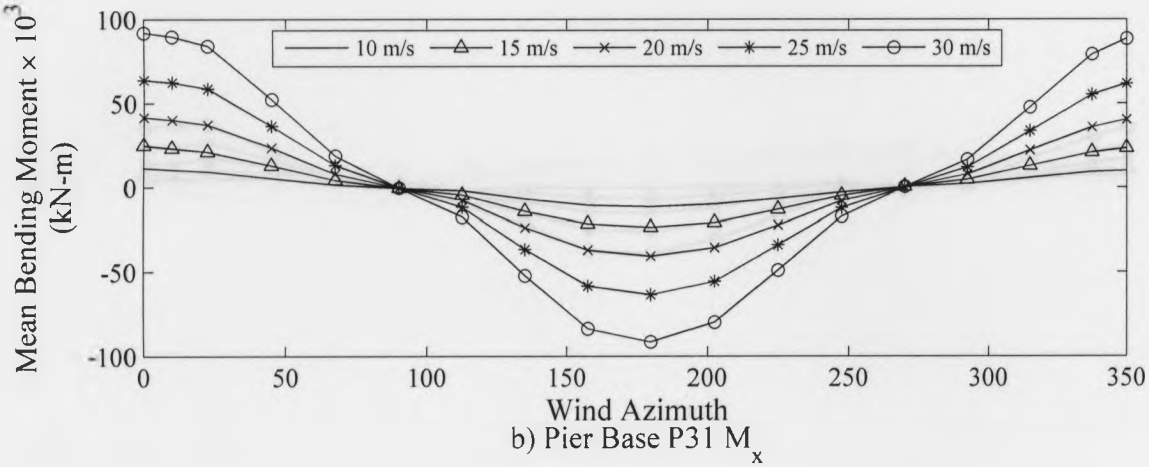

b) Pier Base P31 M_x

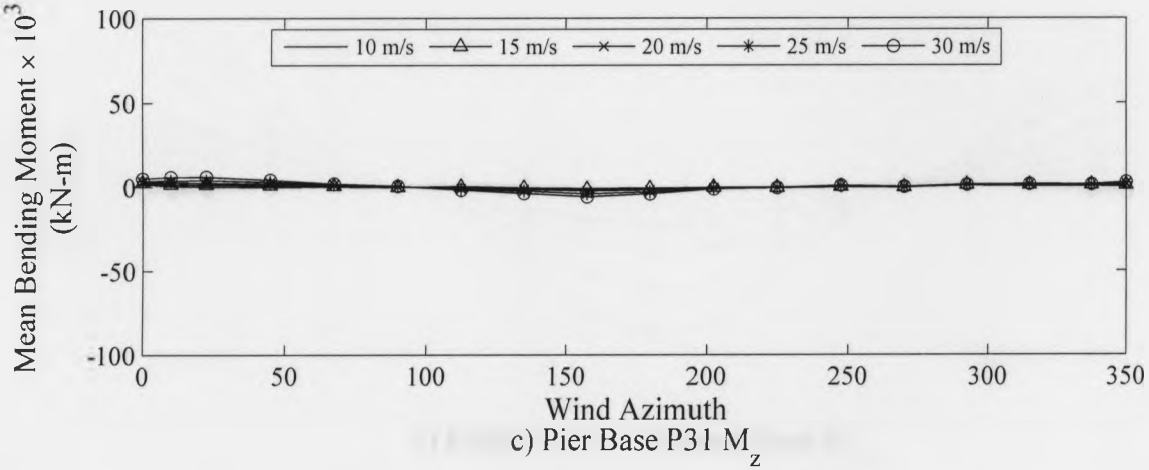

c) Pier Base P31 M_z

Figure 4B.8 – Variation of Mean Bending Moment with Wind Azimuth at the Base of Pier 31

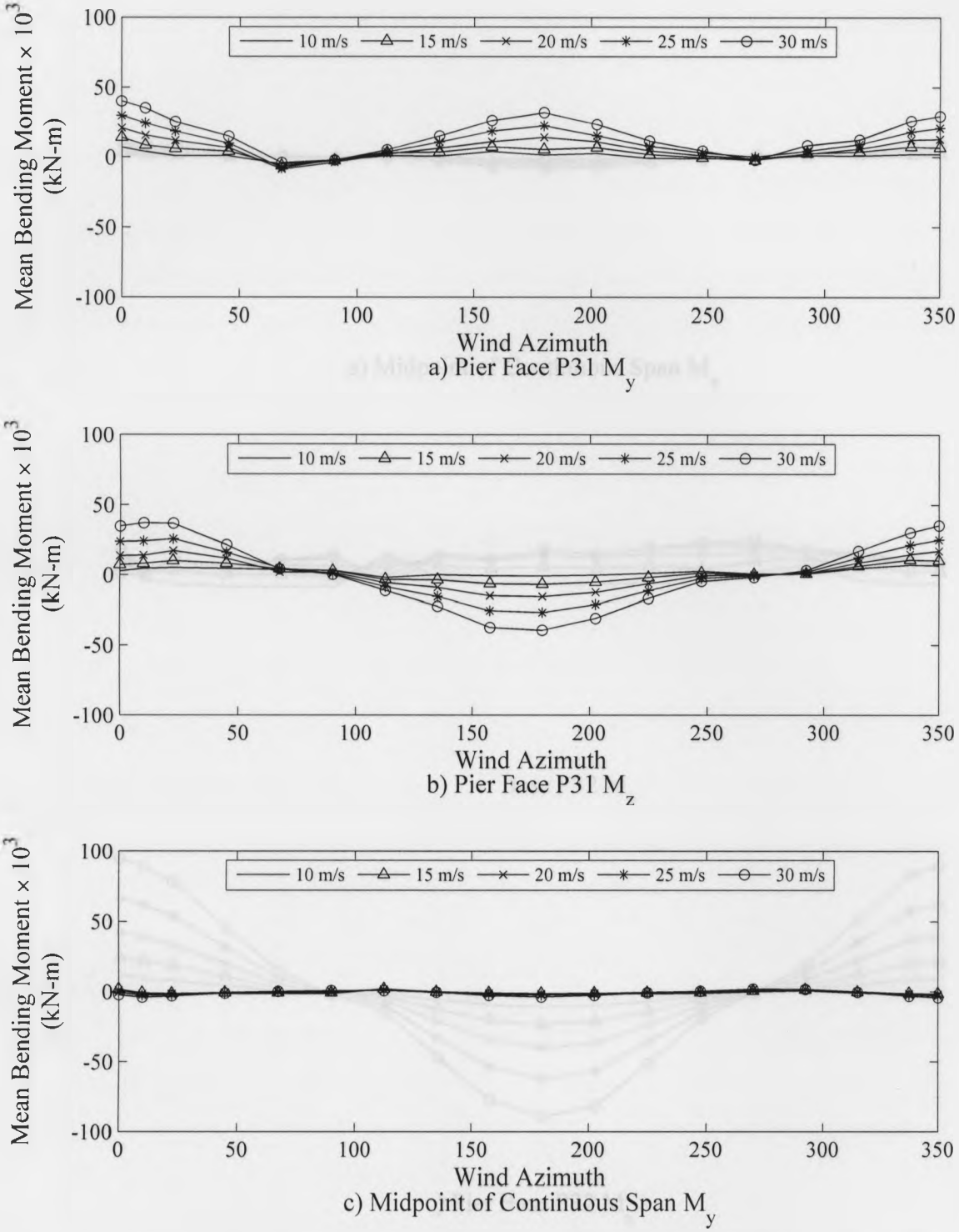

Figure 4B.9 – Variation of Mean Bending Moment with Wind Azimuth at the Face of Pier 31 and Midpoint of the Continuous Span

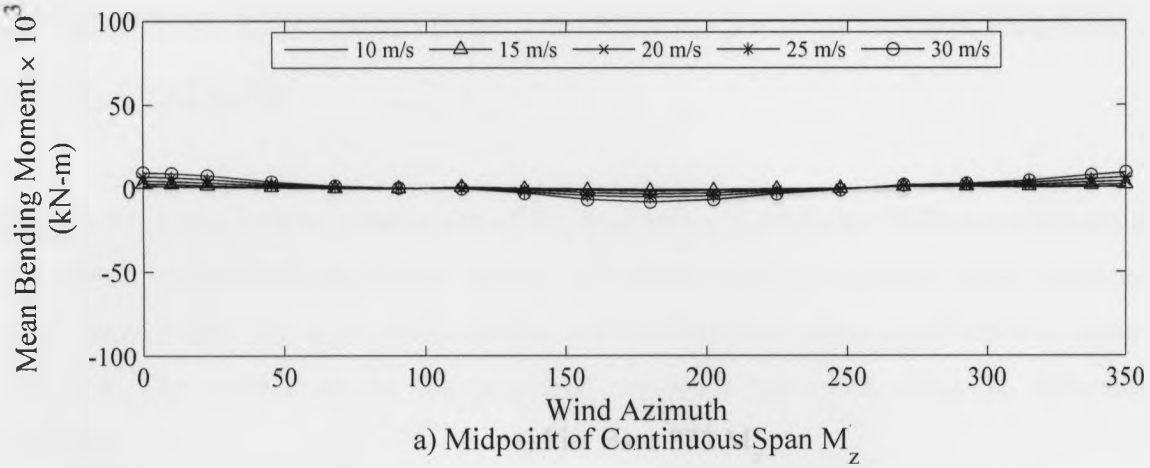

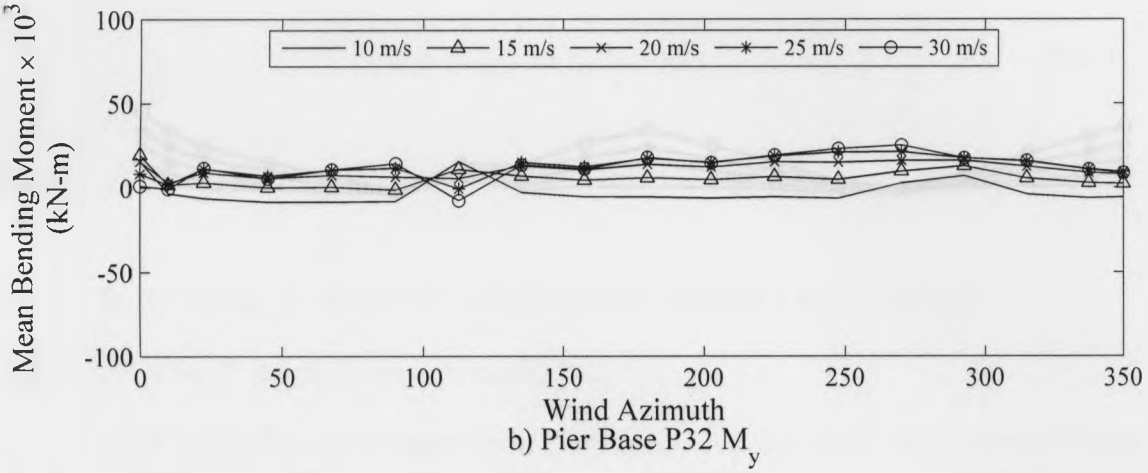

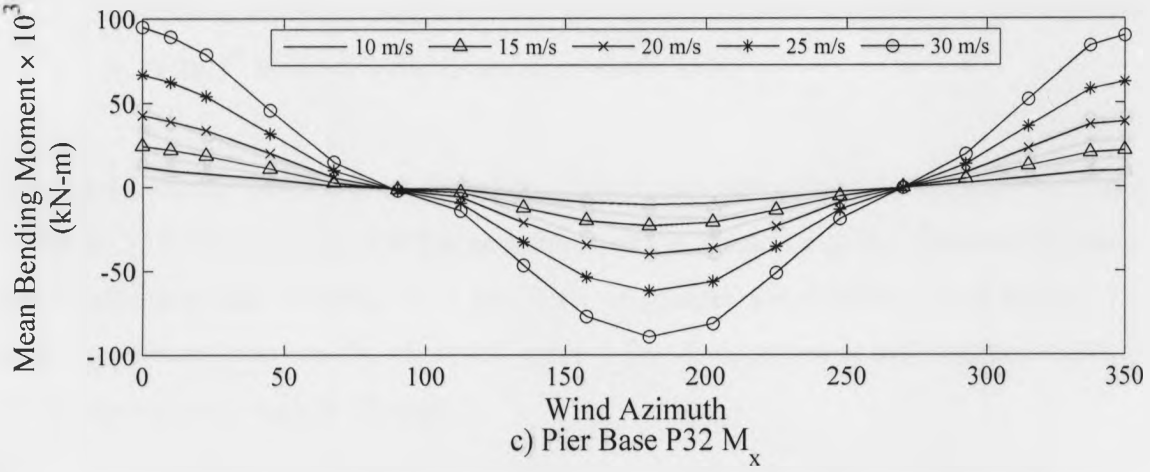

Figure 4B.10 – Variation of Mean Bending Moment with Wind Azimuth at the Midpoint of Continuous Span and Base of Pier 32

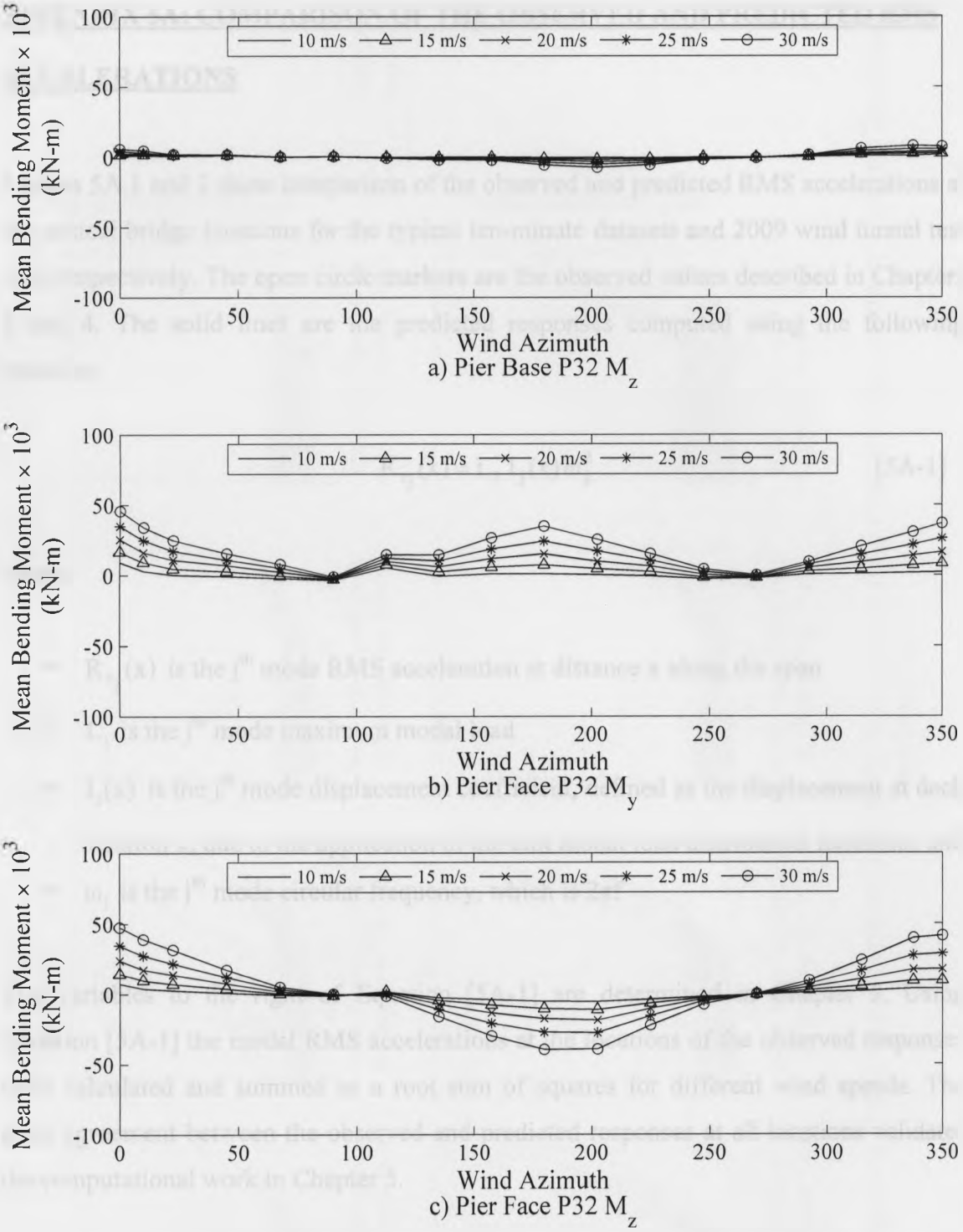

Figure 4B.11 – Variation of Mean Bending Moment with Wind Azimuth at the Base and Face of Pier 32

APPENDIX 5A: COMPARISON OF THE OBSERVED AND PREDICTED RMS ACCELERATIONS

Figures 5A.1 and 2 show comparison of the observed and predicted RMS accelerations at the critical bridge locations for the typical ten-minute datasets and 2009 wind tunnel test data, respectively. The open circle markers are the observed values described in Chapters 3 and 4. The solid lines are the predicted responses computed using the following equation:

$$R_{r_j}(x) = L_j \, I_j(x) \omega_j^2 \qquad [5A\text{-}1]$$

where:

- $R_{r_j}(x)$ is the j^{th} mode RMS acceleration at distance x along the span
- L_j is the j^{th} mode maximum modal load
- $I_j(x)$ is the j^{th} mode displacement coefficient, defined as the displacement at deck location x, due to the application of the unit modal load distribution functions, and
- ω_j is the j^{th} mode circular frequency, which is $2\pi f$

The variables to the right of Equation [5A-1] are determined in Chapter 5. Using Equation [5A-1] the modal RMS accelerations at the locations of the observed responses were calculated and summed as a root sum of squares for different wind speeds. The good agreement between the observed and predicted responses at all locations validates the computational work in Chapter 5.

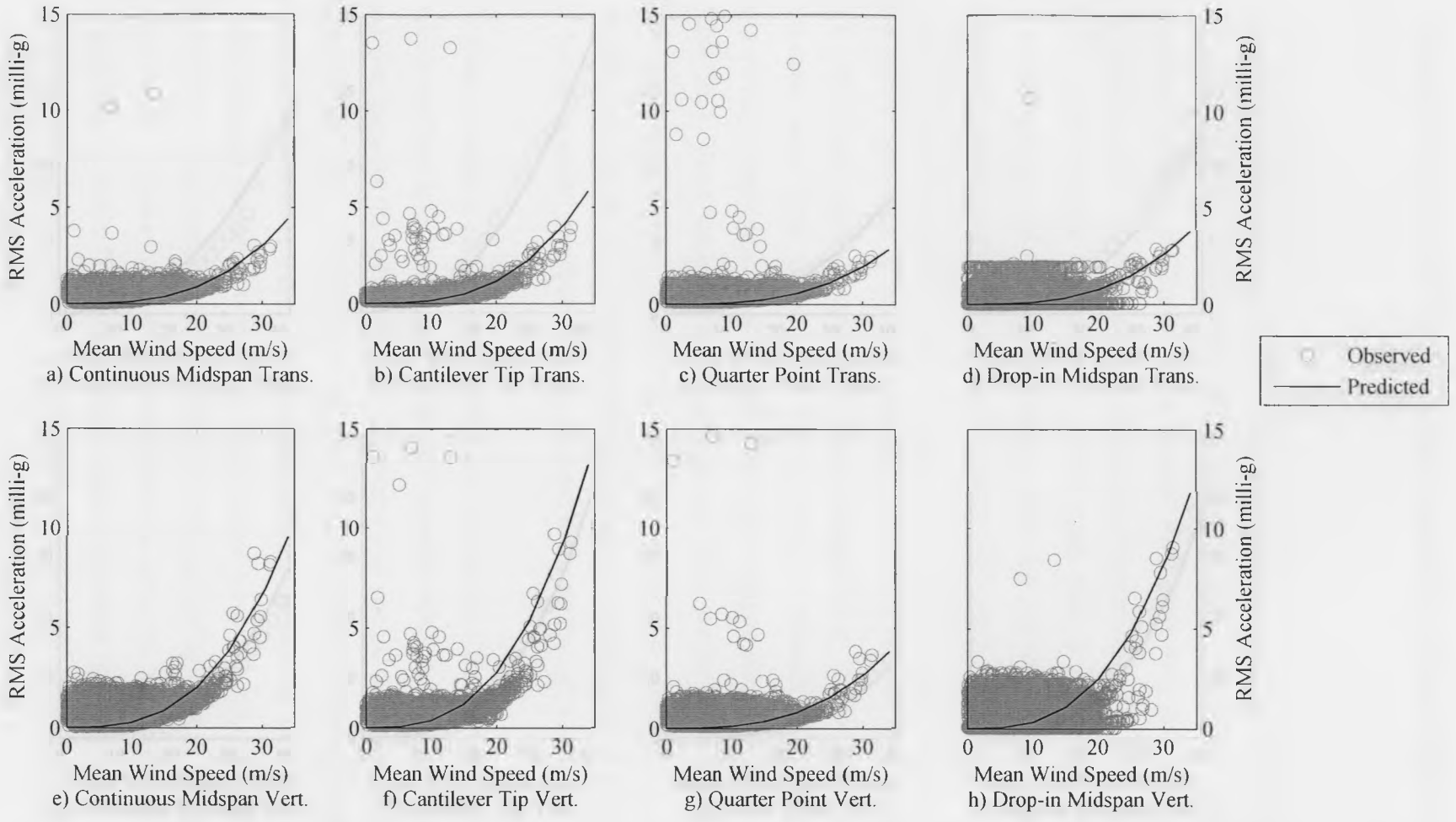

Figure 5A.1 – Comparison of the Observed and Predicted RMS Accelerations at the Critical Bridge Locations – Typical Ten-Minute Time Histories

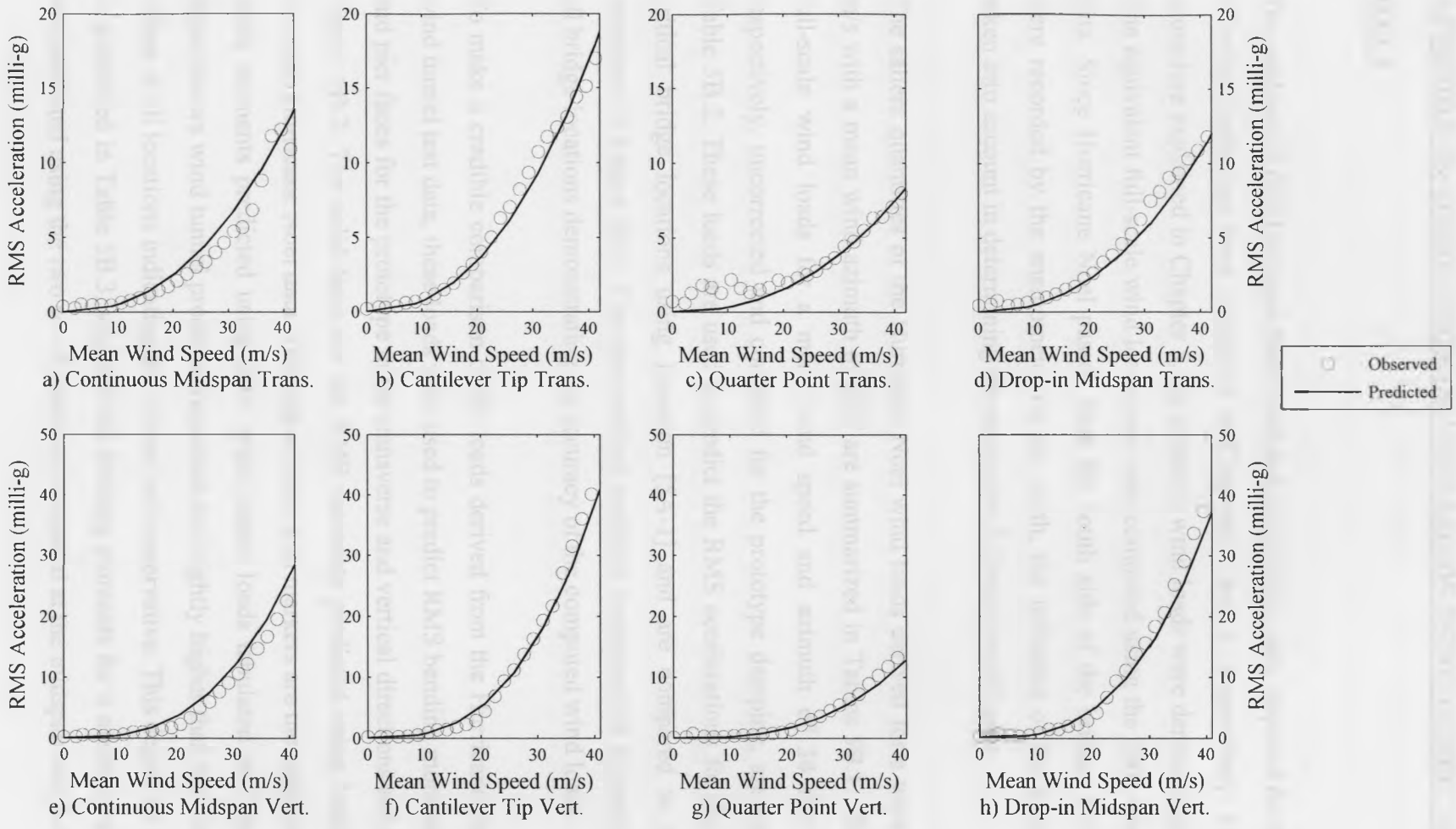

Figure 5A.2 – Comparison of the Observed and Predicted RMS Accelerations at the Critical Bridge Locations – Wind Tunnel Test Data 2009

APPENDIX 5B: DERIVATION OF WIND LOADS USING HURRICANE NOEL DATA

The analysis of the Hurricane Noel wind and acceleration data, required for the derivation of wind loads, has been presented in Chapters 2 and 3, respectively. Following the procedure explained in Chapter 5, the dynamic wind loads were derived using these data. The equivalent full-scale wind loads were also computed using the 2009 wind tunnel test data. Since Hurricane Noel passed from the south side of the bridge, while the winds were recorded by the anemometer on the north, the influence of the bridge deck was taken into account in determining the equivalent full-scale wind loads.

The salient quantities of the Hurricane Noel wind loads derived for a wind speed of 34 m/s with a mean wind azimuth of 200° are summarized in Tables 5B.1. The equivalent full-scale wind loads for a mean wind speed and azimuth of 34 m/s and 202.5°, respectively, uncorrected and corrected for the prototype damping, are summarized in Table 5B.2. These loads are used to predict the RMS accelerations for the prototype at critical bridge locations using Equation [5A-1] and are compared to the observed responses in Figure 5B.1. The observed and predicted responses are in good agreement at all bridge locations demonstrating the accuracy of the computed wind loads.

To make a credible comparison of the loads derived from the Hurricane Noel and 2009 wind tunnel test data, these loads were used to predict RMS bending moments at midspan and pier faces for the prototype in the transverse and vertical directions and are shown in Figure 5B.2. The solid lines are the RMS moments predicted using loads determined from the Hurricane Noel data. The broken lines with markers are the equivalent full-scale RMS moments predicted using 2009 wind tunnel loads tabulated in Table 5B.2. The figure shows wind tunnel predicted responses are slightly higher than the Hurricane Noel values at all locations indicating the former are conservative. This degree of conservatism is quantified in Table 5B.3, where RMS bending moments for a mean wind speed of 34 m/s predicted using the two set of loads are compared at the midspan and pier faces in the

transverse and vertical directions. Values shown in the 3rd column in the table are the RMS moments predicted using the wind tunnel loads normalized using the RMS moments derived from the Hurricane Noel data. The transverse and vertical RMS moments predicted using the 2009 wind tunnel loads are within 12% and 13%, respectively, of the values derived from the Hurricane Noel data.

Table 5B.4 compares peak bending moments predicted using loads derived from the Hurricane Noel data and the 2009 wind tunnel test results for a mean wind speed and azimuth of 34 m/s and $200^{o} \pm 5^{o}$, respectively, with the peak bending moments predicted using the design loads. The mean bending moments are available from the 2009 wind tunnel test results. The dynamic wind loads from the Hurricane Noel data are used to determine RMS bending moments. A mean peak factor of 3.5 is determined from the analysis of the on-site monitoring data in Chapter 3. Using Equation [5-19], peak bending moments are computed for the transverse and vertical directions.

The design peak bending moments are 25% – 46% higher in the transverse direction and 115% - 163% higher in the vertical direction compared to the peak bending moments resisted by the bridge during the passage of Hurricane Noel. These are specified or unfactored peak bending moments. Hence one concludes that the bridge was not subjected to the design wind loads during the passage of Hurricane Noel.

Table 5B.1 – Derivation of Dynamic Wind Loads Using Hurricane Noel Data

On-Site Monitoring Data Chapter - 3	Wind Speed V (m/s)	34						
	Wind Azimuth	200°						
	Direction	Transverse				Vertical		
	β	1.76×10^{-6}				4.22×10^{-6}		
	α	2.6				2.7		
	Mode Shape	TS1	TA1	TS2	TA2	VA1	VS1	VS2
	Frequency f_j (Hz)	0.343	0.397	0.485	0.913	0.57	0.678	0.942
Appendix 5B	$\Delta_{j_{max}} \times 10^{-3}$ (m)	4.96	3.40	2.03	0.40	4.06	2.53	1.03
	$I_{j_{max}} \times 10^{-6}$ m/(N/m)	6.59	5.04	3.61	1.38	2.64	1.83	0.80
	L_j (kN/m)	0.75	0.67	0.56	0.29	1.54	1.38	1.28

Table 5B.2 – Derivation of Dynamic Wind Loads Using 2009 Wind Tunnel Test Data

'09 Wind Tunnel Data Chapter - 4	Wind Speed V (m/s)	34						
	Wind Azimuth	202.5°						
	Direction	Transverse				Vertical		
	β	8.17×10^{-6}				7.65×10^{-6}		
	α	2.2				2.8		
	Mode Shape	TS1	TA1	TS2	TA2	VA1	VS1	VS2
	Frequency f_j (Hz)	9.37	12.16	16.11	29.13	15.59	17.96	20.59
Appendix – 5B	$\Delta_{j_{max}} \times 10^{-3}$ (m)	10.36	5.82	3.13	0.85	8.33	5.59	3.81
	$I_{j_{max}} \times 10^{-6}$ m/(N/m)	6.75	3.86	2.44	0.58	2.13	1.88	1.53
	L_j (kN/m)	1.54	1.51	1.28	1.46	3.92	2.98	2.49
	ζ_{tm_j} (%)	0.5	0.45	0.55	0.45	0.7	0.6	0.5
	ζ_{tp_j} (%)	2.0	1.95	1.68	1.95	3.91	2.06	1.51
	L_{c_j} (kN/m)	0.77	0.72	0.73	0.70	1.66	1.61	1.43

Table 5B.3 – Comparison of RMS Bending Moments for a Mean Wind Speed of 34 m/s – Hurricane Noel versus Wind Tunnel 2009

Data Type	Transverse Modal Wind Loads (kN/m)				Root Mean Square (RMS) Bending Moment (kN-m x 10^3)			RMS Bending Moment Ratio with respect to Hurricane Noel		
	TS1	TA1	TS2	TA2	Midspan	Pier 32 Face	Pier 31 Face	Midspan	Pier 32 Face	Pier 31 Face
Hurricane Noel	0.75	0.67	0.56	0.29	2.02	4.69	4.74	1.00	1.00	1.00
Wind Tunnel '09	0.77	0.72	0.73	0.70	2.27	5.15	5.05	1.12	1.10	1.07
Data Type	Vertical Modal Wind Loads (kN/m)				Root Mean Square (RMS) Bending Moment (kN-m x 10^3)			RMS Bending Moment Ratio with respect to Hurricane Noel		
	VA1	VS1	VS2	VA2	Midspan	Pier 32 Face	Pier 31 Face	Midspan	Pier 32 Face	Pier 31 Face
Hurricane Noel	1.54	1.38	1.28	-	1.00	9.02	8.99	1.00	1.00	1.00
Wind Tunnel '09	1.66	1.61	1.43	-	1.13	9.99	10.10	1.13	1.11	1.12

Table 5B.4 – Comparison of Peak Bending Moments – Hurricane Noel versus Specified Design Loads

Load Type	Direction	Mean Bending Moment (kN-m x 10^3)			RMS Bending Moment (kN-m x 10^3)			Peak Bending Moment (kN-m x 10^3)		
		Midspan	Short Pier Face	Long Pier Face	Midspan	Short Pier Face	Long Pier Face	Midspan	Short Pier Face	Long Pier Face
Wind Tunnel '09 Hurricane Noel (34 m/s)	Transverse	8.38	37.64	37.64	2.02	4.69	4.73	15.44	54.07	54.21
Specified Design Loads (30.5 m/s)	Transverse	8.81	37.88	37.88	3.91	8.54	9.53	22.51	67.79	71.23
Ratio – Design / (WT '09 or H. Noel)	Transverse	1.05	1.01	1.01	1.94	1.82	2.01	1.46	1.25	1.31
Wind Tunnel '09 Hurricane Noel (34 m/s)	Vertical	3.40	27.81	27.81	1.00	9.02	8.99	6.90	59.37	59.28
Specified Design Loads (30.5 m/s)	Vertical	3.19	28.85	28.85	3.33	29.74	36.28	14.85	132.94	155.83
Ratio – Design / (WT '09 or H. Noel)	Vertical	0.94	1.04	1.04	3.33	3.30	4.03	2.15	2.24	2.63

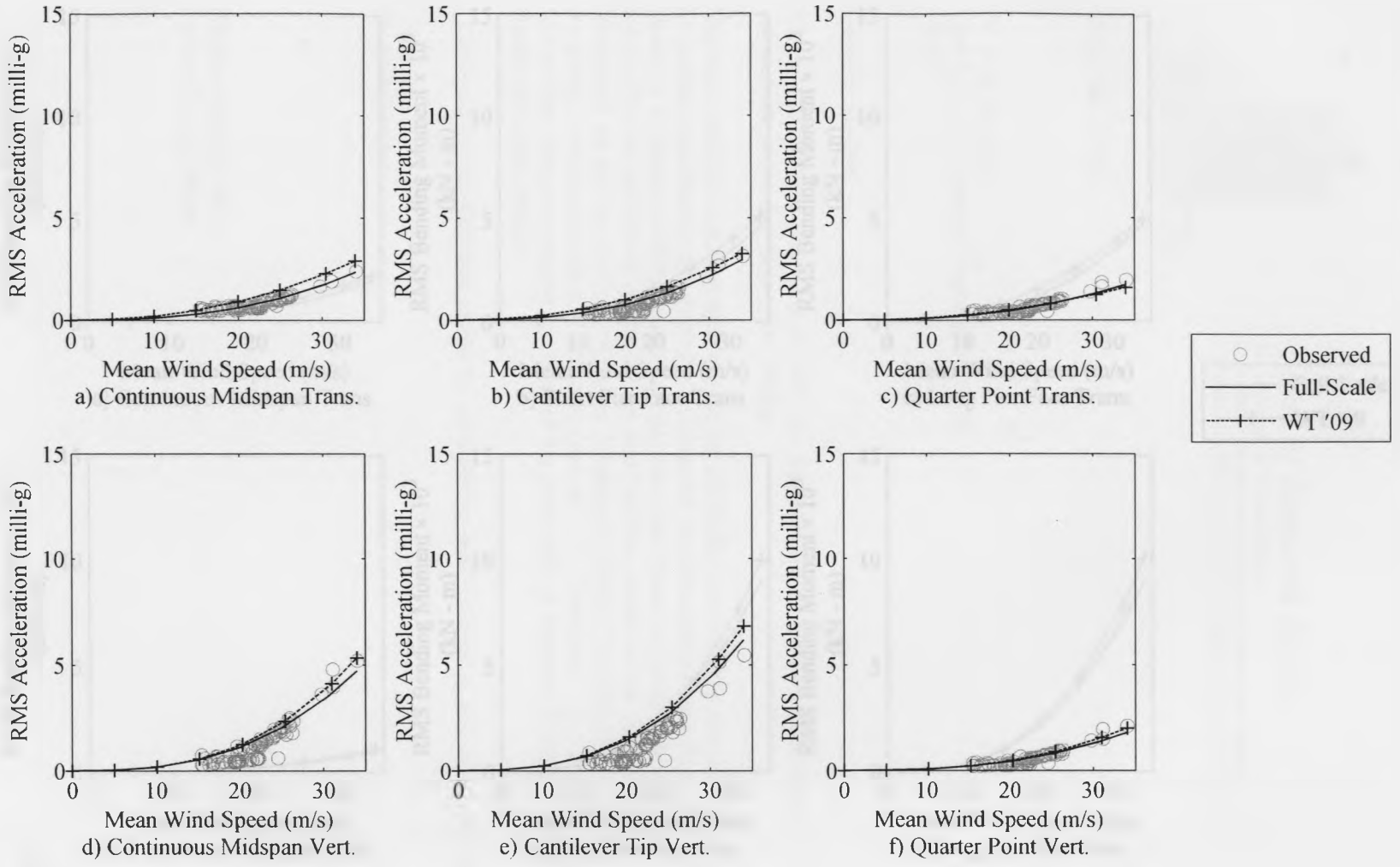

Figure 5B.1 – Comparison of the Observed and Predicted RMS Accelerations at the Critical Bridge Locations Hurricane Noel and 2009 Wind Tunnel Test Data

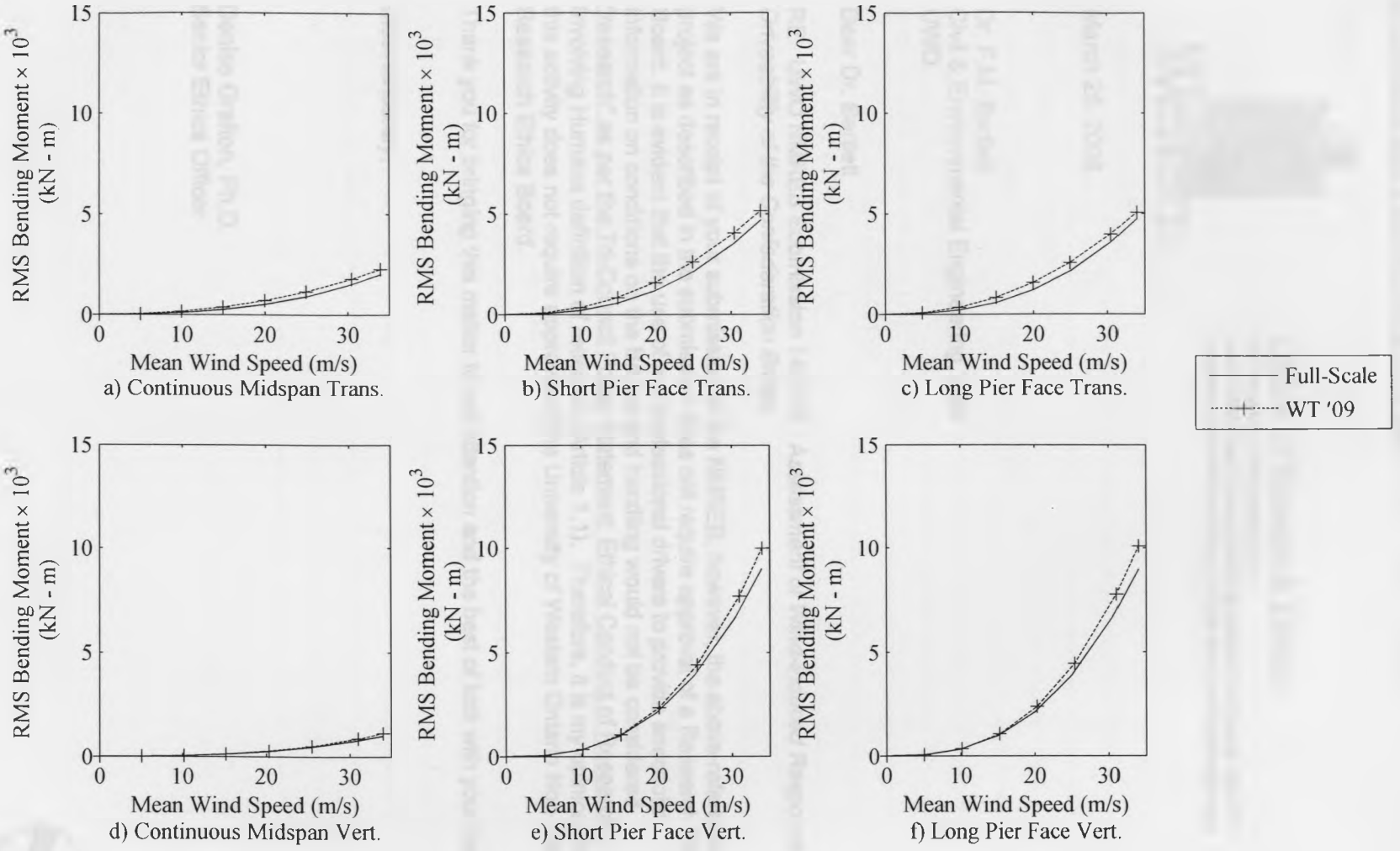

Figure 5B.2 – Full-Scale RMS Bending Moments Predicted Using Hurricane Noel and Wind Tunnel Data

APPENDIX 6A: ETHICS APPROVAL

Western

Office of Research Ethics
The University of Western Ontario
Room 00045 Dental Sciences Building, London ON, Canada, N6A 5C1
Telephone: (519) 661-3036 Fax: (519) 850-2466 Email: ethics@uwo.ca

March 26, 2008

Dr. F.M. Bartlett
Civil & Environmental Engineering, SEB
UWO

Dear Dr. Bartlett

RE: UWO NMREB Submission 14071S - *Assessment of Wind-Induced Response and Driveability of the Confederation Bridge*

We are in receipt of your submission to the NMREB; however, the above-referenced project as described in the submission does not require approval of a Research Ethics Board. It is evident that the use of two professional drivers to provide anecdotal information on conditions on the Bridge and handling would not be considered "research" as per the Tri-Council Policy Statement: Ethical Conduct of Research Involving Humans definition of research (Article 1.1). Therefore, it is my opinion that this activity does not require approval of the University of Western Ontario Non-Medical Research Ethics Board.

Thank you for bringing this matter to our attention and the best of luck with your report.

Most sincerely,

Denise Grafton, Ph.D.
Senior Ethics Officer

ORIGINAL

APPENDIX 6B: CONFEDERATION BRIDGE DRIVABILITY TEST DATA SHEET

Test Date		Fs (Hz)	
East Bound		West Bound	
Vehicle Mean Speed (km/h)			
Distance Travelled (km)			
Required Sweeps @ 64 Hz			
Time Required (minutes)			
Broadcast Trigger Time of Day (HHMMSS)			
Pier 20 Time of Day (HHMMSS)			
Pier 21 Time of Day (HHMMSS)			
Pier 31 – 32 Time of Day (HHMMSS)			
Pier 41 Time of Day (HHMMSS)			
Time of Day Leaving Bridge			
Download CSV Filename			
Trigger Number			

Anecdotal Driver Experience						
	Not Perceptible	Slightly Perceptible	Distinctly Perceptible	Strongly Perceptible	Disturbing	Time
1						
2						
3						
4						
5						
6						
7						
8						
9						
10						

Notes:

APPENDIX 6C: EXPONENTIAL FITS TO THE DISTRIBUTIONS OF TRAILER ACCELERATIONS

Figure 6C.1 shows exponential functions fitted to the curves shown in Figure 6.15. The advantage of the exponential fits to the curves has been discussed in detail in Chapter 6.

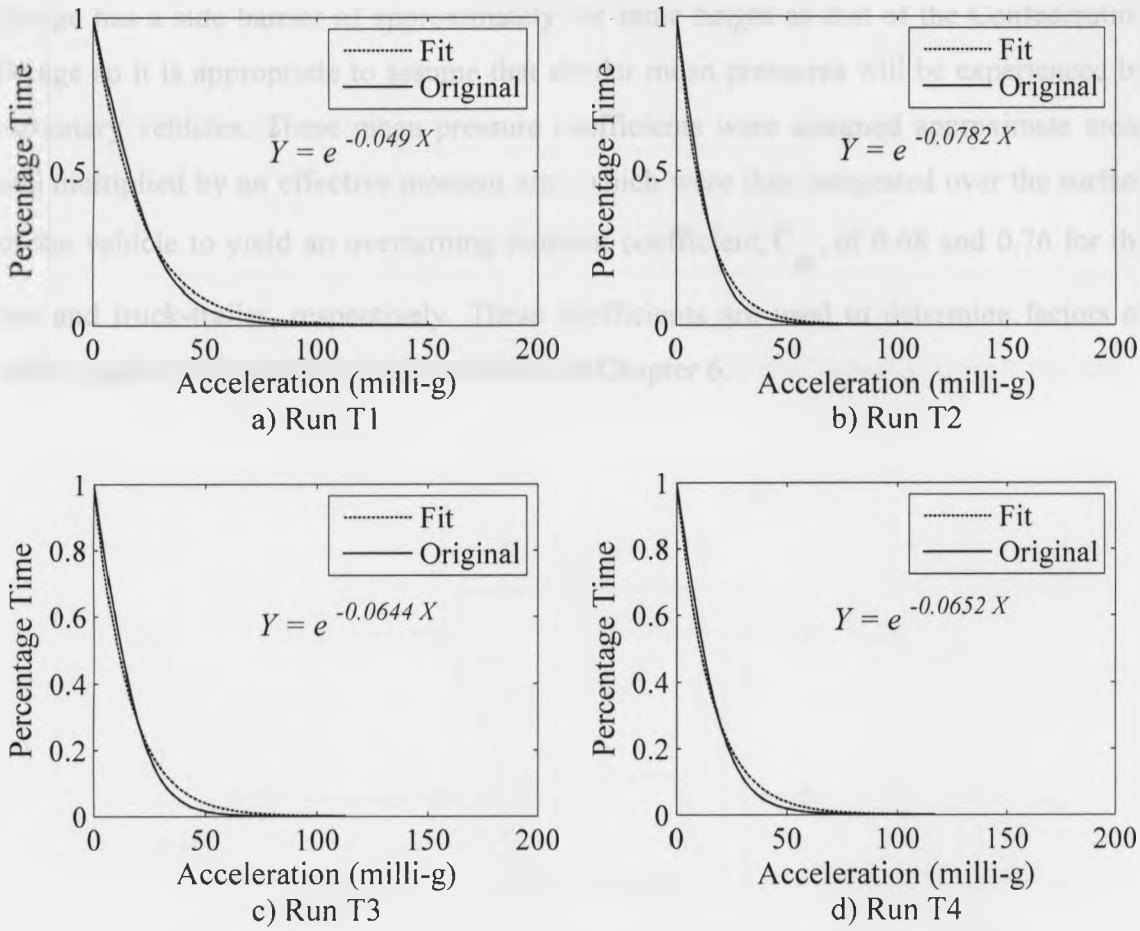

Figure 6C.1 – Fits to the Transverse Accelerations at the Driver's Head Level Derived from Truck Cabin Roof for the East and West Bound

APPENDIX 6D: PRESSURE DISTRIBUTION COEFFICIENTS FOR A BUS AND TRUCK-TRAILER

Pressure tests for a passenger bus and a truck-trailer (as well as two other typical highway vehicles) were performed for the Bronx-Whitestone Bridge section model study at BLWTL in 2001 [King and Kong 2001], yielding the mean pressure coefficients for the bus and truck shown in Figures 6D.1 and 6D.2, respectively. The Bronx-Whitestone Bridge has a side barrier of approximately the same height as that of the Confederation Bridge so it is appropriate to assume that similar mean pressures will be experienced by stationary vehicles. These mean pressure coefficients were assigned approximate areas and multiplied by an effective moment arm, which were then integrated over the surface of the vehicle to yield an overturning moment coefficient, $\overline{C}_m$, of 0.68 and 0.76 for the bus and truck-trailer, respectively. These coefficients are used to determine factors of safety against roll-over for the two vehicles in Chapter 6.

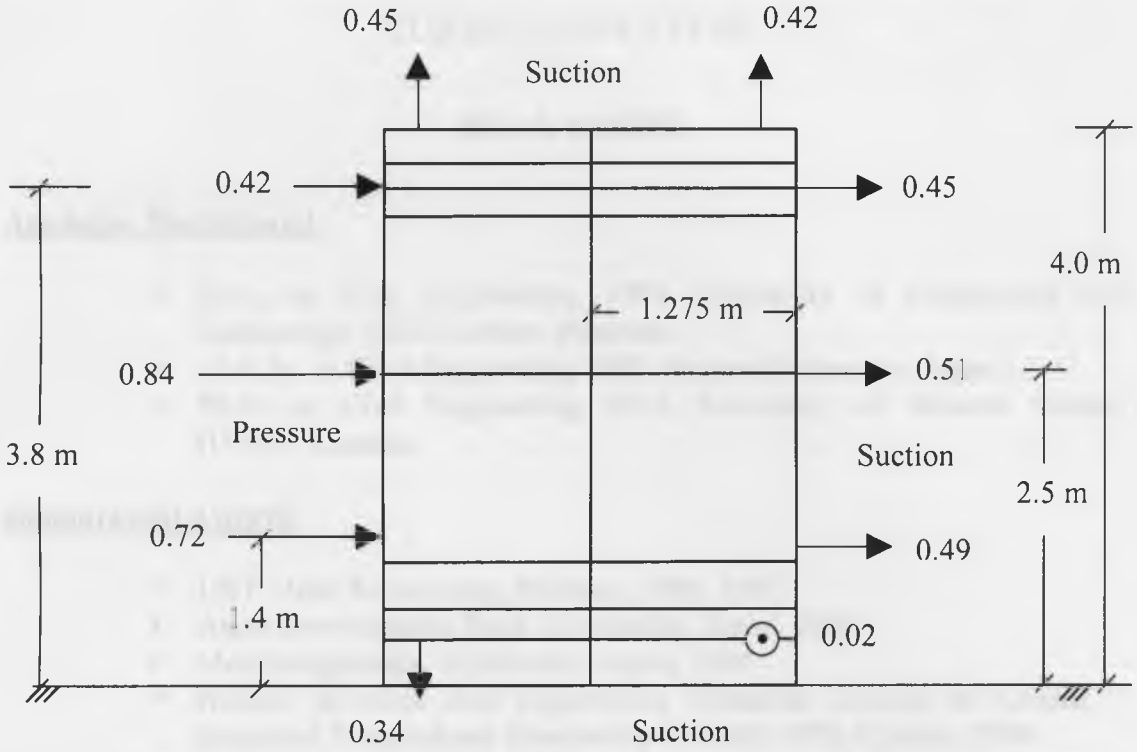

Figure 6D.1 – Pressure Distribution on Cross Section of Bus [adapted from King and Kong 2001]

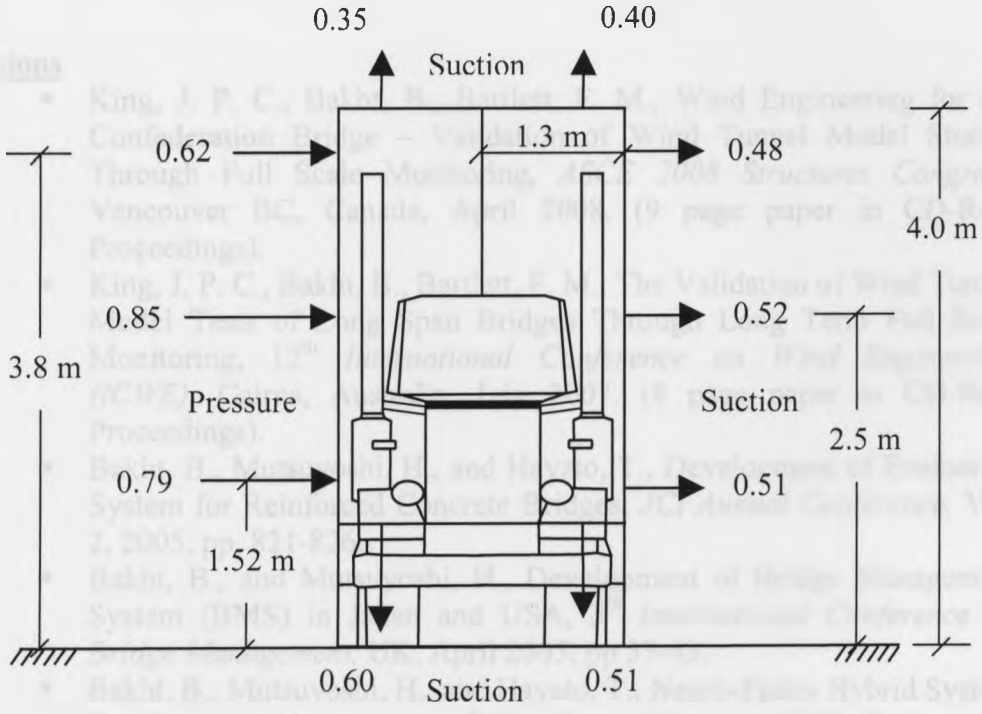

Figure 6D.2 – Pressure Distribution on Cross Section of Truck-Trailer [adapted from King and Kong 2001]